The Dissertation Committee for Julie Ann Hollek
certifies that this is the approved version of the following dissertation:

The Chemical Abundances of Stars in the Halo (CASH) Project

Committee:

Christopher Sneden, Supervisor

Volker Bromm

Harriet Dinerstein

Anna Frebel

Matthew Shetrone

The Chemical Abundances of Stars in the Halo (CASH) Project

by

Julie Ann Hollek, B.S.; B.S.; M.A.

DISSERTATION

Presented to the Faculty of the Graduate School of

The University of Texas at Austin

in Partial Fulfillment

of the Requirements

for the Degree of

DOCTOR OF PHILOSOPHY

THE UNIVERSITY OF TEXAS AT AUSTIN

August 2014

Dedicated to Colby, because I'm not that mean.

Acknowledgments

First, thank you to my committee. My advisor Chris Sneden has been instrumental in gently guiding me to finishing. Harriet Dinerstein has kept me on my toes for the past 6 years, which makes me think a little harder about what I'm trying to present in a very good way. Matthew Shetrone has always provided encouragement and practical advice dating all the way back to 2006. Volker Bromm has been quietly supportive. Finally, I wouldn't be writing this without the guidance of Anna Frebel. Thank you for giving me project ideas and the pushes I needed to get the job done. I would also like to thank my collaborators. Thank you to Ian Roederer for coming before me and helping to start the CASH project. Amanda Karakas provided amazing AGB nucleosynthesis models (and even better insight into them). Vini Placco took Amanda's models and helped to interpret them for our project, in addition to being an amazing sounding board for crazy hypotheses and analysis methods. Finally, thank you to Chris Waters for reading every single one of my paper drafts, whether involved or not, creating Robospect, writing scripts, and general help along the way.

Thank you to everyone who has helped create a community for me in Austin and in life. The best piece of advice that I got about choosing a grad school was to go where you'll be happy outside of the office as well. Chris, Kyle, Irina, Randi, and everyone else, thank you for making that happen. I

am so glad that you all were part of our adopted family down here. Thank you to Ramona for allowing me to ignore you for the past 6 months. Thank you to Eco Kids Pre-K, Dr. Scott the Paleontologist, and my friends and family who have stepped in and loved my child so that she's always around someone who wants what is best for her. Most importantly, thank you to Colby. You picked up the slack when it came to being functional adults and have spent countless hours making sure that we weren't arrested for accidentally letting the baby die.

The Chemical Abundances of Stars in the Halo (CASH) Project

Publication No. _____

Julie Ann Hollek, Ph.D.
The University of Texas at Austin, 2014

Supervisor: Christopher Sneden

This dissertation is a compilation of four separate studies under the umbrella of the Chemical Abundance of Stars in the Halo (CASH) Project. The overall goal of the CASH project is to gain a better understanding of the events and processes that occurred during the early universe that shaped the composition of the stars that we observe today. In order to do so, we have conducted a comprehensive study of the abundances of the oldest observable stars. These stars have preserved the chemical signature of the material from which they formed in their atmospheres. The old, metal-poor stars that make up the stellar halo thus provide a means to study the history of the universe. We will discuss the motivation for the project in Chapter 1, introducing the field of metal-poor halo stars and providing background about the processes that have contributed to the chemical make up of the stars. The first generation

of stars that created much of the material from which these stars formed are discussed, along with the low-mass evolved stars that synthesized additional elements in their interiors that are also observed in metal-poor stars today.

Utilizing so-called "snapshot" spectra obtained with the High Resolution Spectrograph on the Hobby-Eberly Telescope at McDonald Observatory, we provide abundances for 262 stars over the sample. In Chapter 2, we present Robospect, a new code to automatically measure and deblend line equivalent widths for both absorption and emission spectra. We used this code to calculate equivalent width measurements, which provide the foundation of the analysis, from our spectra. We test the accuracy of these measurements against simulated spectra as well as manual equivalent width measurements of five stellar spectra over a range of signal-to-noise values and a set of long slit emission spectra. We find that Robospect accurately matches both the synthetic and manual measurements, with scatter consistent with the expectations based on the data quality and the results of Cayrel (1988).

In Chapter 3, we present a comprehensive abundance analysis of 20 elements for 16 new low-metallicity stars from the CASH project. The abundances have been derived from both Hobby-Eberly Telescope High Resolution Spectrograph snapshot spectra ($R \sim 15,000$) and corresponding high-resolution ($R \sim 35,000$) Magellan MIKE spectra. The stars span a metallicity range from [Fe/H] from -2.9 to -3.9, including four new stars with [Fe/H] < -3.7. These pilot sample stars are the most metal-poor ([Fe/H] $\lesssim -3.0$) of the brightest stars included in CASH and are used to calibrate a newly-developed,

automated stellar parameter and abundance determination pipeline. This code is used for the entire CASH snapshot sample. We find that the pipeline results are statistically identical for snapshot spectra when compared to a traditional, manual analysis from a high-resolution spectrum. We find four stars to be carbon-enhanced metal-poor (CEMP) stars, confirming the trend of increasing [C/Fe] abundance ratios with decreasing metallicity. Two of these objects can be classified as CEMP-no stars, adding to the growing number of these objects at [Fe/H]< -3. We also find four neutron-capture enhanced stars in the sample, one of which has [Eu/Fe] of 0.8 with clear r-process signatures.

In Chapter 4, we present stellar parameters and abundances for the full CASH sample of 263 metal-poor halo star candidates derived from snapshot spectra obtained with the High Resolution Spectrograph on the Hobby-Eberly Telescope at McDonald Observatory. We determine abundance statistics and trends for 16 elements over the full sample. We identify astrophysically-interesting stars that merit further investigation, including carbon-enhanced metal-poor stars, neutron-capture element enhanced stars, and extremely metal-poor stars. We note one Li giant with a unique abundance pattern.

In Chapter 5 we present a detailed abundance analysis of 23 elements for a newly discovered carbon-enhanced metal-poor (CEMP) star, HE 0414−0343, from the CASH sample. Its spectroscopic stellar parameters are $T_{eff} = 4863\,\mathrm{K}$, $\log g = 1.25$, $\xi = 20\,\mathrm{km\,s^{-1}}$, and [Fe/H] $= -2.24$. Radial velocity measurements covering seven years indicate HE 0414−0343 to be a binary. HE 0414−0343 has [C/Fe] = 1.44 and is strongly enhanced in neutron-capture

elements but its abundances cannot be reproduced by a solar-type s-process pattern alone. It could be classified as "CEMP-r/s" star but we find that no r-process component is required as explanation of this and other similar stars classified as "CEMP-s" and "CEMP-r/s" stars. Rather, based on comparisons with AGB star nucleosynthesis models, we suggest a new physically-motivated classification scheme, especially for the still poorly-understood "CEMP-r/s" stars. Importantly, it reflects the continuous transition between these so-far distinctly treated subgroups: CEMP-sA, CEMP-sB, and CEMP-sC. The [Y/Ba] ratio parameterizes the classification and can thus be used to classify any future such stars. Possible causes for the transition include the number of thermal pulses the AGB companion underwent and the effect of different AGB star masses on their nucleosynthetic yields. We then speculate that higher AGB masses may explain "CEMP-r/s" or now CEMP-sB and CEMP-sC stars, whereas less massive AGB stars would account for "CEMP-s" or CEMP-sA stars. Based on a limited set of AGB models, we suggest the abundance signature of HE 0414−0343 to have come from a $> 1.3 M_{\odot}$ mass AGB star and a late-time mass transfer, thereby making it a CEMP-sC star.

Finally, in Chapter 6, we summarize our results and provide future directions for the project.

Table of Contents

List of Tables

List of Figures

Chapter 1

Introduction

1.1 First Stars

The primordial universe existed in a vastly different state than the one we inhabit today. The period of rapid inflation, which occurred 10^{-37} s after the Big Bang, enhanced density fluctuations in the dark matter (DM) in the early universe. In the first three minutes after the Big Bang, the elements hydrogen, helium, and trace amounts of lithium were created in what is known as the Era of Nucleosynthesis. Over the next billion years, the universe cooled and expanded during the Era of Atoms, which allowed these elements to come together to form the first stars, known as Population (Pop) III stars.

Star formation in the early universe is distinct from the star formation observed today. The DM density enhancements formed into DM halos, which attracted baryonic matter in the form of gas made up of the products of Big Bang nucleosynthesis. When the DM halo grew to a virial temperature of $\sim$ 2000 K through hierarchical merging, its gas was then warm enough that molecular gas, in the form of H_2, could be formed (Tegmark et al., 1997). H_2 cooling enabled the baryonic matter to collapse, allowing the formation of a Pop III star. There is still much that is unknown about these stars. One of

the biggest unanswered questions is, what is the characteristic mass of a Pop III star? Before computational power improved such that simulations could be conducted for longer physical time scales at better resolution, it was thought that the first stars were much more massive than any stars observed today. Masses from 500-1000 $M_\odot$ were considered red possible (Bromm et al., 2002). Later simulations revised this number down to $\sim$100 $M_\odot$, but the most recent studies (e.g.,Hosokawa et al. (2011); Stacy et al. (2012)) indicate that the upper limit for the mass of a Pop III star is $\sim 40M_\odot$. Furthermore, simulations by Turk et al. (2009); Stacy et al. (2010); Clark et al. (2011) indicate that Pop III stars may form in binary or multiple systems. This further complicates the question of characteristic mass. However, the current estimate is $\sim$tens of $M_\odot$ (Bromm, 2013).

1.1.1 Initial Mass Function and Nucleosynthesis

The characteristic mass only informs part of the story. The initial mass function (IMF) of the first stars is thought to be "top heavy", which is much different than the bottom-heavy IMF of the stars still observable today. Whereas most Pop I stars are low-mass, the majority of the Pop III stellar mass went into high-mass stars with masses larger than $\sim$ 10 $M_\odot$. While simulations have not ruled out the possibility of a low mass first star, a Pop III star must not grow larger than 0.8 $M_\odot$ in order to be observable today. Large scale surveys have yet to discover such a star, and it would likely be polluted by the products of local or galactic chemical evolution. The charac-

teristic mass of the Pop III stars, coupled with their top-heavy IMF indicate that most should be massive enough to become supernovae at their stellar endpoints. The massive stars are no longer observable. However during their supernova outbursts, they released the elements they synthesized during stellar evolution into the surrounding interstellar medium and also synthesized additional elements. Core collapse supernovae make large amounts of α-elements, such as Si, Mg, and Ca along with Fe-peak elements such as Mn, Fe, and Ni. These elements, along with those synthesized during the course of stellar evolution provide seed nuclei for another form of nucleosynthesis called the rapid neutron-capture (r-) process. In the r-process, heavy seed nuclei are exposed to a very high neutron flux. During the course of a supernova, $\beta-$decay cannot operate effectively, thus these seed nuclei capture neutrons until it becomes energetically impossible for them to capture more, or until spontaneous photodissintegration occurs. Thus, when we consider the chemical fingerprint of Pop III stars, we must also look to the generation of stars that formed from the interstellar medium that was polluted by the violent endpoints of the first stars.

1.2 Metal-Poor Stars

The dividing line between Pop III and Pop II stars is that Pop II stars were formed from gas that receieved chemical feedback, thus these stars are

not made of pure Big Bang nucleosynthesis material. [1] However, the transition from Pop III to Pop II is really a transition from a top-heavy to a bottom-heavy IMF. In order for this to occur, more efficient gas cooling mechanisms were needed. The addition of the materials form by Pop III stars and Pop III stellar endpoints indeed allowed for more efficient cooling mechanisms to work. The two proposed methods are fine structure line cooling and dust cooling. Fine structure line cooling require elements such as O I, C II, Si II, and Fe II to be present in the gas. Electrons in these species are excited to fine structure splitting energy levels and then when the electrons are de-excited, energy is radiated away from the system. In order for fine structure cooling to work efficiently, a critical abundance of these elements is required. Dust-driven cooling works in gas in high density regions, where the dust absorbs and then radiates energy away from the gas.

1.2.1 Asymptotic Giant Branch Stars

Regardless of the cooling mechanism, Pop II stars formed at a much lower characteristic mass than Pop III stars and thus many Pop II stars underwent a stellar evolution similar to stars formed today. This evolution included time spent on the asymptotic giant branch (AGB). AGB stars are important for several reasons; notably, they enable the formation of dust, provide the site for the slow neutron-capture (s-) process, and are one source for carbon

[1] Pop III stars are further subdivided between Pop III.1 and Pop III.2, where Pop III.1 stars form from pristine big bang nucleosynthesis material and Pop III.2 stars form from gas that has undergone radiative feedback.

enhancement. AGB stars have large radii and therefore cool atmospheres in which molecules are able to form. Eventually, high-velocity stellar winds lead to mass loss from the AGB star, enabling the molecules to condense into dust in the circumstellar medium. AGB stars are thought to account for the majority of the stardust formed in the galaxy (Gehrz, 1989).

Beyond dust formation, AGB stars provide a site for production of elements heavier than Fe. The s-process occurs when seed nuclei acquire neutrons one-by-one, over time. The process is referred to as "slow" because the neutron-capture rate, generally on the order of one per several decades, is generally slower than the rate of β-decay, where a neutron is turned into a proton. The s-process is thought to occur over thousands of years. Thus, after the seed nucleus receives a neutron, it can β-decay before acquiring the next one, creating steps up the chart of the nuclides, however the β-decay rates vary greatly from isotope to isotope. The s-process terminates at ^{209}Bi, the last stable isotope that can be created in such a low neutron flux environment. The capture of an additional neutron creates ^{210}Bi which decays to ^{210}Po, an unstable isotope, that decays to ^{206}Pb, which can acquire 3 neutrons before $\beta-$decay occurs, as the decay timescale is longer than the neutron flux rate, where it then turns into ^{209}Pb which $\beta-$decays into ^{209}Bi, which then restarts the cycle. Heavier isotopes do exist, but are only accessible by the r-process.

AGB stars have layers of nucleosynthesis occurring outward from their core. The so-called "onion" model of a star is applicable here, where the interior of the AGB star is fusing the heaviest elements, while successive layers fuse

lighter elements. The fusion in the He layer creates C, which can be brought to the surface of the AGB star, along with other products of nucleosynthesis, during third dredge up events while the star is on the thermally-pulsing AGB. Thus, AGB stars contain many of the products of stellar evolution in their atmospheres that were synthesized in their interiors. For AGB stars in binary or multiple systems, they deposit material onto the surface of their companion. For low-mass, metal-poor stars in these systems, this results in a surface composition with greatly enhanced C abundances, as well as enriched s-process abundances. We observe these stars today as carbon-enhanced metal-poor (CEMP) stars.

1.2.2 The Distribution of Metal-poor Stars in the Galaxy

The history of the Pop III stars and the early universe is encoded in the abundance patterns in the stellar atmospheres of the oldest observable stars today. Where are these stars found? Metal-poor stars exist in several sites throughout the local universe. In the Milky Way, these Pop II stars can most easily be identified in the stellar halo. In total, halo stars have high velocities, spherical kinematics, and low metallicities. Globular clusters belong within the same kinematic profile as the halo. These star clusters formed early in the history of the universe and also contain metal-poor stars and provide an entire population that was formed at the same time to study. Gratton et al. (2004) provides a review of many of the abundance studies of globular clusters.

Within the field halo population, there are stellar streams containg low-

mass groups of metal-poor stars (either globular clusters or small galaxies). These streams are part of the stellar halo, though they still retain some of the kinematic signature of their original galaxy or cluster that is in the process of being shredded by the gravitational field of the Galaxy. These streams are the building blocks of the stellar halo.

Metal-poor stars are also thought to exist in the bulge and the disk of the Galaxy. However, dust and the prevalence of Pop I stars in the bulge make finding bulge Pop II stars a difficult task. The disk of the Milky Way can be divided into the thick and thin disk, where the thick disk contains a metal-poor sample. However, these stars are not as metal-poor as the halo population. The thin disk is comprised of young Pop I stars of which the Sun is a member.

Beyond the Milky Way, ultra-faint dwarf spheroidal galaxies in the Local Group, such as Coma Berenices (Frebel et al., 2010), contain low-metallicity stars. Studies of these galaxies are ongoing, though they indicate that these stars have similar abundance patterns to those of galactic halo stars, providing further evidence that the ultra-faint dwarf galaxies could have been what populated the stellar halo.

1.2.3 Identification and Study of Metal-poor Stars

Given the importance of these stars, many studies have been undertaken to identify and analyze metal-poor stars and they run the gamut from objective prism surveys to high-resolution spectroscopy. Within these studies,

attempts to classify metal-poor stars based on their metallicity and abundance patterns have also been important. These classifications are discussed in Chapters 3 and 4 and at length in Chapter 5.

Bond (1980) identified 132 metal-poor stars with [Fe/H]< -1.5 [2]. These stars were primarily discovered via objective prism plate surveys on the Curtis Schmidt Telescope at Cerro Tololo Inter-American Observatory. Two surveys were carried out in 1967 and between 1971 – 1977. The first set of observations were made as part of a 4000-square degree survey to cover the southern sky. The second set of observations were part of a 4300-square degree survey specifically designed to discover new metal-poor stars. Literature sources were also included in this study. Narrowband *ubvy*-photometry was used in conjunction with the objective prism data to determine metallicity, absolute magnitudes, distances, evolutionary state, and indicators of carbon-enhancement. Although the stars were not kinematically selected to be of the stellar halo, the radial velocities determined in this work suggested that the newly discovered low-metallicity stars could be members of the halo.

The HK survey (Beers et al., 1985, 1992) was an objective prism survey also conducted with the Curtis Schmidt Telescope. This survey was deeper than that of Bond (1980). The observations were recorded on glass plates and the spectra were inspected by eye. The strengths of the Ca II H and K lines were used to select the $\sim$ 1800 metal-poor star candidates. These stars

[2] [A/B]$= \log(N_{\rm A}/N_{\rm B}) - \log(N_{\rm A}/N_{\rm B})_{\odot}$ for N atoms of elements A, B, e.g., [Fe/H] $= -2.0$ is 1/100 of solar Fe abundance.

were then observed at medium resolution and had UBV photometry performed in order to determine stellar parameters and metallicities. The metallicities were determined using the Ca K line, along with several other strong features available in the spectra. This method allowed for determination of the [Fe/H] ratio, as the Ca K line index is related to metallicity in metal-poor stars, which can be easily seen in the typical [Ca/Fe] ratios of halo stars (Beers et al., 1999). Similar to Bond (1980), this survey also aimed to detect metal-poor stars.

The Hamburg/ESO Survey (HES) (Wisotzki et al., 2000), was another objective prism survey. The plates of the HES were digitized, unlike previous surveys where the plates needed to be inspected by eye. The initial aim was to detect bright quasars, although the observations allowed for the study of additional sources, including a significant number of stars (Christlieb et al., 2001). Many metal-poor stars were discovered (Christlieb, 2003). Due to the long exposure times required to detect faint sources, brighter objects (B<14.5) saturated the plates. (Frebel et al., 2006) processed the saturated stellar data, which enabled these stars to be analyzed and ~ 170 new stars with [Fe/H]< -2 were discovered from follow up medium-resolution (R$\sim$ 2000) spectra, making up the Bright Metal-poor Star (BMPS) sample.

The Sloan Digital Sky Survey (SDSS) (York et al., 2000) is a photometric and spectroscopic sky survey. The initial survey has finished, but extensions and follow ups are ongoing and carried out on the 2.5 m Apache Point Observatory telescope. SDSS is unique in that is uses the same telescope to obtain *ugriz* photometric and R$\sim$ 2000 spectroscopic data. The spectro-

graph is fiber-fed to obtain multiple spectra in a single observation, with plates drilled to reflect the positions of the target objects. The photometry is used to select candidates for spectroscopy, as not all objects with photometric observations are observed with the spectrograph. The science of the SDSS spans many topics, with a significant portion dedicated to understanding the stellar content of the Galaxy. Given the success of the initial stellar sample of the first phase of SDSS, a dedicated stellar survey called the Sloan Extension for Galactic Understanding and Exploration (SEGUE) (Yanny et al., 2009) was developed to better study the structure of the galaxy and additional medium-resolution stellar spectra were obtained. Between SDSS and SEGUE, more than 600,000 stellar spectra were obtained. These were analyzed using the Sloan Stellar Parameter Pipeline (SSPP) (Lee et al., 2008), which utilizes several methods, including the Ca II K line index method of Beers et al. (1999), to determine the stellar parameters and metallicity of each star. The SEGUE survey was extended to SEGUE-2 in order to map out the stellar halo, where an additional 120,000 halo stars were observed.

The Southern Sky Survey (SSS) is an ongoing photometric all-sky survey conducted on the SkyMapper Telescope at Siding Springs Observatory. SkyMapper is outfitted with ugriz filters plus a Stromgren v-filter, which allow for photometric determinations of effective temperature, surface gravity, and metallicity. From these measurements, candidate metal-poor stars are chosen for follow up medium-resolution observations. The SkyMapper Telescope has already produced many promising candidates.

Once medium-resolution follow up spectra are obtained and analyzed, the next step is to observe the most promising candidates at higher resolution. Studies such as Roederer et al. (2014) and Cayrel et al. (2004) include high resolution spectra of $R \sim 30,000 - 45,000$, which allow for a precise, detailed analysis of the individual abundances of their sample stars. A more detailed account of several different high resolution studies can be found in Chapters 3 and 4. The biggest disadvantage to high resolution spectroscopy is that it takes a significantly longer amount of time to observe a high S/N spectrum than at medium resolution. Thus, high-resolution samples are much more limited in magnitude than lower-resolution studies. To bridge the gap between time intensive high resolution spectroscopy and low information medium-resolution spectroscopy, some studies have employed the use of so-called "snapshot" spectra.

Snapshot spectra are of moderate resolution (R$\sim$ $15,000 - 20,000$) and moderate S/N ($\sim$ 50). The quality is high enough to derive abundances of individual elements, but with moderate uncertainties ($\sim$ 0.30). Snapshot studies allow for the observation of many more stars in a relatively quick manner to determine abundances for several stars.

The study presented in this dissertation is the Chemical Abundances of Stars in the Halo (CASH) project. The CASH project is a high-resolution stellar snapshot spectra study aimed at betteer understanding the metal-poor stars that make up the halo of these Galaxy. The spectra were used to derive individual stellar parameters and detailed abundances for a statistical sam-

ple of stars that were observed, processed, and analyzed in a homogeneous way. These abundances provide the information required to derive abundance patterns for the stars, trends over the sample, and frequencies of particular elemental abundance signatures within the sample.

This dissertation is comprised of two published papers, one paper that has been submitted to the Astrophysical Journal, and one paper that is in preparation for submission. The order of the chapters is presented in such a way that the major data analysis tools are discussed, along with their calibration and then the results of the large study are presented and interpreted. In the second chapter, we present Robospect, an automated equivalent width measurement software package. Robospect provides the measured equivalent widths that are then used in CASHCODE, the automated stellar parameter and abundance determination software used for the CASH project. In Chapter 3, we present the calibration of CASHCODE using a sample of extremely metal-poor stars. We compared results derived from the snapshot spectra from the CASH project with results from high-resolution observations taken with the MIKE spectrograph on the Magellan-Clay telescope. In Chapter 4, we present the full results of the CASH project. In Chapter 5, we discuss the discovery of one particular star from the CASH project, HE 0414−0343, a CEMP star that shows s-process enrichment. This star was compared to an AGB model along with a sample of other CEMP stars. These stars were then analyzed to obtain a better understanding of CEMP stars with s-process enrichment. In Chapters 2-5, we present introductions to each, with the in-

tent to better explain each chapter. Finally, in Chapter 6, we summarize our conclusions and discuss the future directions of the CASH project.

Chapter 2

ROBOSPECT: Automated Equivalent Width Measurement

We present ROBOSPECT, a new code to automatically measure and deblend line equivalent widths for both absorption and emission spectra. We test the accuracy of these measurements against simulated spectra as well as manual equivalent width measurements of five stellar spectra over a range of signal-to-noise values and a set of long slit emission spectra. We find that ROBOSPECT accurately matches both the synthetic and manual measurements, with scatter consistent with the expectations based on the data quality and the results of Cayrel (1988). This work was published in Waters & Hollek, 2013, PASP, 125, 1164.

2.1 Introduction

Chemical abundance determination from stellar spectra is largely achieved in one of two ways: synthetic spectra matching or measurement of the equivalent widths of important spectral features. The calculation of synthetic spectra is complicated due to the physics that goes into the models, from the simplest set of atmospheric parameters to the much more complicated considerations

required for effects such as non-local thermodynamic equilibrium. Thus, it is difficult to make direct comparisons between studies, not only due to the different methods of dealing with the physics of stellar atmospheres, but also the inclusion or exclusion of various features (e.g., sources of broadening, non-local thermodynamic equilibrium treatments) that can contribute to the formation and shape of a spectral line.

The alternative to this synthesis is to measure the equivalent width of a set of lines. The equivalent width is a geometric measure that describes the total flux of a line as a rectangle with the same area as the line. By requiring the rectangle to have the height of the normalized continuum, the width directly corresponds to the line flux. The equivalent width can be measured without any prior knowledge of an object or consideration for what input physics will be included in the analysis. However, once the equivalent width is measured, further analysis with that information will then generally require the same considerations for physics included in the models used for spectral synthesis.

We have written a new equivalent width fitting program, ROBOSPECT, to provide a consistent way to measure spectral line strengths. By automating these measurements, the data from current and future large-scale studies can be quickly processed without concern about changes in fit quality due to individual, manual measurements. ROBOSPECT is designed to be modular and open source, using freely available software and library packages, to enable users to quickly adapt the code to their data requirements.

Although ROBOSPECT was originally designed for the study of ab-

sorption lines in stellar spectra, the algorithms are general enough to allow it to be used to measure the equivalent widths of lines from emission spectra. Emission lines formed in rarefied gas can be used as diagnostics for temperature, metallicity, density, and ionization structure in astrophysical objects such as planetary nebulae (e.g. Sterling et al. 2005), active galactic nuclei (e.g. Ludwig et al. 2012, and HII regions (e.g. Pellegrini et al. 2010). In many instances, the useful value is not the equivalent width, but rather the total line flux; however, this is simply a mathematical conversion.

In this paper, we describe ROBOSPECT, an automated equivalent width measurement program for absorption and emission lines. In Section 2.2, we outline the fitting algorithm that determines the equivalent widths. We detail the accuracy and performance of ROBOSPECT on simulated and real data in Section 2.3. In Section 2.4, we discuss the features of some other publicly available equivalent width measurement programs and summarize our results in Section 2.5.

2.2 Algorithms

The goal of ROBOSPECT is to generate an accurate model fit to an input spectrum, with a minimum of user interaction. This helps ensure that all fits are performed identically, regardless of the user or their "personal fitting equation[1]". To that end, ROBOSPECT constructs automated fits, with the

[1]The "personal equation" is a term that we use here to describe the phenomena where each spectroscopist fits lines in her own particular way in how she deals with continuum

addition of only a small number of user-defined parameters that control the methods used in fitting. In addition, ROBOSPECT returns a set of flags for each fit performed, to allow the user to note any quality issues, allowing poorly fit lines to be identified largely from the resulting line catalog. Figure 2.1 presents a diagram of the program structure to illustrate the order in which spectrum components are measured.

The only required input to ROBOSPECT is a FITS or ASCII spectrum file, listing the flux at each wavelength. Uncertainties in the fluxes can be supplied as well, but are not used in the fitting process, as they tend to over-constrain the fits (see below). Multi-order spectra are supported, with each order fit independently. This prevents discontinuities between the orders of a combined spectrum from inducing errors in the continuum model. This also allows orders that overlap in wavelength space, such as those obtained with an echelle spectrograph like the High Resolution Spectrograph on the Hobby-Eberly Telescope, to be fit without merging the spectra. A linelist of known lines that should be fit can also be specified, providing the expected line center. These specified lines will always have a line fit attempted, even if there is no obvious feature in the spectrum. This forced measurement method allows a consistent set of lines to be measured across a large number of spectra, yielding upper limits if the presence of an individual line is not obvious.

placement, fitting in the wings versus the core of the line and so forth.

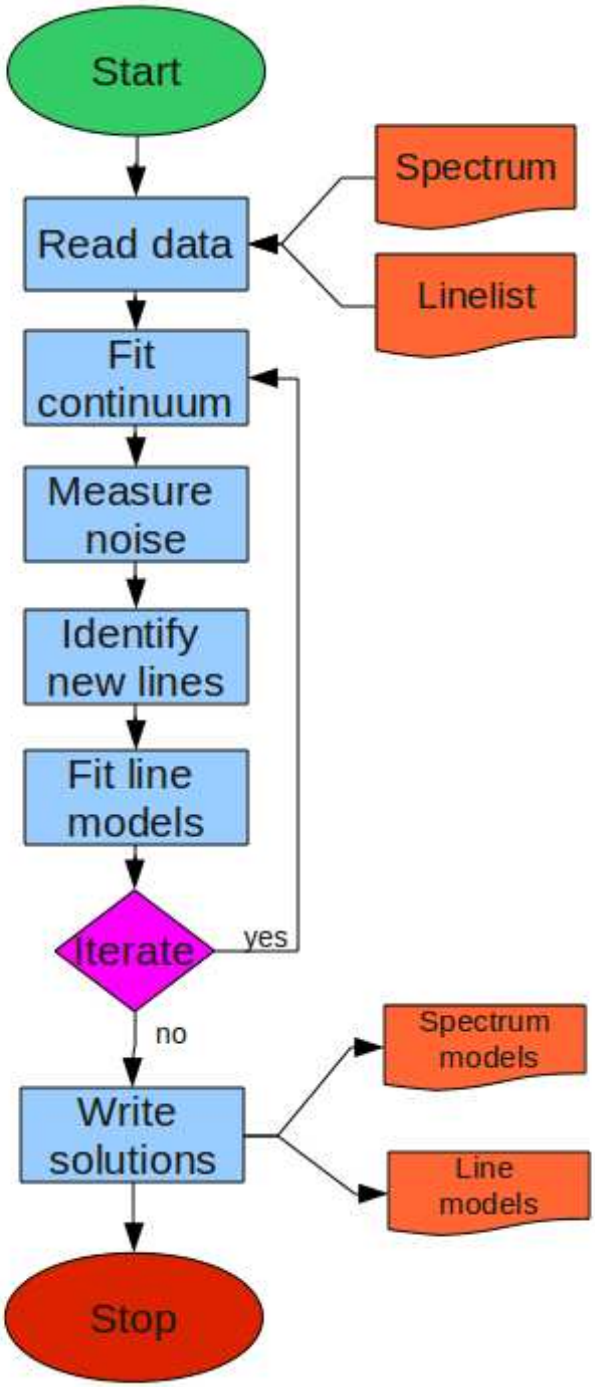

Figure 2.1 Diagram of ROBOSPECT steps used to fit the spectral components.

2.2.1 Spectrum Models

2.2.1.1 Continuum Normalized Spectra

ROBOSPECT models spectra based on the assumption that all spectra are comprised of three components: the continuum level, $C(\lambda)$, the line solution relative to that continuum $L(\lambda)$, and an error component $E(\lambda)$ that contains the deviation between the true spectrum and the current model. By iterating the fitting of these components, we can ensure that the line and continuum solutions are not biased by the other. These components are combined in different ways to measure line strengths, depending on the type of spectrum to be fit. For a continuum normalized spectrum (where the mean input continuum is nearly unity), we assume that any low spatial frequency deviations from unity are due to a poor normalization correction, and high spatial frequency deviations are a combination of unknown and unfit lines and the $E(\lambda)$ component. In this case, we construct a model of the final spectrum,$S(\lambda)$, as:

$$S_{continuum\ normalized}(\lambda) = C(\lambda) * (L(\lambda) + 1.0 + E(\lambda)) \tag{2.1}$$

This relation ensures that in a spectrum with the continuum normalization perfectly performed, the line model and noise add directly to modulate the spectrum around unity. The measured continuum is assumed to represent imperfect normalization, and so is multiplied to the expected final spectrum. Figure 2.2 demonstrates an example of how these components combine to form the observed spectrum.

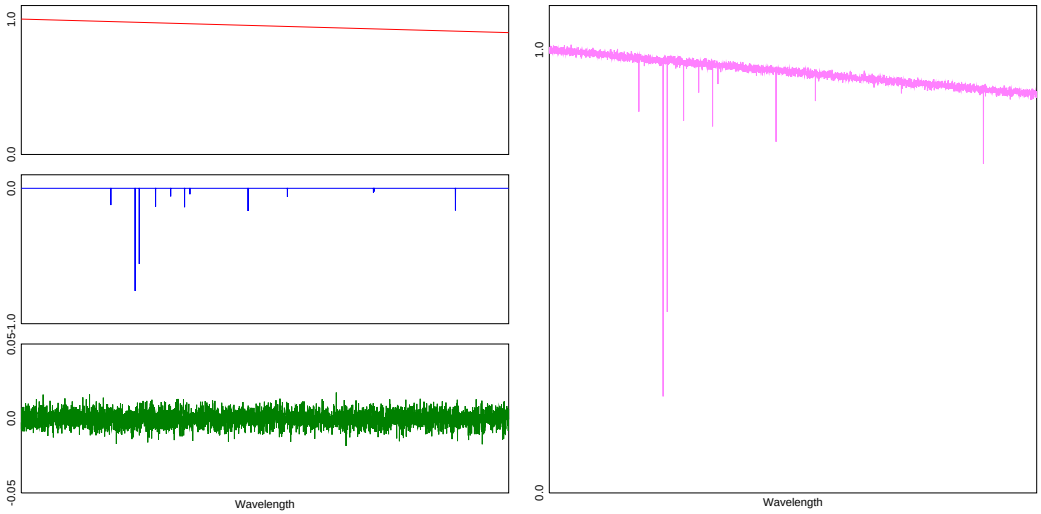

Figure 2.2 Simple diagram for the individual components that are used to make up the observed spectrum. The left panels show the continuum (red), line (blue), and noise (green) models. The right panel contains the expected observed spectrum, which is the product of the continuum model and the sum of the line and noise components.

Using this spectrum model, we can solve Equation 1 for the continuum component, by letting the input spectrum be the expected final spectrum solution. We can then remove the lines from the data, based on previous iterations of the fitting routine. For the initial iteration, we have no knowledge of the correct line solution, and so expect the continuum level to be slightly biased by strong lines. However, as further iterations are performed, this bias decreases, improving the continuum solution. We ignore the error component when measuring the continuum. As the errors should cause deviations in both directions from the true continuum, they should therefore not bias the result. By subtracting the current line model from the input spectrum, we assume that we are simply left with the continuum structure (modulated by the unknown error component). For a continuum normalized spectrum, we must first rescale the individual line measurements to match the possibly imperfect input spectrum continuum normalization:

$$C_{continuum\ normalized}(\lambda) \quad = \quad f_C\left(S_{input}(\lambda) - C(\lambda) * L(\lambda)\right) \qquad (2.2)$$

The function f_C denotes some smoothing operation that returns the continuum model, given the input of a spectrum with all lines removed. ROBOSPECT defaults to a simple median boxcar filter for f_C, which can generally fit continuum models that are smooth and do not have discontinuities. Other continuum smoothing functions are supported, including a spline-based method that can be used when the spectrum does have known discontinuities,

such as those due to the combination of echelle orders into a single spectrum. Functional models, such as a blackbody or power-law model, can also be chosen for f_C, in which a known analytic function is fit to the line-subtracted spectrum.

With the continuum modeled, we can start to investigate the effect that the unknown $E(\lambda)$ has on the data. This error is not, in general, drawn from the per-pixel noise value. As ROBOSPECT only attempts fits for lines in the linelist, any unknown line will create a deviation between the best model spectrum and the input data. Because of this, ROBOSPECT estimates a noise for each pixel that represents the observed scatter in the spectrum, which includes the contribution from small, unfit lines. This measured noise is generally higher than the expected Poissonian noise, due to this extra contribution. This noise is used both in the line fitting stage to determine how well the model matches as well as in the internal line finding stage. Similar to the continuum solution above, we find a noise solution, $E(\lambda)$:

$$E_{continuum\ normalized}(\lambda) \quad = \quad f_E\left((S_{input}(\lambda)/C(\lambda)) - L(\lambda) - 1.0\right) \qquad (2.3)$$

This solution removes the current best fitting continuum and line models from the data, leaving only what should be considered the error component. As above in Equation 2, the function f_E attempts to model the underlying noise that this error component is drawn from. This is also generally a filtering process, with the default filter using the median absolute deviation statistic ($MAD = \text{median}(\text{abs}(x_i - \text{median}(x_i)))$). This value is then converted to an

equivalent Gaussian σ by noting that for a Gaussian distribution, the MAD is half of the interquartile distance, and therefore this equivalent σ is equal to $1.4826MAD$. Using this statistic instead of a directly measured standard deviation allows this estimate of the noise to be robust against the influence of outliers, such as those that may be left behind by large unmodeled spectral features.

At this point in the fitting process, ROBOSPECT can attempt to identify potential lines that are not yet in its linelist. This is done by looking for local peaks that are more than a fixed user-specified number of σ deviant from the continuum subtracted level:

$$Z_{continuum\ normalized}(\lambda) \quad = \quad \left((S_{input}(\lambda)/C(\lambda)) - 1.0\right)/E(\lambda) \qquad (2.4)$$

We expect that a large fraction of lines specified by the linelist will be significant in this measurement. Therefore, after finding all the local peaks that are above the threshold, we merge this list of peaks with those already in the linelist and remove the duplicates. The current line model is not subtracted from the data before looking for new lines, as the model residual can introduce significant local peaks that are not necessarily real.

ROBOSPECT constructs a line solution model using the same methods as when it finds lines, except without normalizing by the spectrum noise:

$$L_{continuum\ normalized}(\lambda) \quad = \quad f_L\left((S_{input}(\lambda)/C(\lambda)) - 1.0\right) \qquad (2.5)$$

Again, f_L is a function that represents the fitting process performed for each line in the current list (whether supplied by the user or found automatically). This fitting process can use various methods, and can use different models for the line profile shape, as described in Section 2.2.2.

2.2.1.2 Flux Calibrated Spectra

For flux calibrated spectra, the same three components are used to describe the input spectrum. However, these components are combined in a different manner than is used for the continuum normalized spectra. For flux calibrated spectra, we assume that the continuum solution combines with the line solution additively and not multiplicatively as in the case of the continuum normalized spectra. Therefore, the spectrum model for flux calibrated data is:

$$S_{flux\ calibrated}(\lambda) = C(\lambda) + L(\lambda) + E(\lambda) \tag{2.6}$$

From this model, we can derive relations for the various components as was done above for the flux normalized spectra.

$$\begin{aligned} C_{flux\ calibrated}(\lambda) &= f_C\left(S_{input}(\lambda) - L(\lambda)\right) && (2.7)\\ E_{flux\ calibrated}(\lambda) &= f_E\left(S_{input}(\lambda) - C(\lambda) - L(\lambda)\right) && (2.8)\\ Z_{flux\ calibrated}(\lambda) &= \left(S_{input}(\lambda) - C(\lambda)\right)/E(\lambda) && (2.9)\\ L_{flux\ calibrated}(\lambda) &= f_L\left(S_{input}(\lambda) - C(\lambda)\right) && (2.10) \end{aligned}$$

The same fitting and estimation algorithms can be used on both kinds of spectra, as we isolate the component being measured in both cases. Due

to the large dynamic range possible for flux calibrated spectra, it is useful to calculate the continuum and noise models using the logarithm of the flux levels. This prevents a large continuum gradient from being dominated by the very largest values.

2.2.2 Line fitting

Figure 2.3 shows a flow chart of the steps used in fitting individual lines. Before doing more complicated fitting, an initial guess for the fit parameters is constructed for each line, under the assumption that the line profile is a Gaussian. The line center is estimated from the centroid around the line peak. The FWHM is calculated by interpolating the line profile at the half-peak value. As heavily blended lines may have excessive contribution from other lines at the half-peak value, we check this value with the width calculated from the 75%-max peak value. In the case of large differences in the expected Gaussian σ between these two values, we take the smaller value to minimize the possible effect of blending. Finally, total line flux, F, is estimated for a simple Gaussian model from the peak flux and the FWHM ($F = P\sigma\sqrt{2\pi}$). After this initial fit is performed for all lines, a set of deblending groups is determined. If the line centers are closer than a given number of line widths (taken by default as six times the Gaussian model σ), then they are assigned to the same deblend group. This deblend group is then simultaneously fit as a single unit, to allow for the contributions of all the lines at a given wavelength.

The full line fitting to find the best fitting set of model parameters

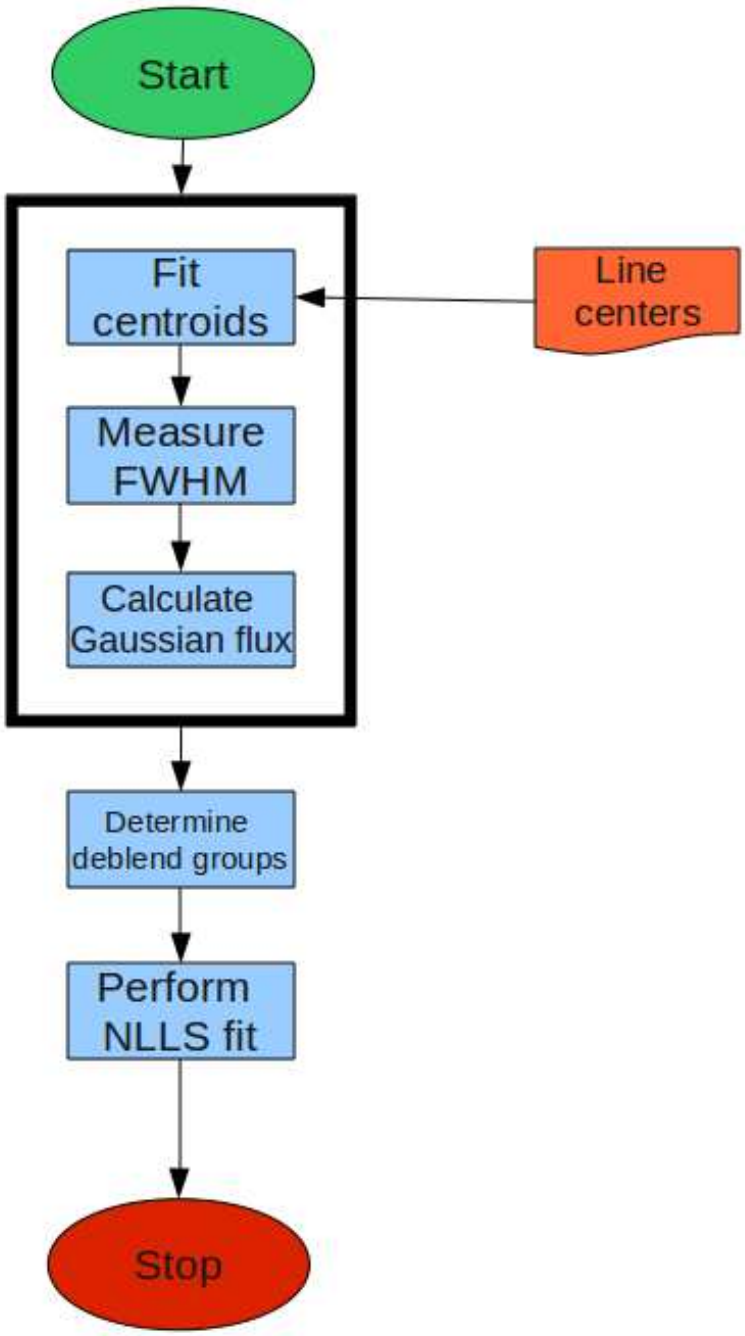

Figure 2.3 Diagram of the steps used by ROBOSPECT to fit individual lines.

is done via non-linear least-squares minimization of $\chi^2 = \sum_\lambda \frac{L(\lambda)-\sum_i Q_i(\lambda)}{E(\lambda)}$ for each deblending group, where $Q_i(\lambda)$ is the component of the ith line at wavelength λ. Different line model choices can made for Q, as described in Section 2.2.3. Once convergence is reached for all the lines in one deblend group, those values are recorded and the fitting moves to the next deblend group, until all lines over the entire spectrum have been fit.

After fitting all lines, a set of quality checks are performed to ensure that only valid fits are retained in the final model. First, any line that did not converge within a fixed number of fitting iterations is flagged and rejected from further consideration. Similarly, lines that have final fit values that are non-finite are flagged and rejected. Finally, the total line solution is calculated by summing only the valid lines, further rejecting any lines that do not reduce the total χ^2 value.

Once the line fitting has been finished and the line solution accumulated, further iterations can be performed starting with these models as an initial set of parameters. As the continuum model is based on the spectrum with lines removed, better line models result in a smaller line residual, allowing for a better continuum model. In turn, with a more accurate continuum model, the line fits are more reliable, with less noise as there are fewer residuals remaining. In Figure 2.4, we show an example output fit from the S/N$\sim$ 300 star for Fe I line λ5429.68.

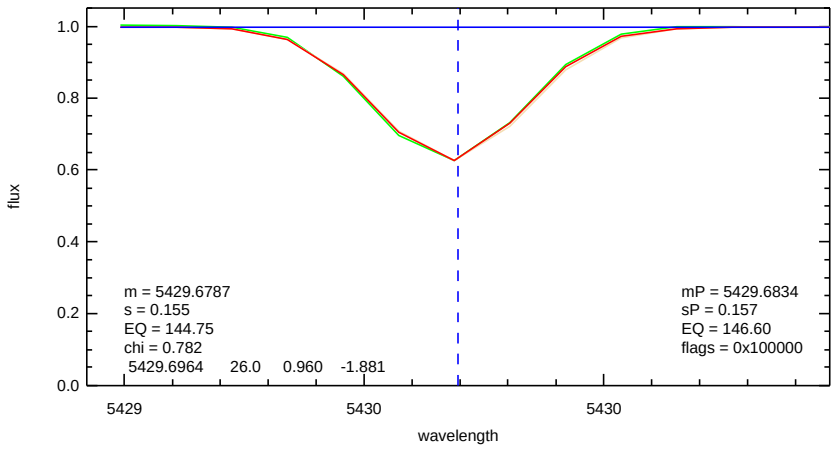

Figure 2.4 Example output fit from the S/N$\sim$ 300 star for Fe I line λ5429.68. The blue dashed line represents the line center, the blue solid line represents the continuum model, the green line represents the spectrum, and the red solid line represents the final line model. In the lower left corner, we list the final fit values for the line center, Gaussian σ, equivalent width, and fit χ^2. The lower right corner lists the measurements based solely on the preliminary fit calculated from the measured line FWHM, along with the hexadecimal value of the fit flags (in this case noting no issues with the line, only marking it as being fit with a Gaussian line model).

2.2.3 Line profile functions

The default assumption for all lines is that they have a profile shape consistent with a simple Gaussian. This is appropriate for most lines used in a typical equivalent width-based stellar abundance analysis. Lines that fall on the linear portion of the curve of growth have a 1:1 ratio between the line width and the absorbers, thus a small change in the number of absorbers is easily reflected in the line profile. However, as the line leaves the linear portion of the curve of growth, this ratio becomes smaller and the assumption of a Gaussian profile begins to break down, resulting in wings that are broader and contain a larger fraction of the total flux. To account for these strong lines, we allow the user to select other profile functions that can better model these lines.

In the extreme case of the line shape generated solely by pressure broadening, we support a Lorentzian model. This is in general not appropriate for most lines included in the typical analysis of a stellar spectrum; however the Gaussian line shape is not appropriate for certain lines from which abundances are derived (e.g., Mg b) and for lines that are important in calculating the continuum (such as the hydrogen lines). Between the extreme Lorentzian and the Gaussian is the Voigt profile, the result of the convolution of a Gaussian and Lorentzian models. This profile is somewhat difficult to directly calculate, and so we utilize the Hjerting approximation given by Harris (1948) that describes the Voigt profile as a polynomial approximation in η, the ratio of the Lorentzian width to the Gaussian (Doppler) width. This function reduces to the simple Gaussian form when $\eta = 0$, allowing this function to be used on all

lines, with the degree of non-Gaussianity allowed to best match the data. This function is significantly more complicated than a simple Gaussian, however, increasing the computation time required for fitting.

2.2.4 Wavelength solutions

Internally, ROBOSPECT has no a priori knowledge of the quality of the wavelength solution. If a linelist is supplied, it is assumed that the specified line centers are consistent with the peaks in the spectrum. If this is not true, then the lines specified may go unfit. We have implemented some rudimentary ways to prevent this situation, but these algorithms assume any errors in the wavelength solution are small, and are not designed as a replacement for accurate wavelength calibration.

Given that the linelist notes where expected lines should be found, ROBOSPECT can use that information to evaluate the wavelength solution of the supplied data. By finding the local peak most consistent with the input linelist, ROBOSPECT can check for systematic offsets between the expected line center and the observed line center, and fit a wavelength correction that makes these match. This correction can either be linear (the observed spectrum has an offset from expectations by some small fixed $\delta\lambda$) or Doppler (the observed spectrum has a velocity offset resulting in an offset $\delta\lambda \propto \lambda$). Once the correction has been measured, this result is applied to shift the expected line centers to match the data, not to change the wavelength solution of the data. This choice is made to avoid issues interpolating the data onto a new

wavelength grid, and the possible resulting degradation in resolution. The calculated correction is returned with the final fit, allowing the user to use it to help re-reduce the data.

2.3 Fitting Accuracy

Although ROBOSPECT returns an error estimate for all measured parameters, this is based on the fit χ^2, and does not fully account for the covariance between line parameters and continuum uncertainty. Therefore, to confirm the fit quality and measurement accuracy, we compare the results from ROBOSPECT to a sample of independently measured lines.

2.3.1 Simulated Spectra

We performed our first test using a sample of 100 simulated spectra, designed to be similar to a sample of high resolution, continuum-normalized stellar absorption spectra. Each spectrum covers a range of 4000Å centered at 6000Å, with 0.1Å spaced pixels. A randomly chosen signal-to-noise ratio was selected logarithmically between $S/N = 10$ and $S/N = 1000$ to represent the a range of common data quality. This S/N value was then used to add random Gaussian noise around 1.0, representing the mean level of the normalized spectra. From this base, we then added 1000 equally spaced Gaussian lines to the spectra. The line equivalent widths were again logarithmically sampled, from a range $1 < EQW < 600$ consistent with what is observed in our spectra of real stars. The FWHM values for these simulated lines was drawn from the

narrow range of $0.2\mathring{A} < FWHM < 0.4\mathring{A}$. As the FWHM is largely a function of the resolution of the data, and dependent on the instrument, there is little need to probe a wide range of values.

In order to represent calibration errors that would shift the continuum level, we multiplied the final spectrum with a spline model. This spline model was defined by taking twelve equally spaced points along the spectrum, and randomly selecting a value from the noise expected by the signal-to-noise ratio. These control points were then interpolated using a cubic spline, and the simulated spectra scaled by this curve. This model assumes that the continuum level is more robust in high signal-to-noise data, a reasonable expectation.

Once these simulated spectra were generated, they were processed using ROBOSPECT, and the measured line parameters were compared with the known simulation inputs. Using the fit quality flags generated by ROBOSPECT, we can exclude lines that were not fit correctly, and use this information to determine the expected completeness of the fitting process. Figure 2.5 shows the completeness as a function of signal to noise and line equivalent width. As is expected, the completeness is worse for weak lines in low signal to noise spectra.

One of the main issues with fitting spectral lines is ensuring that the continuum level is estimated correctly. As we know the input and fit continuum levels, we can determine how much scatter to expect from ROBOSPECT measurements. This scatter is shown in Figure 2.5. As expected, as the spectrum signal-to-noise increases, the accuracy to which ROBOSPECT determines the

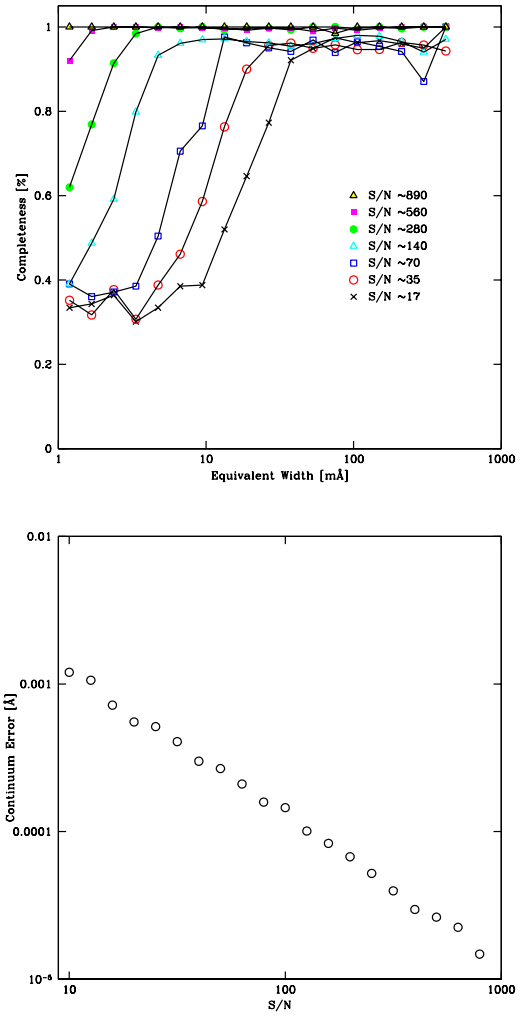

Figure 2.5 The top panel shows the completeness curves as a function of line equivalent width for the simulated spectra at a sample of signal to noise values. The bottom panel shows the decrease in scatter between the measured and input continuum levels as the signal to noise of the spectrum increases.

continuum also increases. This continuum accuracy best represents a lower limit to the uncertainty that is expected in real data. Our simulated spectra do not include the contribution that small faint lines can have. The presence of these lines in real data sets a noise threshold in the continuum that exists in even the highest S/N spectra.

The goal of ROBOSPECT is to accurately measure the equivalent widths of the lines in the spectrum. Therefore, understanding the errors on these measurements is essential. From Cayrel (1988), we expect that the scatter is a function of the line FWHM and the spectrum signal to noise. The simulated spectra provide a very large sample of 65,000 lines with valid line measurements to estimate the observed scatter in the ROBOSPECT fits. These results are displayed in Figure 2.6, along with the Cayrel (1988) predictions. As mentioned before, the presence of faint lines in real data is likely to increase the observed fit scatter, but based on this sample, it is clear that the fits produced by ROBOSPECT are consistent with the expected theoretical accuracy.

2.3.2 CASH Star Comparison

To test ROBOSPECT on a set of real stellar spectra, we compared the equivalent width measurements made for 5 stars of S/N $\sim$ 300, 100, 65, 45, and 30, listed in Table 2.1. These stars were observed as part of the Chemical Abundances of Stars in the Halo (CASH) project Hollek et al. (2011). The CASH project is a study of 500 stars, observed at McDonald Observatory using

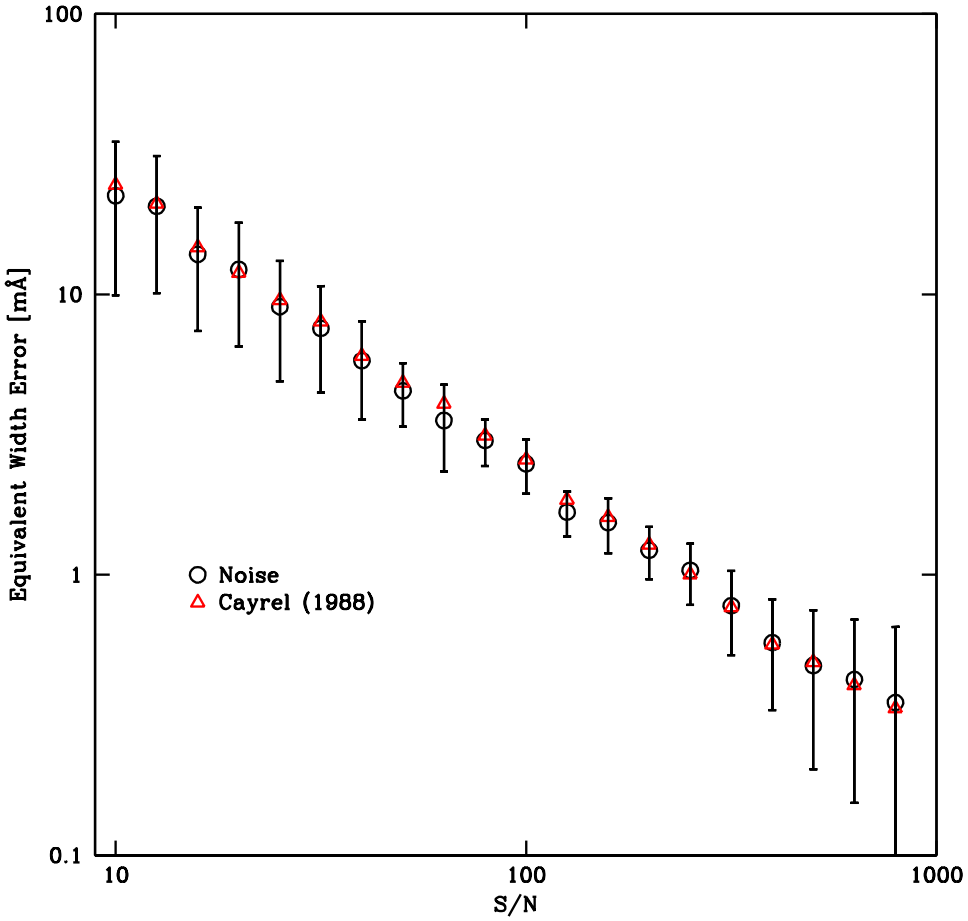

Figure 2.6 Observed equivalent width error distribution as a function of spectrum signal to noise. For comparison, we also display the expected median scatter from Cayrel (1988) using red triangles.

Table 2.1. CASH Comparison Stars

Star	S/N	Expected Manual Equivalent Width Error [mÅ]
HD 122563	300	1.00
HD 140283	100	3.00
HD 115444	65	4.61
HE 2137+0153	45	6.66
HE 1225+0155	30	9.99

Note. — Information on the stars from Hollek et al. (2011) used to test ROBOSPECT.

the High Resolution Spectrograph (Tull, 1998) on the Hobby-Eberly Telescope (Shetrone et al., 2007). The goal of this study is to analyze a statistical sample of stellar spectra to determine chemical abundances and abundance trends in a self-consistent manner. We are using ROBOSPECT to facilitate the analysis for this large spectroscopic study.

These S/N values were chosen to present an ideal case, a good case, the median S/N of the CASH study, a bad, and a very bad case. Observational details of the CASH project are given by Hollek et al. (2011). As these stars are part of a study of the stellar halo, they are of low metallicity, ranging from $-3.0 <$[Fe/H]< -2.4.

These stars were observed at R$\sim 15,000$ and have been measured using a semi-automated IDL routine (Roederer & Lawler, 2012) which was also used

for the stars of equal resolution by Hollek et al. (2011). Here we examine two of the most common parameter settings used in ROBOSPECT: standard Gaussian line profiles and Hjerting line profiles. In both cases, we use the set of default parameters listed in Table 2.2 to test the code, which was run for five iterations of the main fitting loop. The only deviation from the default parameters is for the fits using the Hjerting line profile shape.

Table 2.2. Default ROBOSPECT Settings Use for CASH Star Analysis

Parameter	Description
continuum model	simple boxcar with a width of 40 mÅ
line model	"best" estimating lines from FWHM and use deblending
line profile function	Gaussian
linelist	specify lines for measurement from linelist
find lines	find additional lines to the fit outside of the linelist

Tables 2.3 and 2.4 show the results of statistical tests that quantify the difference between the manually measured equivalent width and the ROBOSPECT measured equivalent width. We also include the S/N, the iteration of fitting loop presented, as well as the number of lines that had fits considered valid by ROBOSPECT. To prevent a small number of outliers from skewing the results, we also list the median and the robust estimate of the standard deviation, σ_Q.

Table 2.3. Deviation Between Manual and ROBOSPECT Equivalent Width Measurements

S/N	Iteration	Mean [mÅ]	σ [mÅ]	Median [mÅ]	Low [mÅ]	High [mÅ]	Q25 [mÅ]	Q75 [mÅ]	σ_Q [mÅ]	N
30	1	10.66	8.573	9.1	-3.7	42.0	5.4	14.6	6.822	76
30	2	9.411	8.458	8.0	-5.5	40.0	4.1	11.7	5.635	79
30	3	8.962	8.249	7.5	-6.6	39.0	3.8	11.6	5.784	79
30	4	8.799	8.264	7.5	-6.8	38.7	3.6	11.6	5.932	79
30	5	8.701	8.234	7.4	-6.8	38.4	3.6	11.6	5.932	79
45	1	5.544	5.198	5.5	-6.2	22.6	2.0	7.6	4.152	55
45	2	5.086	5.212	4.7	-7.4	22.9	2.0	7.5	4.078	57
45	3	5.141	5.110	4.4	-5.3	22.9	2.1	7.5	4.004	58
45	4	5.119	5.088	4.3	-5.8	22.9	2.2	7.4	3.856	58
45	5	5.095	5.024	4.4	-6.0	22.8	2.3	7.4	3.782	59
65	1	2.797	2.598	2.6	-1.9	10.8	1.2	4	2.076	89

Table 2.3 (cont'd)

S/N	Iteration	Mean [mÅ]	σ [mÅ]	Median [mÅ]	Low [mÅ]	High [mÅ]	Q25 [mÅ]	Q75 [mÅ]	σ_Q [mÅ]	N
65	2	2.051	2.573	1.7	-3.1	10.7	0.4	3.6	2.373	90
65	3	1.787	2.582	1.4	-3.5	11.0	0.1	3.2	2.299	90
65	4	1.700	2.572	1.3	-3.7	11.4	-0.1	3.2	2.447	90
65	5	1.660	2.565	1.3	-3.7	11.5	-0.1	3.1	2.373	90
100	1	1.437	2.457	1.2	-7.4	7.2	0.0	2.9	2.150	80
100	2	1.158	2.406	0.9	-7.9	6.8	-0.2	2.3	1.854	78
100	3	1.111	2.435	0.8	-8.0	6.6	-0.3	2.5	2.076	81
100	4	1.169	2.217	0.8	-5.5	6.6	-0.4	2.4	2.076	81
100	5	1.157	2.213	0.8	-5.4	6.5	-0.4	2.3	2.002	81
300	1	1.616	3.733	1.3	-5.9	24.5	0.4	2.2	1.335	89
300	2	1.048	3.215	0.6	-5.7	20.4	-0.2	1.4	1.186	90

Table 2.3 (cont'd)

S/N	Iteration	Mean [mÅ]	σ [mÅ]	Median [mÅ]	Low [mÅ]	High [mÅ]	Q25 [mÅ]	Q75 [mÅ]	σ_Q [mÅ]	N
300	3	0.925	3.134	0.5	-4.5	18.6	-0.4	1.2	1.186	87
300	4	0.802	3.009	0.4	-5.5	17.6	-0.5	1.3	1.335	89
300	5	0.701	2.936	0.3	-6.4	17.2	-0.5	1.1	1.186	89

Note. — Table containing the detailed statistics of the difference in equivalent widths measured between the manual measurements from Hollek et al. (2011) and ROBOSPECT for the Gaussian line fits. For each S/N, we show statistics for each iteration, including the mean, standard deviation (σ), the lowest value (low), highest value (high), 25th Percentile value (Q25), 75th Percentile value (Q75), the σ_Q value, and the number of lines from which these statistics were derived.

Table 2.4. Deviation Between Manual and ROBOSPECT Equivalent Width Measurements: Hjerting Model

S/N	Iteration	Mean [mÅ]	σ [mÅ]	Median [mÅ]	Low [mÅ]	High [mÅ]	Q25 [mÅ]	Q75 [mÅ]	σ_Q [mÅ]	N
30	1	10.51	8.923	9.4	-14.5	42.4	5.8	13.1	5.413	76
30	2	9.647	8.864	8.5	-16.1	40.4	4.6	13.5	6.599	79
30	3	9.756	9.616	8.4	-16.7	45.3	4.4	13.3	6.599	79
30	4	9.222	8.167	7.7	-5.9	39.6	3.6	11.7	6.006	79
30	5	9.08	8.135	7.8	-6.5	39	4	11.7	5.71	79
45	1	5.236	6.029	5.3	-16.2	22.7	1.9	8.1	4.597	56
45	2	5.095	5.46	4.8	-7.7	22.8	2.1	7.5	4.004	57
45	3	5.128	5.604	5.2	-10.4	22.9	2.5	7.7	3.856	57
45	4	5.65	5.849	5.2	-8.9	25.7	2.6	7.7	3.782	58
45	5	5.268	5.826	5.1	-10.3	22.8	2.5	7.7	3.856	59
65	1	2.862	3.164	2.8	-13.1	11.6	1.3	4.3	2.224	89

Table 2.4 (cont'd)

S/N	Iteration	Mean [mÅ]	σ [mÅ]	Median [mÅ]	Low [mÅ]	High [mÅ]	Q25 [mÅ]	Q75 [mÅ]	σ_Q [mÅ]	N
65	2	2.309	4.496	1.8	-8.8	35.1	0.3	3.7	2.521	87
65	3	1.8	2.502	1.5	-3.4	9	0.1	3.7	2.669	84
65	4	1.89	2.51	1.6	-3.6	9.1	0.1	3.7	2.669	89
65	5	1.32	4.242	1.4	-30.5	9	0	3.5	2.595	88
100	1	1.575	2.595	1.2	-8.1	8	0.1	3.1	2.224	80
100	2	1.204	2.657	1	-8.4	8.5	-0.2	2.5	2.002	80
100	3	1.146	2.526	1	-8.1	7.6	-0.2	2.6	2.076	81
100	4	1.068	2.524	0.9	-8.5	6.6	-0.2	2.4	1.928	82
100	5	0.989	2.618	0.8	-8.5	6.6	-0.4	2.4	2.076	82
300	1	-0.004	8.456	1.3	-47.9	24.6	0.4	2.1	1.261	90
300	2	1.147	5.64	0.6	-19.3	20.6	-0.1	1.6	1.261	90

Table 2.4 (cont'd)

S/N	Iteration	Mean [mÅ]	σ [mÅ]	Median [mÅ]	Low [mÅ]	High [mÅ]	Q25 [mÅ]	Q75 [mÅ]	σ_Q [mÅ]	N
300	3	2.414	8.438	0.6	-19.6	55.7	-0.3	2	1.705	85
300	4	2.533	11.03	0.6	-33.2	56.5	-0.4	1.8	1.631	88
300	5	1.912	5.247	0.5	-9.7	26.6	-0.3	1.9	1.631	89

Note. — Table containing the detailed statistics of the difference in equivalent widths measured between the manual measurements from Hollek et al. (2011) and ROBOSPECT for the Hjerting line profile. The columns are the same as in Table 2.3

2.3.2.1 Gaussian Line Profile Statistical Analysis

In the standard case, using the default parameters with a Gaussian line fit, we find that ROBOSPECT matches the manual measurements, with differences between the manually measured result consistent with the expected Cayrel (1988) estimate. We show results for the test spectra for five iterations in Table 2.3. We determined a nominal error in the manually measured equivalent widths as calculated from Cayrel (1988) by basing the wavelength in the region near the Mg b lines. This region was chosen as it was the same one from which the S/N was calculated. We find the errors in equivalent width to be 1.00, 3.00, 4.61, 6.66, and 9.99 mÅ for the 300, 100, 65, 45, and 30 S/N cases respectively. As with the simulated spectra, as the S/N drops the accuracy with which ROBOSPECT matches the manual equivalent width also drops. In all cases but the 300 S/N case, the standard deviation falls below this value. Furthermore, the σ_Q value is well below the error in the manually measured equivalent widths, again with the exception of the S/N 300 case. The likely cause for this exception is the differences in continuum level chosen by the manual and ROBOSPECT measurements. The continuum level from ROBOSPECT passes through the median of the spectra data, which tends to be slightly lower than the manual placement, resulting in a small bias.

Increasing the number of iterations generally decreases both the fitting bias (as measured by the mean and median) as well as the fit scatter (based on σ and σ_Q). Usually, three iterations are sufficient, with a minimal improvement in the scatter beyond this limit of $\sim$ 0.02mÅ. This improvement is small

relative to the expected uncertainty in the manual measurements, suggesting that further iterations are not likely to improve the fit results.

The left panel of Figure 2.7 shows plots of the residuals between the manually measured equivalent widths from Hollek et al. (2011) and the ROBOSPECT equivalent widths, with each S/N value offset by 50 mÅ. The left panel of Figure 2.8 shows the equivalent widths from the manually measured equivalent widths against those of ROBOSPECT for all S/N values.

Although the scatter between the measurements matches the expectations, there is a clear S/N dependence in the bias between the ROBOSPECT and manual measurements. The most plausible reason for this is a difference in the way that the continuum level is set between these two methods. ROBOSPECT assumes that the true continuum level is "hidden" within the scatter in the spectrum data, and places the continuum level to be consistent with the median value of this scatter. In contrast, a manual measurement is likely to set the local continuum at the peaks to either side of the line, substantially higher than the ROBOSPECT value (on the order of $\sigma_{continuum}$, the scatter in the continuum level). Because of this, the increasing deviation between the manual measurements and the ROBOSPECT measurements as the signal to noise decreases is not surprising, and represents the covariance between continuum level and line flux.

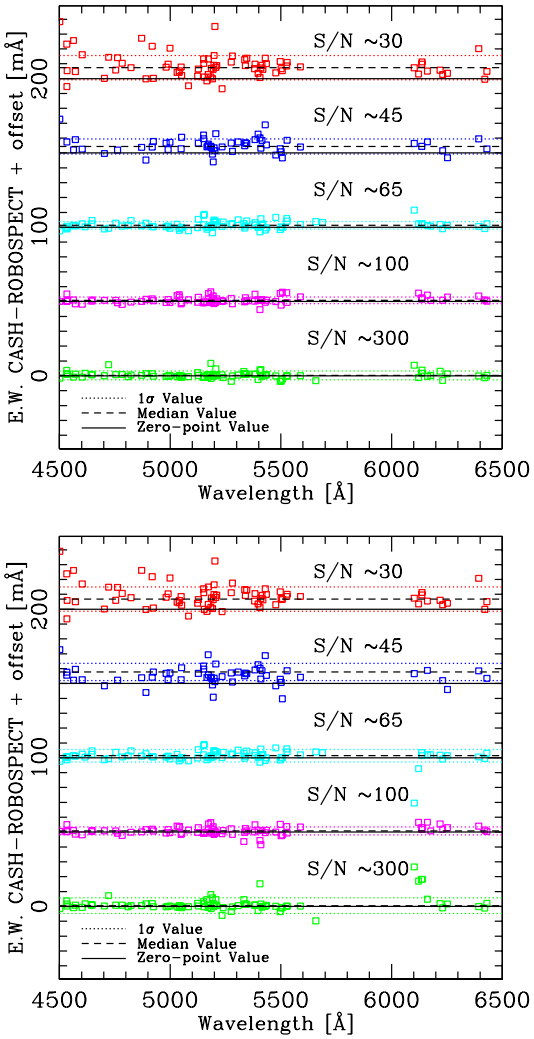

Figure 2.7 Plots of the residuals between the equivalent widths measured by the semi-automated IDL code and ROBOSPECT for all data, with 50 mA offsets for each S/N value. On the top are the residuals for the Gaussian profile and on the bottom the Hjerting (Voigt) profile. In each plot, the green points represent the S/N $\sim$ 300 data, the magenta points S/N$\sim$ 100 data, the cyan points S/N$\sim$ 65 data, the blue points S/N$\sim$ 45 data, and the red points S/N$\sim$ 100 data. For each set of points, there is a color-matched dotted line which represents the relative 1σ value centered around the median value, denoted by the black dashed line. The black solid line represents the zero-point for each S/N value.

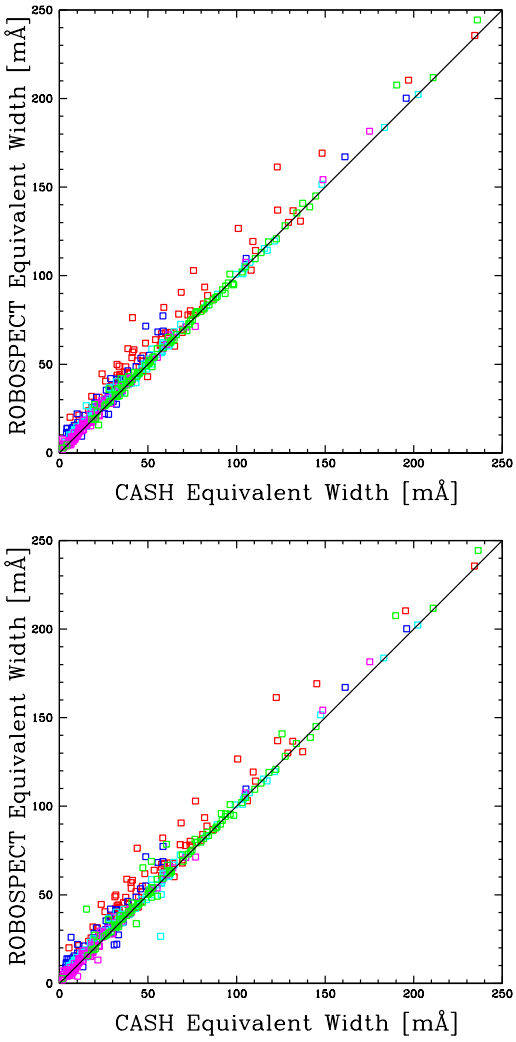

Figure 2.8 Fit comparison for Gaussian (top) and Hjerting (bottom) models at all S/N levels. The green boxes are for S/N 300, magenta for S/N 100, cyan for 65, blue for 45, and red for 30. The thick black line is the 1:1 ratio.

2.3.2.2 Hjerting Line Profile Statistical Analysis

As some very strong lines ($\gtrsim$−4.5 in reduced equivalent width[1]) may have a significantly non-Gaussian line profile shape, we repeated the analysis of these stars with the Hjerting line model instead of a Gaussian. The comparison with the manual equivalent width measurements is detailed in Table 2.4 over all five iterations.

The right panel of Figure 2.7 shows plots of the residuals between the manually measured equivalent widths from Hollek et al. (2011) and the ROBOSPECT equivalent widths, with each S/N value offset by 50 mÅ. The right panel of Figure 2.8 shows the plot of the equivalent widths from the manually measured equivalent widths against those of ROBOSPECT for all S/N values. Upon inspection of the statistical results, we find that the mean and σ values are significantly larger than those associated with the standard Gaussian fits; however, when we evaluate the median and σ_Q values, we find that they are reasonably consistent. As the median and σ_Q values are less sensitive to outliers, this suggests that the added parameters of the Hjerting model may make the code more susceptible to erroneous fits. It should also be noted that night sky lines can pollute the stellar spectrum around 6000Å, which is where many of these outlier fits exist, as seen in the right panel of Figure 2.7.

Figures 2.9-2.13 include a visualization of the line model and model continuum plotted against the input spectrum along with the residuals between

[1]Where reduced equivalent width is $\log_{10}$(Equivalent Width/Wavelength)

the spectrum and line model for each S/N value of the CASH stars presented for the Hjerting line profile fits. The wavelength region shown spans from 5520Å to 5560Å, which is also the width of the deblending region. This region includes a several lines which require deblending, along with some individual features as well. As the metallicity of each of these stars is different, the line strengths vary as well, as strongly evidenced by the λ 5041.07 and λ 5041.76 lines, two prominent Fe features. These example fits also show that strongly deviant points, such as those caused by cosmic rays, are detected and fit as emission features. These fits help minimize the influence that these discrepant points have on the continuum model.

We also tested the Hjerting line profiles against the published equivalent width measurement values for HD 122563, the S/N$\sim$ 300 star, from Cayrel et al. (2004) and for HD 115444, the S/N$\sim$ 65 star, from Fulbright (2000). We find good agreement with both sets of equivalent widths 0.953$\pm$5.796 mÅ and 1.768$\pm$2.621 mÅ for HD 122563 and HD 115444, respectively.

2.3.2.3 Statistical Analysis for a Pared Linelist for Both Gaussian and Hjerting Profiles

In our tests, we used a linelist that was designed for metal-poor stars. However, not all stars have every line in the list, and artifacts such as cosmic rays and noisy spectral regions often make certain lines that have been measured by ROBOSPECT undesirable for further analysis. Even when using manual programs to measure equivalent widths, there are lines that simply

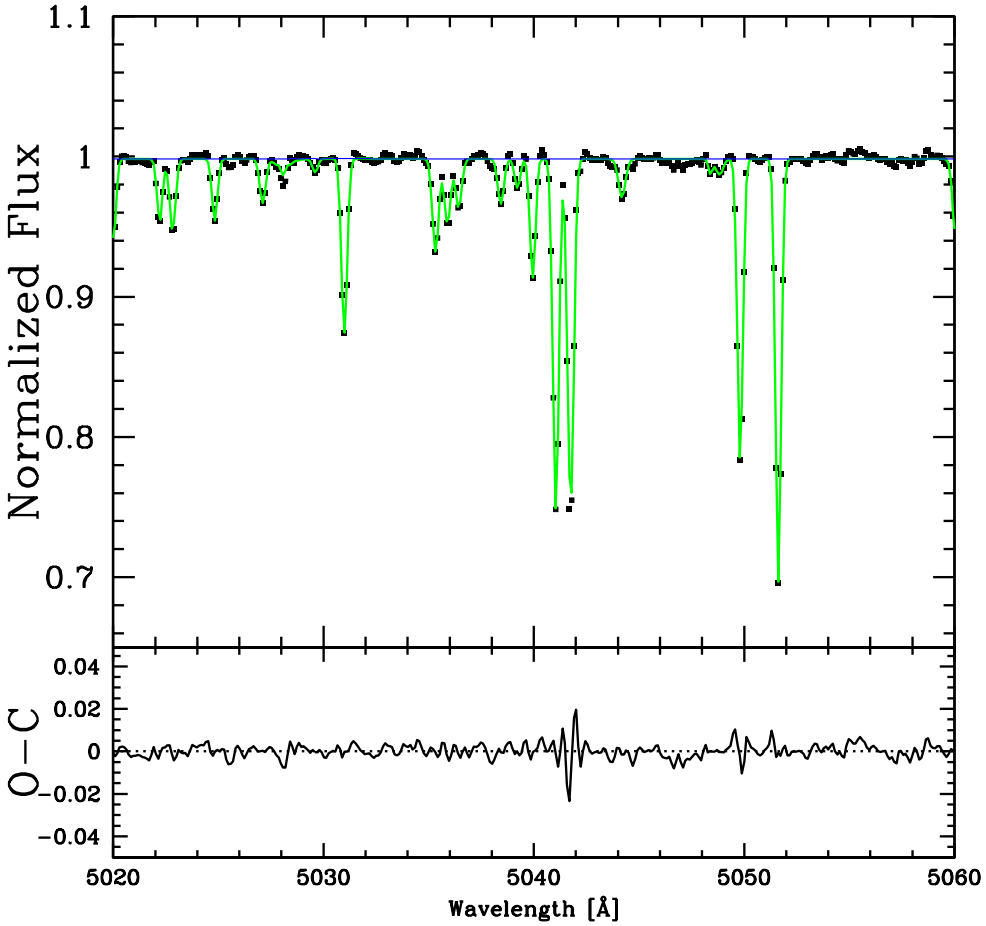

Figure 2.9 Plot of the line model (solid green line) and continuum model (solid blue line) against the input spectrum (black squares), with the residuals between the input spectrum and line model plotted at the bottom (solid black line) for the S/N 300 case.

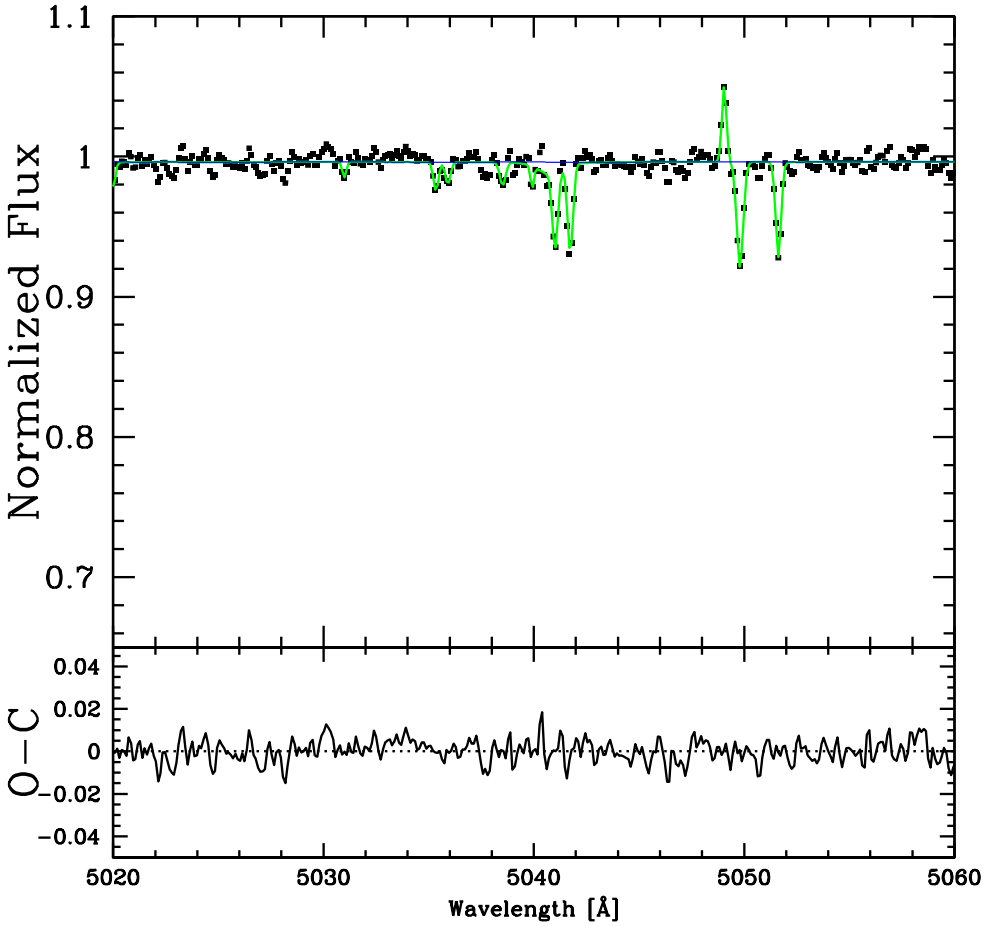

Figure 2.10 Plot of the line model (solid green line) and continuum model (solid blue line) against the input spectrum (black squares), with the residuals between the input spectrum and line model plotted at the bottom (solid black line) for the S/N 100 case. One noisy peak is fit as emission lines at λ5048.

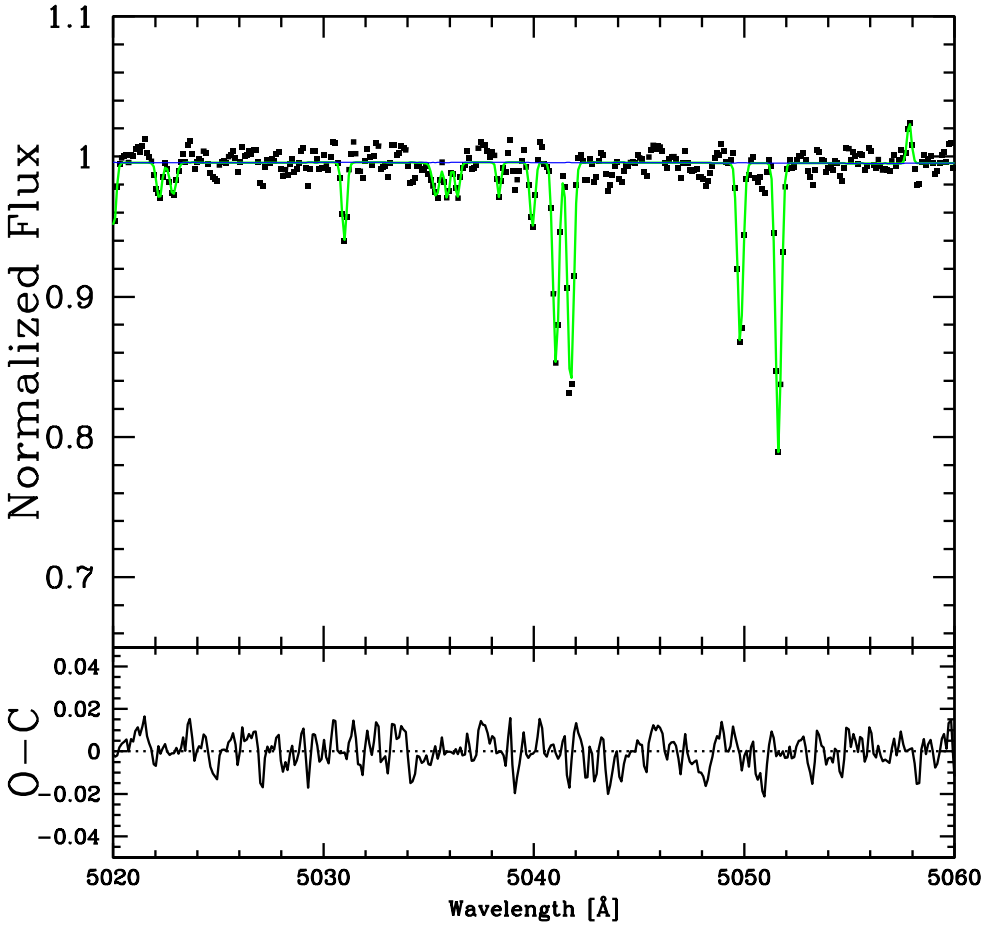

Figure 2.11 Plot of the line model (solid green line) and continuum model (solid blue line) against the input spectrum (black squares), with the residuals between the input spectrum and line model plotted at the bottom (solid black line) for the S/N 65 case.

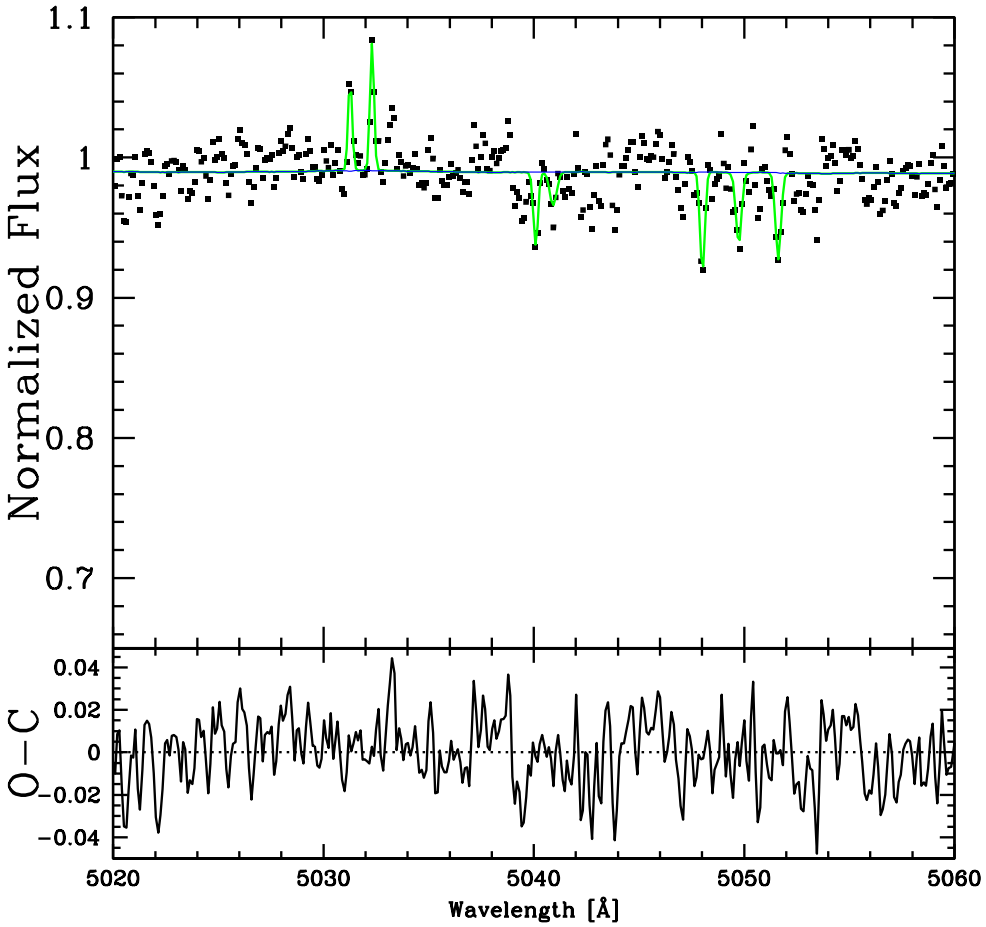

Figure 2.12 Plot of the line model (solid green line) and continuum model (solid blue line) against the input spectrum (black squares), with the residuals between the input spectrum and line model plotted at the bottom (solid black line) for the S/N 45 case. Two noisy peaks are fit as emission lines at λ5031 andλ5032.

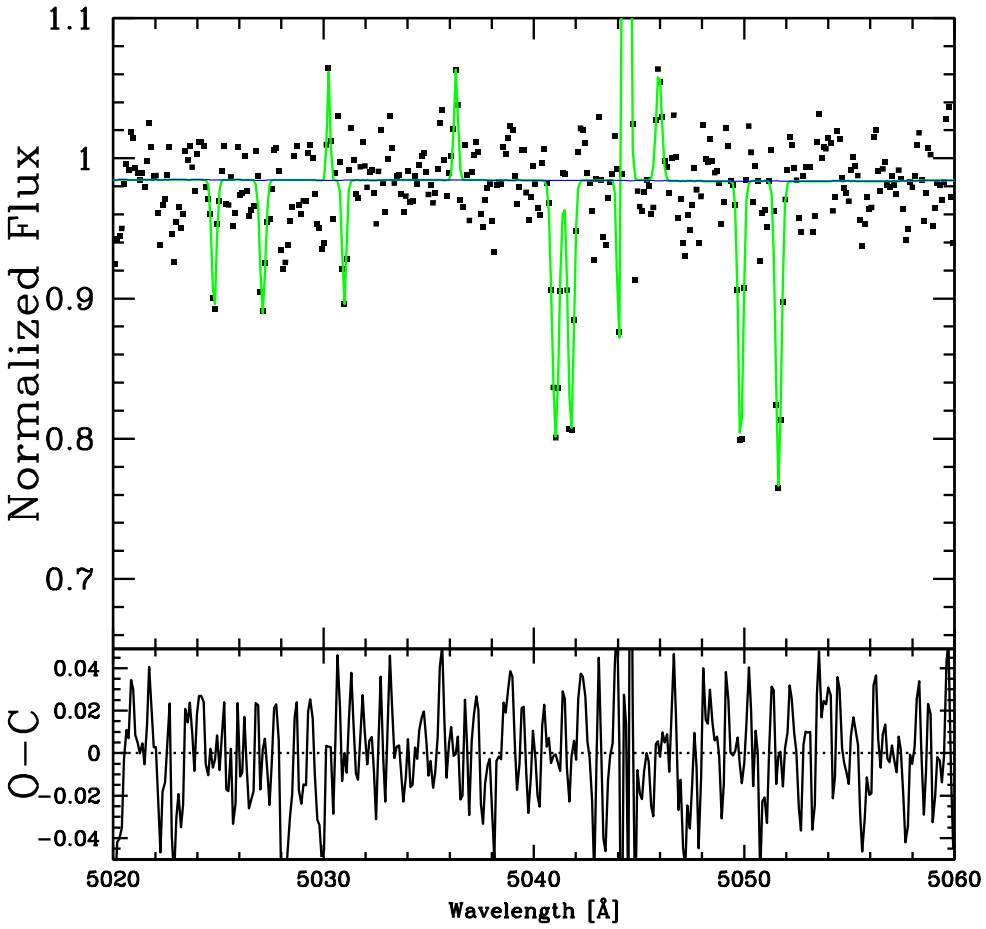

Figure 2.13 Plot of the line model (solid green line) and continuum model (solid blue line) against the input spectrum (black squares), with the residuals between the input spectrum and line model plotted at the bottom (solid black line) for the S/N 30 case. Three noisy peaks are fit at λ5030, λ5038, and λ5046 as emission lines. A cosmic ray is also fit as an emission line at λ5044.

cannot be measured well enough for inclusion subsequent analysis such as stellar parameter determination. The previous set of statistics included all lines that were measured by ROBOSPECT and not flagged by the code as invalid. As such, they may include lines with these undesirable features. We performed a statistical analysis on a subset of these lines which have been deemed suitable for stellar abundance analysis and present the results in Table 2.5. We include only the statistical results from the fifth iteration, as these are the final fit values.

Table 2.5. Equivalent Width Deviations Using A Restricted Set of Lines

S/N	Setting	Mean [mÅ]	σ [mÅ]	Median [mÅ]	Low [mÅ]	High [mÅ]	Q25 [mÅ]	Q75 [mÅ]	σ_Q [mÅ]	N
300	Gaussian	0.445	2.240	0.2	-6.4	8.4	-0.5	1.0	1.112	82
300	Hjerting	0.654	1.900	0.3	-3.6	8.3	-0.3	1.2	1.112	74
100	Gaussian	0.881	2.112	0.5	-5.4	6.5	-0.5	1.8	1.705	72
100	Hjerting	0.496	2.220	0.4	-8.5	6.4	-0.6	1.4	1.483	68
65	Gaussian	1.421	2.273	1.2	-3.7	8.7	-0.2	2.7	2.150	85
65	Hjerting	1.353	2.016	1.1	-2.9	6.0	0.0	2.6	1.928	76
45	Gaussian	4.747	4.828	4.2	-6.0	22.8	2.1	7.4	3.930	55
45	Hjerting	3.808	4.817	4.1	-10.3	13.1	2.0	6.8	3.559	48
30	Gaussian	6.854	5.716	6.7	-5.3	25.7	3.1	9.8	4.968	68
30	Hjerting	6.602	5.859	6.2	-6.5	26.1	3.0	9.6	4.894	63

Note. — Table containing the detailed statistics of the difference in equivalent widths measured between the manual measurements from Hollek et al. (2011) and ROBOSPECT for line fits including only those lines which would be considered fit for an abundance analysis. For each S/N, we show the same statistics as in Table 2.3 for the final iteration using both of the fitting parameters (Gaussian and Hjerting line profiles).

In general, we find the same trend in these improved statistics: high S/N values correspond with smaller mean differences, medians, σ, and σ_Q values. By removing spurious lines, we find better agreement with the manual equivalent width measurements. Of particular importance is that once the outliers are removed, the Hjerting line profile fits match slightly better than the Gaussian fits as compared to the manual measurements. When accepting all lines that ROBOSPECT deemed valid, the Gaussian fits performed better; hence, the Hjerting profile is more susceptible to outliers, but should be used when the user can remove particularly bad fits. Below we highlight some statistics of note.

In the 45 S/N Gaussian case, the σ, mean, and median improve, but the σ_Q value increases. This is likely because the line fits that were deemed bad were less discrepant from the manual measurements than some of the lines that were left in the re-analysis of the statistics. These seemingly "very bad" lines were left in because the discrepancy in the measured equivalent widths is a result of the different choices in the continuum level. It is likely that this creates a problem for the 45 S/N case and not the others because the S/N is low enough to begin to hide weak lines in the noise which would pull down the continuum level to a significant level, but not so low that a large fraction of the lines are lost in the noise.

In the 65 S/N Hjerting case, we find that the mean increases in the re-run after removing the bad fits. For this run, the extreme outliers were on the lower end, bringing the mean down closer to 0. By removing the

highly negative outliers, the mean increased; however, the median, which is more robust against outliers decreased along with the σ_Q and σ values as is expected.

2.3.3 Emission Spectrum Comparison

As discussed in Section 2.2.1, the method used for fitting flux calibrated data is slightly different than that used for normalized spectra. To test the accuracy of this fitting mode, we examined a set of long slit emission spectra of the Orion nebula. These data were taken on the 1.5-meter Cassegrain Spectrograph at CTIO. Three gratings were used, providing a blue, red, and high resolution spectrum for each pointing. The characteristics of these gratings is provided in Table 2.6.

Table 2.6. Orion spectra grating data

Grating	Blaze Wavelength (Å)	Wavelength Coverage (Å)	Resolution FWHM (Å)	Median Relative Flux Difference (%)	Relative Flux Difference Scatter (%)
Blue	5000	6900	17.2	0.36	2.48
High	6750	1725	4.3	-1.32	2.20
Red	8000	6550	16.4	-1.03	3.26

The spectra were flux calibrated, and apertures defined to bin the spectra to ensure an average signal-to-noise of $S/N \approx 10$. This results in thirty binned spectra for each of the 24 input images. A manual measurement of the lines was performed using the IRAF task SPLOT, with the continuum and center set manually.

ROBOSPECT was then used to measure each spectrum as well, using a single list of lines and a Gaussian line model. The relative flux difference $((F_{ROBOSPECT} - F_{SPLOT})/F_{ROBOSPECT})$ and the scatter are listed in Table 2.6. For the majority of lines, the results agree very well, again illustrating that ROBOSPECT produces measurements consistent with other methods of spectral line measurement. Figure 2.14 shows the scatter observed in individual lines for each grating. It is clear from this that the scatter in the high resolution spectra is much lower than for the other two gratings. For the lines with the largest difference, a comparison of the SPLOT and ROBOSPECT measurements shows that ROBOSPECT fluxes are generally lower than those measured by SPLOT. This decreased flux is a result of ROBOSPECT deblending neighboring lines that were fit with a single Gaussian in the SPLOT analysis. Therefore, this increased scatter is largely a result of the manual measurement incorrectly modeling the data.

2.3.4 Solar Spectrum Analysis

The assumption that all lines can be fit by Gaussians or the Hjerting model is certainly not valid for the strongest lines. For these very broad lines,

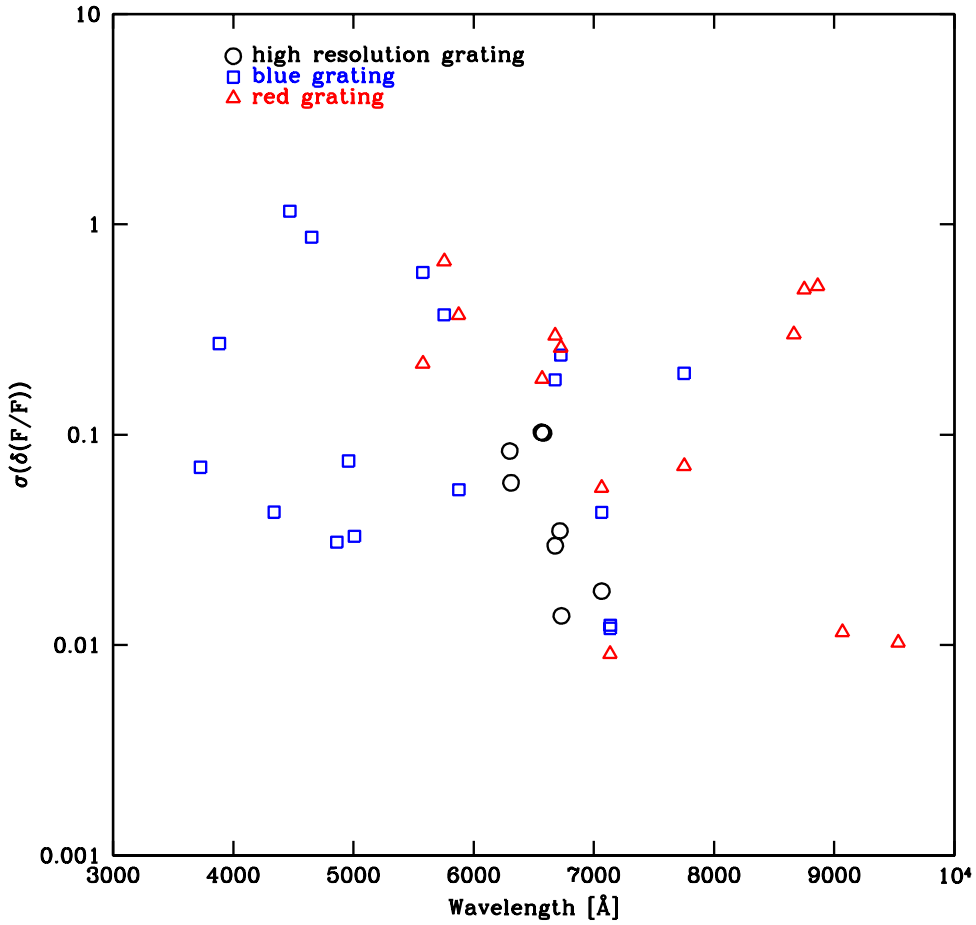

Figure 2.14 Observed relative flux scatter between the ROBOSPECT and manual SPLOT measurements for individual lines in the Orion emission spectra. The three gratings are plotted separately, illustrating that the two methods are more consistent for the higher resolution data, which has fewer issues with blending.

ROBOSPECT will underestimate the line flux as the true line shape deviates from the analytic forms. Such lines are not commonly used in the calculation of stellar properties in studies like the CASH project, but knowing the point at which the analytic models break down is essential.

This break down point can be calculated with a well-calibrated real spectrum that contains a large number of lines that vary over many orders of magnitude in equivalent width. Furthermore, using a spectrum with a very high signal-to-noise ratio and resolution reduces the possibility that faint lines blended into the wings of strong lines will make those strong lines deviate from the analytic form. The solar spectrum presented by Wallace et al. (2011) satisfies all of these requirements, and in addition, has a well-calibrated continuum level that we can take as fixed to reduce the influence that the ROBOSPECT continuum level can have on the line measurements.

From this high quality spectrum, we selected the region between 3825 and 4561 Å to study. This region contains many lines, with a range of equivalent width values from 1 to 1000 mÅ. To do the comparison, we first ran ROBOSPECT with the Hjerting line model selected. For each of the well-fit lines in the output catalog, we attempted to construct an independent non-parametric measurement. As these lines may still have contaminating blended lines, we constrain the non-parametric model curve in two ways. First, the line must be symmetric about the central wavelength. This constraint helps remove these blends, as we can use symmetry to exclude the influence on the line under consideration. Secondly, we demand that a line monotonically ap-

proaches the continuum. This also helps prevent issues with blending, and ensures that the line has a finite total flux. Once each line shape was defined by this non-parametric model, we used a direct integration of the line flux to obtain the total equivalent width.

Unsurprisingly, this non-parametric model generally produces larger equivalent widths than the standard Hjerting fits, as it can probe further out into the wings of the lines. For weak lines, this effect is minimal, as any wings are small and reasonably fit by the analytic model. For lines with non-parametric equivalent widths less than $EQW \sim 100$, the residuals between the non-parametric model and Hjerting model are largely random, with an average deviation of $6.1 \pm 12.7 m\mathring{A}$. Above this limit, however, the deviations and scatter increase dramatically, as the lines become increasingly dominated by the wings instead of the core. This change is poorly modeled by the Hjerting function, resulting in a larger average deviation of $52.6 \pm 51.1 m\mathring{A}$. Separating out the measurements above $EQW = 100$, we can fit a line to the deviations and note that the error in the Hjerting fits is largely linear with the true equivalent width, such that $\Delta EQW = 40.22 - 0.56 EQW$.

2.4 Other Equivalent Width Measurement Software

The future of astronomical study is in large collaborations, specifically large surveys, such as those like the Sloan Digital Sky Survey (SDSS) York et al. (2000) and the subsequent Sloan Extension for Galactic Understanding and Exploration (SEGUE) Yanny et al. (2009), both of which included a large

spectroscopic component. For these surveys, and for any statistical stellar sample, it is necessary to analyze the spectra in a self-consistent manner so that the resultant abundance trends and frequencies are meaningful. SDSS and SEGUE employ the Sloan Stellar Parameter Pipeline (SSPP) (Lee et al., 2008) for such analysis of its medium resolution spectra. However, for studies with higher resolution data, there exist several codes to measure equivalent widths, although are truly fully-automated. ROBOSPECT has been written to fill this niche, and perform automated fits to high resolution spectra.

A variety of very good publicly available programs exist, and can largely be divided into three categories: manual, semi-automated, and fully automated methods. Manual programs, such as SPLOT in IRAF[2], require continuous user interaction, and due to this, the measurements can be significantly influenced by the decisions of the user. This "personal equation" includes a variety of factors that can vary from user to user, such as how the continuum level is set, the line width in wavelength space, and considerations for smoothing. In order to obtain a consistent set of measurements, all of these factors must be kept the same, usually resulting in a single spectroscopist performing all measurements. For large scale, labor-intensive projects, such as CASH, it can be difficult to remain consistent over hundreds of lines in hundreds of stars.

[2]IRAF is distributed by the National Optical Astronomy Observatories, which is operated by the Association of Universities for Research in Astronomy, Inc., under cooperative agreement with the National Science Foundation.

This problem is somewhat resolved by the semi-automated methods, which reduce the level of user interaction. However, even in these programs, the initial equivalent width can be flawed as the automated continuum placement is rudimentary. Weak lines and noise can be indistinguishable, which can bias the continuum level calculated, requiring user input into the continuum placement, which is generally the largest component of error associated with the measurement. Additionally, the line-finding algorithms often have difficulties in detecting and measuring weak lines that are adjacent to large features.

Fitline (François et al., 2003) is an example of a semi-automated equivalent width measurement code. It utilizes a genetic algorithm to fit Gaussian profiles to the lines of a linelist by generating random Gaussian parameters, mutating those parameters based on the lines that are best fit, and iterating until convergence to the best fits. Fitline requires some initial user interaction to dictate files. It can also be used with a post-processing code where the user can flag fit quality. A detailed description of the code can be found in Lemasle et al. (2007).

DAOSPEC (Stetson & Pancino, 2008) is another equivalent width measurement software that is written in FORTRAN, for use with IRAF libraries and supermongo for graphical support. It works over five iterations to determine the equivalent widths and in many ways is similar to ROBOSPECT, using a line-fitting and continuum-fitting cycle. DAOSPEC is not interactive, although it does require the user to set input values, including a FWHM

estimate and the polynomial order used to fit the continuum.

ROBOSPECT was written with the intent of being deterministic, therefore the inputs required by ROBOSPECT do not greatly affect the resultant equivalent width measurements. It was also written to be user-friendly. It utilizes freely available libraries and graphics support so it is free of cost as well as open source. Additionally, since it is written in C, it is not under any peculiar constraints in terms of the formatting of input files and is easily modified for specific projects.

2.5 Conclusions

With the increasing scale of data in astronomical projects, automating the process of measuring features is essential to make use of the corresponding increase in computational power. To support this goal for the CASH project, we have written ROBOSPECT, a fully-automated equivalent width measurement code. Although ROBOSPECT was designed for metal poor stars, it is capable of fitting absorption and emission features in a variety of astronomical sources.

Based on the results of a large number of simulated spectra with known line parameters, we are confident that the fitting accuracy of ROBOSPECT is consistent with the expected theoretical accuracy as presented by Cayrel (1988). These results are confirmed by the comparing the ROBOSPECT results with manual measurements of both a sampling of CASH project stars at a variety of S/N, as well as a set of long-slit spectra of the Orion nebula.

While ROBOSPECT can be used to greatly reduce the labor involved in determining the equivalent widths of spectral lines, it is not written with the intention to be a substitute for actually looking at the data. Thus, a re-analysis of a subset of the lines that are visually confirmed to be valid for stellar parameter determination and abundance analysis shows an expected improvement in the scatter relative to the manual measurements. We found that our statistics improved over all of our S/N values and for both of the ROBOSPECT parameter settings we investigated. In the case of the Hjerting model, we found that extreme outliers, which would not be considered valid for stellar abundance work, can bias the results.

Another caveat is that due to the method used to fit the lines and measure the continuum, ROBOSPECT has difficulty with spectra in which there is no discernible continuum over large wavelength regions. In metal-poor stars, these regions can be found in cool stars with molecular bandheads, often from titanium and also in stars with enhanced carbon abundances. These features are also difficult to define mathematically, preventing minimization process from finding a single best fitting set of parameters. Thus, ROBOSPECT should not be used for these stars; however, most other routines will also have difficulties with these stars. Similarly, in the case of the most carbon-enhanced stars, it is better to skip the equivalent width measurement analysis in favor of a spectral synthesis.

JKH acknowledges support for this work from NSF grants AST 0708245 and AST 0908978. CZW acknowledges support for this work through the

PanSTARRS Science Consortium, which has been made possible through contributions of the Institute for Astronomy, the University of Hawaii, the Pan-STARRS Project Office, the Max-Planck Society and its participating institutes, the Max Planck Institute for Astronomy, Heidelberg and the Max Planck Institute for Extraterrestrial Physics, Garching, The Johns Hopkins University, Durham University, the University of Edinburgh, Queen's University Belfast, the Harvard-Smithsonian Center for Astrophysics, and the Las Cumbres Observatory Global Telescope Network, Incorporated, the National Central University of Taiwan, and the National Aeronautics and Space Administration under Grant No. NNX08AR22G issued through the Planetary Science Division of the NASA Science Mission Directorate. Partial support for this work was provided by National Science Foundation grant AST-1009749. We are very grateful to Jack Baldwin for supplying the Orion nebula spectra used in this paper. We also appreciate useful conversations with Christopher Sneden, Harriet Dinerstein, Anna Frebel, Matthew Shetrone, Randi Ludwig, and Eugene Magnier.

Chapter 3

The Chemical Abundances of Stars in the Halo (CASH) Project. II. A Sample of 16 Extremely Metal-poor Stars

We present a comprehensive abundance analysis of 20 elements for 16 new low-metallicity stars from the Chemical Abundances of Stars in the Halo (CASH) project. The abundances have been derived from both Hobby-Eberly Telescope High Resolution Spectrograph snapshot spectra (R $\sim 15,000$) and corresponding high-resolution (R $\sim 35,000$) Magellan MIKE spectra. The stars span a metallicity range from [Fe/H] from -2.9 to -3.9, including four new stars with [Fe/H] < -3.7. We find four stars to be carbon-enhanced metal-poor (CEMP) stars, confirming the trend of increasing [C/Fe] abundance ratios with decreasing metallicity. Two of these objects can be classified as CEMP-no stars, adding to the growing number of these objects at [Fe/H]< -3. We also find four neutron-capture enhanced stars in the sample, one of which has [Eu/Fe] of 0.8 with clear r-process signatures. These pilot sample stars are the most metal-poor ([Fe/H] $\lesssim -3.0$) of the brightest stars included in CASH and are used to calibrate a newly-developed, automated stellar parameter and abundance determination pipeline. This code will be used for the entire ~ 500 star CASH snapshot sample. We find that the pipeline results are statistically

identical for snapshot spectra when compared to a traditional, manual analysis from a high-resolution spectrum. This work was published in Hollek et al. 2011, ApJ, 742, 54.

3.1 Introduction

The first stars formed from metal-free material in the early universe and therefore are thought to have been massive ($\sim 100 M_{\odot}$; e.g., Bromm et al. 1999). Many of these first stars polluted the surrounding local environment with their chemical feedback through core-collapse supernovae. From this enriched material, subsequent generations of stars were born. Due to the presence of additional cooling mechanisms, these stars had a range of lower masses and thus were longer lived (e.g., Bromm & Loeb 2003).

Today, we observe the surviving low-mass stars as the most metal-poor stars in the Galaxy. The atmospheres of these objects contain the chemical signatures of early supernova events. By studying these stars, constraints can be placed on the specific types of nucleosynthetic events responsible for the observed abundances patterns.

Efforts to classify metal-poor stars have been based upon metallicity, [Fe/H][1], and chemical composition, [X/Fe], to better understand the diversity of the observed abundance patterns (Beers & Christlieb, 2005). Stars with [Fe/H] < -3.0 are labeled as extremely metal-poor (EMP). The metallicity

[1] $[A/B] \equiv \log(N_A/N_B) - \log(N_A/N_B)_{\odot}$ for N atoms of elements A, B, e.g., [Fe/H] $= -3.0$ is 1/1000 of the solar Fe abundance.

distribution function shows that as metallicity decreases, the number of stars in each metallicity bin rapidly decreases (Ryan & Norris, 1991; Carney et al., 1996; Schörck et al., 2009; Li et al., 2010). Only ~ 25 of these EMP stars have [Fe/H] $\lesssim -3.5$. Below [Fe/H] ~ -3.6 there is a sharp drop in the number of stars, so extreme EMPs are an important probe of this tail. To date, only three stars with [Fe/H] < -4.5 have been discovered, with two considered to be hyper metal-poor ([Fe/H] < -5.0; Christlieb et al. 2004; Frebel et al. 2005; Norris et al. 2007).

The majority of metal-poor stars ([Fe/H]< -1) show abundance patterns similar to the Solar System, but scaled down by metallicity, with two main differences: there is an enhancement in the α-elements (e.g., [Mg/Fe]) and a depletion in some of the Fe-peak elements (e.g., [Mn/Fe]) compared to the solar abundance ratios. This pattern can be explained with enrichment by previous core-collapse supernovae (e.g., Heger & Woosley 2010). The chemical outliers among stars with [Fe/H] < -2.0, which make up perhaps 10%, show great diversity in their abundance patterns. Many stars have overabundances in selected groups of elements, e.g., the rapid (r) neutron-capture process elements (Sneden et al., 2008) and/or the slow (s) neutron-capture process elements. The frequency of chemically unusual stars increases with decreasing metallicity, with stars often belonging to multiple chemical outlier groups. Not included in this estimate of chemically unusual stars are the so-called carbon-enhanced metal-poor (CEMP) stars (where [C/Fe] > 0.7), which make up at least $\sim 15\%$ of stars with [Fe/H] < -2.0. At the lowest metallic-

ities, the frequency of CEMP stars also increases (Beers & Christlieb, 2005; Lucatello et al., 2006; Frebel et al., 2006; Cohen et al., 2006; Carollo et al., 2011). In fact, all three [Fe/H] < -4.5 stars are CEMP stars.

Medium-resolution spectra (R $\sim 2,000$) can be used to determine the overall metallicity based upon the strength of the Ca II K line. However, medium-resolution spectra provide limited information on the abundances of individual elements, especially at low metallicity. High-resolution (e.g., R $\sim 40,000$) observations are necessary to carry out detailed analyses which yield abundances with small uncertainties ($\sim$ 0.1 dex). These observations are, however, more time consuming and require large telescopes to achieve an adequate S/N ratio in the data.

"Snapshot" spectra, with intermediate resolution (R $\sim 15,000$-$20,000$) and moderate S/N ($\sim$ 40) fill the gap between time intensive high- and medium-resolution observations. From such snapshot data, abundances for $\sim$ 15 elements can be derived with moderate uncertainties ($\sim$ 0.25 dex; Barklem et al. 2005). This allows for a more efficient confirmation of EMP stars and chemical outliers. The Barklem et al. (2005), Hamburg/ESO R-process Enhanced Star, (hereafter HERES) study itself determined abundances (and upper limits) for a total of $\sim$ 250 stars based on VLT/UVES snapshot spectra.

The Chemical Abundances of Stars in the Halo (CASH) project is a dedicated effort that aims to provide abundances for $\sim$ 500 metal-poor stars primarily based on R $\sim 15,000$, moderate-S/N snapshot spectra taken with the High Resolution Spectrograph (HRS) (Tull, 1998) on the fully queue scheduled

(Shetrone et al., 2007) Hobby-Eberly Telescope (HET). One of the earliest results of the CASH project was the discovery of an unusual, Li-enhanced giant, HKII 17435−00532 (Roederer et al., 2008). Given the large number of stars in the sample, it is expected that there will be additional chemically-unusual stars.

In this paper, we study the CASH pilot sample of 16 stars, spanning a metallicity range of $\sim$ 1.0 dex, from [Fe/H] ~ -2.9 to -3.9. The aim of the present study is twofold: to present abundance analyses for the 16 most metal-poor stars included in the CASH project and to use those abundances to calibrate the newly developed stellar parameter and abundance pipeline. We will use it to obtain abundances for the full $\sim$ 500 star CASH sample (Hollek et al. 2012, in prep.).

In Section 3.2 we discuss the spectra in terms of the sample selection, observational information, and data reduction. In Section 3.3 we introduce our spectral analysis tools, including our linelist, equivalent width measurement routines, and model atmosphere analysis code. In Sections 3.4 and 3.5 we describe acquisition of our stellar parameters for both sets of data and a comparison between the two. In Section 3.6 we discuss the abundance analysis methods for each element we measure, including the error analysis and comparison of our results to those in the literature. Section 3.7 includes a summary of our abundance results and discussion of the implications of our derived abundances. In Section 3.8 we list our summary.

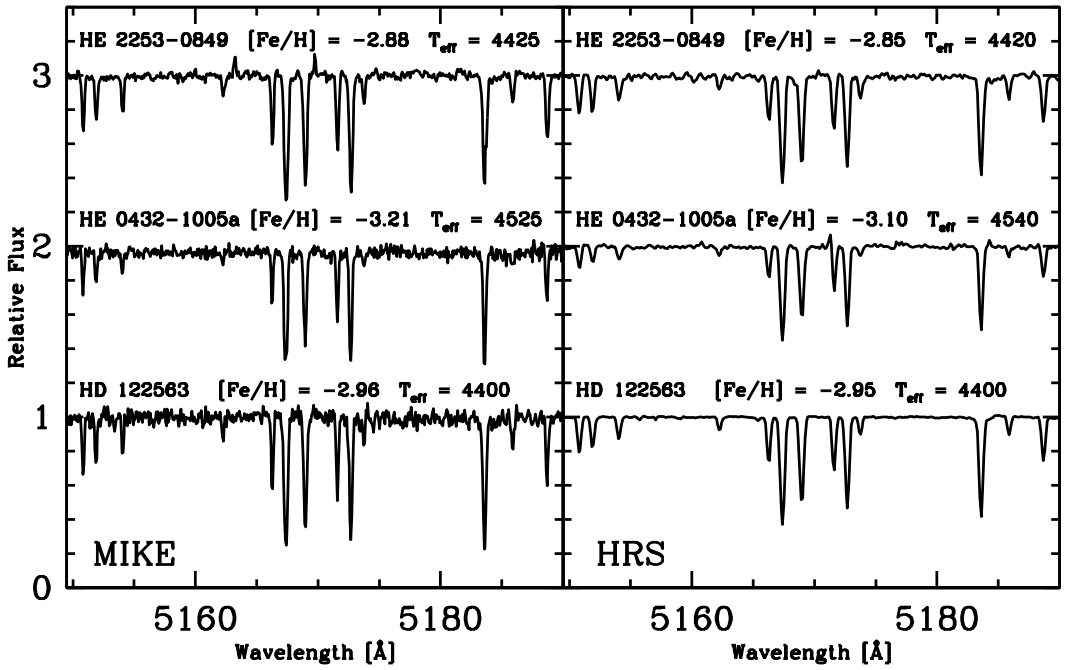

Figure 3.1 MIKE (left) and HRS (left) spectra of three stars with derived spectroscopic $T_{eff} \sim 4500$ K. Both HRS and MIKE derived [Fe/H] values are listed for each star.

3.2 Observations

3.2.1 Sample Selection

The stars of the pilot study were chosen from the Hamburg/ESO Bright Metal-Poor Sample (BMPS; Frebel et al. 2006) of the Hamburg/ESO objective-prism plate Survey (HES; Christlieb et al. 2001). These stars (B<14.5) required extra processing due to saturation of the photographic plates. Around 170 new metal-poor stars with [Fe/H] < -2.0 were identified from medium-resolution spectra; most of the BMPS stars observable from McDonald Observatory were added to the CASH sample in order to obtain snapshot spectra

with the HET. This paper includes 16 HES BMPS objects, chosen as the most metal-poor HES BMPS stars in the CASH study. We also included five new high-resolution observations of well studied stars from the literature for comparison purposes. All 16 HES objects have high-resolution observations. Of these objects, 14 have HRS spectra. Only one standard star, HD 122563, has an HRS spectrum. Figure 3.1 shows both the HRS and MIKE spectra of three representative stars in this sample. The full ~ 500 star sample contains targets from other surveys including the Sloan Digital Sky Survey (York et al., 2000), the Sloan Extension for Galactic Understanding and Exploration (Yanny et al., 2009), and the HK (Beers et al., 1985, 1992) surveys.

Of the HRS snapshot spectra included in this study, three spectra were substantially contaminated with the solar spectrum, with no available sky fibers to properly correct the data. From these spectra, we were able to determine that the [Fe/H] values for the stars were roughly -3.0; however, these spectra require further processing in order to derive accurate stellar parameters and abundances. The snapshot-derived results for these stars will be included in a future paper, though we present the abundances derived from the high-resolution MIKE spectra here.

3.2.2 Spectroscopy

The snapshot spectra for the CASH project were obtained using the fiber-fed HRS on the HET at McDonald Observatory. The CASH spectra were obtained with a $2''$ fiber yielding R $\sim 15,000$. The 2×5 on-chip CCD binning

leads to 3.2 pixels per resolution element. Two CCDs were used to record the red and blue portions of the spectrum. The useful wavelength range is from 4200−7800 Å, or from the CH G-band to the oxygen triplet. The median S/N value for the entire 500 star sample is $\sim$ 65, with a median S/N value for the pilot sample of 70; see Table 3.1. There is substantially lower S/N at the blue ends of the spectra, given the combination of the somewhat poor blue response of the HRS and the lack of blue flux for many of the objects observed in CASH, especially the cool giants.

High-resolution spectra for 21 stars were obtained using the MIKE instrument (Bernstein et al., 2003) on the Magellan-Clay Telescope at Las Campanas Observatory. We used the $0''.7$ slit with 2×2 on-chip binning, yielding a nominal resolution of R $\sim 35,000$ in the blue and 28,000 in the red with average S/N $\sim$ 85 at 5200 Å. MIKE spectra have nearly full optical wavelength coverage from $\sim$ 3500-9000 Å. Table 3.1 lists the details of the observations for each star on both telescopes.

Table 3.1. Observations

Star	Telescope	UT Date	RA (J2000)	Dec (J2000)	t_{exp} sec	S/N at 5180 Å	v_{rad} km s^{-1}
HE 0013−0257	HET	28 Jul 2007	00 16 04.2	−02 41 06	630	65	47.7
	Magellan	28 Sep 2006			600	34	45.4
HE 0013−0522	HET	08 Aug 2007	00 16 28.1	−05 05 52	678	85	−174.7
	Magellan	08 Aug 2010			1800	81	−175.5
HE 0015+0048	HET	10 Aug 2007	00 18 01.4	+01 05 08	888	70	−40.8
	Magellan	08 Aug 2010			1800	56	−48.8
HE 0302−3417a	Magellan	27 Sep 2006	03 04 28.6	−34 06 06	300	88	121.7
HE 0324+0152a	HET	24 Feb 2008	03 26 53.8	+02 02 28	316	65	107.3
	Magellan	27 Sep 2006			450	70	106.1
HE 0420+0123a	HET	05 Jan 2008	04 23 14.4	+01 30 49	207	180[a]	−53.3
	HET	12 Nov 2009			800	···	−52.8

Table 3.1 (cont'd)

Star	Telescope	UT Date	RA (J2000)	Dec (J2000)	t_{exp} sec	S/N at 5180 Å	v_{rad} km s^{-1}
	Magellan	28 Sep 2006			300	64	−55.3
HE 0432−1005a	HET	10 Nov 2008	04 35 01.2	−09 59 36	890	80[a]	198.0
	HET	12 Nov 2009			1800	···	199.6
	Magellan	28 Sep 2006			900	44	197.3
HE 1116−0634	HET	contaminated[b]	11 18 35.8	−06 50 46	···	···	···
	Magellan	03 Jul 2010			1200	121	115.5
HE 1311−0131	HET	06 Apr 2008	13 13 42.0	−01 47 16	250	45	125.8
	Magellan	05 Aug 2010			2736	48	124.7
HE 1317−0407	HET	contaminated[b]	13 19 47.0	−04 23 10	···	···	···
	Magellan	03 Jul 2010			487	135	124.7
HE 2123−0329	HET	28 Jun 2008	21 26 08.9	−03 16 58	1473	65	−218.8

Table 3.1 (cont'd)

Star	Telescope	UT Date	RA (J2000)	Dec (J2000)	t_{exp} sec	S/N at 5180 Å	v_{rad} km s^{-1}
	Magellan	05 Aug 2010			1800	85	−219.4
HE 2138−0314	HET	13 Nov 2009	21 40 41.5	−03 01 17	600	85[a]	−371.0
	HET	14 Jul 2008			891	···	−371.6
	Magellan	05 Aug 2010			1304	93	−373.5
HE 2148−1105a	HET	contaminated[b]	21 50 41.5	−10 50 58	···	···	···
	Magellan	06 Aug 2010			300	61	−87.17
HE 2238−0131	HET	13 Nov 2008	22 40 38.1	−01 16 16	494	60	−185.0
	Magellan	08 Aug 2010			1200	96	−186.7
HE 2253−0849	HET	13 Nov 2008	22 55 43.1	−08 33 28	427	75	−89.4
	Magellan	08 Aug 2010			1200	63	−91.1
HE 2302−2154a	Magellan	28 Sep 2006	23 05 25.2	−21 38 07	450	55	−17.8

Table 3.1 (cont'd)

Star	Telescope	UT Date	RA (J2000)	Dec (J2000)	t_{exp} sec	S/N at 5180 Å	v_{rad} km s^{-1}
HD 122563	HET	01 Mar 2009	14 02 31.8	+09 41 10	30	300	−25.4
	Magellan	26 Jul 2009			5	35	−25.7
CD −38 245	Magellan	27 Jul 2009	00 46 36.2	−37 39 33	250	65	47.1
CS 22891−200	Magellan	05 Aug 2010	20 19 22.0	−61 30 15	900	52	137.7
CS 22873−166	Magellan	27 Jul 2009	19 35 19.1	−61 42 24	120	53	−16.2
BD −18 5550	Magellan	27 Jul 2009	19 58 49.7	−18 12 11	87	157	−125.3

[a]S/N for combined HET spectra

[b]Sky contamination in spectrum, excluded from this analysis

3.2.3 Data Reduction

The HRS spectra were reduced using an IDL pipeline called REDUCE (Piskunov & Valenti, 2002), which performs standard echelle reduction techniques (trimming, bias subtraction, flat fielding, order tracing, extraction). The data were wavelength calibrated using ThAr lamp exposures taken before or after every observation. Comparisons have been made between a by-hand IRAF[2] reduction and the REDUCE reduction of medium-S/N HRS data. Both yield comparable S/N across the spectrum, and the measured equivalent widths for 121 different lines differ between the two different reductions by 3 ± 8m Å, which is statistically insignificant (Roederer et al., 2008). In addition, earlier tests of REDUCE versus IRAF have shown that the optimized extraction in REDUCE for high S/N spectra yields an extracted spectrum that is less noisy than that of a spectrum extracted in IRAF (see Figure 8 in Piskunov & Valenti 2002). Standard IRAF routines were then used to coadd (in the case of multiple observations) and continuum normalize the individual observations into a final one-dimensional spectrum. Radial velocities (RVs) were computed by cross-correlating the echelle order containing the Mg b triplet against another metal-poor giant observed with the same instrumental setup. Typical uncertainties were $2-3$ km/s for a single observation. Barycentric velocity corrections were computed using the IRAF "rvcorrect" routine.

[2]IRAF is distributed by the National Optical Astronomy Observatories, which is operated by the Association of Universities for Research in Astronomy, Inc., under cooperative agreement with the National Science Foundation.

Spectra observed using the MIKE instrument were reduced using an echelle data reduction pipeline made for MIKE[3] and then normalized and coadded using the same method as the HRS spectra.

3.3 Spectral Analysis

3.3.1 Linelist

The linelist to analyze the HRS spectra was based on the lines included in Roederer et al. (2010). Only those lines which are unblended at the median S/N and resolution of the typical HRS snapshot spectrum were included in our final list.

The linelist for the MIKE data is a composite of the lines from Roederer et al. (2010), supplemented with additional lines from Cayrel et al. (2004), and Aoki et al. (2007b). This linelist includes those lines used for the HRS snapshot spectra analysis. In the instances where the same line was included in more than one linelist, the most up to date oscillator strength was used, following Roederer et al. (2010). We confirmed that all important lines for our abundance analysis were included in this linelist by plotting the position of each line against a high-resolution MIKE spectrum of a star with a higher metallicity than that of any star in the pilot sample. Compared to the sample stars, this star displays many more absorption lines. This also allowed us to visually inspect for features that were not present in both an EMP star and

[3]available at http://obs.carnegiescience.edu/Code/python

star that is still considered to be metal-poor, but with substantially higher (1 dex) [Fe/H].

3.3.2 Line Measurements

In each spectrum, we measured equivalent widths of unblended lines of various elements. Table 3.2 lists the element and ionization state, equivalent widths, wavelength, excitation potential, and oscillator strengths of each measured line in the MIKE spectra. These equivalent widths were used to determine stellar parameters and abundances for ~ 10 elements. The equivalent widths in the HRS spectra were measured using an IDL routine. Here we briefly summarize the features important to this work. The routine works to automatically fit a Voigt profile to each line. The user can then manually adjust the continuum level, the number of spectral points over which the line is fit, and the line center, among other features. Given the limitations in resolution and S/N, some lines used in the analysis for HRS spectra depart from the linear portion of the curve of growth, thus line fits using the Voigt profile, rather than simply a Gaussian fit, are preferred.

The equivalent widths in the high-resolution spectra were measured with an ESO/Midas routine which automatically fits Gaussian profiles to each line. The user can calculate a fit to the continuum level by selecting line free continuum regions. This code takes into account any possible non-zero slope of the continuum.

We chose a different equivalent width measurement routine because

Table 3.2. Equivalent Widths

Star	Ion	Wavelength Å	XP	log gf	EW m Å
HE 0015+0048	12.0	3986.75	4.35	−1.030	27.5
HE 0015+0048	12.0	4057.50	4.35	−0.890	41.9
HE 0015+0048	12.0	4167.27	4.35	−0.710	64.9
HE 0015+0048	12.0	4571.09	0.00	−5.688	57.7
HE 0015+0048	12.0	4702.99	4.33	−0.380	65.1
HE 0015+0048	12.0	5528.40	4.34	−0.498	78.2
HE 0015+0048	13.0	3961.52	0.01	−0.340	125.1
HE 0015+0048	20.0	4226.73	0.00	0.244	210.3
HE 0015+0048	20.0	4289.36	1.88	−0.300	51.7
HE 0015+0048	20.0	4318.65	1.89	−0.210	42.5
...					

Note. — Table 3.2 is published in its entirety in the electronic edition. A portion is shown here for guidance regarding its form and content. We list the ionization state of each element where .0 indicates a neutral species and .1 indicates a singly-ionized species.

the higher S/N of the MIKE spectra allowed us to detect deviations from zero in the slope of the continuum that may arise from small-scale variation in imperfectly normalized spectra or nearby strong lines. Thus, it was helpful to be able to make a linear fit when determining the continuum. Additionally, the larger wavelength range allowed for more lines to be measured, thereby enabling us to exclude lines near the flat part of the curve of growth. Table 3.2 lists the equivalent widths for all our stars in the pilot sample.

Figure 3.2 shows our measured equivalent widths from the MIKE spectrum of BD −18 5550 plotted against the equivalent widths measured for the same star by Cayrel et al. (2004). We find a mean difference of −0.6 mÅ with a $\sigma = 2.4$ mÅ between the MIKE and Cayrel et al. (2004) measurements for lines included in our analysis. We also made a comparison between the equivalent widths measured from the HRS and MIKE spectra for a representative star, as we did not have an HRS spectrum for BD −18 5550 because it is not observable from McDonald Observatory. We find a mean difference of 2.5 mÅ with $\sigma = 3.4$ mÅ. In both comparisons, between the MIKE spectra measured equivalent widths and those of the Cayrel et al. (2004) study as well as between the MIKE spectra and the HRS spectra, the measured offset between the measurements shows no significant disagreement between the techniques.

3.3.3 Analysis Techniques

The large number of stars in the full ~ 500 star CASH snapshot sample calls for automation of the analysis. Stellar parameters and elemental

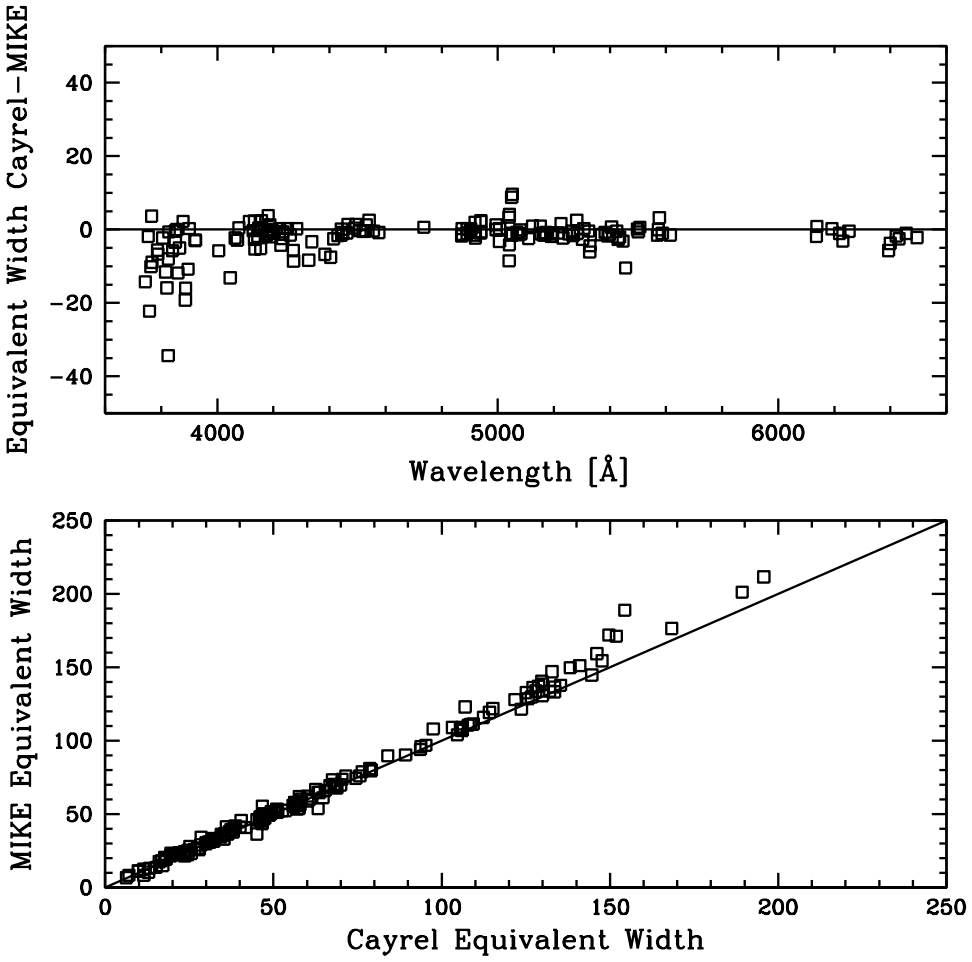

Figure 3.2 Comparison of the equivalent widths measured from the MIKE and Cayrel et al. (2004) spectra of BD −18 5550 . In the upper panel, residuals of the equivalent widths (Cayrel−MIKE) are plotted against wavelength. In the bottom panel, the measured equivalent widths from Cayrel and MIKE are plotted against each other.

abundances from the snapshot HRS spectra were determined using our newly developed spectroscopic stellar parameter and abundance analysis pipeline, Cashcode. The pipeline is written around the existing platform of the local thermodynamic equilibrium (LTE) stellar line analysis and spectrum synthesis code MOOG (the latest version, 2010; Sneden 1973). The most recent version of MOOG accounts for the fact that Rayleigh scattering becomes an important source of continuum opacity at short wavelengths, blueward of 4500 Å. This is important for our sample stars, as the effect is more pronounced in cool giants (Sobeck et al., 2011).

We compared the results of four representative stars, two from the pilot sample and two standard stars, using the newest version of MOOG and an older version that did not distinctly deal with Rayleigh scattering in the calculation of the continuum opacities. We find that the spectroscopic effective temperatures and microturbulences are lower, thus the derived [Fe/H] abundances are lower in the version that deals with Rayleigh scattering by $\sim$ 0.1-0.2 dex. Generally, the abundance ratios [X/Fe] remain within $\sim$ 0.05 dex. These abundances were determined using lines down to $\sim$ 3750 Å; however, for studies with a spectral range that encompasses shorter wavelengths, this effect may be larger. Table 3.3.3 shows the stellar parameter comparison and Table 3.4 shows the abundance ratio comparison.

Table 3.3. Stellar Parameter Comparison

Star	Scattering Treatment Included				No Scattering Treatment			
	T_{eff} [K]	log g	ξ [km/s]	[Fe/H]	T_{eff} [K]	log g	ξ [km/s]	[Fe/H]
HD 122563	4450	0.50	2.30	−2.96	4475	0.40	2.55	−2.85
CS 22891−200	4500	0.45	2.60	−3.93	4600	0.65	3.00	−3.72
HE 0015+0048	4600	0.90	1.85	−3.07	4675	1.05	2.15	−3.00
HE 0432−1000a	4525	0.50	2.00	−3.21	4600	0.65	2.60	−3.08

Table 3.4. Abundance Comparison for Different Treatments of Scattering In MOOG

	CS 22891−200		HD 122653		HE 0015+0048		HE 0432−1000a	
Elem	$[X/Fe]_{scat}$	$[X/Fe]_{non}$	$[X/Fe]_{scat}$	$[X/Fe]_{non}$	$[X/Fe]_{scat}$	$[X/Fe]_{non}$	$[X/Fe]_{scat}$	$[X/Fe]_{non}$
[Mg/Fe]	0.53	0.66	0.54	0.41	0.65	0.69	0.50	0.52
[Ca/Fe]	0.68	0.72	0.39	0.36	0.44	0.43	0.39	0.35
[Cr/Fe]	−0.43	−0.44	−0.18	−0.23	−0.17	−0.15	−0.15	−0.18
[Ni/Fe]	−0.08	−0.31	0.19	0.17	−0.02	0.05	0.01	0.16

3.4 Stellar Parameters

The first step in our abundance analysis is to determine the atmospheric parameters of each star. We accomplished this in two ways: with the Cashcode pipeline and the traditional, manual way.

In order to test the robustness of the snapshot abundances one must answer two questions: first, for a given set of stellar parameters, with what precision can abundances be determined from snapshot spectra? Secondly, does the pipeline give reasonable stellar parameters (effective temperature, surface gravity, metallicity, and microturbulent velocity) for snapshot spectra? The first question has been partially answered by the HERES study, which finds that the uncertainties are ~ 0.25 dex, but the systematic uncertainties associated with the stellar parameter and abundance determination methods and the inherent scatter of our snapshot data set must be explored. This is addressed in Section 3.6.6. The second question can be answered by testing the pipeline in detail and comparing the results from the literature with previously studied standard stars of comparable stellar parameters and metallicity; this is discussed in Section 3.6.7. Table 3.5 lists our adopted stellar parameters.

Table 3.5. Stellar Parameters

Star	MIKE				HRS			
	T_{eff} [K]	log g	ξ [km/s]	[Fe/H]	T_{eff} [K]	log g	ξ [km/s]	[Fe/H]
HE 0013−0257	4500	0.50	2.10	−3.82	4710	1.35	2.25	−3.40
HE 0013−0522	4900	1.70	1.80	−3.24	5120	2.30	2.00	−2.90
HE 0015+0048	4600	0.90	1.85	−3.07	4630	1.10	1.90	−3.00
HE 0302−3417a	4400	0.20	2.00	−3.70	...	...	...	...
HE 0324+0152a	4775	1.20	1.80	−3.32	4800	1.65	2.00	−3.05
HE 0420+0123a	4800	1.45	1.50	−3.03	4800	1.45	1.80	−3.00
HE 0432−1005a	4525	0.50	2.00	−3.21	4540	0.65	2.00	−3.10
HE 1116−0634	4400	0.10	2.40	−3.73	4650	1.00	3.80	−3.35[a]
HE 1311−0131	4825	1.50	1.95	−3.15	4820	1.50	2.00	−2.85

Table 3.5 (cont'd)

Star	MIKE				HRS			
	T_{eff} [K]	log g	ξ [km/s]	[Fe/H]	T_{eff} [K]	log g	ξ [km/s]	[Fe/H]
HE 1317−0407	4525	0.30	2.15	−3.10	4600	0.25	3.20	−3.10[a]
HE 2123−0329	4725	1.15	1.80	−3.22	4700	1.40	2.00	−3.05
HE 2138−0314	5015	1.90	1.75	−3.29	4940	2.30	2.00	−3.20
HE 2148−1105a	4400	0.20	2.65	−2.98	4450	0.20	3.20	−3.05[a]
HE 2238−0131	4350	0.15	2.45	−3.00	4300	0.30	2.15	−3.05
HE 2253−0849	4425	0.20	2.65	−2.88	4420	0.15	2.30	−2.85
HE 2302−2154a	4675	0.90	2.00	−3.90	···	···	···	···
CS 22891−200	4500	0.45	2.60	−3.92	···	···	···	···
HD 122563	4450	0.50	2.30	−2.96	4400	0.30	2.25	−2.95

Table 3.5 (cont'd)

Star	MIKE				HRS			
	T_{eff} [K]	log g	ξ [km/s]	[Fe/H]	T_{eff} [K]	log g	ξ [km/s]	[Fe/H]
BD −18 5550	4600	0.80	1.70	−3.20	···	···	···	···
CD −38 245	4650	0.95	2.15	−4.00	···	···	···	···
CS 22873−166	4375	0.20	2.80	−3.14	···	···	···	···

[a]Sky contamination in this spectrum

3.4.1 HRS Snapshot Data

The effective temperature of a star is spectroscopically determined by minimizing the trend of the relation between the abundance and excitation potential of the lines from which the abundance is derived. The microturbulent velocity is determined by doing the same for the abundance and reduced equivalent width. The surface gravity is determined from the balance of two ionization stages of the same element (e.g., Fe I and Fe II). The HRS snapshot spectra have few detectable Fe II lines, thus we use Ti I and Ti II lines in addition to Fe I and Fe II lines in the pipeline to more robustly determine the stellar parameters, in particular the gravity, from these spectra, with Fe weighted twice compared to Ti. Often, only the ionization balance of Fe is considered. The metallicity used in the model atmosphere, in this case [M/H], is an average of the abundances from individual lines of Fe I, Fe II, Ti I, and Ti II.

The pipeline works iteratively. The first process is to determine the stellar parameters from the equivalent width measurements of Ti I, Ti II, Fe I, and Fe II. An approximate initial guess to the effective temperature, surface gravity, metallicity, and microturbulent velocity are input as well as constraints on the parameters over which the code iterates. Generally for the HRS snapshot data, we require that the trend between abundance and excitation potential is $< |0.03|$ dex/eV, the reduced equivalent width and abundance trend is $< |0.15|$ dex/log(mÅ), the surface gravity criterion $\Delta_{ion} < |0.10|$ dex, and the difference between the metallicity of the model atmosphere and the

calculated metallicity is $< |0.10|$ dex. As a result of the ionization balance constraints, the abundance difference between Ti I and Ti II is allowed to be no greater than 0.3 dex if the Fe I abundance equals the Fe II abundance or the abundance difference between Fe I and Fe II is allowed to be no greater than 0.2 dex if the Ti I abundance equals the Ti II abundance. This information is used to construct an initial Kurucz stellar atmosphere with α-enhancement (Castelli & Kurucz, 2004) to begin the stellar parameter determination, in which the pipeline iterates until the various constraints that determine each stellar parameter fall within the user-defined thresholds specified in the beginning.

We used the pipeline to derive abundances for each line from its equivalent width. We used synthetic spectra to determine abundances for particular lines (e.g., Ba II λ4554) for various reasons, including hyperfine structure and blending with other features. For these lines, we used an equivalent width-derived abundance guess as an initial input for the spectral syntheses.

3.4.2 High-Resolution MIKE Spectra

The high-resolution MIKE data were analyzed manually. The large wavelength coverage allowed us to perform a more in-depth analysis with smaller uncertainties for a later comparison to the pipeline analysis of the corresponding snapshot spectra. Spectroscopic stellar parameters for all but two of the MIKE spectra were determined from equivalent width measurements of Fe I and Fe II lines. The resonance lines of Fe I were excluded in

this analysis, as they often are near the flat portion of the curve of growth. In essence, all of the steps in the Cashcode pipeline were performed, but each step was executed manually. This allowed us to compare the pipeline results with those of a manual analysis to confirm that the pipeline reproduced the results derived from the high-resolution data.

It is also possible to determine effective temperatures photometrically, using calibrations between colors and temperature for given color and metallicity ranges. We have chosen to adopt spectroscopic temperatures for these stars, as well as for the entire CASH sample, in order to present a homogeneous set of atmospheric parameters and, therefore, the resulting chemical abundances. However, we determined photometric temperatures to check the accuracy and systematic uncertainties of our method. Accurate long baseline colors (i.e., V−K) for the entire $\sim$ 500 star sample do not exist; however, we used 2MASS photometry for the pilot sample and standard stars in order to determine photometric temperatures in order to compare them to the adopted spectroscopic temperatures.

We determined reddening corrections for our stars using the Schlegel et al. (1998) dust maps. We dereddened the J−K 2MASS color and then, according to equations 1a-1c in Ramírez & Meléndez (2004), transformed J and K 2MASS photometry into the TCS system in order to use the Alonso et al. (1999) calibration to determine photometric temperatures. We determined the formal linear relation between the (J−K) photometric temperatures from the sample stars and the spectroscopic temperatures. Within the uncertainty of

the fit, there exists an offset between the spectroscopic and photometric temperatures. Thus, we adopted the mean difference between the spectroscopic and photometric temperatures to be $T_{spec} = T_{(J-K)} - 225\,K$. The uncertainties associated with the spectroscopic and photometric temperatures are 160 and 140 K, respectively. See the next subsection for further details. Figure 3.3 shows the spectroscopic temperature plotted against the (J−K) photometric temperature for the sample stars. Plotted are lines that show a 1:1 agreement, the adopted offset, and the least squares fit.

Two stars in the sample, HE 1116−0634 and HE 2302−2154a, did not have convergent spectroscopic stellar parameter solutions irrespective of the analysis method. The Fe I and Fe II abundances were not in agreement (i.e., the surface gravity criterion was not met) when the temperature criterion was met. This is likely because these stars are near the edge of the stellar atmosphere grid in terms of metallicity, temperature, and gravity. For these stars, we adopted a "pseudo-spectroscopic" effective temperatures of 4400 and 4675 K for HE 1116−0634 and HE 2302−2154a, respectively. Those were obtained by applying the previously determined offset between the spectroscopic and photometric temperatures of 225 K to their photometric temperatures. The pseudo-spectroscopic temperatures were used to determine the remaining parameters, surface gravity, microturbulence, and metallicity spectroscopically, ignoring the nonzero slope of −0.065 and −0.090 dex/eV for HE 1116−0634 and HE 2302−2154a, respectively, of the excitation potential. Typically, this slope is < 0.02 dex/eV.

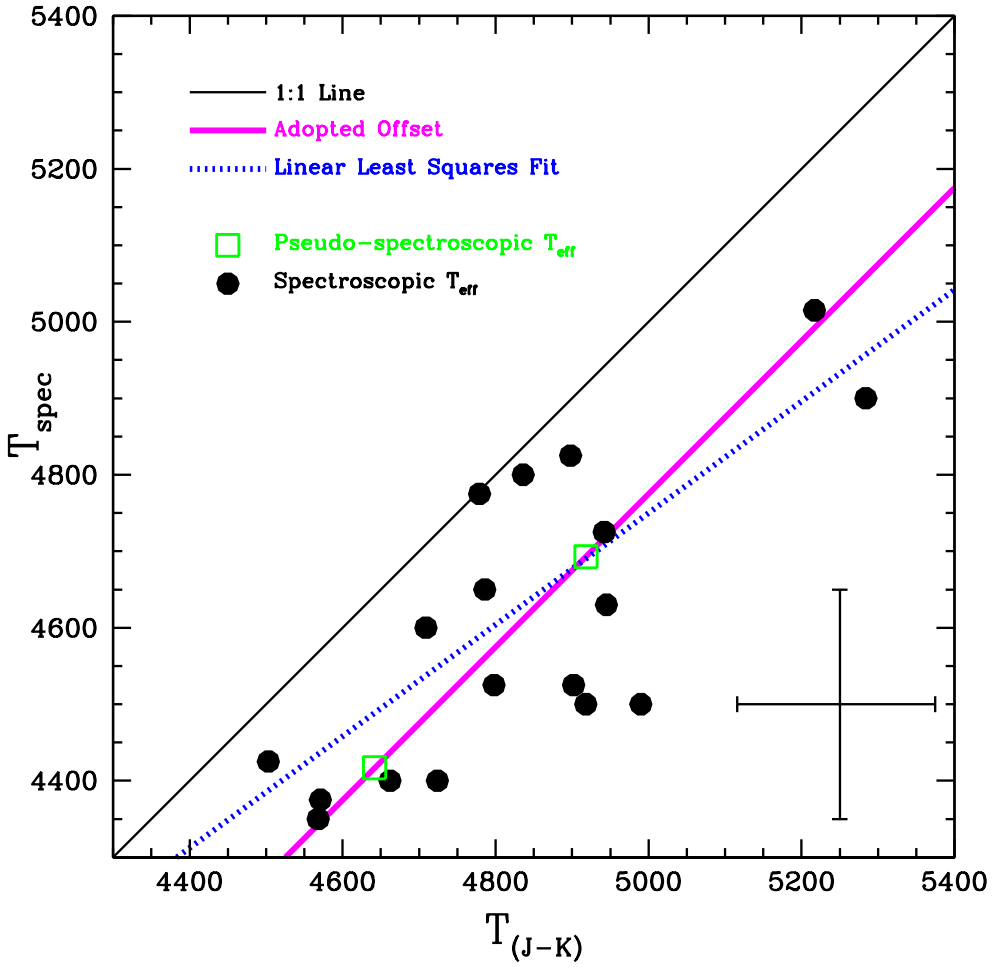

Figure 3.3 Comparison of the spectroscopic temperatures to those derived from (J−K) 2MASS photometry using the Alonso et al. (1999) calibration. The thin black line is the 1:1 comparison, the dotted blue line is the linear least squares fit to the data, and the thick pink line shows the adopted offset applied to HE 1116−0634 and HE 2302−0317a, which are both represented by the green square points.

Figure 3.4 shows the derived effective temperatures and surface gravities for all stars in the sample plotted against 12 Gyr Yale-Yonsei isochrones (Green et al., 1984; Kim et al., 2002) for [Fe/H] = −2.0, −2.5, and −3.0, as well as a Cassisi et al. (2004) horizontal-branch mass track. For the standard stars, we show the stellar parameters derived from the MIKE spectra, as well as literature values taken from Cayrel et al. (2004) for BD −18 5550, CD −38 245, and CS 22873−166, McWilliam et al. (1995) for CS 22891−200, and Fulbright (2000) for HD 122653. Due to the low-metallicity of CD −38 245, the corresponding MIKE spectrum shows very few absorption lines, thus we included this star only in the calibration of the stellar parameter offset.

3.4.3 Uncertainties

Each star has two or three measurements of temperature: spectroscopic temperatures derived from the MIKE and HRS spectra (when available) and a photometric temperature based on JHK 2MASS colors using the Alonso et al. (1999) calibration.

We determined random uncertainties in the spectroscopic temperatures based upon the uncertainty in the slope determined by the Fe I line abundances. For a representative star, we varied the temperature until the resultant Fe abundance was one standard deviation away from the original derived abundance. We found this value to be $\sim 125\,\mathrm{K}$; we adopt this as our random uncertainty. We determined random uncertainties in the photometric temperatures based upon the uncertainties given for the 2MASS colors. We found

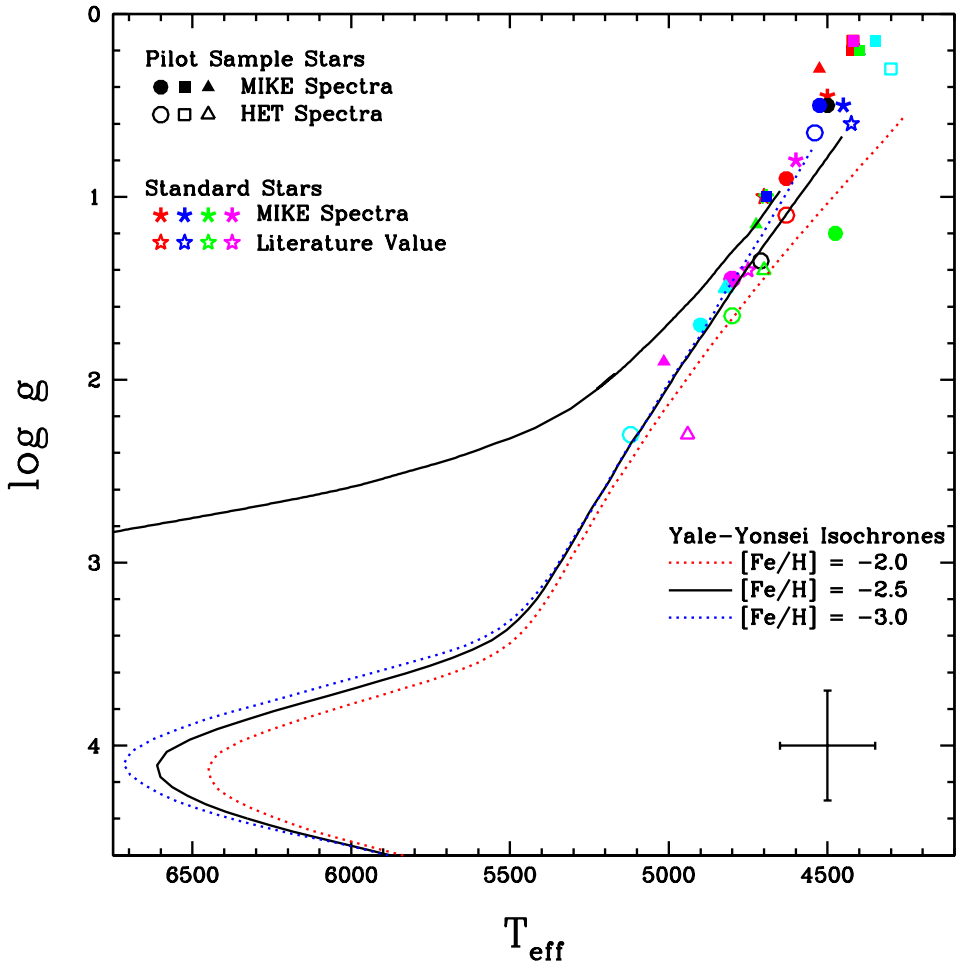

Figure 3.4 HR diagram of the pilot sample and standard stars. For the pilot sample, open symbols represent the stellar parameters derived from the HRS spectra and the solid symbols represent stellar parameters derived from the MIKE spectra. For the standard stars, open stars represent stellar parameters from the literature and asterisks represent stellar parameters derived from the MIKE spectra. Overplotted are the Yale-Yonsei isochrones (Green et al., 1984; Kim et al., 2002) for 12 Gyr, at [Fe/H] = −2.0 (red line), −2.5 (black line), and −3.0 (blue line) as well as a horizontal-branch mass track from Cassisi et al. (2004).

this uncertainty be $\sim 140\,\mathrm{K}$.

We also compared the derived spectroscopic and photometric temperatures. We remind the reader that the offset between the two temperature scales is $\sim 225\,\mathrm{K}$, where $\Delta T_{eff} = T_{eff}^{Phot} - T_{eff}^{Spec}$. Given this offset, we derive a systematic uncertainty for our spectroscopic temperatures of ~ 160 K. This is of the same order as the random uncertainties.

We obtained the random uncertainty in the surface gravity by allowing the Fe I and Fe II values to vary until they no longer agree within the uncertainty of Fe I, which is ~ 0.25 dex. Since all the pilot sample stars are on the giant branch, uncertainties in effective temperature at the $\sim 150\,\mathrm{K}$ level lead to changes in the surface gravities of ~ 0.5 dex. We conservatively adopt this as our σ_{logg} uncertainty.

We calculated the standard error of the mean Fe I abundance, obtained from individual Fe I line abundances and found it to be ~ 0.01 dex. This is rather small, as the calculation does not take continuum placement uncertainties into account. With that in mind, we adopt the scatter of the individual Fe line abundances as a more conservative random [Fe/H] uncertainty, which is ~ 0.12 dex, although it varies slightly by star.

In order to ascertain the uncertainty in the microturbulence, we determined the maximum change to the microturbulence values which would still yield the same [Fe/H] value within the uncertainties. This leads to $\sigma_{\xi} \sim 0.3$ km/s.

3.5 Robustness of the Stellar Parameter and Abundance Pipeline

3.5.1 Stellar Parameters

One of the main purposes of this paper is to test the stellar parameter and abundance pipeline that will be used for the larger CASH sample. The first test is to compare the manually derived stellar parameter results with those determined with the Cashcode pipeline. This can be done in three ways: i) comparing the stellar parameters and abundances of a manual analysis of a given spectrum with each Cashcode result; ii) comparing the results derived from snapshot spectra taken of standard stars with those of well determined literature values of the stellar parameters; and iii) comparing the stellar parameter results of a snapshot spectrum with those of a corresponding high-resolution spectrum.

We first tested the accuracy of the pipeline and the precision of our iteration criteria by comparing the results derived from a representative manual analysis of a high-resolution MIKE spectrum to those derived using the pipeline. We find ΔT_{eff}=10 K, Δlog g = 0.0, $\Delta\xi$ = 0.05, and Δ[Fe/H]= 0.02 dex. We find that the [X/Fe] values (where X is a given element) agree to within $\sim$ 0.05 dex.

By comparing the Cashcode results of standard stars to the literature values, we can test how accurately the snapshot data are able to reproduce the results of independent studies derived from high-resolution, high-S/N data using traditional manual methods. We evaluated an absolute consistency be-

tween the Cashcode results and the literature. See Subsection 3.6.7 for details on the abundance differences. A caveat to this comparison is that standard stars are usually bright targets, such that their snapshot spectra have much higher S/N than the median value for a snapshot spectrum. Generally, Cashcode produces abundance results with smaller uncertainties for higher-S/N, higher-resolution data because in these cases the line abundance scatter is decreased, therefore the user-defined parameter fitting criteria can be tightened.

However, the purpose of this study is to test the pipeline for the median S/N snapshot star. Unfortunately, we did not observe a low S/N snapshot spectrum of the standard stars, which precludes the best possible comparison. To resolve the issue, we instead turn to high-resolution data for testing the pipeline for a median S/N snapshot data. We compared the HRS pipeline-derived results to those of the manual, high-resolution analysis for all stars. We find agreement in the stellar parameters to be within $\Delta T_{eff} \pm 55\,\mathrm{K}$, Δ log g$\pm$ 0.3 dex, Δ[Fe/H] $\pm$ 0.15 dex, and $\Delta\xi \pm 0.21$ dex.

3.5.2 Chemical Abundances

For each star with an HRS spectrum, we compared the derived abundances with the high-resolution MIKE spectrum. For the 12 stars in common, we found the offset between the two to have a standard error, or standard deviation of the mean, of 0.07 dex. The average Δ[X/Fe] over all elements was 0.09 dex, thus the abundances derived from the HRS data with Cashcode can reproduce a manual analysis to within 1.5σ. Over all the elements, there

is no statistically significant difference between the HRS/Cashcode and the MIKE/manual analysis. For individual elements, some discrepancies do exist. We found that the largest discrepancies between the HRS and MIKE spectra arose for those elements whose lines occurred in regions of low S/N (e.g., the Δ[X/Fe] for Sr II is larger than that of Ba II, as the only Sr II line in the HRS occurs at 4215 Å, while there are Ba II lines at longer wavelengths).

For a given element, there is a discrepancy in the measured abundances derived from HRS and MIKE spectra. These range from 0.08 dex, in the case of Ti, which has 9 lines across the HRS spectrum, to 0.36 dex, in the case of Sr, which has one feature at 4215 Å in the HRS spectrum. This value is dependent upon the location in wavelength and number of lines per element; bluer features from lower S/N spectral regions have larger discrepancies. Figure 3.5 illustrates the Δ[X/Fe] for each element that was measured in both the HRS and MIKE spectrum of a particular star. We also compared the full set of [X/Fe] CASH and MIKE derived abundances to those of the Cayrel et al. (2004) study. Figure 3.6 shows the comparison between the three data sets. Manganese abundances are sometimes largely discrepant; however, this is likely because there are only four Mn lines available to detection in the HRS spectra and often only one of these lines was detected. It has been previously noted (Cayrel et al., 2004; Roederer et al., 2010) that the line selection for Mn is critical in understanding the derived abundances and the Cayrel et al. (2004) study included additional lines not available in the HRS spectra.

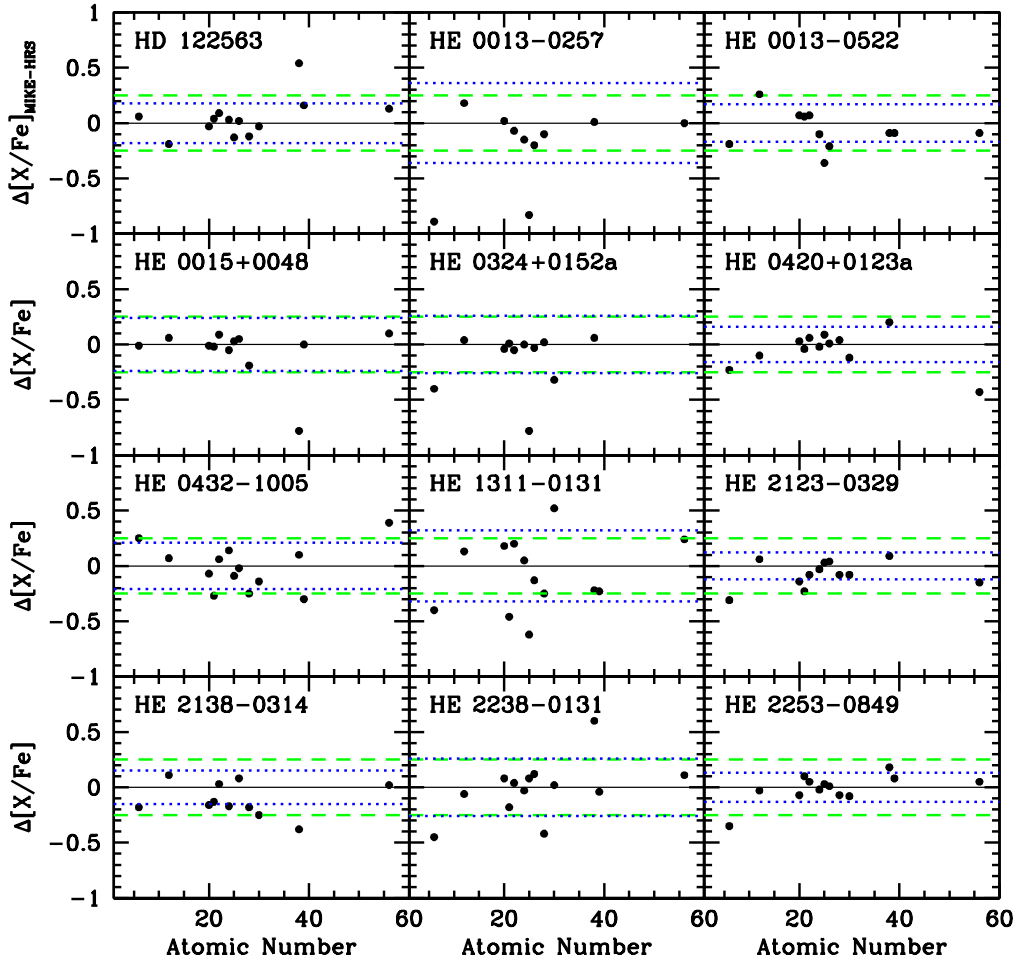

Figure 3.5 Abundance differences, Δ[X/Fe], defined as $[X/Fe]_{MIKE}$ - $[X/Fe]_{HRS}$, shown as a function of atomic number for each star that was observed with both HRS and MIKE. The black solid line represents zero offset, the green dashed line represents the 0.25 dex random error derived in the HERES study, and for comparison, the blue dotted line represents the calculated spread for each star.

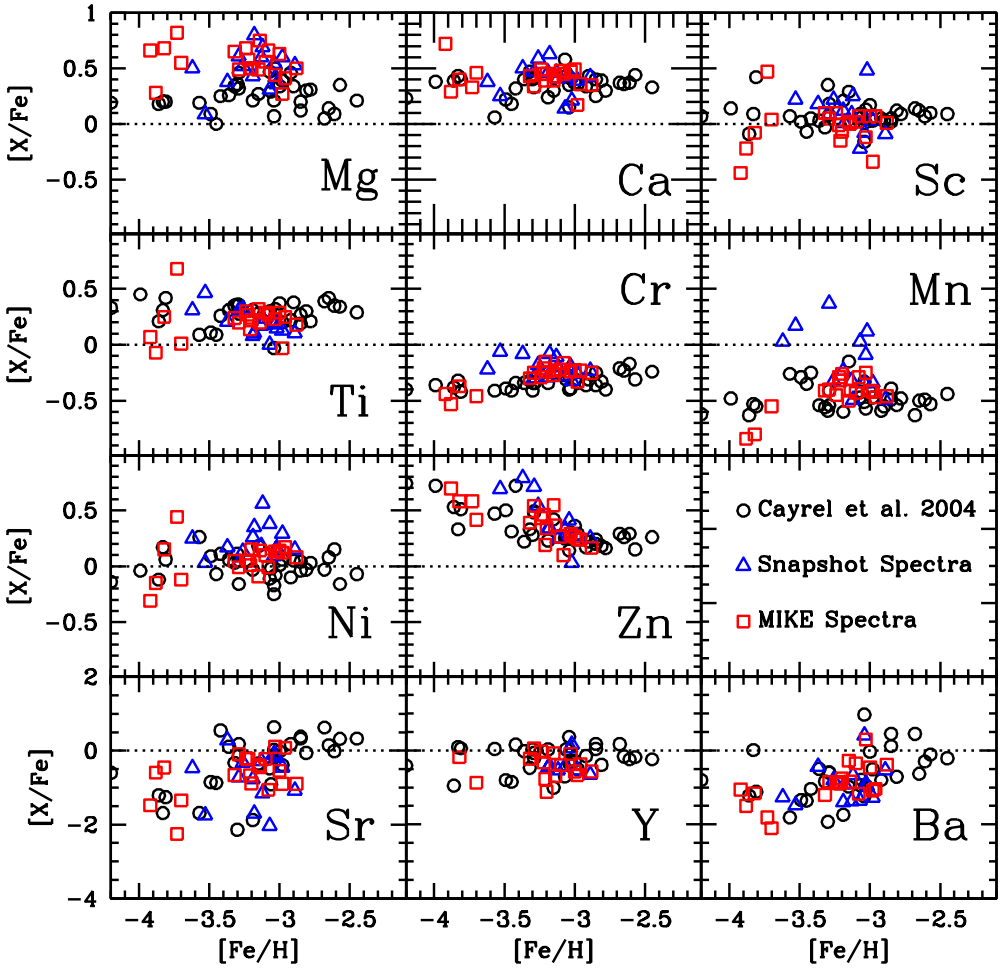

Figure 3.6 [X/Fe] abundance ratios vs. [Fe/H] for each of the elements measured using Cashcode in the HRS snapshot spectra (blue triangles) compared with the MIKE abundances (red squares) and the Cayrel et al. (2004) abundances (black circles). The black dotted line represents the solar abundance ratio. The HRS Ni abundances shown are preliminary.

3.6 Abundance Analysis

We present chemical abundances and upper limits for 13 elements derived from the HRS spectra and 18 elements from the MIKE spectra in Table 3.6. We now describe the details of our abundance analysis. For each element, we discuss the method of abundance determination, the relevant spectral features, the number of stars in which this element was measured, and any differences in the analysis between the high-resolution and snapshot spectra.

3.6.1 Light Elements: Li, C, Al, Si

Lithium abundances were determined from both the HRS and MIKE spectra through synthesis of the Li I doublet at 6707 Å. Both spectra cover this feature. Lithium is most easily detected in main-sequence stars, but as a star ascends the RGB, its Li abundance becomes depleted. Thus, we only expect to detect the Li feature in our warmest giants. We detected the doublet in 5 of 12 stars stars with HRS spectra and 7 of 20 stars MIKE spectra.

Carbon abundances were determined from the CH G-band feature at 4313 Å. The S/N near the G-band head region in the HRS snapshot spectra is low, such that we have to perform a manual synthesis of the G-band head in order to determine the C abundances. At low S/N, Cashcode does not yield reliable results mostly due to uncertainties in continuum placement. For synthesis we assumed an [O/Fe] abundance ratio of 0.0. When the [O/Fe] ratio reaches $\sim$ 1, the C abundances determined from molecular features is

Table 3.6. Abundances

Elem	logϵ(X) dex	[X/Fe] MIKE	σ dex	n	[X/Fe] HRS
		HE 0015-0048			
Mg I	5.18	0.66	0.18	6	0.62
Ca I	3.71	0.45	0.14	15	0.44
Sc II	0.14	0.07	0.14	8	0.06
Ti I	1.98	0.11	0.18	18	0.11
Ti II	2.14	0.27	0.15	39	0.06
Cr I	2.40	−0.16	0.20	14	−0.14
Mn I	2.06	−0.29	0.14	4	−0.28
Co I	1.97	0.06	0.14	6	···
Ni I	3.13	−0.01	0.16	8	···
Zn I	1.58	0.10	0.14	1	0.68
Sr II	−1.06	−0.87	0.14	2	−0.39
Ba II	−2.07	−1.17	0.14	3	−1.30

Note. — Table 3.6 is published in its entirety in the electronic edition. A portion is shown here for guidance regarding its content.

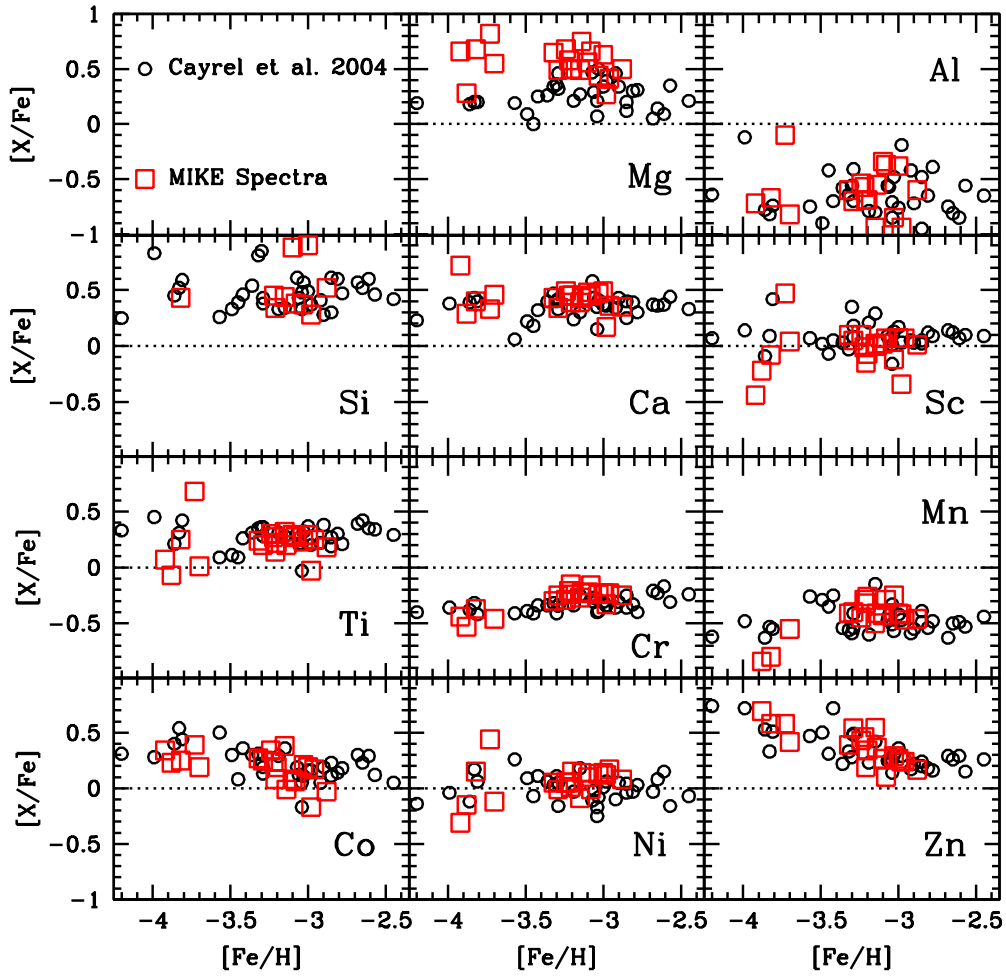

Figure 3.7 [X/Fe] abundance ratios vs. [Fe/H] for each of the elements up to Zn manually measured in the MIKE spectra (red squares) compared with the Cayrel et al. (2004) abundances (black squares). The black dotted line represents the solar abundance ratio.

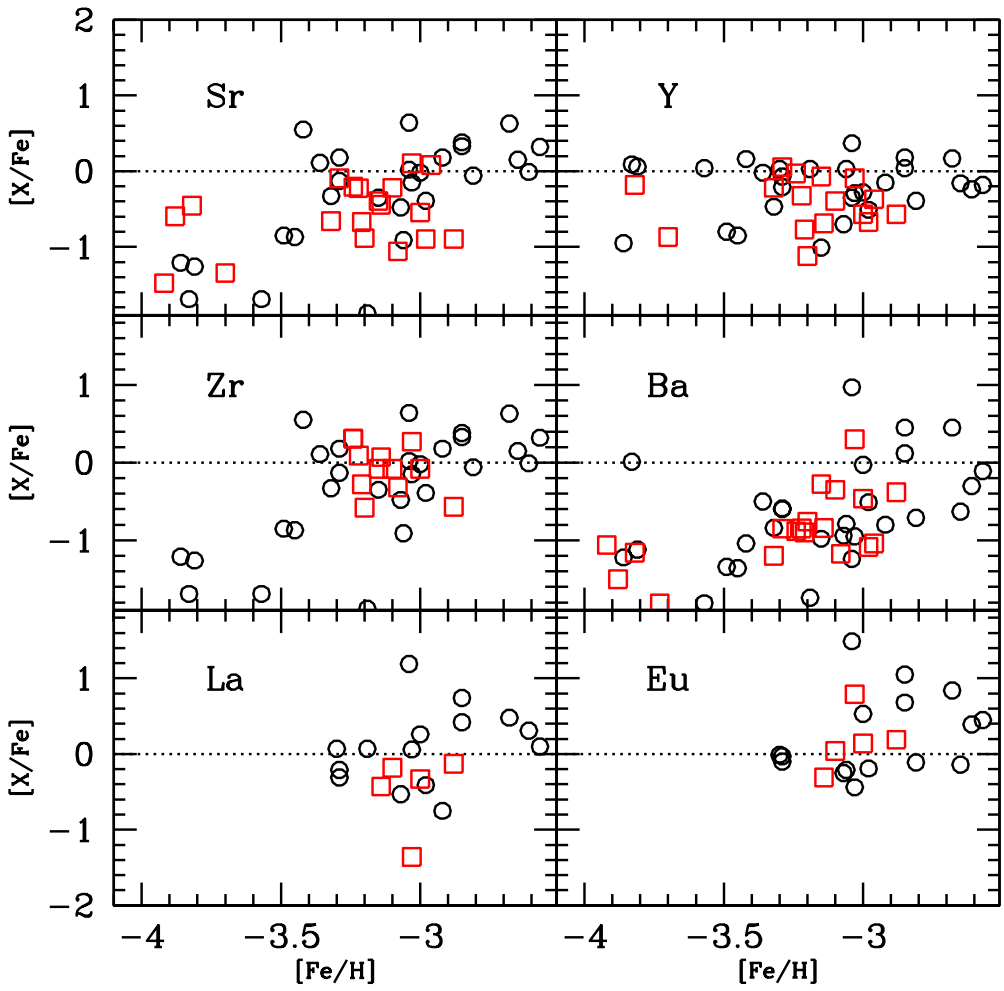

Figure 3.8 [X/Fe] abundance ratios vs. [Fe/H] for six neutron-capture elements measured in the MIKE spectra (red squares) compared with the Cayrel et al. (2004) abundances (black circles). The black dotted line represents the solar abundance ratio.

affected, though none of our stars indicate such a high O abundance. We detected this feature in all stars in both sets of spectra. The two available O indicators in our spectra are the forbidden line at 6300 Å and the O triplet. At the metallicity of our sample, we are unable to detect the forbidden line except for cases of extreme O enhancement. The triplet lines are known to have NLTE effects and thus we did not measure an O abundance.

Sodium abundances were not included in this analysis as we have not implemented a routine in the pipeline to discern the stellar absorption lines from the interstellar emission.

Aluminum abundances were determined using equivalent width measurements of the λ3961 line of the Al I resonance doublet. We opted to use only the λ3961 line for our abundance analysis because the other line, λ3944, is blended with CH. Neither feature falls within the HRS snapshot wavelength regime. We measured this line in 19 of the MIKE spectra. We did not measure the Al abundance in HD 122563 due to the low S/N of that spectrum.

Two Si lines are detectable in metal-poor stars: λ3906 and λ4103. The λ3906 line is heavily blended with CH in a low S/N region of the spectrum; however, we prefer to use only unblended lines for our analysis. The λ4103 line falls within the wing of the Hδ line, thus we adopt a local continuum in the wing of the Hδ line. We present spectral synthesis derived abundances from the MIKE spectra using the λ4103 line. Neither feature is available in the snapshot spectra due to limited wavelength coverage. We measured this line in 19 stars with MIKE spectra.

3.6.2 α-Elements: Mg, Ca, Ti

Abundances for Mg, Ca, and Ti were determined for all stars in the sample from both the HRS and MIKE spectra from equivalent width analysis. Only 4 unblended Mg I lines are available in the HRS snapshot spectra: λ4703, λ5173, λ5184, and λ5528. The Mg b lines are often near the flat part of the curve of growth, but their abundances generally agree with those of the abundances of the other two lines. Thus, they were included in the abundance determination. There are $\sim$ 12 detectable lines in the MIKE spectra, although in these spectra we exclude lines on the flat part of the curve of growth. This is determined on a line-by-line basis for each star.

There are four available Ca I lines in the snapshot spectra: λ5589, λ6103, λ6122, λ6162. Of the 4 lines, the latter 3 are sometimes blended with telluric features. This was assessed on a line-by-line basis in each star. There are $\sim$ 30 Ca I lines in the MIKE spectra. Though the Ca I λ4226 line is available in the HRS spectra, we did not include it in our analysis because of the low S/N of the feature. Additionally, this line is often excluded from the MIKE analysis because it is in the flat part of the curve of growth.

Titanium abundances were determined from 6 Ti I and 9 Ti II lines in the snapshot spectra and $\sim$ 30 Ti I lines and $\sim$ 60 Ti II in the high-resolution spectra.

3.6.3 Fe-Peak Elements: Sc, Cr, Mn, Co, Ni, Zn

All abundances were determined from equivalent width measurements except for Zn because it has only two weak lines. There are 4 detectable Sc II lines in the snapshot data: λ5031, λ5239, λ5526, and λ5657. There are $\sim$ 15 Sc II lines detectable in the MIKE spectra. We detected Sc lines in 20 MIKE spectra and 11 HRS spectra.

We measured five Cr I lines in the snapshot spectra: λ4616, λ4646, λ5206, λ5346, and λ5410. We measured $\sim$ 20 Cr I lines and 4 Cr II lines in the MIKE spectra: λ3409, λ4559, λ4588, and λ4592. There is a difference between the abundances derived between Cr I and Cr II, with Cr II abundances typically$\sim$ +0.35 dex larger than Cr I. We detected the Cr I lines in 19 MIKE spectra and 12 HRS spectra. In all plots, we adopt the [Cr I/Fe] values as [Cr/Fe].

We measured 4 Mn I lines in the HRS spectra: λ4754, λ4762, λ4783, and λ4823. We measured 8 Mn I lines in the MIKE spectra. We detected Mn I lines in 19 MIKE spectra and 11 HRS spectra.

In the MIKE data we measured $\sim$ 30 Ni I lines, but only the λ5477 and λ6177 Ni I lines are available in the HRS spectra. Abundances derived from the λ5477 line sometimes are erroneously large by $\sim$ 0.2 dex. We will develop a calibration for the large CASH sample, but here we only report Ni abundances derived from the MIKE spectra for all 20 stars.

We measured 11 Co I lines in the MIKE spectra that fall between 3502 Å

and 4122 Å. These lines are not covered by the snapshot spectra. We detected Co I lines in all 20 MIKE spectra.

Zinc abundances were determined via spectral synthesis of the λ4722 and λ4810 Zn I lines in both the HRS and MIKE spectra. We detected Zn I lines in 19 MIKE spectra and 9 HRS spectra.

3.6.4 Neutron-Capture Elements

We measured abundances for six neutron-capture elements via spectral synthesis. The Sr II λ4215 and λ4077 lines are covered by the MIKE spectra, while only the λ4215 line is available the HRS spectra. We detected Sr II lines in all stars in both the HRS and MIKE spectra.

We synthesized the λ4883 and λ5087 Y II lines in the HRS snapshot spectra and the λ3949 and λ4883 lines in the MIKE spectra. The λ3949 line was chosen because it is a prominent line and can still be detected when a giant star has sub-solar neutron-capture abundances. We excluded the λ5087 line because it falls in a region in the MIKE spectra with low S/N, as it is at the edge of both the blue and red edges of the CCD. We detected Y II lines in 16 MIKE spectra and 6 HRS spectra. We report upper limits from the MIKE spectra for 5 stars.

We synthesized the Zr II λ4209 line to determine the abundance for the MIKE spectra. Even though this line is available in the HRS snapshot spectra, the S/N in the blue region of all spectra is too low for such a weak feature. We detected the line in 12 MIKE spectra. We report upper limits

from the MIKE spectra for 9 stars.

For the HRS spectra we used 3 Ba II lines: λ4554, λ5854, and λ6142; however often only the λ4554 line can be measured given the low S/N of the HRS data as well as the low metallicity of the sample. The same lines were measured in the MIKE spectra, with the addition of the λ6496 line. Generally, these weaker lines are preferable because the λ4554 line is usually on the damping part of the curve of growth, especially in neutron-capture enhanced stars. We measured Ba in 20 MIKE spectra and 11 HRS spectra.

We synthesized 2 La II lines at 4086 and 4123 Å in the MIKE spectra. The HRS spectra do not cover these wavelengths.

We synthesized two Eu II lines at 4129 and 4205 Å in the MIKE spectra. The HRS spectra do not cover these wavelengths. We detected La II and Eu II features in the 5 same stars in the MIKE spectra. We report upper limits from the MIKE spectra for 15 stars for both Eu and La.

3.6.5 Non-LTE Effects

Chemical abundances are generally derived under the assumption of one dimensional (1D) model atmospheres in LTE, but non-LTE effects may alter our derived values. The non-LTE effects in the elements Mg, Sr, and Ba have been studied in the stars of the Cayrel et al. (2004) sample by Andrievsky et al. (2010), Andrievsky et al. (2011), and Andrievsky et al. (2009), respectively. Based upon their reanalysis of the Cayrel et al. (2004) sample, the non-LTE corrections would be ~ 0.15 for Mg and Ba in our sample. In the case of Sr,

the non-LTE abundances vary, and can be larger and smaller than the LTE abundances even for stars of similar temperature and gravity, so it is difficult to say what this effect would be in our stars. See also Asplund (2005) for a comprehensive review of non-LTE effects on stellar abundances for a range of elements. Such effects are very sensitive to stellar parameters and individual lines from which the abundances are derived. In the absence of "full grid" non-LTE correction calculations, we are not able to apply such corrections to our sample; however, we remind the reader that these corrections have implications for interpretations of Galactic chemical evolution models and should be taken into account for such investigations. To illustrate the magnitude of non-LTE effects, we discuss Al and Mn here, as both have some of the most severe non-LTE corrections.

Baumueller & Gehren (1997) present a non-LTE-corrected [Al/H] abundance analysis for four sets of stars for the λ3961, λ6696, λ6698, λ8772, λ8773 lines. Only the first line is detected in stars with [Fe/H] < -2.0, and thus applicable to this study. The λ3944 line is also detectable in metal-poor stars, but it is blended with CH features. They calculated non-LTE abundances for 6500 K and 5200 K main sequence stars, a 5780 K solar analog, and a 5500 K turn-off star, with [Fe/H] varying from -3.00 to 0.00 dex. For a given set of atmospheric parameters, the $[\mathrm{Al/H}]_{\mathrm{NLTE}}$ correction increases with decreasing [Fe/H]. The most evolved star ($T_{eff} = 5500$ K , log g = 3.5) in their analysis has a non-LTE correction of 0.65 dex. All the stars of the pilot sample are on the giant branch and generally are more metal poor than the Baumueller

& Gehren (1997) models, which indicates that our stars would have a larger non-LTE correction for the λ3961 line, though they would likely all have a similarly large correction.

Bergemann & Gehren (2008) note that Mn has strong NLTE effects, which increase with decreasing metallicity. These effects have been shown to be stronger in the λ4030 resonance triplet, which we do not include in our analysis. The most evolved, metal-poor model analyzed in Bergemann & Gehren (2008) (T_{eff}=5000 K, log g=4, [Fe/H]=$-$3) has an average [Mn/Fe] NLTE correction of 0.42 dex for the lines that we include in our Mn linelist (λ4030, λ4033, λ4034, λ4041, λ4754, λ4783, and λ4823). They also included HD 122563 in their sample of stars and calculated an NLTE correction of +0.44 dex to the [Mn/Fe] ratio. Again, we do not adopt an NLTE correction for any of our sample, though corrections of this magnitude would indicate that our average [Mn/Fe] trend is elevated to a slightly sub-solar level. The aforementioned elements have large non-LTE corrections, though other elements do not have corrections of this magnitude, thus their abundances can be used for interpretation in a straightforward manner.

3.6.6 Uncertainties

To determine the random uncertainty of our abundances, we calculated the scatter of the individual line abundances for each ionization state of each element measured. For any abundance determined from equivalent width measurements of less than 10 lines, we determined an appropriate small sample

adjustment for the σ (Keeping, 1962). In the case of any abundance uncertainty that was calculated to be less than the uncertainty in the Fe I lines, we conservatively adopted the value from Fe I for that particular star. Typically the Fe I uncertainty is ~ 0.12 dex.

For those lines with abundances determined via spectral synthesis, we determined abundance uncertainties based upon the uncertainties associated with equivalent width measurements. Continuum placement is the greatest source of uncertainty, along with the S/N of the region containing the particular line. Most of these abundances were determined from only two lines, thus we calculated the uncertainties for small samples. For those elements with only one line, we adopt the uncertainties determined for the Fe I abundance.

To obtain the systematic uncertainties in the abundances, we redetermined abundances by individually varying the stellar parameters by their adopted uncertainties. We chose a nominal value of 150 K for the effective temperature uncertainty, as this value is similar to the random and systematic uncertainties. Table 3.7 shows these results. We find that the effective temperature contributes most to the abundance uncertainty. The uncertainty in the surface gravity is somewhat less significant for most species. For elements with particularly strong lines, especially those whose abundances are determined with spectral synthesis, the microturbulence can be an important source of error.

Table 3.7. Example Systematic Abundance Uncertainties for HE 0015−0048a

Elem	ΔT_{eff} +150 K	Δ log g +0.5 dex	$\Delta\xi$ +0.3 km/s
CH	0.35	−0.20	0.00
Mg I	0.11	0.06	−0.04
Al I	0.17	0.18	0.11
Si I	0.15	−0.05	−0.05
Ca I	0.13	0.06	0.04
Sc II	0.07	−0.15	−0.05
Ti I	0.23	0.06	−0.02
Ti II	0.05	−0.14	−0.08
Fe I	0.18	−0.05	−0.05
Fe II	−0.01	0.15	−0.06
Cr I	0.21	0.08	−0.10
Mn I	0.21	0.08	−0.14
Co I	0.24	0.06	−0.11
Ni I	0.21	0.09	−0.17
Zn I	0.00	0.00	−0.05
Sr II	0.10	0.10	−0.20

Table 3.7 (cont'd)

Elem	ΔT_{eff} +150 K	Δ log g +0.5 dex	$\Delta\xi$ +0.3 km/s
Ba II	0.10	0.10	−0.07

3.6.7 Standard Stars

We compared our stellar parameters and [X/Fe] abundances for our four standard stars (HD 122563, BD −18 5550, CS 22873−166, and CS 22891−200) against three studies: McWilliam et al. (1995), Fulbright (2000), and Cayrel et al. (2004). We also compared our derived stellar parameters for CD −38 245 against McWilliam et al. (1995). The McWilliam et al. (1995) study differs from the other two and this study as those spectra had comparatively low S/N ($\sim$ 35). These stars were chosen from the literature because they have [Fe/H]$\sim$ −3 or below and are in similar evolutionary stages. Table 3.8 lists the stellar parameters derived in all three studies, as well as ours, for the five stars and Table 3.6 includes the derived abundances.

Table 3.8. Literature Values for Stellar Parameters

Study	T_{eff} [K]	log g	[Fe/H]	ξ [km/s]
HD 122563				
This study	4450	0.50	−2.96	2.30
Fulbright	4425	0.60	−2.79	2.05
McWilliam	...	...	...	...
Cayrel	4600	1.10	−2.82	2.00
BD −18 5550				
This study	4600	0.80	−3.20	1.70
Fulbright	...	...	...	...
McWilliam	4790	1.15	−2.91	2.14
Cayrel	4750	1.40	−3.06	1.80
CD −38 245				
This study	4560	0.95	−4.35	2.15
Fulbright	...	...	...	...
McWilliam	4730	1.80	−4.01	1.97
Cayrel	4800	1.50	−4.19	2.20
CS 22873−166				

Table 3.8 (cont'd)

Study	T_{eff} [K]	log g	[Fe/H]	ξ [km/s]
This study	4375	0.20	−3.14	2.60
Fulbright	...	...	...	...
McWilliam	4480	0.80	−2.90	3.01
Cayrel	4550	0.90	−2.97	2.10
CS 22891−200				
This study	4500	0.45	−3.92	2.60
Fulbright	...	...	...	...
McWilliam	4700	1.00	−3.49	2.51
Cayrel	...	...	...	...

Note. — References: Fulbright (2000), McWilliam et al. (1995), Cayrel et al. (2004)

The McWilliam et al. (1995) study contains four stars that overlap with our study (including CD −38 245). That work utilized model atmospheres from Kurucz (1993) with MOOG. We use an updated version of this code, which does explicitly deal with Rayleigh scattering as a continuum opacity source; see paragraph 1 of Subsection 3.3.3. The effective temperatures for this study were derived from photometry, with the microturbulence determined from Fe I lines and the surface gravity determined from the ionization balance of Fe I and Fe II lines. We find that our temperatures are lower by ~ 170 K. Our derived surface gravities are also lower, as a result of the lower temperatures. We also find a ~ -0.3 dex offset in the [Fe/H] values. The

cause of these discrepancies is likely twofold: the different temperature scales and how the most recent version of MOOG explicitly deals with the Rayleigh scattering opacity (see Table 3.3.3). Both lead to lower temperatures, surface gravities, and abundances.

Despite these absolute offsets, the derived abundance ratios have only small offsets, with the average offset between the two studies in $\langle\Delta$[X/Fe]$\rangle$ for all three stars is 0.04±0.24 dex, where Δ[X/Fe] is $[\mathrm{X/Fe}]_{\mathrm{Standard}} - [\mathrm{X/Fe}]_{\mathrm{MIKE}}$. For all three stars, Al and Si had the largest offsets, where McWilliam et al. (1995) derive systematically higher abundances. The McWilliam et al. (1995) Al abundances may be generally high, as they were found to be higher (Δ[Al/Fe] $\sim$ 0.5 dex) than Gratton & Sneden (1988), with no conclusion for the cause of the offset being reached. The Al and Si lines are located in low S/N regions in both studies; however, the measurement of the Al lines is difficult due to the suppression of the continuum from Ca H and K lines. As stated in Baumueller & Gehren (1997), even under the assumption of LTE, small changes in the effective temperature and surface gravity greatly change the line profiles. In addition, the proximity of the Hδ line produces larger uncertainties in our Si measurement, even when the feature is taken into account in the synthetic spectra. These reasons would produce a larger scatter in the measurements of Al and Si lines, compared to the other elements, and may explain the derived abundance discrepancy. When these two elements are removed from consideration the $\langle\Delta$[X/Fe]$\rangle$ becomes -0.02 ± 0.13 dex.

The only star which overlaps with the Fulbright (2000) study is HD

122563, though this particular study was chosen because the stellar parameters were determined spectroscopically, in the same manner as the stellar parameters determined from the MIKE spectra. Fulbright (2000) used Kurucz (1993) model atmospheres with MOOG as well. We found that the effective temperatures, surface gravities, and microturbulence values agree within the uncertainties associated with both studies, while Δ[Fe/H] is -0.17 dex. Similar to the effects seen in comparison with the McWilliam et al. (1995) study, this is due to the fact that the version of MOOG used in the Fulbright (2000) study did not explicitly handle the calculation of scattering from pure absorption in terms of the continuum opacity.

The derived abundance ratios are in good agreement, with $\langle\Delta[\mathrm{X/Fe}]\rangle = 0.02 \pm 0.09$ dex. The largest discrepancy lies with the [Mg/Fe] ratio, with Δ[Mg/Fe] = 0.20 dex, which was derived with a different set of lines and different oscillator strengths between this study and the Fulbright (2000) study.

The Cayrel et al. (2004) study has four stars in common with ours (including CD -38 245). This study uses OSMARCS atmospheric models with the LTE synthetic spectrum code "turbospectrum", which does explicitly handle the calculation of the scattering contribution with regard to the continuum opacity. The effective temperatures were determined via (V$-$K) colors, which leads to higher temperatures ($\sim$ 200 K) and surface gravities ($\sim$ 0.6 dex) compared to our spectroscopically derived stellar parameters. We ran the measured equivalent widths of Cayrel et al. (2004) for BD -18 5550 through Cashcode and found that our derived stellar parameters (4560 K, 0.6

dex, −3.22, and 1.7 km/s in effective temperature, surface gravity, [Fe/H], and microturbulence, respectively) were in agreement (Δ[Fe/H]= 0.02 dex).

In comparing the [X/Fe] values between our analysis of the Cayrel et al. (2004) equivalent widths and theirs, we find that our spectroscopically derived stellar parameters also lead to higher [Mg/Fe] values by $\sim$ 0.25 dex due to the gravity sensitive nature of the Mg lines.

The derived abundance ratios also agree well, with $\langle\Delta$[X/Fe]$\rangle = -0.03\pm$ 0.14 dex. The largest sources of discrepancy for all stars are Al and Si, in addition to Mg. In CS 22873−166, there is a 0.45 discrepancy between the [Sr/Fe] values. The S/N near both lines in the MIKE spectrum is $\sim$ 20. Additionally, the lines are very strong, making continuum placement a large source of uncertainty, as minor adjustments to the continuum level result in large changes in the abundance.

3.7 Abundance Results and Discussion

Table 3.6 lists abundance results derived from the MIKE spectra. Figures 3.6 and 3.7 include the [X/Fe] abundance ratios derived from the MIKE spectra plotted against [Fe/H] for all stars in the sample. These abundance ratios are overplotted against the Cayrel et al. (2004) abundances as a point of comparison. The table also includes the abundances derived from the HRS spectra, though we do not discuss these further. These abundances will later be included in the full $\sim$ 500 star CASH sample. For each element, Table 3.9 lists the parameters of a least squares linear trend versus metallicity, the abun-

dance scatter, and the average [X/Fe] value, if applicable.

3.7.1 Light Elements

We detected Li in six of our stars: HE 0324+0152a, HE 0420+0123a, HE 1311−0131, HE 2123−0329, HE 2138−0314, HE 2302−0849a, and in one standard star, BD −18 5550. These detections were seen in both the snapshot and high-resolution spectra for HE 0420+0123a, HE 1311−0131, HE 2123−0329, and HE 2138−0314. BD −18 5550 and HE 2302−0849 do not have a corresponding snapshot spectrum. In Figure 3.9 we show the Li line in the HRS and MIKE data for all these stars. Otherwise, we determined upper limits. In each case the S/N of the region was measured and the corresponding 3σ upper limit on the equivalent width was calculated following Bohlin et al. (1983) and Frebel et al. (2007b). Figure 3.10 shows the Li abundance as a function of metallicity and effective temperature, along with the HR diagram of the stars with detected Li.

The Spite plateau (Spite & Spite, 1982) is an observational discovery that describes a constant Li abundance in low-metallicity stars near the main-sequence turn-off. Metal-poor stars near or on the main sequence have not yet burned their surface Li; it is therefore thought that the stars that populate the Spite plateau can be used to infer details about the primordial Li abundance. As stars evolve off the main sequence and up the red giant branch (RGB), their convection zone deepens and the atmospheric Li abundance is depleted through burning and convective dredge up. Any enhancement in the

Table 3.9. Summary of Abundance Trends

Elem	⟨[X/Fe]⟩	slope vs [Fe/H]	σ	n_{stars}
CH	0.02[a]	−0.52[b]	0.41	20
Mg I	0.56	···	0.14	20
Al I	···	0.11	0.22	19
Si I	···	−0.20	0.16	19
Ca I	0.42	···	0.11	20
Ti II	0.22	···	0.16	20
Sc II	···	···	0.19	20
Cr I	···	0.26	0.02	19
Mn I	−0.49	0.24	0.09	19
Co I	0.42	···	0.11	20
Ni I	0.05	···	0.15	20
Zn I	···	−0.42	0.04	19
Sr II	−0.66	···	0.57	20
Y II	−0.46	···	0.32	15
Zr II	−0.08	···	0.26	11
Ba II	−0.95	···	0.25	20

[a]Average [C/Fe] value calculated for non-CEMP stars.

[b]Slope calculated for $\log(L/L_{\odot})$ vs [C/Fe]. See Figure 3.11.

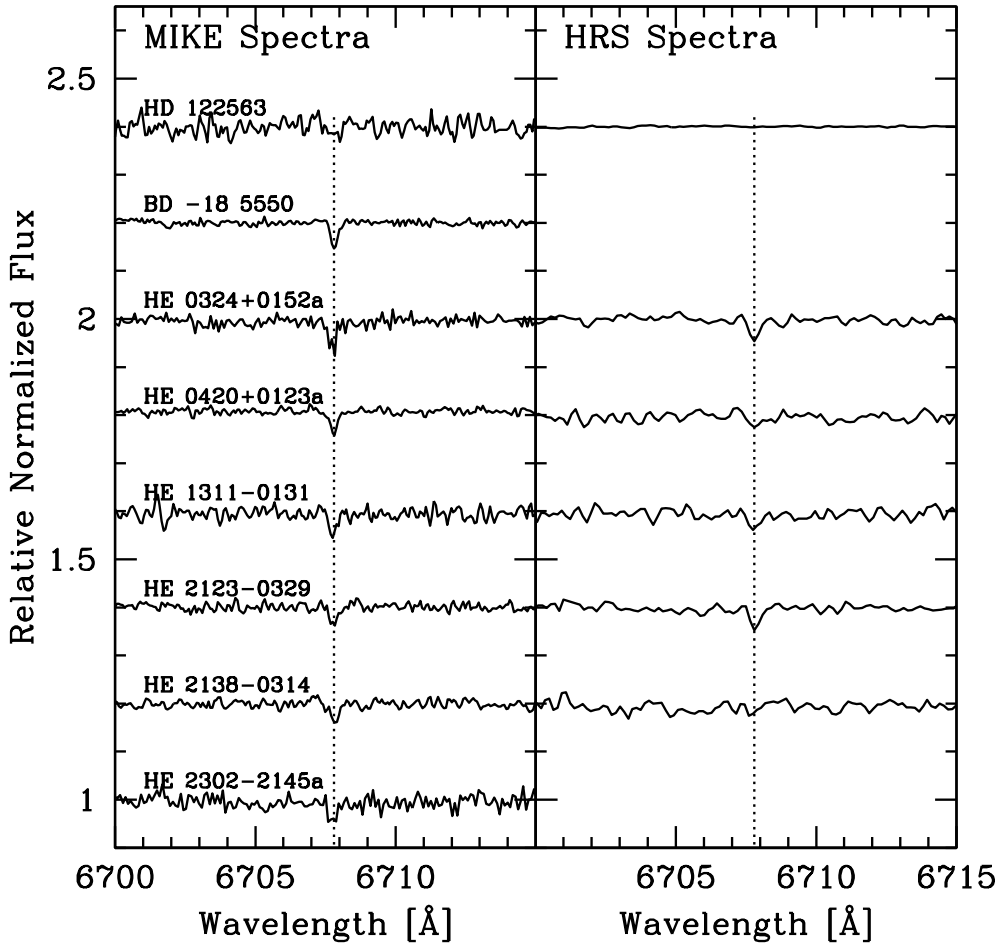

Figure 3.9 Li λ6707 line detections in MIKE (black solid line) and CASH (red dotted line). Plotted (dashed line) is the location of the feature. Also included for comparison is HD 122563, a star for which no Li was detected.

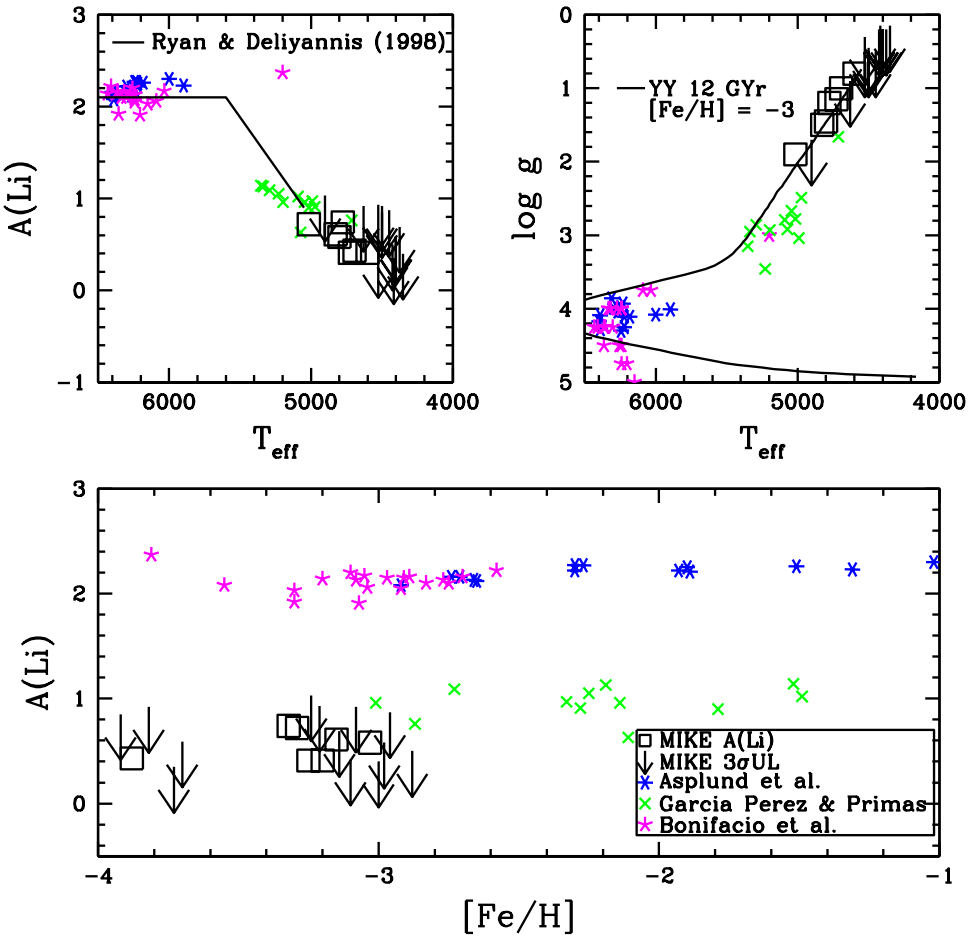

Figure 3.10 MIKE Li abundances (open squares) and upper limits (arrows) plotted against [Fe/H] along with Li abundances from Asplund et al. (2006), García Pérez & Primas (2006), and Bonifacio et al. (2007) (bottom), and effective temperature with the expected Li dilution curve from Ryan & Deliyannis (1998) (top left) overlayed. Effective temperatures and surface gravities are plotted, along with a [Fe/H]=−3, 12 Gyr Yale-Yonsei isochrone (Green et al., 1984; Kim et al., 2002) for each star plotted in the bottom panel (top right).

Li abundance (e.g., Roederer et al. 2008) is likely from some form of Li synthesis that occurs during the course of stellar evolution, perhaps due to the Cameron-Fowler mechanism (Cameron & Fowler, 1971). All of the stars in the pilot sample are on the giant branch and, thus, are expected to have depleted Li abundances. Due to the evolutionary status of the pilot sample, we cannot comment on the nature of the Spite plateau. Accurate Li abundances require great care in the effective temperature determination, as the Li abundance is extremely temperature sensitive. Most Li abundance studies (e.g., Ryan et al. 1996; Asplund et al. 2006; García Pérez & Primas 2006; Bonifacio et al. 2007; Meléndez et al. 2010) employ long baseline (e.g., V−K) photometric effective temperatures. Keeping the different temperature scales in mind, we find that our abundances qualitatively fall along an extrapolation of the Ryan & Deliyannis (1998) Li dilution curve.

Figure 3.11 shows a plot of our derived [C/Fe] abundances against [Fe/H] and luminosity. The Cayrel et al. (2004) abundances are also shown for reference. The abundance offset as a function of luminosity between the two samples is due to the different temperature scales used, as also quantified in Table 3.7. Generally, we find a large spread in the [C/Fe] abundance ratios, from ~ -0.80 to ~ 0.8 dex, with $\sigma = 0.41$ dex. In Figure 3.12, we show spectra for two stars of similar temperature (~ 4550 K) that differ in [C/Fe] by ~ 1.0 dex.

However, the interpretation of the observed [C/Fe] ratio must be carefully evaluated. As stars evolve up the RGB, the C abundance drops due to

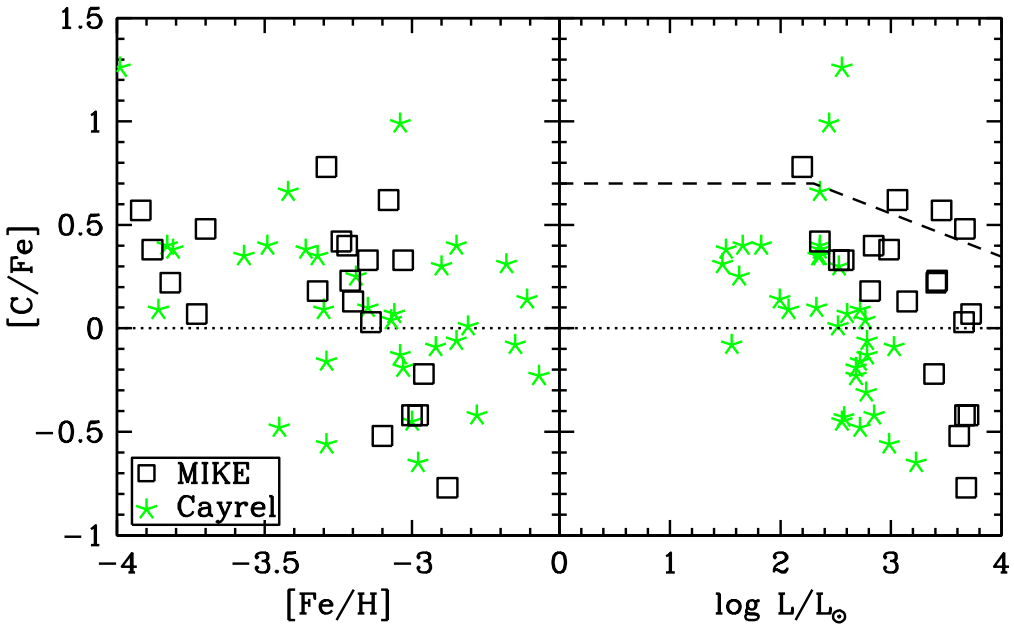

Figure 3.11 [C/Fe] abundance ratios plotted against [Fe/H] (left) and luminosity along with the CEMP defining line, which changes over the course of the stellar lifetime (Aoki et al., 2007) (right), along with the calculated Cayrel et al. (2004) C abundances. The [C/Fe] abundances clearly decline as stars ascend the giant branch.

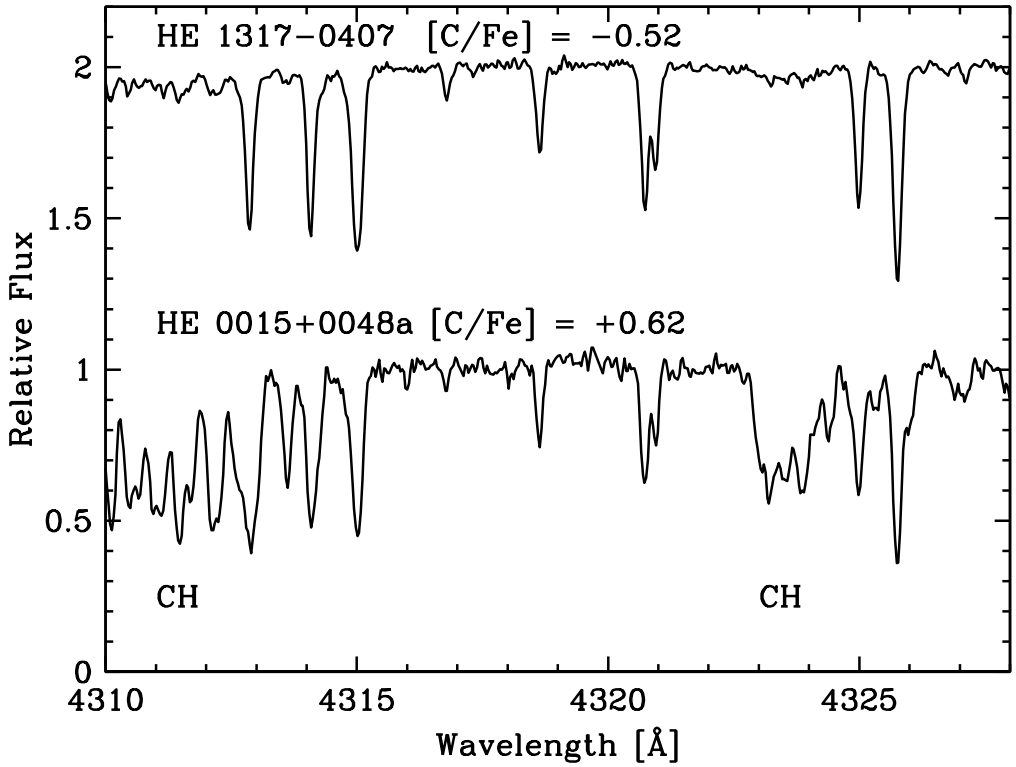

Figure 3.12 HRS spectra of a CEMP star (HE 0015+0048a) and a non-CEMP (HE 1317−0407) star of similar temperatures ($\sim$ 4550 K) and metallicities (~ -3.1).

CN cycling and convective dredge up. Thus, we expect that the observed C abundances derived for our stars should be lower than their initial abundances. Gratton et al. (2000) found that metal-poor field stars on the upper RGB had [C/Fe] ratios that were ~ 0.5 dex lower than metal-poor field stars on on the main sequence or turn-off. We very clearly see this trend in the pilot sample stars, all of which are on the RGB, in Figure 3.11, where the [C/Fe] ratio drops by ~ 1.2 dex over one solar luminosity.

Aoki et al. (2007) provided a new definition for CEMP star status: stars with $\log(L/L_{\odot}) <\sim 2.3$ and [C/Fe] ≥ 0.70 and stars with $\log(L/L_{\odot}) >\sim 2.3$ and [C/Fe] $> (3.0-\log(L/L_{\odot}))$ are considered CEMP stars (see the right panel of Figure 3.11). This definition takes into account the decrease in the surface C abundances as a function of evolutionary status. For our sample, the definition would indicate that 4 stars are significantly enhanced in their [C/Fe] ratios compared to the rest of the sample. This is still true when the effects on the abundances due to the use of different temperature scales is taken into account. In order to study the initial stellar abundances, corrections, up to ~ 1 dex for the highest luminosity stars, should be applied. Thus, if we were to correct for this depletion, one can estimate that the ISM from which these stars formed was enriched in C by a factor of ~ 10 or more.

Nevertheless, the large scatter in the [C/Fe] ratios of metal-poor stars indicates a complex production history of C. Additionally, the sizable fraction of metal-poor stars that show enhancement in their [C/Fe] ratio (Frebel et al., 2006; Cohen et al., 2006; Carollo et al., 2011) make it important to study the

origin of C in the early universe. For metal-poor stars, the most important production site of C is massive stars that can release CNO elements during the course of stellar evolution through various supernova outbursts (e.g., Fryer et al. 2001; Meynet et al. 2006; Kobayashi et al. 2011).

With these considerations in mind, our C abundances suggest one of the following three scenarios: i) strong stellar winds from massive stars released C from their atmospheres, enriching only the local ISM, ii) after enrichment from the supernovae of massive stars and/or stellar winds in the early universe, there was only inhomogeneous mixing of the ISM, or iii) the sample stars did not all form from the same molecular cloud or in the same host system. For example, some of the surviving ultra-faint dwarf spheroidal galaxies show a ~ 1 dex spread in their C abundances (Norris et al., 2010a,b). Scenario two does not agree with the small scatter seen in their α-element ratios. The first and third scenarios, however, are not mutually exclusive. Future modeling of the nucleosynthetic yields of massive Population III stars will facilitate a better understanding of early carbon production. Given the size and metallicity range of the pilot sample, unfortunately nothing can be said about the CEMP frequency, though we will be able to evaluate this using the full CASH sample.

Finally, fine-structure lines of C and O are thought to play a role in the transition from Population III to Population II stars through the cooling of gas clouds of the early universe (Bromm & Loeb, 2003). This hypothesis can be tested by comparing the abundances of C and O of metal-poor stars to an abundance transition discriminant as described in Frebel et al. (2007a). Stars

with [Fe/H]< -3.5 are particularly interesting in this regard; however, all stars of the pilot sample are too C-rich to indicate that fine structure cooling *did not* play a role.

3.7.2 α-Elements

The α-elements are created both in core-collapse supernova and through stellar nucleosynthesis in high-mass stars. While the dominant isotope of Ti is not technically an α-element, it shows a similar abundance pattern to the α-elements and thus is included here (e.g., Woosley & Weaver 1995). Magnesium and Ca, as well as the other α-elements, have been shown to be overabundant, compared to the Solar System [α/Fe] ratio, at low metallicities in field halo stars at the ~ 0.4 dex level (e.g., McWilliam 1997, Cayrel et al. 2004, Frebel 2010). This has been explained by the occurrence of core-collapse supernovae in the early universe, which produce an overabundance of the α-elements compared to Fe. Later generations of supernovae, specifically Type Ia, produce more Fe, driving down the [α/Fe] ratio to what we see today in the Sun and similar young, metal-rich stars. This downturn in the [α/Fe] ratio occurs at [Fe/H] ~ -1.5. As our sample does not reach [Fe/H]> -2.0, we do not expect to see this downturn in the [α/Fe] abundance ratios.

As seen in other halo stars, the [Mg/Fe] ratio is enhanced relative to the solar ratios in all our sample stars at 0.56 dex. This is also seen in the Cayrel et al. (2004) stars as well, though there is an offset of ~ 0.25 dex between these two samples, with ours having the larger value. This is due to the differences

in the effective temperature scales chosen. The Cayrel et al. (2004) study used (higher) photometric temperatures. To demonstrate this, we took the Cayrel et al. (2004) equivalent widths for BD −18 5550 and ran them through the Cashcode pipeline. We obtained a temperature different by 150 K, resulting in an offset of 0.5 dex in the surface gravity. In most elemental ratios these effects cancel, but Mg, especially the triplet, is gravity sensitive, resulting in a ~ 0.25 dex offset in [Mg/Fe] between the two studies.

The [Ca/Fe] ratio is also enhanced in our sample stars relative to the solar ratio at 0.42 dex. The [Ti/Fe] ratio is found to be enhanced relative to the solar ratio in all but two stars, HE 2148−1105a and HE 2302−2145a, with [Ti/Fe] values of −0.14 and −0.03 respectively; however, these stars both show the expected enhancement in [Ca/Fe] (0.17 and 0.31). The [Mg/Fe] values (0.27 and 0.30) in these stars is somewhat lower compared to the values in our other stars. The average [Ti/Fe] value for this study is 0.22. The average [α/Fe] value is ~ 0.4 dex and thus corresponds well to the average halo [α/Fe] values.

3.7.3 Fe-Peak Elements

The [Sc/Fe] ratio for the stars in the sample is generally clustered around the solar abundance ratio. The [Cr/Fe] and [Mn/Fe] abundance ratios for all our sample stars are found to be deficient relative to the solar abundance by −0.23 and −0.49 dex, respectively. We remind the reader that the [Cr/Fe] ratios are based upon only the Cr I abundances, as there is a ~ 0.35

dex offset between Cr I and Cr II derived abundances. The [Co/Fe], [Ni/Fe], and [Zn/Fe] ratios in the sample stars are generally enhanced relative to the solar abundance ratios by 0.42, 0.05, and 0.25 dex, respectively.

The Fe-peak elements are created in various late burning stages (see Woosley & Weaver 1995), as well as in supernovae. Our Fe-peak abundance trends follow those of other halo star samples and generally indicate a successive increase of these elements over time (e.g., McWilliam 1997). We will use the Fe-peak elemental abundances of the large CASH sample to put constraints on the nucleosynthesis yields of the progenitor stars. For example, the measured Zn abundances, which we can measure in the HRS spectra, are sensitive to the explosion energy of supernovae (Nomoto et al., 2006; Heger & Woosley, 2010).

3.7.4 Neutron-Capture Enhanced Stars

The study of neutron-capture elements allows for testing of different sites of nucleosynthesis, beyond proton and α-capture. See Sneden et al. (2008) for a comprehensive overview of the neutron-capture stellar abundances. Neutron capture occurs mainly in two locations: in the envelopes of highly evolved asymptotic giant branch (AGB) stars (s-process) and in some sort of explosive event, likely a core-collapse supernova (r-process). The contributions of each process to the total elemental abundance of the neutron-capture elements in a given star can be determined by evaluating the collective neutron-capture abundance patterns. For example, in the Solar System abundances, the s-

process contributes $\sim 80\%$ of the Ba abundance, with a $\sim 20\%$ contribution from the r-process, whereas Eu is made almost entirely from the r-process (Sneden et al., 2008); however, these ratios may differ in the early universe. Unfortunately, there are not enough neutron-capture elements detectable in the HRS snapshot spectra to determine whether the abundances of neutron-capture elements in a given star have an s- or r-process origin.

We measured Sr and Ba for all stars in the MIKE sample. We also detected Y and Zr in many of the stars as well, though the S/N near the Y lines often preclude us from measuring it, and the Zr feature is often too weak. We measured La in only four pilot sample stars: HE 2238−0131, HE 0420+0123a, HE 1317−0407, and HE 2253−0840 and in the standard star CS 22873−166. Europium lines have been detected in the high-resolution spectra of the same five stars. In Figures 3.13 and 3.14 we show line detections of La and Eu in each star, respectively. The four sample stars are all neutron-capture enhanced, ranging in [Eu/Fe] from 0.02 to 0.79 dex, while CS 22873−166 is depleted in [Eu/Fe] relative to the solar abundance ratio. According to Christlieb et al. (2004) HE 0420+0123a is a mildly r-process enhanced (r-I) star due to its [Eu/Fe] ratio (0.79) and Ba/Eu ratio (−0.71).

For each of these neutron-capture enhanced stars, we normalized their log ϵ(X) abundances relative to the Ba abundance and plotted them against a Solar System r-process abundance pattern. We also normalized the Solar System s-process abundance pattern to fit the derived Ba abundance. We found that the r-process pattern seemed to fit the ratio of La to Eu better

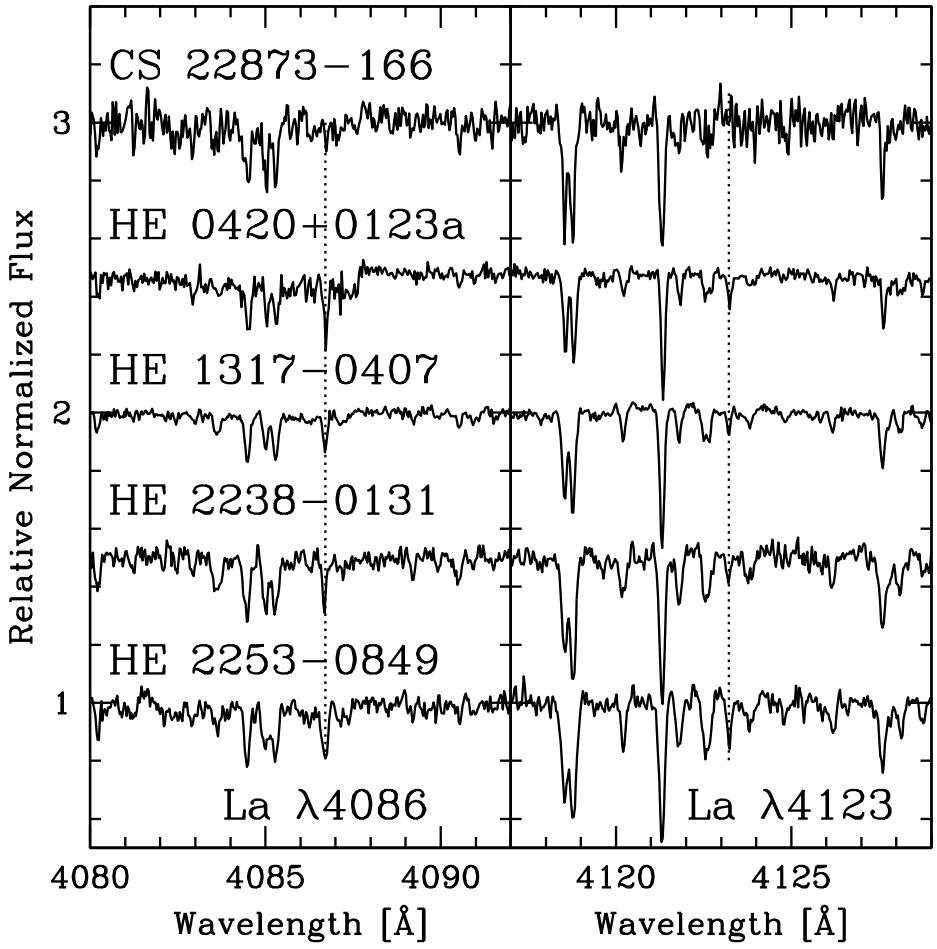

Figure 3.13 La λ4086 and λ4123 line detections in MIKE (black solid line) spectra. Plotted in each panel (dashed line) is the location of the features. For CS 22873−166, only the λ4086 line is a detection.

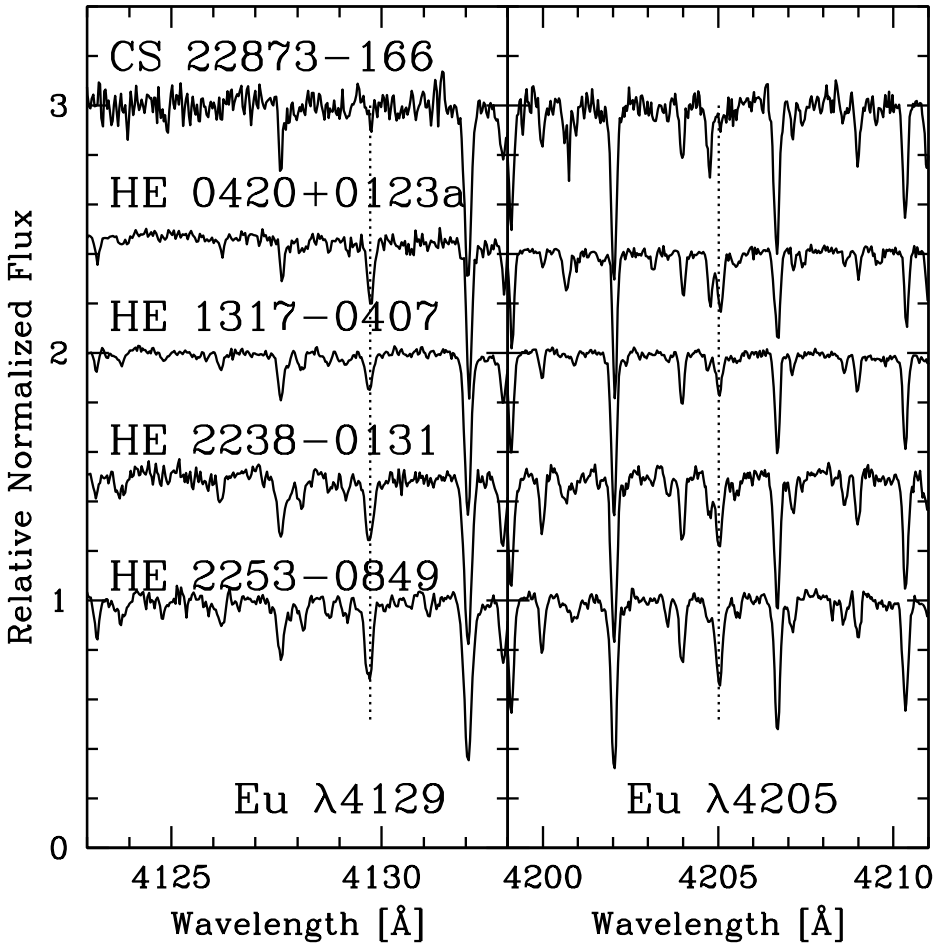

Figure 3.14 Eu λ4129 and λ4205 line detections in MIKE (black solid line) spectra. Plotted in each panel (solid dashed) is the location of the features. For CS 22873−166, only the λ4129 line is a detection.

than the s-process pattern, as the Eu abundances would have to be an order of magnitude lower to match the s-process pattern. Figure 3.15 shows this analysis. The first neutron-capture peak elements (Sr, Y, Zr) show a ~ 0.3 dex range of abundances, though some are enhanced relative to the r-process curve. This may indicate two things: i) the r-process seems a likely explanation for the Eu abundances and ii) a nucleosynthetic event besides the same r-process that formed a portion of the neutron-capture elements in the Solar System must be contributing in some of the stars to explain their first neutron-capture peak elemental abundance range.

3.7.5 Stars with [Fe/H]< -3.5

Four stars in the pilot sample have [Fe/H]< -3.5, along with an additional standard star, CS 22891−200, which was found to have a lower [Fe/H] value (-3.92) than was previously published by McWilliam et al. 1995 (-3.49).

All these extreme EMP (EEMP) stars have enhancements in the [α/Fe] ratios, depletion in some of the Fe-peak abundance ratios, and none are neutron-capture enhanced. We detected the λ6707 Li I line in HE 2302−2154a, which can be expected given that it is the warmest of the EEMP stars at $T_{\rm eff} = 4675$ K. Generally, these stars are indistinguishable from the rest of the sample, with the following exception.

It is noteworthy that all five EEMP stars show enhancement in their [C/Fe] abundance ratios. This confirms the trend toward higher [C/Fe] ratios towards lower values of [Fe/H], noted first by Rossi et al. (2005) and Lucatello

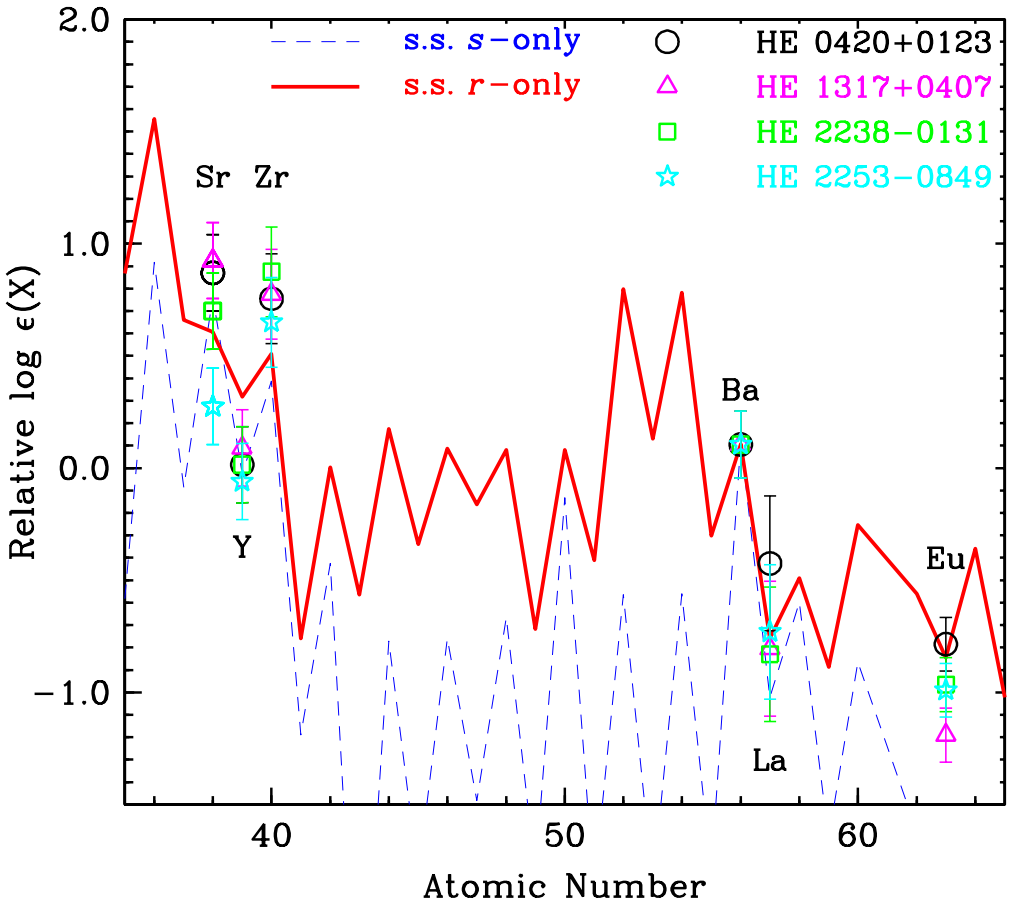

Figure 3.15 Relative log ϵ(X) abundances for all r-process enhanced stars in the MIKE sample. Abundances are adjusted to the Ba abundance to fit a scaled Solar System r-process curve (red line). The Solar System s-process curve is also plotted (blue dashed line).

et al. (2006). Without consideration for the evolutionary stage of the stars, the average [C/Fe] ratio for the EEMP stars is 0.43, while the rest of the sample has an average [C/Fe] ratio of 0.07 dex. However, given the high luminosity of the EEMP stars, the [C/Fe] ratios have been depleted due to the operation of the CN cycle. Taking this effect into account, two stars are mildly C enriched and two are considered CEMP stars following the definition of Aoki et al. (2007). The two CEMP stars lack neutron-capture enhancement, which indicates that these stars are CEMP-no stars (Beers & Christlieb, 2005), adding to the growing number of these objects at the lowest metallicities.

We did not detect either the La or Eu lines in any of these stars. This is largely due to the fact that it is difficult to detect Eu in EMP stars unless the Eu abundance is significantly enhanced. Given that we do not see strong La enhancement along with the carbon enhancement in the EEMP stars, it is likely that their observed abundance patterns were the result of massive stars, rather than low mass stars, which produce La in the AGB stage of stellar evolution.

3.7.6 Binary Fraction

For twelve of the pilot sample stars, we derived multiple-epoch measurements of their radial velocity. For three stars, we have additional radial velocity measurements from the solar spectrum-contaminated HET HRS spectra. For the remaining two stars, we do not have multiple measurements. Generally, the radial velocity measurements were taken with a baseline of at least one

year and in some cases, three years. The HRS and MIKE radial velocities agree to within 2.5 km/s for those stars. We find one binary candidate in our sample. HE 0015+0048a is the one exception; the time span between measurements is three years and we find a radial velocity variation of 8.0 km/s. Future monitoring of this star will confirm its binarity. This sample is too small to make any definitive statement on the binary fraction of metal-poor stars.

3.8 Summary

We have presented the abundances or upper limits of 20 elements (Li, C, Mg, Al, Si, Ca, Sc, Ti, Cr, Mn, Fe, Co, Ni, Zn, Sr, Y, Zr, Ba, La, and Eu) for 16 new stars and four standard stars derived from high-resolution, high S/N MIKE spectra via traditional manual analysis methods using the MOOG code. We find that, with the exception of Mg, our abundances match well with those of other halo stars reported in the literature, e.g., Cayrel et al. (2004).

In the pilot sample we find several distinct chemical groupings of stars, indicating different enrichment mechanisms may apply for each of these groups, though the exact mechanism is still uncertain. We find four new stars with [Fe/H] < -3.6, where the metallicity distribution function severely drops. We find CS 22891−200 to have a lower [Fe/H] value than reported by McWilliam et al. (1995), bringing the total number of [Fe/H] < -3.6 stars to five. All of these stars are enhanced in their [C/Fe] abundance ratios relative to the solar values. We have four CEMP stars in our sample. Two of these are EEMP

CEMP-no stars, which confirms the trend of an increasing enhancement in C towards lowest metallicities without invoking the contribution of AGB stars at the lowest metallicities. This may suggest that massive stars released C from their atmospheres and enriched the local ISM and/or that the sample stars did not all form in the same region. We detected La and Eu in five stars. Of these, four are neutron-capture element enhanced with r-process signatures, based upon their [Eu/Fe] ratios, ranging from 0.02 to 0.79; the star with the highest [Eu/Fe] abundance ratio is an r-I star. For the remaining stars, we generally find scaled Solar System abundance ratios with very small scatter in the abundances. This may indicate the presence of core-collapse supernovae in the early universe. In the pilot sample, we have one star that is a binary candidate. Future monitoring of this star will determine its binarity status.

We presented a calibration of the Cashcode pipeline. We find agreement between the spectroscopic stellar parameters derived from the high-resolution spectra and the snapshot spectra to within $\Delta T_{eff} \pm 55\,\mathrm{K}$, Δ log g$\pm$ 0.3 dex, Δ[Fe/H] $\pm$ 0.15 dex, and $\Delta\xi \pm 0.21$ km/s. These fall within the expected uncertainties associated with snapshot-quality data. We also find that the abundances derived from the HRS spectra using the pipeline are in agreement to within 1.5 σ. The Cashcode pipeline will be employed for the full $\sim$ 500 star snapshot sample. This sample will be used to determine carbon and neutron-capture enhancement frequencies, to better understand supernova nucleosynthesis and early universe chemical enrichment processes, and find new astrophysically interesting stars that merit further study. One star

has already been identified as neutron-capture enhanced in our sample, based on its high Eu abundance and another separate star has also been singled out. The latter star is a CEMP star, with r-process and s-process elemental abundance enhancements. Both of these will be further analyzed in a later paper as part of this series.

The Hobby-Eberly Telescope (HET) is a joint project of the University of Texas at Austin, the Pennsylvania State University, Stanford University, Ludwig-Maximilians-Universitt Mnchen, and Georg-August-Universitt Gttingen. The HET is named in honor of its principal benefactors, William P. Hobby and Robert E. Eberly. We are grateful to the Hobby-Eberly staff for their assistance in obtaining the data collected for this paper. We thank John Norris and Norbert Christlieb for their valuable contributions to the discovery of the bright metal-poor stars analyzed here. J.K.H. and T.C.B. acknowledge partial support through grants PHY 02-16783 and PHY 08-22648: Physics Frontier Center/Joint Institute for Nuclear Astrophysics (JINA). A.F. acknowledges support of a Clay Fellowship administered by the Smithsonian Astrophysical Observatory. I.U.R. is supported by the Carnegie Institution of Washington through the Carnegie Observatories Fellowship. C.S. is supported through NSF grant AST-0908978.

Chapter 4

The Chemical Abundances of Stars in the Halo (CASH) Project. IV. Abundances, Ratios, and Trends for a Sample of 262 Metal-poor Stars

We present stellar parameters and abundances for 262 metal-poor halo star candidates derived from "snapshot" spectra obtained with the High Resolution Spectrograph on the Hobby-Eberly Telescope at McDonald Observatory. We determine abundance statistics and trends for 16 elements over the sample. We identify astrophysically-interesting stars that merit further investigation, including carbon-enhanced metal-poor stars, neutron-capture element enhanced stars, and extremely metal-poor stars. We note one Li giant with a unique abundance pattern.

4.1 Introduction

The study of the most metal-poor, currently-observable Population II stars is an opportunity to better understand the history of the universe. These so-called metal-poor stars were formed from the remnants of the first generation of stars, called Population III, and thus preserve the chemical signature of Pop III stars in their spectra. By studying the spectra of these stars, we

can begin to construct the early chemical enrichment events and processes in the universe, including Type Ia supernovae, asymptotic giant branch (AGB) star evolution, and perhaps even the initial mass function of Pop III stars.

Given the importance of these stars, many surveys and studies have been undertaken to find them. Large scale objective prism plate surveys have been conducted to observe thousands of objects. From there, candidate stars are selected for medium resolution (R$\gtrsim 1,000$) follow up spectroscopic observations, and ultimately, the best candidates are selected for high-resolution spectroscopy.

4.1.1 Searches for Metal-Poor Stars

Bond (1980) identified 132 metal-poor stars with [Fe/H]< -1.5 [1]. These stars were primarily discovered via two objective prism plate surveys on the Curtis Schmidt Telescope at Cerro Tololo Inter-American Observatory. These surveys were carried out in 1967 and between 1971 – 1977. Narrowband *ubvy*-photometry was used in conjunction with the objective prism data to determine metallicity, absolute magnitudes, distances, evolutionary state, and indicators of carbon-enhancement. Although the stars were not kinematically selected to be of the stellar halo, the radial velocities determined in this work suggested that the newly discovered low-metallicity stars could be members of the halo.

[1] [A/B]$= \log(N_{\rm A}/N_{\rm B}) - \log(N_{\rm A}/N_{\rm B})_{\odot}$ for N atoms of elements A, B, e.g., [Fe/H] $= -2.0$ is 1/100 of solar Fe abundance.

The HK survey (Beers et al., 1985, 1992) was an objective prism survey also conducted with the Curtis Schmidt Telescope. This survey was deeper than that of Bond (1980). The strengths of the Ca II H and K lines were used to select the $\sim$ 1800 metal-poor star candidates. These stars were then observed at medium resolution and had UBV photometry performed in order to determine stellar parameters and metallicities. The metallicities were determined using the Ca K line index (Beers et al., 1999), along with several other strong features available in the spectra. Similar to Bond (1980), this survey also aimed to detect metal-poor stars.

The Hamburg/ESO Survey (HES) (Wisotzki et al., 2000), was another objective prism survey. The plates of the HES were digitized, unlike previous surveys where the plates needed to be inspected by eye. From these plates, many metal-poor stars were discovered (Christlieb, 2003). Due to the long exposure times required to detect faint sources, brighter objects (B<14.5) saturated the plates. (Frebel et al., 2006) processed the saturated stellar data, which enabled these stars to be analyzed and $\sim$ 170 new stars with [Fe/H]< -2 were discovered from follow up medium-resolution (R$\sim$ 2000) spectra, making up the Bright Metal-poor Star (BMPS) sample.

The Sloan Digital Sky Survey (SDSS) (York et al., 2000) is a photometric and spectroscopic sky survey, carried out on the 2.5 m Apache Point Observatory telescope. SDSS is unique in that it uses the same telescope to obtain both *ugriz* photometric and R$\sim$ 2000 spectroscopic data. The photometry is used to select candidates for spectroscopy, as not all objects with photometric

observations are observed with the spectrograph. The results from the stellar sample of the initial survey led to a dedicated stellar survey called the Sloan Extension for Galactic Understanding and Exploration (SEGUE) (Yanny et al., 2009) in order to better study the structure of the galaxy. Between SDSS, SEGUE, and the follow-up SEGUE-2, more than 720,000 stellar spectra were obtained.

The Southern Sky Survey (SSS) is an ongoing photometric all-sky survey conducted on the SkyMapper Telescope at Siding Springs Observatory. SkyMapper is outfitted with *ugriz* filters plus a Stromgren *v*-filter, which enable photometric determinations of effective temperature, surface gravity, and metallicity. From these measurements, candidate metal-poor stars are chosen for follow up medium-resolution observations. The SkyMapper Telescope has already produced many promising candidates.

4.1.2 Spectroscopic Studies of Metal-Poor Stars

Surveys such as the HK, the HES, SDSS, and the SSS use medium-resolution observations ($R \sim 1000 - 2000$) to follow up on metal-poor star candidates. These spectra can provide somewhat accurate stellar parameters, including metallicity, but do not contain enough information for a full stellar abundance analysis. The metal-poor star candidates are then further observed at higher resolution. Studies that range from one star (e.g. Roederer et al., 2008) to hundreds (e.g. Yong et al., 2013) have been undertaken in order to verify the metal-poor categorization of the stars and to further describe their

elemental abundances.

McWilliam et al. (1995) determined stellar parameters and abundances for 25 elements for a sample of 33 metal-poor stars from R$\sim$22,000 spectra. This resolution places it well beyond the realm of medium-resolution spectra, but it is on the low end of high-resolution. This study was one of the first to identify elemental abundance trends with metallicity in metal-poor stars. Generally, the majority of abundance ratios for stars with [Fe/H] > -2 tend to be similar to the solar abundance ratios, with certain exceptions. The α-element ratios (e.g., [Ca/Fe]) are enhanced and some Fe-peak element ratios are depleted (e.g., [Mn/Fe]) relative to the solar abundance ratios.

Another influential high-resolution study was that of Cayrel et al. (2004), part of the First Stars series. Abundances of the light elements (Z$\leq$ 30) for 34 halo giants were determined from R$\sim 45,000$, S/N$\gtrsim 100$ spectra. The sample was carefully selected to include only those stars that represent typical halo star abundances, including many of the same stars analyzed in McWilliam et al. (1995). From these abundances, statistics and trends were determined. Additional papers in the First Stars series explored heavier elements in these stars, along with a sample of halo dwarfs. The First Stars series and other studies that derive abundances from high-resolution stellar spectra (e.g., Lai et al. 2008) are necessary to characterize the abundances of different elemental species in individual metal-poor stars and thus the resultant abundance patterns. However, obtaining high-resolution spectra is costly in terms of dedicated observing time, and limits such analyses to relatively bright stars for

efficiency.

In between medium-resolution spectra and high-resolution spectra are so-called snapshot spectra. These snapshot spectra are of moderate resolution (R$\sim$15,000$-$20,000) and S/N ($\sim$ 40) and require much shorter exposure times than high-resolution spectra. This is beneficial for two reasons: first, more stars can be observed; and second, fainter stars can also be included in these studies. Snapshot spectra allow for a quicker evaluation than high-resolution spectra and a more thorough analysis than medium-resolution (R $\sim$ 1000 $-$ 2000) spectra. Snapshot spectra offer enough information from which to derive individual abundances with moderate uncertainties ($\sim$0.25 dex), which is not quite possible in medium-resolution spectra.

The Hamburg/ESO R-process Enhanced Survey (HERES) (Barklem et al., 2005) is one study that utilized snapshot spectra. HERES determined the stellar parameters and abundances via spectral synthesis of $\sim$ 250 metal-poor stars using VLT/UVES snapshot spectra. They derived abundances for 22 elements from their stars, providing a statistical sample of abundances from which to derive trends and frequencies. Studies such as HERES are beneficial because they are able to include fainter stars, while observing larger numbers of stars due to the nature of snapshot spectra.

4.1.3 The Chemical Abundances of Stars in the Halo Project

The flexibility of queue-scheduled telescopes, like the Hobby-Eberly Telescope (HET, Shetrone et al. 2007) at McDonald Observatory, provides an

excellent means of obtaining snapshot spectra for large studies. From 2006-2009, we obtained R $\sim 15,000$ snapshot spectra of ~ 500 metal-poor halo star candidates using the High Resolution Spectrograph (HRS Tull 1998) on the HET as part of the Chemical Abundances of Stars in the Halo (CASH) project (Hollek et al., 2011). These stars were selected from SDSS, SEGUE, the HES BMPS, and the HK survey. For most of these stars, the HET snapshot spectra are the highest resolution spectra that have been obtained to date. The intent of this project is to perform a consistent analysis on a stellar sample that is well beyond the realm of small number statistics, based on a homogeneous set of data. From this, we determine stellar parameters and elemental abundances, and derive abundance trends as a function of [Fe/H]. We are also aiming to determine the frequencies of abundance anomalies of particular elements, including C and heavier elements such as Sr and Ba. Finally, we use this sample as a discovery data set to find astrophysically interesting stars. This phase of the project has already produced many results.

The CASH study represents the first detailed abundance analysis in the literature for many of the stars in the sample, and has yielded several new results. (1) Roederer et al. (2008) provided an in-depth analysis of HKII 17435−00532, a Li-enhanced giant with enhanced C and s-process elements as well. (2) In Hollek et al. (2011), we presented a calibration of the automated stellar parameter and abundance determination pipeline for this project, Cashcode. The calibration was performed by comparing the derived stellar parameters and abundances from snapshot spectra from the HET with

high-resolution spectra observed with the Magellan/Clay Telescope of the same star. The stars were selected by metallicity for this test and we presented detailed abundance analyses for 16 new stars with [Fe/H]~ -3. (3) We initially selected HE 0414−0343 for follow up observations to be part of the Hollek et al. calibration, but further inspection of its CASH snapshot spectrum revealed that it had a greatly enhanced C abundance. In Hollek et al. (2014) we presented a detailed abundance analysis of this star from a high-resolution MIKE spectrum. We evaluated its radial velocity measurements from several spectra taken over the years (including the CASH snapshot spectrum) and found it to show variations over time, indicating that it is likely in a binary or multiple system. We evaluated the [Y/Ba] ratio of HE 0414−0343, along with a sample of similar carbon-enhanced metal-poor (CEMP) stars, with neutron-capture element enhancements from the literatre (Placco et al., 2013) and found that the [Y/Ba] values of the CEMP stars formed a continuum of ratios. We compared the derived neutron-capture element abundance patterns of all the stars to the nucleosynthetic yields of a metal-poor asymptotic giant branch star model. We re-classified the CEMP-s and CEMP-r/s stars into three groups: CEMP-sA, CEMP-sB, and CEMP-sC, where the CEMP-sA stars have [Y/Ba] ratios closest to the solar ratio and CEMP-sC stars have the most negative [Y/Ba] ratios. We suggested two plausible scenarios to explain the continuous distribution of these values. First, abundance patterns of these stars represent the timing of the mass-transfer, where CEMP-sA stars received the material earlier in their evolution as compared to the CEMP-sC stars. Alternatively,

the mass of the donor AGB companion may be responsible for the difference, since the yields of lower-mass AGB stars are more consistent with the observed abundance patterns of CEMP-sA stars, and those of higher-mass AGB stars with CEMP-sC stars (Hollek et al.). (4) To measure equivalent widths more effectively, consistently, and quickly, we developed Robospect (Waters & Hollek, 2013), an automated equivalent width measurement software.

4.1.4 Classification of Metal-Poor Stars

Large surveys like HES, studies such as CASH, and the multitude of smaller studies (e.g.,McWilliam et al. 1995) have allowed astronomers not only to discover metal-poor stars, but also to analyze the chemical abundance trends and frequencies of metal-poor stars. One of the simplest ways to classify metal-poor stars is based upon its Fe content. Beers & Christlieb (2005) suggested such a classification scheme, with the term metal-poor referring to stars with [Fe/H] < -1. They labelled stars with [Fe/H] < -2, -3, -4, -5, and -6 are considered very (VMP), extremely (EMP), ultra (UMP), hyper (HMP), and mega metal-poor (MMP), respectively. Efforts to detect ever lower metallicity stars have been successful. To date, we know of three stars with [Fe/H]< -5, 2 HMP stars, HE 0107$-$5240 (Christlieb et al., 2002) and HE 1327$-$2326 (Frebel et al., 2005) with [Fe/H]$= -5.1$ and -5.6 respectively and an MMP star, SMSS J031300.36$-$670839.3, with an upper limit of [Fe/H] < -7.1 (Keller et al., 2014).

The elemental abundance patterns of these stars are also used for classi-

fication. As discussed in McWilliam (1997), the halo population of metal-poor stars generally follows a scaled-solar abundance pattern with a few distinct differences. The $\alpha-$elements tend to be enhanced relative to the solar ratio, while certain Fe-peak elements are depleted. However, $\sim$10% of metal-poor stars show deviations from these general abundance trends. Of particular interest are stars with abundance enhancements of neutron-capture elements.

The abundances of neutron-capture elements with respect to Fe have been found to be enhanced relative to the solar ratio in many metal-poor stars. The rapid neutron capture (or r-) process is thought to occur in an explosive event (Mathews & Cowan, 1990) such as a supernova. Seed nuclei gain neutrons at rates faster than they can β-decay and elements such as Eu are created. The r-process is thought to be a primary process and was able to occur during the stellar endpoints of Pop III stars. The r-process materials would then have been injected into the surrounding medium from which the r-process enhanced stars were subsequently formed. Beers & Christlieb (2005) further divide r-process enhanced metal-poor stars into two groups, r-I and r-II, where r-I stars have $0.3 \leq$ [Eu/Fe] ≤ 1.0 and [Ba/Eu] < 0, while the r-II stars have [Eu/Fe] > 1.0 and [Ba/Eu] < 0.

The main component of the slow-neutron capture (or s-) process occurs in the inner layers of evolved low-mass asymptotic giant branch (AGB) stars (Gallino et al., 1998), thus it is believed that the s-process began at a later time in the history of the universe, after lower-mass stars had time to evolve to the AGB. The s-process works on timescales longer than the amount of

time that nuclei will β-decay; seed nuclei acquire neutrons one at a time and then β-decay as they climb the valley of stability on the chart of the nuclides, creating elements such as La. Bismuth is the termination point of the s-process. There are three stable peaks of the s-process centered around Sr, Ba, and Pb and these elements are enhanced in s-process enriched metal-poor stars. Low-metallicity s-process stars also are enriched in their C abundances, as AGB stars create C and s-process elements (Masseron et al., 2010).

The previously mentioned carbon-enhanced metal-poor (CEMP) stars are another chemically peculiar metal-poor star group. These stars are easily identified through the prominent molecular CH and CN features in their spectra. Beers & Christlieb (2005) first categorized CEMP stars as any metal-poor star with [C/Fe]$>$ 1. This early categorization allowed the classification of many CEMP main sequence and turn-off stars, but excluded more evolved stars that had depleted their C abundance through CN cycling during their ascent up the red giant branch. Hence, Aoki et al. (2007) presented a revised CEMP definition of [C/Fe] $>$ 0.7 for stars with $\log(L/L_{\odot}) \leq$ 2.3 and [C/Fe] $> 3 - \log(L/L_{\odot})$ for stars with $\log(L/L_{\odot}) \geq$ 2.3.

The CEMP stars can be further subdivided into three groups: s-enriched CEMP(-s) stars (e.g. Lucatello et al. 2005), r-process enriched CEMP stars, and CEMP(-no) stars (e.g. Placco et al. 2014) with otherwise normal neutron-capture element abundances. There are only few known instances of CEMP stars with pure r-process enrichment, most famously CS 22892$-$052 (Sneden et al., 2003). The enhancements in C and s-process elements are expected

to be correlated, since both can result from AGB nucleosynthesis and third dredge-up (Sneden et al., 2008). Typically, these stars present with [Ba/Fe] > 1.0 along with their C-enhancement. Radial velocity studies of CEMP-s stars indicate that they are all in binary or multiple systems (Starkenburg et al., 2014). Thus, the enhancement scenario is that both C and s-process elements are created in an unseen AGB binary companion from which the observed CEMP star accretes material onto its surface. However, much is still unknown about these systems. Many CEMP stars exhibit enhancements in elements typical in the r-process as well as s-process elements, hence a CEMP-r/s classification was developed by Beers & Christlieb. Yet this classification did not explain the origin of those elements and none of the scenarios presented proved satisfactory in explaining the origins of CEMP-r/s stars (e.g., Jonsell et al. 2006). Hence, we explored a new classification system in Hollek et al. (2014) based upon the [Y/Ba] ratio. CEMP-no stars tend to be more metal-poor than any of the other CEMP subgroups. In fact, the two HMP stars are part of this subgroup. The C-enhancement mechanism is still unknown for these stars. More radial velocity variation studies need to be performed for the CEMP-no stars.

4.1.5 CASH IV

In this paper, we present the results of the snapshot spectra of the CASH project. In Section 4.2, we discuss the selection criteria for the stars of the CASH study. In Section 4.3 we describe the details of the observations,

data reduction, and radial velocity measurements. We describe the analysis in the next two sections in Section 4.4, beginning with the equivalent width measurement procedures and linelist development and then outline the automated stellar parameter and abundance determination pipeline, Cashcode, in Section 4.5. We present our abundance results in Section 4.6, along with average values, trends, and frequencies where appropriate and we compare these results to the literature. In Section 4.7, we compare a set of stars that the CASH sample has in common with Roederer et al. (2014). In Section 4.8, we present astrophysically interesting stars that likely merit follow up observations and conclude in Section 4.9.

4.2 Sample Selection

The CASH sample was chosen with the aim of carrying out a consistent analysis of the metal-poor stellar halo of the galaxy. We selected the candidates based on analysis from medium-resolution observations and aimed to include stars with [Fe/H] < -2. The CASH sample was drawn from four main studies: the HK survey, BMPS of the Hamburg/ESO Survey, SDSS, and SEGUE. The HK and HES candidates represent the brightest stars in our sample and consequently they also have the highest S/N ratios. The SDSS and SEGUE studies included fainter objects. Hence, the faintest SDSS and SEGUE spectra for our sample are among those with the lowest S/N. We discuss the determination of the S/N ratio in Section 4.3. Given the moderate spectral resolution of our data, we determined that S/N$\geq$ 30 was required to

obtain consistent and reliable results. Spectra of lower S/N were difficult to obtain stellar parameters from due to the lack of available Fe II lines. Thus, we made a cut at S/N$\geq$ 30 to include in our analysis.

We discuss the stellar parameter determination in Section 4.5, however here we discuss the metallicity distribution of the sample. The metallicity derived from the CASH snapshot spectra of our stars ranged from $-3.3 \leq$ [Fe/H] ≤ -0.1. The left panel of Figure 4.1 displays a histogram of the [Fe/H] values for the entire CASH sample, divided into bins of width 0.20 dex, which reflects the uncertainty in the derived metallicities. The sample is also shown divided up in different S/N bins. The lowest S/N stars skew towards the higher metallicity, as these stars are faint and it is difficult to distinguish between hot, metal-rich stars and metal-poor stars. In the right panel of Figure 4.1, we also show a histogram of the S/N ratio broken down into different metallicity groups. Fortunately, due to the selection criteria, this cut still included the most metal-poor stars of the sample.

4.3 Observations, Data Reduction, Radial Velocity Measurements

4.3.1 Observations

The snapshot spectra of the CASH project were taken from November 2006−October 2009 using the High Resolution Spectrograph on the Hobby-Eberly Telescope at McDonald Observatory. The spectra have R$\sim 15,000$, median S/N$\sim$ 55 at 5200Å, and cover a wavelength range from 4200−7800Å

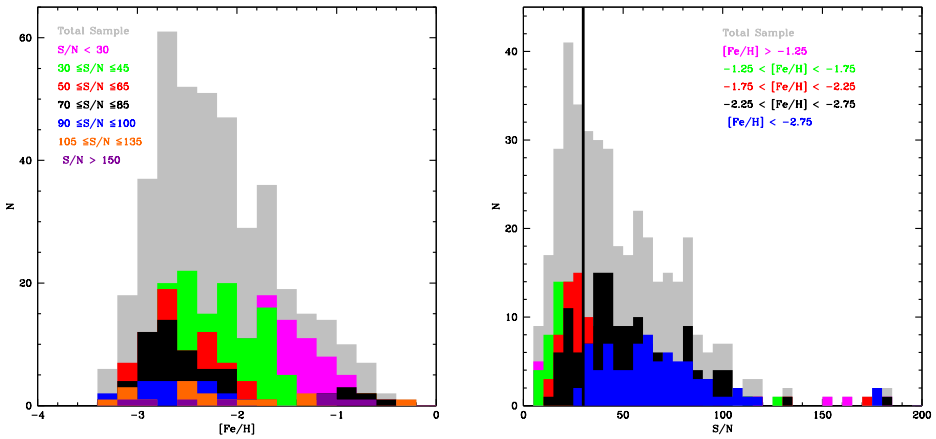

Figure 4.1 Histogram of the derived metallicities of the CASH sample stars in the left panel. The grey histogram shows all stars that were observed as part of the program. The remaining colored histograms show the distribution of metallicity for a given S/N range. In the right panel, we show the histogram of S/N ratios calculated for the snapshot spectra of the CASH sample. The grey histogram again shows all the stars that were observed. The black line drawn at S/N = 30 indicates the S/N cut applied to the sample. The remaining colored histograms correspond to the distribution of S/N for given metallicity ranges.

(which essentially covers the CH G-band to the Ca triplet). Table 4.1 includes the observation information for the CASH sample.

Table 4.1. Observations

Star	UT Date	RA (J2000)	Dec (J2000)	t_{exp} sec	S/N at 5180Å	v_{rad} km s^{-1}
HE 0414−0343	11 March 2007	04 17 16.4	−03 36 31	3000	120	−30

Note. — This table is available in its entirety in a machine-readable form, available by request. A portion is shown here for guidance regarding its form and content.

4.3.2 Data Reduction and Radial Velocity Measurements

The data were reduced using the IDL Reduce software (Piskunov & Valenti, 2002). The spectra were then continuum normalized using the "continuum" task in IRAF [2]. The radial velocities were calculated by cross correlating the echelle order that contained the Mg b triplet against the spectrum of a metal-poor giant star using the "fxcorrect" task in IRAF. This leads to typical uncertainties of ~ 3 km s^{-1}. In the case of multiple observations, the spectra were first radial velocity corrected and then co-added in IRAF. Heliocentric corrections were computed using the "rvcorrect" routine. Details of the data reduction can be found in Roederer et al. (2008) and Hollek et al. (2011). Table 4.1 also lists the radial velocity measurements for each observation of each star.

4.4 Equivalent Width Measurement, Linelist Development

4.4.1 Equivalent Width Measurement

The equivalent widths were measured using Robospect(Waters & Hollek, 2013), an automated equivalent width measurement software package[3]. Robospect makes an initial fit to the continuum by smoothing over the spectrum, using a smoothing box that is wider than most lines. The local spectrum noise

[2]IRAF is distributed by the National Optical Astronomy Observatories, which is operated by the Association of Universities for Research in Astronomy, Inc., under a cooperative agreement with the National Science Foundation.

[3]Available at http://ifa.hawaii.edu/ watersc1/robospect.html

is evaluated on the same scale, and used to identify peaks in the unsmoothed spectrum that are considerably deviant from the smoothed continuum. These identified peaks, along with a user-specified linelist, are then fed into a routine that fits Voigt-profile models to the lines. Bad line fits are flagged by the code to signify possible problems with the equivalent width measurements. The major sources of these bad fits are fits that simply do not converge and unrealistic model fits for highly blended lines. Voigt profiles were also adopted in the earlier CASH studies of Roederer et al. (2008) and Hollek et al. (2011), although both of these used a semi-automated IDL fitting routine from Roederer et al. (2014).

Robospect is well suited for snapshot spectra because it deblends features and can fit multiple lines that are in close wavelength proximity. The deblending process occurs during line fitting, where Robospect uses an internal linelist to identify lines that may potentially blend with other lines. It then performs simultaneous fits on these groups of neighboring lines. Robospect iterates the fitting process, subtracting the previous line fits before smoothing the residual continuum. This results in an improvement to the continuum level, a decreased noise measurement, and therefore more reliable fits to the lines. For the CASH snapshot spectra, we determined that 5 iterations were sufficient for determining a realistic continuum model, while maintaining efficiency.

The robustness of the Robospect-derived equivalent width measurements was tested with snapshot spectra acquired as part of the CASH project.

Table 4.2. Sample Equivalent Width Table

Species	λ [Å]	χ [eV]	log gf	W mÅ
Mg I	4571.10	0.00	−5.69	66.3
Mg I	4702.99	4.33	−0.38	70.2
Mg I	5528.40	4.34	−0.50	67.8
Mg I	5711.09	4.34	−1.72	19.5
Ca I	4283.01	1.89	−0.22	60.5
Ca I	4435.69	1.89	−0.52	43.8
Ca I	4454.78	1.90	0.26	92.1
Ca I	4455.89	1.90	−0.53	37.5
Ca I	5262.24	2.52	−0.47	22.7
Ca I	5349.47	2.71	−0.31	11.1
Ca I	5581.97	2.52	−0.56	16.6
Ca I	5588.76	2.52	0.21	65.9
Ca I	5590.12	2.52	−0.57	9.4
Ca I	5594.47	2.52	0.10	52.9
Ca I	5598.49	2.52	−0.09	46.0
Ca I	5601.28	2.53	−0.52	23.2

For S/N$\sim$ 65, Robospect reproduces manually-derived equivalent width measurements within 1.7$\pm$0.5 mÅ, where 0.5 is the standard error. See Section 3.2 of Waters & Hollek (2013) for an in-depth analysis of its fitting accuracy with regard to CASH spectra. In Table 4.2, we show a set of sample equivalent width measurements for form and content.

Table 4.2 (cont'd)

Species	λ [Å]	χ [eV]	log gf	W mÅ
Ca I	5857.45	2.93	0.23	26.4
Ca I	6102.72	1.88	−0.79	41.1
Ca I	6122.22	1.89	−0.32	70.9
Ca I	6162.17	1.90	−0.09	72.9
Ca I	6449.81	2.52	−0.50	25.5
Sc II	4325.00	0.59	−0.44	91.5

Note. — This table is available in its entirety in a machine-readable form, available by request. A portion is shown here for guidance regarding its form and content.

4.4.2 Linelist Development

The linelist used for the CASH sample is based on the one used to analyze HE 0414−0343 in Hollek et al. (2014), though it has been modified to reflect the lower resolution and lower S/N ratio of the snapshot spectra. The linelist that we previously used for our snapshot spectra is presented in Hollek et al. (2011). However, that version typically resulted in artificially low $\log g$ values due to the lack of a sufficient number of Fe II lines. To construct an improved linelist for the present study, we chose a sample of 18 stars from the CASH spectra to evaluate the Hollek et al. linelist. These stars were selected to be represent the full range of metallicity and stellar parameters across the

CASH sample. These stars were chosen from the HES sample from our spectra. In general, these stars have moderate-to-high S/N ratios as compared to the rest of the snapshot spectra. However, we developed this linelist with the idea that it could take advantage of the line-flagging functionality in Robospect for the low S/N spectra of our study.

These test stars were run through Robospect using the full Hollek et al. (2014) linelist, and each line was then evaluated for inclusion in the CASH IV linelist. Lines that were consistently blended with other features to the point that the deblending algorithm of Robospect could not disentangle their equivalent widths were omitted. Similarly, weak features that did not appear in a majority of these relatively high S/N spectra were also omitted. This pared-down linelist was then used in the stellar parameter and abundance determination software, Cashcode. The resultant stellar parameters and derived abundances were then examined on a line-by-line basis. Lines that provided spuriously high or low results were removed from the linelist. Lines that consistently yielded high abundances were generally the result of blends that could not be resolved at the resolution and S/N level of the snapshot spectra. We find that the number of available Fe II lines are still a limiting factor in our linelist. However, we were able to include more of these lines, which are carefully inspected for quality of fit to derive the most realistic stellar parameters.

4.5 Determination of Stellar Parameters

Stellar parameters and elemental abundances were determined from equivalent width measurements of Fe I, Fe II, Ti I and Ti II using the automated spectroscopic stellar parameter and abundance analysis pipeline, Cashcode (Hollek et al., 2011). Cashcode uses the LTE line analysis and spectral synthesis code, MOOG (Sneden, 1973). For these spectra, we use a version of MOOG that properly treats Rayleigh scattering opacities (Sobeck et al., 2011). Rayleigh scattering is an opacity source that is important in cool metal-poor giant stars, which make up a significant portion of the sample. We used Kurucz model atmospheres (Castelli & Kurucz, 2004) with α-enhancement and convective overshoot, as the expectation is that the metal-poor sample stars are α-enhanced.

Cashcode automatically iterates to determine the stellar parameters by evaluating abundances from individual lines of Fe I, Fe II, Ti I, and Ti II. The choice of spectroscopic effective temperatures results in values cooler than those derived from photometry, typically by ~ 150 K for giants. This offset in temperature leads to ~ -0.5 dex offset in surface gravity. Thus, we adjust the effective temperature values according to the procedure of Frebel et al. (2013) as follows.

We first determine spectroscopic stellar parameters in the usual way. That is, we determine the effective temperature by demanding that there be no slope in the relation between excitation potential and the individual line abundances. We note here that lines with log (reduced equivalent width)> -4.5

were excluded from this analysis, as they are often saturated on the the flat portion of the curve of growth. The $\log g$ value is determined via ionization balance of Fe I/Fe II and Ti I/Ti II. For these CASH spectra, we require that $|\log \epsilon(X_I) - \log \epsilon(X_{II})| < 0.15$ dex. The microturbulence value is derived from the $\log g$ value, following Figure 6 of Frebel et al. (2013), and is calculated at each iteration once the $\log g$ is determined. The metallicity of the model is then adjusted to match the derived [Ti/H] and [Fe/H] values, with [Fe/H] twice weighted compared to the [Ti/H], as in the ionization balance criterion. Once the initial spectroscopic stellar parameters are determined, we then apply Equation 1 of Frebel et al. to our derived effective temperature. This equation is a temperature adjustment to derive effective temperature values using spectroscopy that better match the effective temperatures determined using photometric data. This adjustment was determined by analyzing 7 metal-poor stars that had been previously well-studied in the literature. New observations of these stars were used to derive spectroscopic stellar parameters. These were then compared to the stellar parameters derived from photometry found in the literature. The relation between the photometric temperatures and the spectroscopic temperatures was then used to derive equation 1 of Frebel et al.. The largest adjustment in the effective temperature occurs for giant stars. With this adjusted effective temperature, Cashcode iterates again to achieve Fe I/Fe II and Ti I/Ti II ionization balance, with the microturbulence value again determined from the $\log g$ value. However, in this set of iterations, we hold the effective temperature fixed, ignoring the slope of the relation between

the excitation potential and abundances derived from the individual lines. Finally, the metallicity of the model is adjusted to match the derived abundances to complete the stellar parameter set and a model atmosphere is created that is used for both the equivalent width and synthetic spectra abundance derivations.

When the effective temperature is adjusted to higher temperatures, the adjusted $\log g$ is higher than the initially determined $\log g$ and thus the inferred metallicity is higher. We explored the effects of the effective temperature adjustment on the same set of stars used to construct the new linelist used for the entire CASH sample. In Figure 4.2 we show the effects of expanding the linelist and adopting the effective temperature adjustment. We plot three sets of points for each star, the first of which being the stellar parameters derived using the linelist from Hollek et al. (2011) and no effective temperature adjustment (shown as light blue triangles). We then show the stellar parameters derived for the same stars using the new linelist (orange hexagons). Finally, we show the transformation from the new linelist stellar parameters to those determined using the temperature adjustment (black dots). The three sets of points for each star are linked together with a grey line. The effects of the new linelist are somewhat hotter effective temperatures and lower gravities, especially on the giant branch, but the effects are somewhat random for less evolved stars. The effect when we consider the temperature adjustment along with the new listlist is that the adjusted temperatures are hotter by an average of 112 K and the subsequent $\log g$ values are higher by 0.3 dex. This

results in higher derived metallicities by 0.13 dex. The linelist-expanded, effective temperature-adjusted stellar parameters match the 12 Gyr Yale-Yonsei isochrones (Kim et al., 2002; Green et al., 1984) better than the previous iterations of the derived stellar parameters.

Figure 4.3 shows the HR diagram for the stars of the CASH sample along with Cayrel et al. (2004), Barklem et al. (2005), and Roederer et al. (2014) for comparison. The scatter in the CASH sample is larger than that of Cayrel et al. and Roederer et al. and on the same order of Barklem et al.. This large scatter is mainly due to the lower resolution and S/N of our spectra than these other studies, along with the large range of [Fe/H] of our sample. Table 4.3 lists the stars that made up the calibration sample, along with the stellar parameters associated with the linelist and technique from the Hollek et al. (2011) study (C2) and the new linelist and updated technique used for this study (C4). Table 4.4 lists the derived stellar parameters of T_{eff}, $\log g$, [Fe/H], and v_T for the full CASH sample.

Table 4.3. Calibration Stellar Parameter Table

Star	$T_{eff,C2}$ [K]	$T_{eff,C4}$ [K]	$\log g_{C2}$	$\log g_{C4}$	$[Fe/H]_{C2}$ dex	$[Fe/H]_{C4}$ dex
HE 0007−0819	5690	5853	3.10	3.55	−1.70	−1.49
HE 0011−0648	5720	5925	3.25	3.50	−2.05	−1.97
HE 0013−0257	4560	5169	1.10	2.25	−3.75	−3.09
HE 0013−0522	4870	5169	1.30	2.00	−3.30	−2.98
HE 0015+0048	4660	5115	1.00	1.95	−3.05	−2.57
HE 0028−1023	4660	4953	1.00	1.85	−2.80	−2.30
HE 0039−0216	5440	6834	2.00	4.35	−3.35	−1.83
HE 0041−1034	4460	4827	0.85	1.35	−2.65	−2.41
HE 0048−1109	5700	6222	2.05	3.60	−2.85	−2.33
HE 0104−0540	5150	5340	2.45	2.90	−2.80	−2.46
HE 0117−0201	4810	5169	0.85	1.65	−3.05	−2.66
HE 0117−0202	4810	5169	0.75	1.45	−2.95	−2.60
HE 0136−0318	6650	6546	3.20	3.60	−1.05	−0.90
HE 0145−1057	5830	6123	2.55	3.60	−2.30	−1.96
HE 0148−0914	4600	5070	1.05	2.05	−2.75	−2.31
HE 0201−0046	5770	5772	3.15	3.40	−1.95	−1.89

Table 4.3 (cont'd)

Star	$T_{eff,C2}$ [K]	$T_{eff,C4}$ [K]	$\log g_{C2}$	$\log g_{C4}$	$[Fe/H]_{C2}$ dex	$[Fe/H]_{C4}$ dex
HE 0223−0906	5970	6339	3.30	3.80	−2.75	−2.26
HE 0236−0242	5960	5925	3.15	3.20	−2.15	−2.09

Table 4.4. Adopted Stellar Parameters

Star	T_{eff} K	log g	ξ kms^{-1}	[Fe/H] dex
HKII 15620−03932	5115	2.25	1.74	−2.59
HKII 15623−01251	5178	2.45	1.68	−2.77
HKII 15623−02997	5439	1.45	2.08	−2.47
HKII 16029−05859	5601	3.00	1.50	−2.06
HKII 16029−05926	5025	2.05	1.80	−2.79
HKII 16033−00081	4962	1.80	1.88	−2.58
HKII 16034−02049	5187	2.00	1.82	−2.87
HKII 16078−00870	4746	1.05	2.42	−2.78
HKII 16079−00138	5979	3.25	1.50	−2.08
HKII 16080−00093	4998	1.45	2.08	−3.10
HKII 16080−01635	5007	1.50	2.03	−3.07
HKII 16084−00160	4710	1.10	2.37	−3.24
HKII 16088−06146	4980	1.35	2.16	−2.63
HKII 16469−00075	5052	1.85	1.87	−3.05
HKII 16474−02793	4980	1.80	1.88	−2.59
HKII 16541−00909	5934	2.30	1.72	−2.67

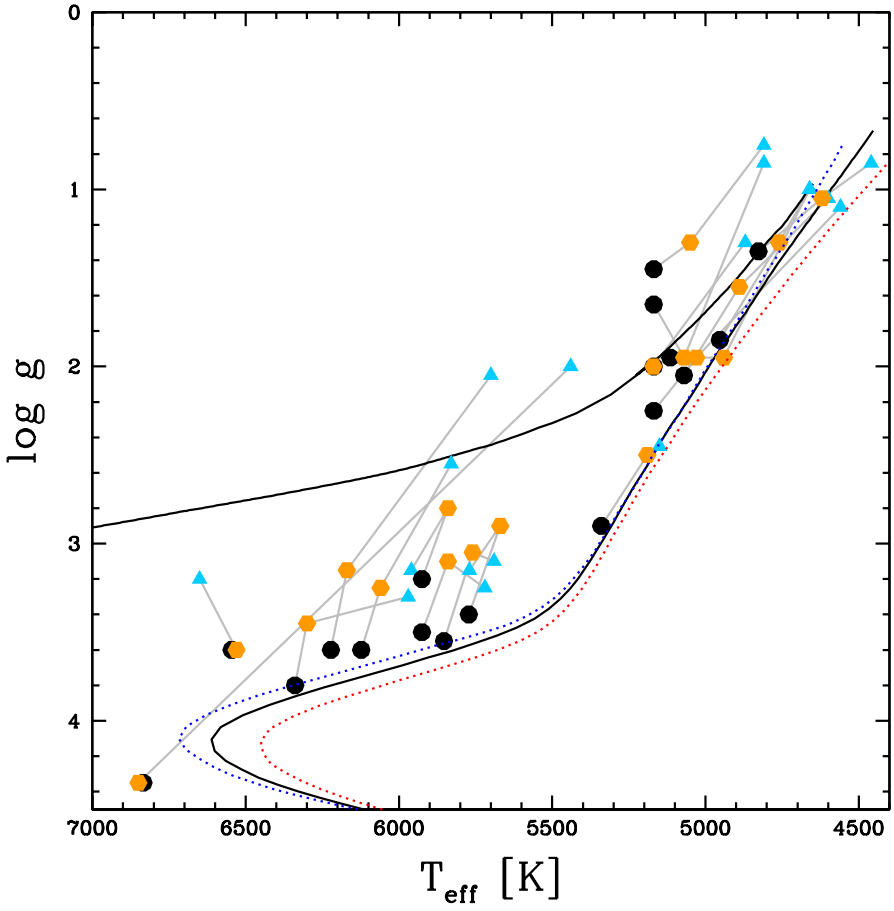

Figure 4.2 HR diagram of the calibration sample. The stellar parameters derived using the linelist from Hollek et al. (2011) are shown as light blue triangles. The stellar parameters were then rederived using the linelist for CASH IV, as represented as the orange hexagons. Finally, same stars were analyzed using the CASH IV linelist with the effective temperature adjustment of Frebel et al. (2013) are shown as black circles. This linelist and stellar parameter determination method was then adopted for the full CASH sample. A grey line connects each set of stellar parameters for a given star. Overplotted are the Yale-Yonsei isochrones (Kim et al., 2002; Green et al., 1984) for 12 Gyr, at [Fe/H] = −2.0 (red line), −2.5 (black line), and −3.0 (blue line, as well as a horizontal-branch mass track from Cassisi et al. (2004).

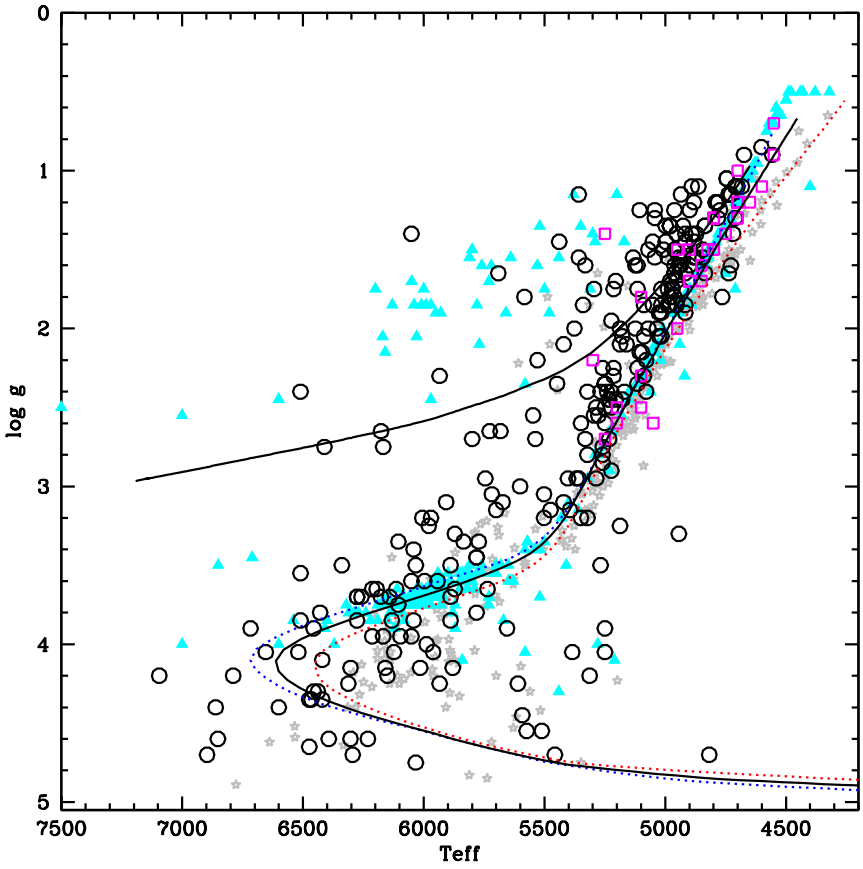

Figure 4.3 HR diagram of the CASH sample stars (black circles) along with the stars from Cayrel et al. (2004) (magenta open squares), Barklem et al. (2005) (grey stars), and Roederer et al. (2014) (cyan triangles). The symbols and color-scheme represented here follow these studies throughout the figures in this text. Overplotted are the Yale-Yonsei isochrones (Kim et al., 2002; Green et al., 1984) for 12 Gyr, at [Fe/H] = −2.0 (red line), −2.5 (black line), and −3.0 (blue line, as well as a horizontal-branch mass track from Cassisi et al. (2004).

Table 4.4 (cont'd)

Star	T_{eff} K	log g	ξ kms^{-1}	[Fe/H] dex
HKII 16541−04917	4953	1.85	1.87	−3.16
HKII 16541−04930	5529	2.20	1.76	−2.28
HKII 16542−00002	5070	1.50	2.03	−2.51
HKII 16542−00519	4836	1.35	2.16	−2.99
HKII 16545−00082	5718	3.05	1.50	−2.62
HKII 16548−00070	5223	2.50	1.66	−2.29
HKII 16548−00446	5025	1.90	1.85	−2.85
HKII 16548−02637	4863	1.10	2.37	−3.19
HKII 16548−03778	5475	3.15	1.50	−1.70
HKII 16550−02649	4872	1.40	2.12	−2.85
HKII 16553−01203	5871	3.30	1.50	−2.47
HKII 16555−00033	5385	4.05	1.50	−1.14
HKII 16555−00050	6303	4.15	1.50	−2.15
HKII 16556−01811	5331	1.60	1.95	−2.56
HKII 16934−00002	4710	1.30	2.20	−2.89
HKII 16934−00060	5889	3.50	1.50	−2.81

Table 4.4 (cont'd)

Star	T_{eff} K	log g	ξ kms^{-1}	[Fe/H] dex
HKII 16936−02204	5259	2.75	1.58	−2.98
HKII 16942−01372	5673	3.10	1.50	−1.90
HKII 16981−02194	5133	1.55	1.99	−2.63
HKII 16990−02560	5259	2.85	1.55	−2.34
HKII 17435−00024	5781	3.80	1.50	−2.73
HKII 17435−00532	5214	1.75	1.90	−2.43
HKII 17440−01458	4836	1.35	2.16	−2.74
HKII 17569−00049	4782	1.30	2.20	−2.75
HKII 17575−10478	4818	4.70	1.50	−1.21
HKII 17576−00074	4944	1.60	1.95	−2.89
HKII 17577−00209	6177	2.65	1.61	−1.74
HKII 17581−08474	6033	3.50	1.50	−2.42
HKII 17583−09708	4980	1.70	1.92	−2.51
HKII 17586−03935	4737	1.15	2.33	−3.01
HKII 17586−07617	6276	3.85	1.50	−2.39
HKII 22175−00007	5124	2.00	1.82	−2.91

Table 4.4 (cont'd)

Star	T_{eff} K	log g	ξ kms^{-1}	[Fe/H] dex
HKII 22179−01563	4773	1.25	2.25	−2.68
HKII 22180−02390	6168	3.95	1.50	−1.85
HKII 22183−00001	4935	1.60	1.95	−2.35
HKII 22183−00015	6213	3.95	1.50	−2.20
HKII 22183−00031	5025	1.90	1.85	−3.29
HKII 22878−00101	4962	1.25	2.25	−3.15
HKII 22878−07131	4989	1.75	1.90	−2.58
HKII 22886−00042	4872	1.55	1.99	−2.83
HKII 22952−00015	5106	2.15	1.77	−2.92
HKII 22957−00022	5016	1.90	1.85	−3.09
HKII 22957−00027	5547	2.55	1.64	−2.57
HKII 22965−00016	4998	1.35	2.16	−2.82
HKII 29502−00042	5322	2.80	1.56	−2.93
HKII 29502−00092	5160	2.10	1.79	−2.92
HKII 29502−01516	4953	1.40	2.12	−2.48
HKII 29512−00051	5097	2.15	1.77	−2.44

Table 4.4 (cont'd)

Star	T_{eff} K	log g	ξ kms^{-1}	[Fe/H] dex
HKII 29516−00024	4953	1.70	1.92	−2.83
HKII 29516−00041	5277	2.55	1.64	−3.01
HKII 30301−00015	5376	2.00	1.82	−2.21
HKII 30301−00059	5016	2.05	1.80	−2.17
HKII 30301−00094	4980	1.85	1.87	−2.70
HKII 30301−00107	6195	3.65	1.50	−2.44
HKII 30306−00132	4971	1.75	1.90	−2.78
HKII 30306−03335	5691	1.65	1.93	−1.70
HKII 30312−00006	6132	3.85	1.50	−2.09
HKII 30312−02585	5340	1.85	1.87	−2.37
HKII 30312−03416	4782	1.20	2.29	−3.21
HKII 30320−00109	5682	2.65	1.61	−2.04
HKII 30320−03492	4962	1.65	1.93	−2.56
HKII 30325−00028	4890	1.40	2.12	−2.95
HKII 30325−00094	4989	1.85	1.87	−3.30
HKII 30329−00004	5115	1.60	1.95	−2.74

Table 4.4 (cont'd)

Star	T_{eff} K	log g	ξ kms^{-1}	[Fe/H] dex
HKII 30338−05739	5592	4.45	1.50	−2.13
HKII 31069−00064	5511	4.55	1.50	−2.77
HKII 31085−00024	6177	3.70	1.50	−2.39
51820−0400−247	5232	2.45	1.68	−2.99
52316−0559−303	6168	2.75	1.58	−2.34
52325−0573−605	6339	3.50	1.50	−1.74
52520−1083−579	6051	3.60	1.50	−2.39
52618−1059−429	6438	4.30	1.50	−1.89
52643−1078−265	5322	3.20	1.50	−2.83
52937−1269−571	6051	1.40	2.12	−3.48
52972−1213−507	6897	4.70	1.50	−1.70
52991−1489−251	5700	3.15	1.50	−2.60
53227−1108−410	6159	4.15	1.50	−2.31
53262−1880−288	5250	2.35	1.71	−2.63
53299−1961−045	6456	4.30	1.50	−2.22
53299−1961−164	5268	2.40	1.69	−2.88

Table 4.4 (cont'd)

Star	T_{eff} K	log g	ξ kms^{-1}	[Fe/H] dex
53384−2040−170	5421	2.10	1.79	−2.31
53384−2040−407	5367	2.95	1.52	−2.80
53401−2050−406	5223	1.95	1.84	−2.88
53431−2054−033	4980	1.35	2.16	−2.94
53446−2053−188	5043	1.25	2.25	−2.66
53536−2183−549	5772	3.35	1.50	−1.53
53729−1914−357	4935	1.15	2.33	−3.13
53738−2051−245	6141	3.70	1.50	−2.52
53740−2337−168	5223	2.40	1.69	−2.70
53741−1502−261	5322	2.40	1.69	−2.91
53757−2316−395	4899	1.25	2.25	−2.62
53759−2378−429	5214	2.25	1.74	−2.63
53759−2380−094	5043	1.55	1.99	−2.70
53763−2397−563	6654	4.05	1.50	−2.01
53770−2387−530	4674	0.90	2.54	−2.71
54065−2441−309	5169	2.40	1.69	−2.76

Table 4.4 (cont'd)

Star	T_{eff} K	log g	ξ kms^{-1}	[Fe/H] dex
54094−2390−102	4764	1.80	1.88	−2.31
54095−2622−483	4791	1.20	2.29	−3.27
54179−2676−230	5250	3.90	1.50	−2.25
54208−2714−429	5043	1.30	2.20	−2.86
54271−2449−050	6042	3.40	1.50	−2.41
54331−2311−200	4881	1.45	2.08	−2.46
54368−2679−217	5349	2.60	1.63	−2.74
54368−2799−502	5250	2.35	1.71	−3.02
54368−2804−126	6474	4.35	1.50	−2.21
54380−2624−330	6600	4.40	1.50	−2.25
54441−2309−290	4890	1.10	2.37	−3.25
54507−2941−222	6006	3.20	1.50	−2.14
54515−2939−109	5088	1.85	1.87	−2.22
54515−2939−414	5241	2.40	1.69	−2.82
54524−2808−510	5331	2.70	1.60	−2.85
54529−2888−615	6393	4.60	1.50	−1.83

Table 4.4 (cont'd)

Star	T_{eff} K	log g	ξ kms^{-1}	[Fe/H] dex
54551−2253−050	5448	2.35	1.71	−2.41
54552−2551−121	6150	4.20	1.50	−2.59
54629−2178−485	5187	2.10	1.79	−2.80
54630−2910−287	6717	3.90	1.50	−1.81
54772−3143−464	4944	1.55	1.99	−2.47
54773−3146−421	6096	3.95	1.50	−2.34
54789−3133−145	4926	1.55	1.99	−2.52
54802−3157−140	4926	1.35	2.16	−2.91
54833−3183−489	4899	1.60	1.95	−2.94
54860−3230−532	5178	2.05	1.80	−2.87
54876−3005−348	6510	2.40	1.69	−2.24
54876−3229−171	4944	3.30	1.50	−2.59
BD +17 3248	5295	1.75	1.90	−2.08
BS 17 569−049	4791	1.20	2.29	−2.80
G018−021	5313	4.20	1.50	−2.81
G028−031	5961	4.05	1.50	−2.09

Table 4.4 (cont'd)

Star	T_{eff} K	log g	ξ kms^{-1}	[Fe/H] dex
G040−014	6105	3.75	1.50	−2.49
G064−012	6852	4.60	1.50	−2.38
G079−043	6258	3.70	1.50	−2.27
G083−045	5574	4.55	1.50	−2.05
G090−003	5781	3.45	1.50	−2.29
G115−034	6213	3.65	1.50	−2.23
G146−076	5079	2.40	1.69	−2.08
G191−052	5250	4.05	1.50	−2.52
G192−041	5457	4.70	1.50	−2.38
G193−026	5610	4.25	1.50	−2.69
G195−035	5187	3.25	1.50	−2.88
HD 108317	5250	2.50	1.66	−2.44
HD 115444	4746	1.05	2.42	−3.13
HD 216143	4719	1.40	2.12	−2.10
HD 221170	4728	1.60	1.95	−1.99
HE 0007−0819	5943	3.60	1.50	−1.35

Table 4.4 (cont'd)

Star	T_{eff} K	log g	ξ kms^{-1}	[Fe/H] dex
HE 0011−0648	6042	3.85	1.50	−1.75
HE 0013−0257	5088	2.05	1.80	−3.14
HE 0013−0522	5259	2.25	1.74	−2.90
HE 0015+0048	4989	1.55	1.99	−2.76
HE 0028−1023	4881	1.55	1.99	−2.59
HE 0041−1034	4845	1.50	2.03	−2.35
HE 0048−1109	6105	3.35	1.50	−2.48
HE 0104−0540	5421	3.10	1.50	−2.31
HE 0117−0201	5052	1.45	2.08	−2.79
HE 0117−0202	5205	1.70	1.92	−2.56
HE 0145−1057	6276	3.70	1.50	−1.81
HE 0148−0914	4953	1.85	1.87	−2.49
HE 0201−0046	5781	3.45	1.50	−1.86
HE 0223−0906	6429	3.80	1.50	−2.28
HE 0236−0242	5970	3.20	1.50	−2.05
HE 0241+0205	5079	2.20	1.76	−2.45

Table 4.4 (cont'd)

Star	T_{eff} K	log g	ξ kms^{-1}	[Fe/H] dex
HE 0243+0203	5655	3.90	1.50	−2.58
HE 0243−0244	5583	1.80	1.88	−2.24
HE 0247−0533	4962	1.65	1.93	−2.60
HE 0311−1046	5223	2.90	1.53	−3.06
HE 0313+0214	5403	2.95	1.52	−2.36
HE 0313−0911	5889	3.70	1.50	−2.57
HE 0324+0122	5232	2.70	1.60	−2.40
HE 0324+0152	5034	2.00	1.82	−3.09
HE 0349−0725	5502	3.20	1.50	−2.49
HE 0352−0645	5124	1.60	1.95	−2.58
HE 0403−0954	5106	1.25	2.25	−2.74
HE 0414−0343	4962	1.50	2.03	−2.16
HE 0418−0403	5907	3.10	1.50	−2.12
HE 0420+0123	4935	1.75	1.90	−3.00
HE 0429−0638	5286	2.95	1.52	−2.31
HE 0432−1005	4881	1.20	2.29	−2.89

Table 4.4 (cont'd)

Star	T_{eff} K	log g	ξ kms^{-1}	[Fe/H] dex
HE 0438−1055	4845	1.55	1.99	−2.48
HE 0440−1049	5889	3.85	1.50	−2.55
HE 0926−0508	6420	4.10	1.50	−2.49
HE 1001+0003	5295	2.55	1.64	−2.48
HE 1005−0739	6420	4.35	1.50	−1.86
HE 1225+0155	4917	1.90	1.85	−2.78
HE 1226+0010	6519	4.05	1.50	−1.91
HE 1304−0651	5205	2.45	1.68	−2.48
HE 1311−0131	4962	1.60	1.95	−2.92
HE 1348+0135	5232	2.45	1.68	−2.61
HE 1408−0124	4917	1.40	2.12	−2.44
HE 1429−0347	5214	2.30	1.72	−2.56
HE 1504−0246	4917	1.85	1.87	−2.32
HE 1523−0901	4683	1.10	2.37	−2.83
HE 2121−0214	6231	4.60	1.50	−1.18
HE 2123−0329	4971	1.75	1.90	−3.01

Table 4.4 (cont'd)

Star	T_{eff} K	log g	ξ kms^{-1}	[Fe/H] dex
HE 2123−0330	4917	1.45	2.08	−3.06
HE 2125−0417	4557	0.90	2.54	−2.69
HE 2131+0010	5997	3.60	1.50	−2.60
HE 2131−0815	5358	1.15	2.33	−2.00
HE 2137+0153	6033	4.75	1.50	−2.41
HE 2138−0314	5115	2.35	1.71	−3.13
HE 2144−0829	5250	2.60	1.63	−3.03
HE 2150−0147	5088	2.30	1.72	−2.22
HE 2156+0115	4737	1.65	1.93	−2.38
HE 2201−0825	5835	3.35	1.50	−2.06
HE 2208−0240	5070	2.00	1.82	−2.37
HE 2210−0250	5349	3.20	1.50	−2.06
HE 2220−0842	5880	4.15	1.50	−2.25
HE 2221−0113	4980	1.35	2.16	−2.49
HE 2227−0108	4836	1.65	1.93	−2.47
HE 2237+0217	6114	3.65	1.50	−2.13

Table 4.4 (cont'd)

Star	T_{eff} K	log g	ξ kms^{-1}	[Fe/H] dex
HE 2238−0131	4701	1.10	2.37	−2.70
HE 2243−0244	5358	1.55	1.99	−2.44
HE 2253−0849	4737	1.15	2.33	−2.72
HE 2301−0248	5871	3.65	1.50	−2.28
HE 2304−0024	5286	2.50	1.66	−2.86
HE 2316−0025	6303	4.60	1.50	−1.69
HE 2319−0303	4917	1.65	1.93	−2.65
HE 2324−0215	4602	0.85	2.59	−2.96
HE 2325−0233	5268	3.50	1.50	−2.67
HE 2326−1040	5394	3.15	1.50	−2.10
HE 2332−0113	5259	2.80	1.56	−2.59
HE 2335−1112	5358	2.95	1.52	−2.35
HE 2337−0953	6276	3.70	1.50	−2.20
S2_0287−535	6789	4.20	1.50	−1.86
S2_0351−215	5736	3.65	1.50	−2.45
S2_0582−625	5988	4.00	1.50	−2.16

Table 4.4 (cont'd)

Star	T_{eff} K	log g	ξ kms^{-1}	[Fe/H] dex
S2_0742−484	6456	3.90	1.50	−1.74
S2_0840−359	6051	3.95	1.50	−2.14
S2_0950−554	6510	3.85	1.50	−1.91
S2_1051−066	6474	4.65	1.50	−1.93
S3_0900−409	6312	4.25	1.50	−2.19
S3_1041−232	6294	4.70	1.50	−1.93
S3_1197−419	7095	4.20	1.50	−1.56
S3_1236−045	6861	4.40	1.50	−1.77
S4_1571−617	6510	3.55	1.50	−1.70
S5_1108−410	5934	4.25	1.50	−2.46
S5_1659−091	6411	2.75	1.58	−1.96
S5_1761−128	5745	2.95	1.52	−2.38
SEG2045−014	6465	4.35	1.50	−1.99
SEG2183−228	5115	1.75	1.90	−2.87
SEG2183−549	5502	3.05	1.50	−1.69
SEG2184−120	5016	1.75	1.90	−2.60

Table 4.4 (cont'd)

Star	T_{eff} K	log g	ξ kms^{-1}	[Fe/H] dex
SEG2337−151	6015	4.15	1.50	−2.23
SEG2380−094	5016	1.85	1.87	−2.79
SEG2381−323	5727	2.65	1.61	−2.54
SEG2387−530	4728	1.15	2.33	−2.67
SEG2387−580	5538	2.70	1.60	−2.56

4.5.1 Stellar Parameter Uncertainties

We determined the characteristic random uncertainty in metallicity by averaging over the σ values for the individual line abundances for Ti I, Ti II, Fe I, and Fe II for all the stars in the sample. We double weighted the σs for the Fe species as compared to the Ti values, as the model metallicity is calculated from both the Ti and Fe lines, with the Fe double weighted compared to Ti. The mean dispersion for the entire CASH sample is $\sigma_{CASH} = 0.35$. We then increased the effective temperature until the resultant Fe I/Fe II and Ti I/Ti II abundances differed by the σ_{CASH} value. For a typical star in our sample with an average S/N value, we find $\Delta T_{eff} = 325$ K. A change in effective temperature of that magnitude results in $\Delta \log g = 0.75$ on the giant branch. Given that most of our sample lies in this region and that the temperature calibration affects the giants most strongly, we conservatively adopt this value as the uncertainty in $\log g$. The corresponding microturbulence is then $\Delta v_{mic} = 0.30$, based on its relation with $\log g$.

4.6 Results

With the model atmospheres created using the final parameters listed in Table 4.4, we determined abundances for 16 elements. We discuss the abundances derived from their CASH snapshot spectra and their implications, for these elements across several different elemental groups: Li, C, $\alpha-$elements, Fe-peak elements, and neutron-capture elements. For Li, we present the A(Li)[4] abundances as a function of [Fe/H] and effective temperature. For C, we examine the [C/Fe] ratios as a function of [Fe/H] and luminosity, as the criterion for CEMP status takes the evolutionary stage into account.

For all other elements, we present [X/Fe] as a function of [Fe/H] at four different S/N cuts. The S/N cut at 80 represents the highest quality CASH spectra and illustrate the limits of snapshot spectra and our methodologies. The S/N cut at 65 represents the median S/N value for the HES spectra of our sample and the S/N cut at 50 represents a cut at the median value of the entire CASH sample. These two cuts show how our abundance ratio dispersions improve when lowest quality CASH snapshot spectra are omitted. S/N$\sim$ 30 represents the lowest S/N value from which stellar parameters and abundances can be consistently and reliably determined. The "full" CASH sample refers to all stars with S/N$\gtrsim$30. For each metallicity cut, we provide the mean value and the dispersion for each element.

We provide a mean and weighted mean or trend where appropriate for

[4]where A(X) = $\log n(X)/n(H) + 12.00$

each element in the full sample. The mean values are calculated in the usual way; however, the weighted means are calculated using an inverse variance technique. This method favors the overall stellar abundance of a given element that has lower individual line abundance dispersion. This results in a weighted mean value with a much lower dispersion than the average value. In addition we include a systematic error based on the S/N ratio of a given star. This systematic error has been calculated based on the results of Table 7 of Waters & Hollek (2013), which evaluated the Robospect calculated equivalent width values of Hjerting line profiles, which is an analytic way of determing the Voigt profile, against the equivalent widths that were were manually determined for a series of CASH snapshot spectra at S/N values of 30, 45, 65, 100, and 300. See Waters & Hollek for futher details of this analysis. For species with many lines (e.g., Ti), the mean and weighted mean tend to be very close in value. For those species with few lines that can be tricky to measure (e.g., Mg), especially in low S/N spectra, the weighted mean likely provides a more realistic determination of the average value of the sample.

We compare our results with those from three other studies: Cayrel et al. (2004), Barklem et al. (2005), and Roederer et al. (2014). The Cayrel et al. study represents a careful analysis of high-resolution, high-S/N spectra. The results of this study had very low uncertainties, such that the dispersion seen in the results are due to an intrinsic scatter, rather than observational scatter. The Barklem et al. study is similar to CASH in that it is a snapshot spectra study, though in this case, the wavelength range is different and

the stars were selected to optimize the discovery of r-process enhanced stars. Finally, Roederer et al. is a high-resolution study with high-S/N spectra of 313 stars, with a similar sample size to that of CASH. In this study, they calculate the elemental abundances for each star by determining the offsets for a particular line abundance from the mean and apply it to determine the mean abundance value for a given element in a particular star. This was done to ensure that the derived abundances were not dependent upon which lines were used to calulate the mean value. Generally, we can say that our results match those of these three studies within the uncertainties, with exceptions that reflect the limitations of our data quality and wavelength range. We determine mean abundances for each of these elements. Table 4.5 highlights the specifications of each study. Table 4.6 summarizes the abundance trend equations, as well as the mean values for the S/N cut at 70, the full sample, and the weighted mean along with the associated dispersions. Table 4.7 shows a sample table of abundances for a given star for form and content.

Table 4.5. Literature Studies

Study	Reference	R	S/N	λ	Telescope	N_{stars}
CASH	Hollek et al. (2011)	15,000	55	4300−7800	HET/HRS	263
HERES	Barklem et al. (2005)	20,000	55	3760−4980	VLT/UVES	253
A Search For	Roederer et al. (2014)	35,000	95[a]	3350−9150	Magellan/MIKE	250
Stars of Very		33,000	...	3900−6800	Smith/Tull	52
Low Metallicity		30,000	...	4300−7800	HET/HRS	19
First Stars	Cayrel et al. (2004)	45,000	200	3300−10000	VLT/UVES	34

[a]Median S/N for all A Search For Stars of Very Low Metallicity sample

Table 4.6. Abundance Statistics and Trends

Element	slope	$\sigma_{\rm slope}$	intercept	$\sigma_{\rm b}$	mean$_{80}$[X/Fe]	σ_{80}	mean$_{full}$[X/Fe]	$\sigma_{\rm full}$	weighted mean [X/Fe]
			dex	dex	dex	dex	dex	dex	dex
O	−0.63	0.35	−0.49	0.86	1.14	0.41	1.28	1.01	0.37
Mg	−0.21	0.27	−0.14	0.70	0.39	0.20	0.21	0.26	0.38
Ca	−0.05	0.27	0.22	0.70	0.35	0.11	0.29	0.18	0.33
Sc	0.08	0.27	0.20	0.70	−0.01	0.29	0.02	0.31	0.04
Ti	0.11	0.27	0.61	0.70	0.32	0.15	0.30	0.17	0.31
Cr	0.13	0.27	0.21	0.70	−0.11	0.13	−0.09	0.19	−0.10
Mn	0.13	0.29	0.08	0.73	−0.23	0.21	−0.14	0.26	−0.28
Ni	−0.08	0.27	0.01	0.70	0.21	0.18	0.29	0.25	0.27
Zn	−0.06	0.29	0.21	0.73	0.37	0.32	0.39	0.30	0.24
Sr	0.64	0.30	1.50	0.75	−0.11	0.59	−0.15	0.70	−0.15

Table 4.6 (cont'd)

Element	slope	$\sigma_{\rm slope}$	intercept	$\sigma_{\rm b}$	mean$_{80}$[X/Fe]	σ_{80}	mean$_{full}$[X/Fe]	$\sigma_{\rm full}$	weighted mean [X/Fe]
			dex	dex	dex	dex	dex	dex	dex
Y	0.57	0.35	1.45	0.85	0.07	0.50	0.10	0.47	0.04
Zr	−0.48	0.76	−0.84	1.78	0.27	0.29	0.27	0.30	0.27
Ba	1.07	0.27	2.49	1.07	−0.18	0.84	−0.31	0.69	−0.44

Table 4.7. Sample Elemental Abundance Table

Element	log ϵ(X)	[X/Fe]	σ	n
CH	5.87	0.03	0.30	1
Mg I	5.40	0.39	0.20	4
Ca I	4.10	0.35	0.14	17
Sc II	0.48	−0.08	0.44	9
Ti II	2.51	0.15	0.18	33
Cr I	2.95	−0.01	0.20	9
Mn I	2.31	−0.53	0.21	4
Ni I	3.62	−0.01	0.21	9
Zn II	2.24	0.27	0.01	2
Sr II	0.11	−0.17	0.00	1
Y II	−0.84	−0.46	0.13	2
Ba II	−0.95	−0.54	0.15	5

Note. — This table is available in its entirety in a machine-readable form, available by request. A portion is shown here for guidance regarding its form and content.

4.6.1 Error Analysis

The random error in the abundance for a particular species in a star in our sample is defined by the σ value of the individual line abundances. For the stars with the highest S/N spectra, the random error could be desribed as the standard error, $\sigma/\sqrt{N}$ where N is the number of lines used to determine the abundance. However, generally the quality of the CASH snapshot spectra is not high enough that the random uncertainty in the line measurements can be realistically represented by the standard error. In order to evaluate the systematic error in the stars, we created model atmospheres for a representative star and varied each stellar parameter (effective temperature, $\log g$, microturbulence, and metallicity) by the uncertainties determined in Section 4.5.1.

Table 4.8. Abundance Uncertainties

Species	ΔT_{eff} +325 K	$\Delta \log g$ +0.75 dex	Δv_{mic} +0.30 km s^{-1}	$\Delta[M/X]$ +0.35 dex	σ_{char} dex	Total dex
Li I	0.31	−0.03	−0.01	0.00	0.35	0.47
Mg I	0.25	−0.04	−0.01	−0.01	0.28	0.38
Ca I	0.21	−0.02	0.00	0.00	0.28	0.35
Sc II	0.17	0.26	−0.01	0.02	0.39	0.50
Ti I	0.36	−0.04	−0.02	−0.01	0.31	0.48
Ti II	0.16	0.26	0.00	0.02	0.39	0.50
Cr I	0.34	−0.05	−0.01	−0.01	0.34	0.48
Mn I	0.29	−0.02	−0.01	0.00	0.29	0.41
Fe I	0.32	−0.04	−0.01	−0.01	0.32	0.45
Fe II	0.05	0.27	0.00	0.02	0.38	0.47
Ni I	0.27	−0.01	−0.01	−0.01	0.35	0.44
Zn I	0.16	0.14	−0.01	0.01	0.21	0.30
Sr II	0.25	0.20	0.01	0.01	0.35	0.47
Ba II	0.26	0.25	0.00	0.03	0.35	0.50

Table 4.8 lists our typical random, systematic, and total uncertainties for the abundances of the CASH sample.

4.6.2 Lithium

Lithium abundances were determined via spectral synthesis of the λ6707 Li I doublet. Li is an extremely delicate element, as it is easily destroyed below the photosphere. Hence, its abundance is depleted as it evolves off the main sequence and up the giant branch. We derived Li abundances for 148 stars. Over the sample, hotter stars have higher Li abundances and cooler stars have

lower Li abundances. In Figure 4.4, we show the Li abundance plotted as function of [Fe/H] in the left panel and T_{eff} in the right panel.

This abundance-temperature relation is consistent with the observationally-discovered Spite plateau (Spite & Spite, 1982), which describes a regime for which constant Li abundance is seen for metal-poor stars near the main-sequence turn-off. This uniform abundance in the less-evolved, hotter stars implies that these metal-poor stars were formed with the primordial Li created during Big Bang nucleosynthesis in their atmospheres and have not yet begun to deplete it. The primordial Li abundance has cosmological implications, as the theory of Big Bang nucleosynthesis predicts a particular Li abundance for a given baryonic matter density. It is difficult to draw conclusions on the nature of the Spite plateau from the CASH data because the derived Li abundance is, in addition to its fragility, very sensitive to the effective temperature (Sbordone et al., 2010). Typically, studies specifically aimed at determining Li abundances use photometric effective temperatures. Sbordone et al. explored four different effective temperature determination methods and their effect on the derived Li abundances. Additionally, the abundance uncertainties of snapshot spectra are large; however, the CASH sample does reproduce the Spite plateau.

Cooler, more evolved stars have a deep convention zone, which depletes the surface Li abundance through burning and convective dredge up. Thus, Li-enhancements in giant stars indicate that the Li abundance is not primordial, but rather produced at some point during the course of stellar evo-

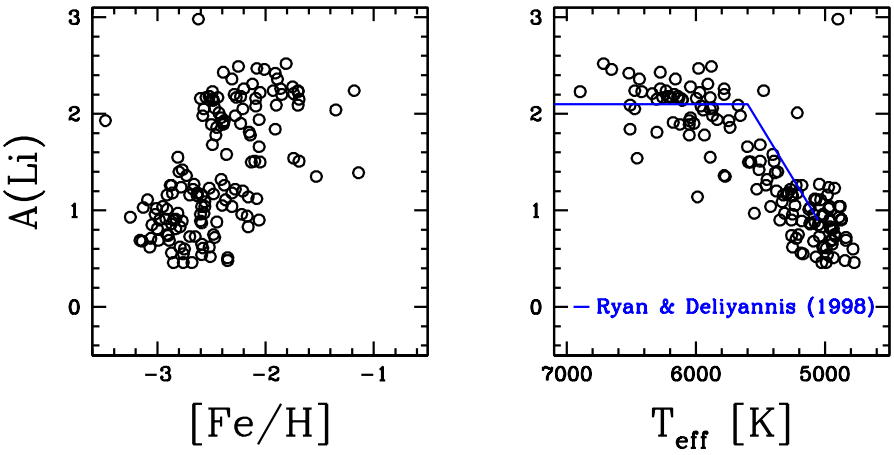

Figure 4.4 A(Li) plotted against [Fe/H] in the left panel and against T_{eff} in the right panel. Overplotted in the right panel is the Li dilution track determined by Ryan & Deliyannis (1998).

lution. Roederer et al. (2008) presented one such Li-enhanced giant. Within the CASH sample, we have discovered another giant star with A(Li) = 2.98, which is much larger than the Spite value and inconsistent with its evolutionary stage. We will discuss this star in Section 4.8.

4.6.3 Carbon

Carbon abundances were determined via spectral synthesis of a small region of the G-band near 4323Å. This CH "bump" provides more reasonable C abundances for the snapshot spectra than using the entire G-band, as there are two small regions of continuum on either side of the bump that aid in the normalization of the feature. This is particularly helpful in highly C-enhanced stars that have virtually no continuum available near the G-band bandhead, thus the CH bump is often the only part of the G-band that is well-normalized in these stars. Figure 4.5 shows the [C/Fe] abundances plotted against [Fe/H] in the left panel and against log ($L/L_{\odot}$). Plotted in green are the stars of Cayrel et al. (2004), provided for comparison here. The [C/Fe]< -2.0 represent upper limits in the [C/Fe] ratio, while the [C/Fe]> 2.0 represent lower limits on the [C/Fe] ratio. For the latter stars, synthesis of a weaker C feature is needed to determine a more accurate abundance. These stars are CEMP stars and will be identified and addressed in Section 4.8.2.

The CEMP frequency of metal-poor stars is an important number that can only accurately be determined from large numbers of stars. The C frequency is challenging to determine in the CASH sample, as CEMP stars are

not well-measured by our pipeline. This difficulty arises for several reasons. First, the method by which Robospect determines the continuum level creates issues for the CEMP stars, as the molecular C bandheads cause a much lower continuum placement than one would determine manually. Second, many linefits do not converge, especially as the code attempts to deblend large C features that include hundreds of lines. Third, the deblending solution can ultimately be wrong and thus provides potentially inaccurate equivalent width measurements in addition to the continuum placement. Fourth, as previously mentioned, the CH bump feature can easily become saturated in CEMP stars. Finally, the temperature adjustment also tends to push the gravity higher, which lowers the luminosity. This has the effect that stars that may be identified as CEMP according to the Aoki et al. (2007) prescription may be missed. The Aoki et al. includes stars with lower [C/Fe] ratios with increasing luminosity because the C abundance in stars is typically diluted over the course of stellar evolution up the giant branch due to dredge up of C-poor material from the interior onto the atmosphere. The luminosity-dependent CEMP criterion is shown as a blue dashed line in the right panel of Figure 4.5. Given these caveats, the CEMP frequency is 4.3% for stars with [Fe/H]< -2.0.

4.6.4 α-Elements

The O abundances we present here were determined via spectral synthesis of the O triplet lines λ7771, λ7774, and λ7775 when available. O was measured in 166 stars of the sample. We show our [O/Fe] ratio plotted against

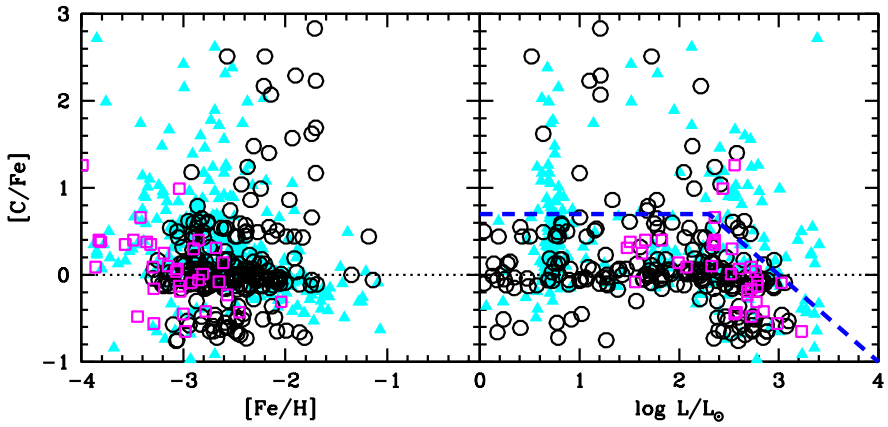

Figure 4.5 [C/Fe] ratio plotted against [Fe/H] in the left panel and log ($L/L_{\odot}$ in the right. The black open circles represent the CASH results and the green stars represent the Cayrel et al. (2004) sample, provided as a reference point. In both plots, the Solar ratio is indicated by a dotted line in black in the left panel and in magenta in the right. In the right panel, we also plot the Aoki et al. (2007) CEMP criteria in a blue dashed line.)

[Fe/H] in Figure 4.6. For this figure and in each of the 12 subsequent figures, we show the CASH data as black open circles. The Cayrel et al. (2004) data are plotted as magenta open squares for all elements up to Zn. For the neutron-capture elements of Sr, Y, Zr, and Ba, we plot the François et al. (2007) results as magenta squares as this study was a continuation of the previous one. The Barklem et al. (2005) results are plotted as grey stars, and the Roederer et al. (2014) data are plotted as cyan triangles. In each panel, we indicate S/N $\geq$ 80, 65, 50, or 30. These refer only to the S/N cut made to the CASH data and do not reflect the S/N of the comparison studies.

For the S/N cut at 80, we find [O/Fe] = 1.01$\pm$0.37. We find that for decreasing metallicity, the [O/Fe] ratio increases, with a slope of -0.62. When considering the full sample, we find an average [O/Fe] value of 1.07$\pm$0.45, a weighted mean of 1.20$\pm$0.01, and a slope of -0.71. The main cause of the slope between [O/Fe] and [Fe/H] is non-LTE effects. That the slope persists even in the highest quality data indicate that this non-LTE effect is much larger than the dispersion of the snapshot data. These non-LTE effects are known to increase at low metallicities with corrections of ~ -0.5 at [Fe/H] = -3(Fabbian et al., 2009), which is reproduced in this data. Determining non-LTE offsets for the O triplet for the entire sample is non-trivial, as many correction schemes are well-tested for only hotter stars or do not extend to the mean metallicity of the sample. We show our non-LTE corrected [O/Fe] abundances in Figure 4.7. We used the non-LTE correction of Fabbian et al. for our sample. The grid is calculated for a range of 4500K $\leq T_{\rm eff} \leq$ 6500K

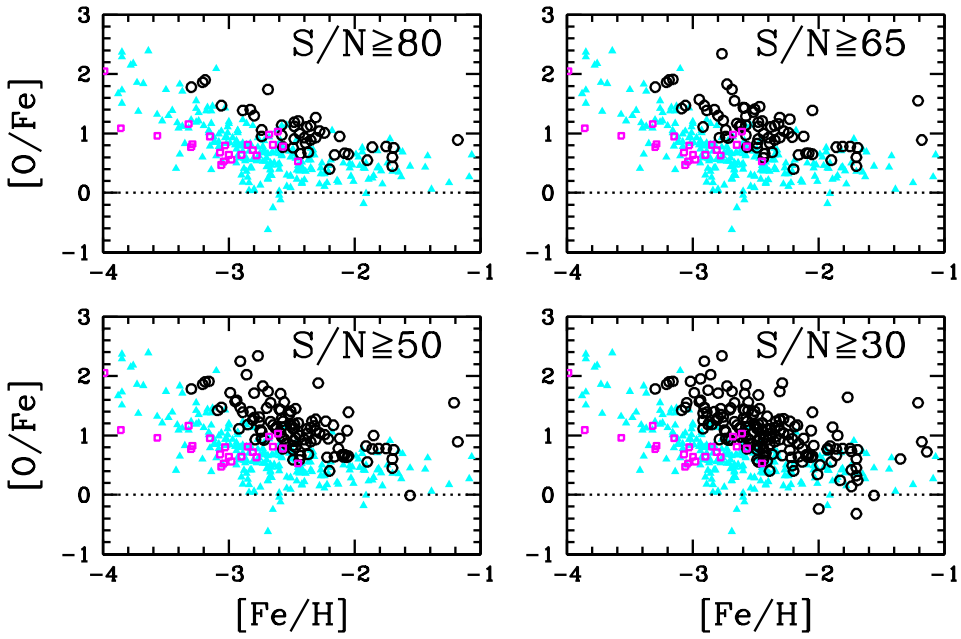

Figure 4.6 [O/Fe] plotted against [Fe/H] for the CASH sample and from the Cayrel et al. (2004) (magenta squares), and Roederer et al. (2014) (cyan triangles). On the y-axis of each plot is the [O/Fe] element and on the x-axis is [Fe/H]. In each panel, we denote the S/N cut made on the CASH data. In the upper panels, we show the cut at S/N$\sim$ 80 and $\sim$ 65 on the left and right, respectively. This plot scales 4 orders of magnitude on the y-axis. In the lower panels, we show the S/N cut at $\sim$ 50 on the left and $\sim$ 30 on the right. The cut at S/N $\sim$ 30 represents the lowest S/N value for which we could reliably and consistently determine abundances. This configuration of symbols, symbol colors, axes, and S/N cuts is consistent in each of the 8 subsequent figures.

and $2.0 \leq \log g \leq 5.0$ and up to a certain LTE logϵ(O) abundance based on [Fe/H]. If the stellar parameters of a given star fell beyond the grid or the LTE O abundance was too high, we adopted the correction of the nearest grid point. Using this correction with a H-collision frequency of 1, we find that the mean [O/Fe] = 0.89 with a slope of -0.69 between [Fe/H] and [O/Fe] for the S/N$>$ 80 sample and 0.96 with a slope of -0.76 for the full sample. The non-LTE corrections do lower the [O/Fe] ratios, but it does not account for the slope. In fact, the correction makes the relation between [O/Fe] and [Fe/H] stronger.

The Cayrel et al. (2004) study measured the λ6300 forbidden [OI] line, which is not strong enough to be measured in our spectra. Their mean [O/Fe] abundance is $\sim$ 0.70, which is quite a bit smaller than our value. They also implemented 3-D corrections, which brought the mean [O/Fe] abundance to 0.47. The slope in the relation between the [O/Fe] and [Fe/H] is much lower for this sample using a different indicator. Roederer et al. (2014) uses the triplet lines, but applies a non-LTE correction, as well as using an abundance offset of -0.50 for each of these lines for all evolutionary stages of their sample. The correlation between [O/Fe] and [Fe/H] is also seen in this study. The mean [O/Fe] value for Roederer et al. is 0.50. When this line correction is applied to the CASH sample, our mean [O/Fe] values are 0.39 and 0.46 for the S/N$>$ 80 stars and for the full sample, respectively. While this does bring our mean [O/Fe] values closer to those derived by Cayrel et al. and Roederer et al., it does not account for the slope. It has been noted that the non-LTE

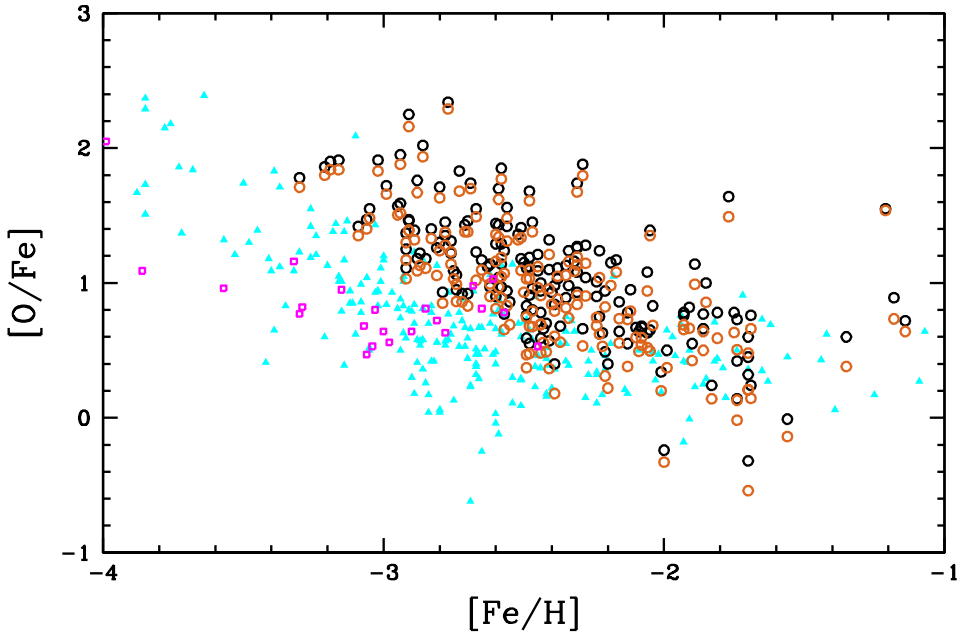

Figure 4.7 [O/Fe] plotted against [Fe/H] for the CASH sample using LTE abundances (black circles) and non-LTE corrected abundances (orange cirlces) and from the Cayrel et al. (2004) (magenta squares), and Roederer et al. (2014) (cyan triangles).

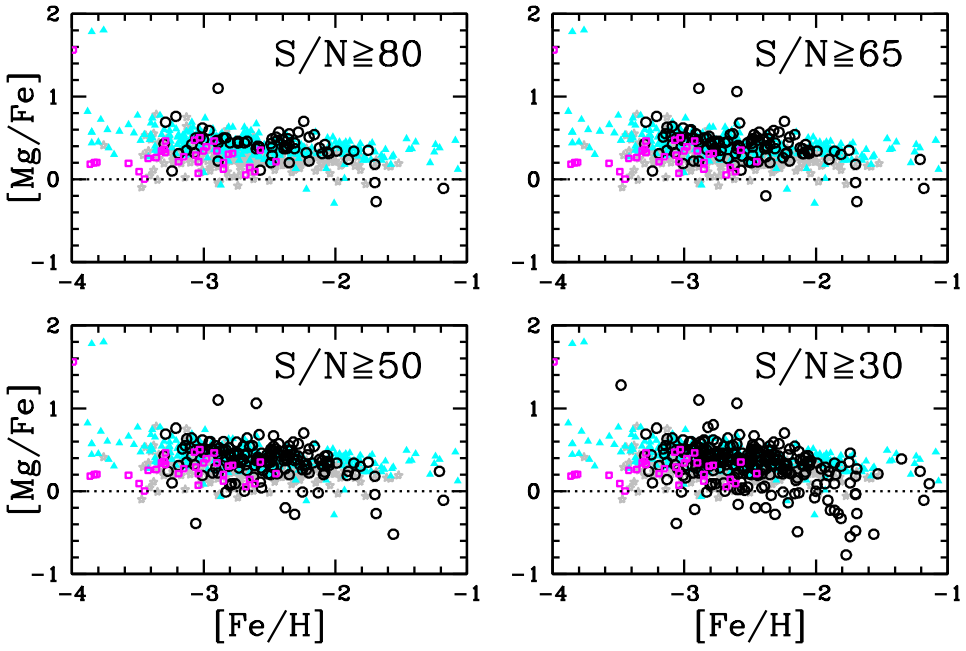

Figure 4.8 [Mg/Fe] plotted against [Fe/H] for four S/N cuts. The scale on the y-axis spans 3 orders of magnitude. The points, axes, and labels remain the same as Figure 4.6.

effects increase with lower metallicities (e.g., Fulbright & Johnson 2003). The O triplet lines have extremely high excitation potentials, and thus are formed much deeper in the star than typical spectral lines used for abundance analysis. Thus a standard LTE analysis does not allow for an accurate calcuation of the O abundances. It seems likely that the non-LTE correction of the O triplet in the most metal-poor stars needs to be much larger, especially when compared to other features, such as the λ6300 forbidden line used by Cayrel et al.. The possibility of 3-D effects further complicate the picture.

The Mg abundances are determined via equivalent width measurements of 6 lines. Figure 4.8 shows the [Mg/Fe] values plotted against [Fe/H]. As with O, not all lines were available in all stars. Mg abundances were determined for 263 stars. The mean value for stars with spectra that have S/N$\geq$ 80 is [Mg/Fe] = 0.39$\pm$0.20. The Mg abundances are often difficult to accurately assess. The specific set of lines used to determine the Mg abundance can have a great effect on the mean value, and often the only lines available are the Mg b lines, which can be very strong to point of saturation. The Cayrel et al. (2004) value is 0.27, which is somewhat lower than ours, but still well within 1σ. The Roederer et al. (2014) value is 0.43 over that entire sample, which is very close to ours. Over the entire sample the average [Mg/Fe] ratio is 0.31 ± 0.26 while the weighted mean is 0.40$\pm$0.01. The weighted mean represents the mean abundance derived from the high S/N spectra well. The [Mg/Fe] ratio for the Barklem et al. (2005) sample is 0.26, very close to the Cayrel et al. value and the average value for the full CASH sample. We note 2 stars with potentially low Mg abundances.

Ca abundances are determined via equivalent width measurements of 19 lines and were derived for 262 stars. We show the [Ca/Fe] abundances plotted against [Fe/H] Figure 4.9. Many of these lines are weak or in the blue portion of the spectrum that has lower S/N than the red portion, thus not all Ca lines are measured in all stars. The mean value for [Ca/Fe] in the S/N$\geq$ 80 stars is 0.35$\pm$0.11. The value for Cayrel et al. (2004) is 0.33 and 0.34 in Roederer et al. (2014). Across all these studies, the dispersion in Ca is quite

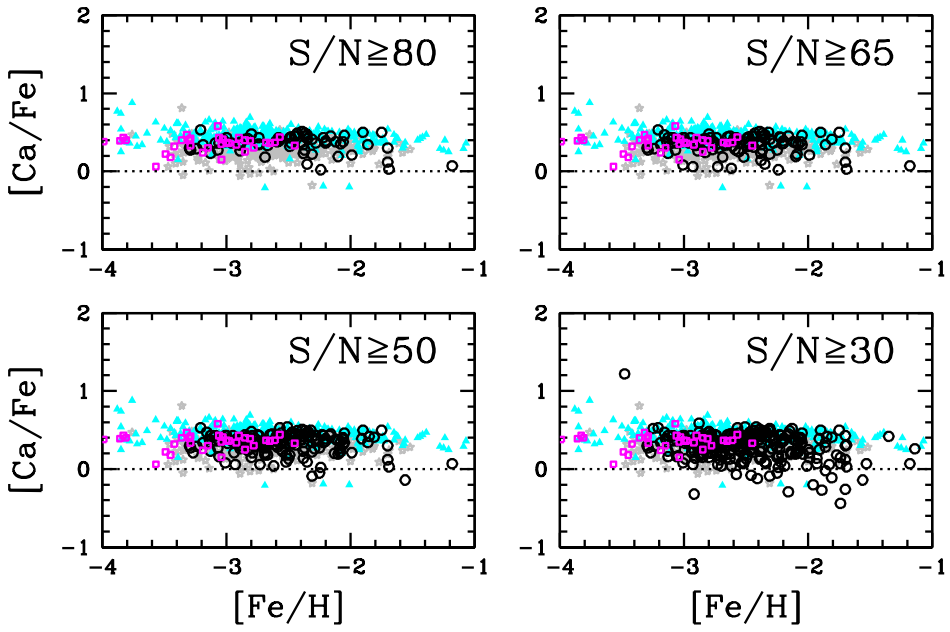

Figure 4.9 [Ca/Fe] plotted against [Fe/H] for four S/N cuts. The scale on the y-axis spans 3 orders of magnitude.The points, axes, and labels remain the same as Figure 4.6.

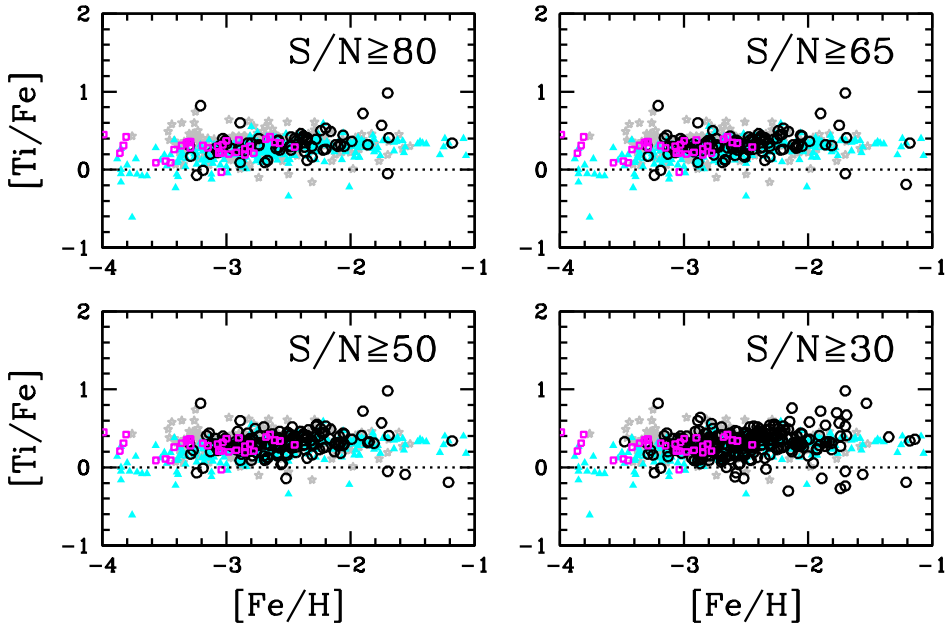

Figure 4.10 [Ti/Fe] plotted against [Fe/H] for four S/N cuts. The [Ti/Fe] values are determined using the abundances from Ti II, which has more lines measured than Ti I. The scale on the y-axis spans 3 orders of magnitude. The points, axes, and labels remain the same as Figure 4.6.

low. Over the full sample, the average value for [Ca/Fe] is 0.29 ±0.18, where the weighted mean gives 0.34 ±0.01. Again, the weighted mean accurately represents the average value for the high S/N data. The Barklem et al. (2005) average [Ca/Fe] ratio is 0.27.

While not technically an $\alpha-$element, Ti behaves as one, thus we include it here. Ti I and Ti II lines are available across the spectrum. We show our [Ti/Fe] abundances in Figure 4.10. We use the Ti lines along with the Fe lines to determine stellar parameters. The Ti I and Ti II derived abundances

are forced to agree within 0.45 dex, though generally their agreement is much better. We use new oscillator strengths from Lawler et al. (2013) for the Ti I lines. For the purposes of Figure 4.10, we show Ti II abundances in the lower right panel. When considering only S/N≥80 spectra, the mean [TiII/Fe] value is 0.33±0.17 This value matches well with all three other studies. For the full sample, the average [TiII/Fe] value is 0.30±0.17. The weighted mean gives the same result, where [TiII/Fe] = 0.30±0.02. Thus, our mean [Ti/Fe] is preserved over the entire sample, which is reassuring since the Ti abundances are used to derive the stellar parameters.

The mean [α/Fe] ratio of the sample is typically calculated by averaging over the mean values of Mg, Si, Ca, and Ti, but Si lines are not available in the CASH spectra. We calculate [α/Fe] as [Mg+Ca+TiII/Fe] = 0.30 ±0.01 over the full CASH sample. Generally, we see no relation between metallicity and the [X/Fe] values of any of the $\alpha-$elements. The exception here is the O abundances, which have increasing [O/Fe] values with decreasing metallicity for both LTE and non-LTE corrected abundances. However, the non-LTE correction is likely insufficiently large when comparing the results of the CASH sample to those of Cayrel et al. (2004).

4.6.5 Fe-Peak Elements

Sc abundances were derived via equivalent width measurements of 10 Sc II lines and were measured in 259 stars. Figure 4.11 shows [Sc/Fe] plotted against [Fe/H]. Many of these lines are in the low-S/N, blue portion of the

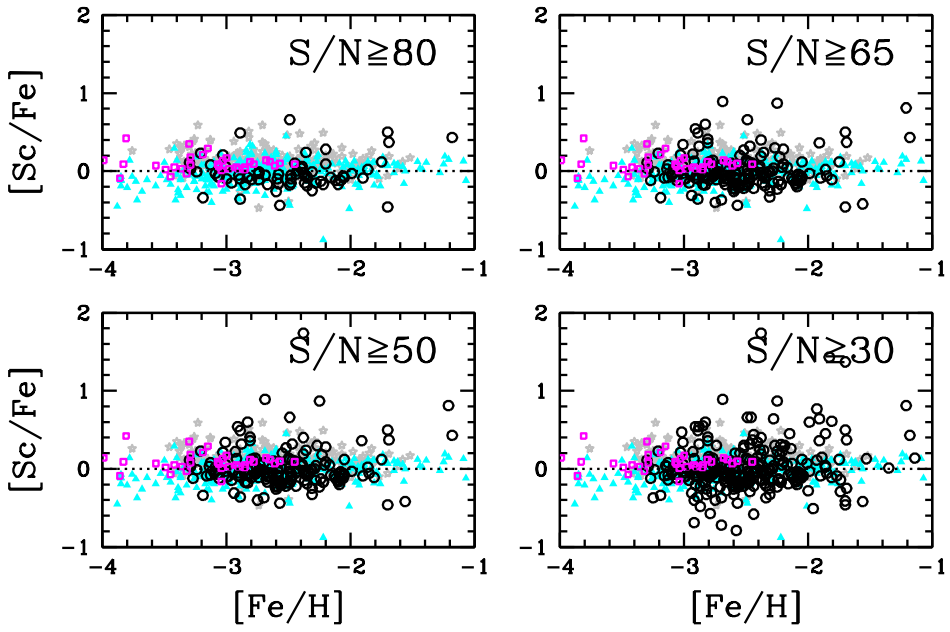

Figure 4.11 [Sc/Fe] plotted against [Fe/H] for four S/N cuts. The [Sc/Fe] values are determined using the abundances from Sc II. The scale on the y-axis spans 3 orders of magnitude. The points, axes, and labels remain the same as Figure 4.6.

spectrum and thus create a large dispersion in our measurements. When considering only stars with S/N$\geq$ 80, we find that the mean [Sc/Fe] value is -0.02 ± 0.30. This value is somewhat in agreement with Cayrel et al. (2004) and Roederer et al. (2014), and substantially lower than that from Barklem et al. (2005). The Sc value is very sensitive to line selection. The significantly bluer wavelengths available to the other three studies allows for different Sc lines to be measured. Cayrel et al. indicated that the intrinsic scatter in Sc is expected to be large because the Sc yields are sensitive to the mass of the progenitor star in which it is produced. Over the full CASH sample, the mean [Sc/Fe] value is 0.02$\pm$0.31, which agrees well with the weighted mean of 0.01$\pm$0.01.

The Cr abundances were determined from Cr I equivalent width measurements of 10 lines and were derived for all but one star in the sample. Figure 4.12 shows [Cr/Fe] plotted against [Fe/H]. While two Cr II lines are available in principle, they are difficult to measure in these snapshot spectra and thus did not yield reliable values. There is a correlation with [Fe/H], as the Cr abundance increases with [Fe/H]. We find a slope of 0.21 between [Cr/Fe] and [Fe/H], whereas Cayrel et al. (2004) determined a slope of 0.17. When we consider the average value of the high quality data, we find [Cr/Fe] $= -0.10 \pm 0.12$. The intrinsic scatter of Cr is very low, as witnessed by all three studies. The scatter in Roederer et al. (2014) is smaller than in CASH, but the scatter of Barklem et al. (2005) is slightly larger when we cut our sample at S/N $\geq$ 80. The remaining scatter represents the limits of snapshot

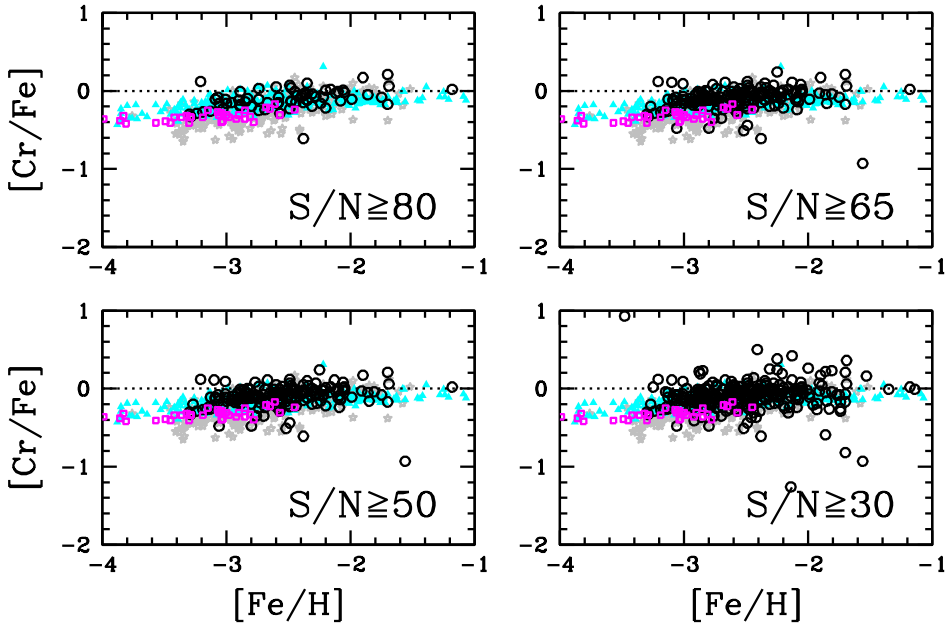

Figure 4.12 [Cr/Fe] plotted against [Fe/H] for four S/N cuts. The [Cr/Fe] values are determined using the abundances from Cr I, which has more lines measured than Cr II and are generally in agreement with each other. The scale on the y-axis spans 3 orders of magnitude. The points, axes, and labels remain the same as Figure 4.6.

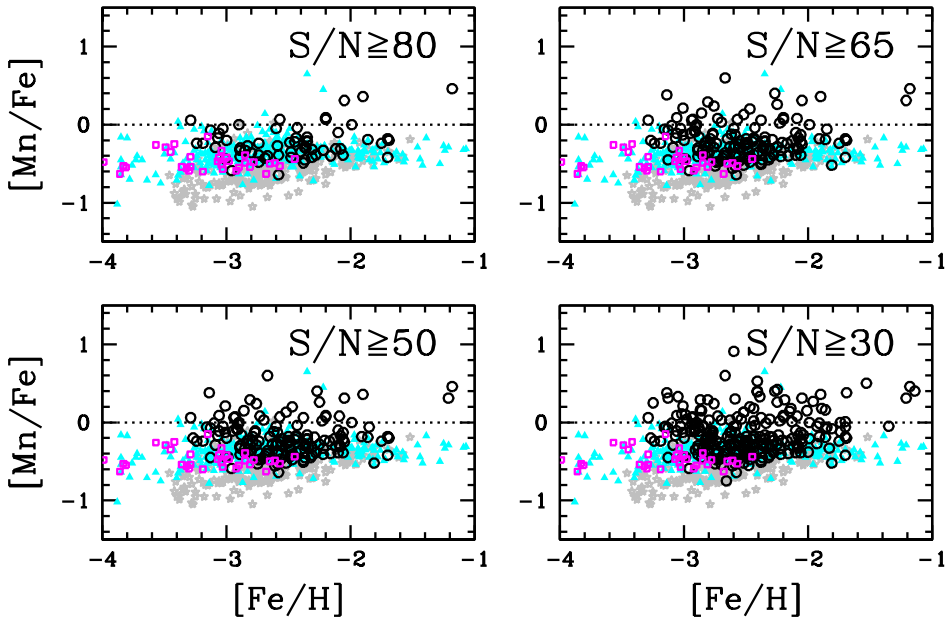

Figure 4.13 [Mn/Fe] plotted against [Fe/H] for four S/N cuts. The [Mn/Fe] values are determined via equivalent width measurements. The scale on the y-axis spans 3 orders of magnitude. The points, axes, and labels remain the same as Figure 4.6.

spectra. The same effect can also be seen in the low-scatter [Ca/Fe] ratio as well. The mean value over the full CASH sample of [Cr/Fe] $= -0.09 \pm 0.19$, while the weighted mean is -0.12 ± 0.01. Both these values demonstrate the relative depletion of Cr as compared to the Solar ratio.

Mn abundances were determined via equivalent width measurements of 5 lines for 236 stars. Figure 4.13 shows the [Mn/Fe] ratio plotted against [Fe/H]. Mn lines have hyperfine structure, which is not accounted for in our analysis of the CASH spectra. This has the effect of yielding slightly higher

abundances. For the full sample, the dispersion in the Mn abundances is so large that this hyperfine structure effect is not easily verified. When we compared Mn abundances derived via spectral synthesis and via equivalent width measurements in stars of typical S/N for the CASH sample, there was a negligible difference. When we adopt a S/N cut at 80, the mean [Mn/Fe]= -0.23 ± 0.21. This is 0.24 dex higher than the average value of Cayrel et al. (2004) and 0.15 dex higher than Roederer et al. (2014). Mn abundances are highly dependent upon the lines that are measured. Many studies use the Mn triplet near 4030Å, which consistently yield the order of ~ 0.40 dex lower than other Mn lines (Cayrel et al.). Over the whole sample, the average [Mn/Fe] value is -0.14 ± 0.26, whereas the weighted mean gives [Mn/Fe]= -0.24 ± 0.01. In this instance, the weighted mean is much lower than the average value and better matches the trend of the [Mn/Fe] ratios derived from S/N$>$ 80 spectra. The average [Mn/Fe] value is -0.54 in the Barklem et al. (2005) sample, however their linelist includes the Mn resonance triplet. Thus, the Mn abundances indeed are low when using the triplet in the absence of any additional corrections (e.g.,Roederer et al. 2014). The hyperfine structure accounts for part of this discrepancy as well, along with the overall large spread in the [Mn/Fe] values for the CASH spectra.

The Ni abundance is determined via equivalent width measurement of 14 different lines for 262 stars. Figure 4.14 shows [Ni/Fe] plotted against [Fe/H]. For the stars with S/N$\geq$ 80, we find [Ni/Fe] = 0.21 ± 0.18. This value is larger than Cayrel et al. (2004), Roederer et al. (2014), and Barklem et al.

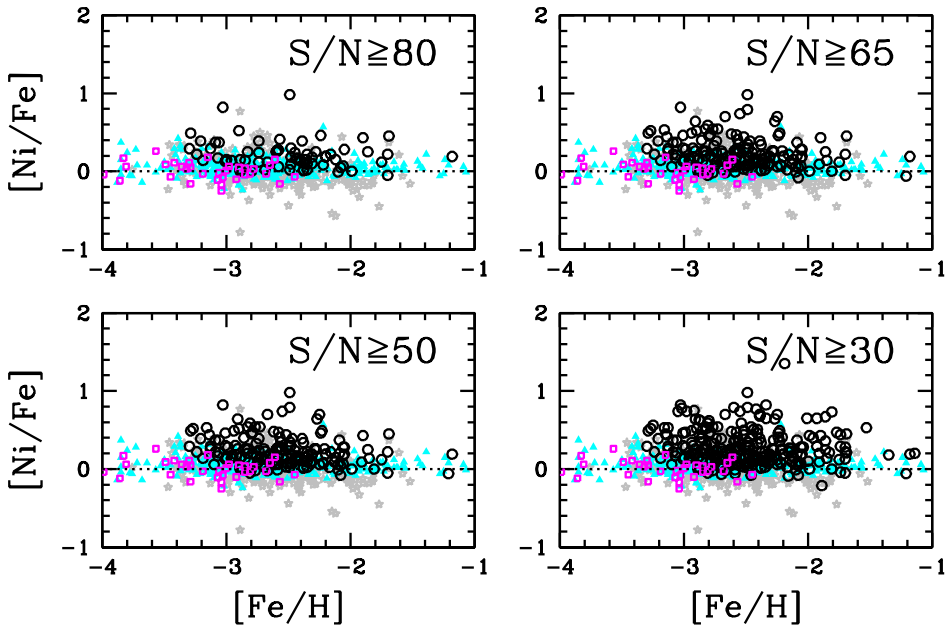

Figure 4.14 [Ni/Fe] plotted against [Fe/H] for four S/N cuts. The scale on the y-axis spans 3 orders of magnitude. The points, axes, and labels remain the same as Figure 4.6.

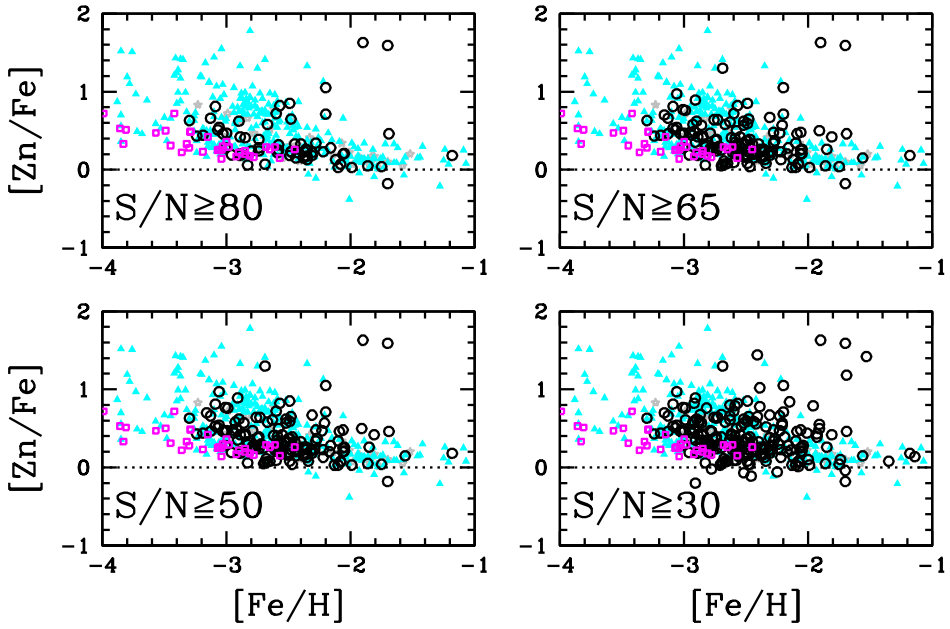

Figure 4.15 [Zn/Fe] plotted against [Fe/H] for four S/N cuts. The scale on the y-axis spans 3 orders of magnitude. The points, axes, and labels remain the same as Figure 4.6.

(2005) who derive 0.01, 0.05, and −0.02 respectively. Much of this discrepancy is due to the availability of lines in the CASH wavelength regime. McWilliam et al. (1995) indicated that Ni abundances are difficult to derive in snapshot-quality spectra. Many of these lines are quite weak, thus a large dispersion is seen in our results. The average value over the full sample is [Ni/Fe] = 0.29±0.25, while the weighted mean gives [Ni/Fe] = 0.19±0.01. The lower weighted mean value is in better agreement with the Cayrel et al. sample, though it is still quite high.

The Zn abundance is determined via spectral synthesis of the λ4722 and λ4810 lines. We show the [Zn/Fe] ratio plotted against [Fe/H] in Figure 4.15. Zn provides a challenge in that only two lines are available and the λ4722 line can be too weak to measure. Abundances were determined for 208 stars in the sample. Visually, the S/N $\geq$ 80 stars of the CASH sample match well with the Cayrel et al. (2004) set. The Roederer et al. (2014) and Barklem et al. (2005) studies both show scatter, but all four studies show an increasing [Zn/Fe] ratio with decreasing metallicity. For the S/N $\geq$ 80 stars, the slope of this relation is -0.27. The trend of increasing [Zn/Fe] is preserved in the CASH sample, albeit with a large dispersion. The mean value over the full sample is [Zn/Fe] = 0.39$\pm$0.29 with the weighted mean value being 0.24$\pm$0.01. Again, the weighted mean much better matches the Cayrel et al. abundances when the relation between Zn and metallicity is considered, seen in Figure 4.15.

In general, the dispersions of the Fe-peak elements are larger than those of the $\alpha-$elements. This is likely due to the number of available lines and their locations, as Fe-peak elements tend to have fewer available features that are often in the blue portion of the spectrum.

4.6.6 Neutron-Capture Elements

The Sr abundance is determined via spectral synthesis of the λ4215 Sr II line in 239 stars. These abundance ratios are shown in Figure 4.16. The stronger λ4077 line is not available in the CASH spectra. Sr is produced primarily in the s-process (Arlandini et al., 1999). The spread in [Sr/Fe] from

our S/N$\geq$ 80 spectra is larger than that of Cayrel et al. (2004) and Roederer et al. (2014). Over the full CASH sample we find a similarly large spread in [Sr/Fe] as in [Ba/Fe], spanning 5 dex with a dispersion of 0.70, as seen in Figure 4.16. The S/N of the Sr λ4215 line is quite low, hence the large spread observed in the [Sr/Fe] ratios derived from the CASH spectra includes observational scatter as well as intrinsic scatter.

The Y abundance is determined via spectral synthesis of the λ4883 and λ5087 lines and was determined in 145 stars, as shown in Figure 4.17. When we make the S/N$\geq$ 80 cut, it is difficult to make meaningful comparisons between the other three samples, as there are too few stars with [Y/Fe]. However, over the full CASH sample, the average value [Y/Fe] is 0.01$\pm$0.45, while the weighted mean is -0.02 ± 0.01. Again, the weighted mean is consistent with the François et al. (2007) sample. As with Sr and Ba, Y is primarily created in the s-process.

The Zr abundances are determined via spectral synthesis of the λ4208 line. In Figure 4.18, we show the [Zr/Fe] values plotted against [Fe/H]. This feature is weak and thus is not detected in many stars. We determined abundances for 30 stars. Generally, these stars were the ones in which [Ba/Fe] > 0.50. It is difficult to compare these values to those of other studies, as we can only detect Zr in the stars with relatively large abundances. This biases our sample and artificially reduces the spread in our abundances via sample selection.

Ba abundances were determined via synthesis of the Ba II lines λ4554

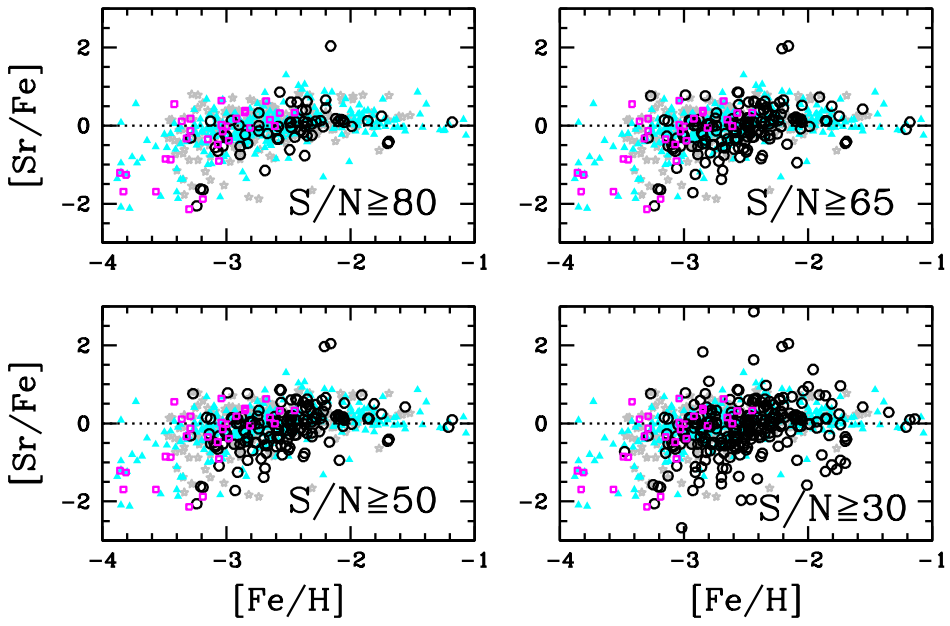

Figure 4.16 [Sr/Fe] plotted against [Fe/H] for the CASH sample and from the François et al. (2007) (magenta squares), Barklem et al. (2005) (grey stars), and Roederer et al. (2014) (cyan triangles). On the y-axis of each plot is the [Sr/Fe] element and on the x-axis is [Fe/H]. In each panel, we denote the S/N cut made on the CASH data. In the upper panels, we show the cut at S/N$\sim$ 80 and $\sim$ 65 on the left and right, respectively. In the lower panels, we show the S/N cut at $\sim$ 50 on the left and $\sim$ 30 on the right. The cut at S/N $\sim$ 30 represents the lowest S/N value for which we could reliably and consistently determine abundances. This configuration of symbols, symbol colors, axes, and S/N cuts is consistent in each of the 3 subsequent figures.

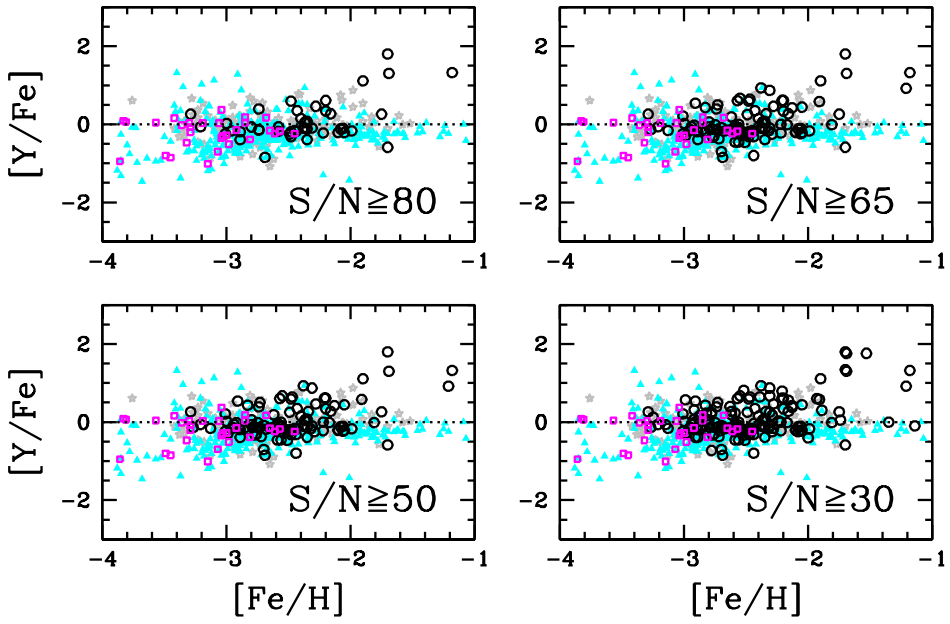

Figure 4.17 [Y/Fe] plotted against [Fe/H] for four S/N cuts. The scale on the y-axis spans 5 orders of magnitude. The points, axes, and labels remain the same as Figure 4.16.

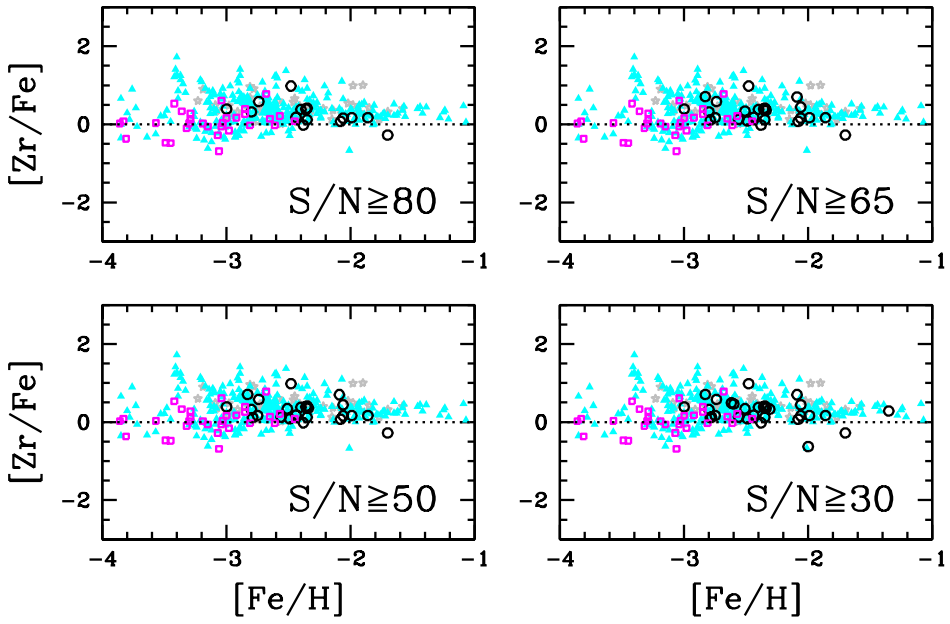

Figure 4.18 [Zr/Fe] plotted against [Fe/H] for four S/N cuts. The scale on the y-axis spans 5 orders of magnitude. The points, axes, and labels remain the same as Figure 4.16.

λ4934, λ5853, λ6141, and λ6496 lines, measured in 259 stars. The [Ba/Fe] ratio is plotted against [Fe/H] in the bottom panel of Figure 4.19. The dispersion in [Ba/Fe] = 0.69 and the values span 5 dex of magnitude. This dispersion remains roughly consistent for all S/N cuts. The spread in the [Ba/Fe] ratios generally matches that of François et al. (2007) and Roederer et al. (2014). The spread in Barklem et al. (2005) is slightly larger than in our sample, skewing towards higher [Ba/Fe], though it is notable that the HERES survey was set up to detect stars with r-process enhancement. Ba is often used as an indicator for s-process enhancement, though it is also produced in the r-process. Here, we designate Ba as the indicator of general neutron-capture enhancement, as the prominent λ4554 feature is generally available to measure. In this sample, we find that $\sim 10\%$ of the stars have [Ba/Fe]> 0.5.

For those stars with [Ba/Fe] > 0.5, we evaluated the [X/Fe] ratios for Ce, Nd, Sm, and Eu. When compared to studies such as François et al. (2007), all of these other elements show spuriously large abundances. We ascribe this to the fact that many of these lines are to weak to be reliably measured in the snapshot spectra. Also, the stars with [Ba/Fe] >0.5 are also the ones that tend to have higher [C/Fe] ratios, thus the small features of Ce, Nd, Sm, and Eu are often blended with C in a way that is not easily resolved by our machinery. Hence, we treat these abundances for Ce, Nd, Sm, and Eu as simply indicating that these elements have been detected. Unfortunately, there is no reliable r-process element that can be measured in these snapshot spectra, so our assessment of these Ba-rich metal-poor stars is that they have

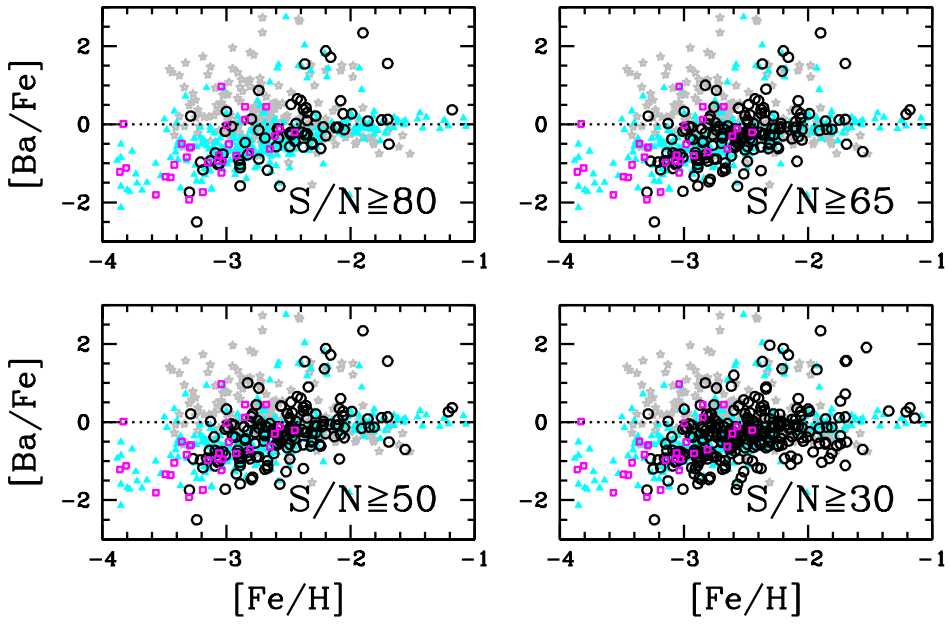

Figure 4.19 [Ba/Fe] plotted against [Fe/H] for four S/N cuts. The scale on the y-axis spans 5 orders of magnitude. The points, axes, and labels remain the same as Figure 4.16.

neutron-capture element enhancement and some of them also appear to be C-enhanced.

4.7 Comparision to Literature Sample

In Section 4.6 we presented the comparison of the CASH sample abundance results to the studies of Cayrel et al. (2004), Barklem et al. (2005), and Roederer et al. (2014). In order to better understand the systematic differences between the studies, and importantly, the constraints placed on the results of the CASH sample due to the use of snapshot spectra, we compare a set of stars that are in common with Roederer et al.. In Table 4.9, we compare the stellar parameters and the overall [X/Fe] abundances derived from the CASH snapshot spectrum and Roederer et al.. The [X/Fe] column refers to the mean value for Δ[X/Fe], where Δ refers to CASH $-$ Roederer et al. for this and all subsequent comparisons. In Table 4.10, we compare the difference between the derived values for a given element over the common stars. In Figure 4.20, we show the HR diagram for the common stars using the stellar parameters derived from the CASH spectra and from Roederer et al..

Overall, we find that on average the stellar parameters differ by $\Delta T_{\rm eff}$ = 237 K, $\Delta \log g = 0.34$, $\Delta\xi = 0.27 {\rm kms}^{-1} = 0.27$, and Δ[Fe/H] = 0.22. This difference in stellar parameters is expected, as the Roederer et al. (2014) study used spectroscopic stellar parameters and our parameters were adjusted to better reflect stellar parameters derived from photometry. Photometric temperatures are hotter than spectroscopic temperatures and thus the CASH study

Table 4.9. Stellar Parameter Comparision with Roederer et al. (2014)

Star	ΔT_{eff}[a] K	$\Delta \log g$	$\Delta\xi$ kms^{-1}	Δ[Fe/H] dex	Δ[X/Fe] dex
22183−00031	175	0.30	0.30	0.21	0.07
22878−00101	312	0.20	0.35	0.15	0.11
22952−00015	606	1.60	0.02	0.76	0.37
22957−00022	156	0.25	0.30	0.08	0.14
22957−00027	327	−0.10	0.19	0.43	0.20
22965−00016	228	−0.05	0.31	0.11	0.00
29502−00092	340	0.60	0.29	0.28	0.14
G 090−003	101	−0.15	0.30	−0.05	0.06
G 146−076	99	0.30	0.39	0.05	0.08
HD 108317	220	0.40	0.21	0.16	0.06

[a]Δ refers to CASH− Roederer et al. for all quantitites.

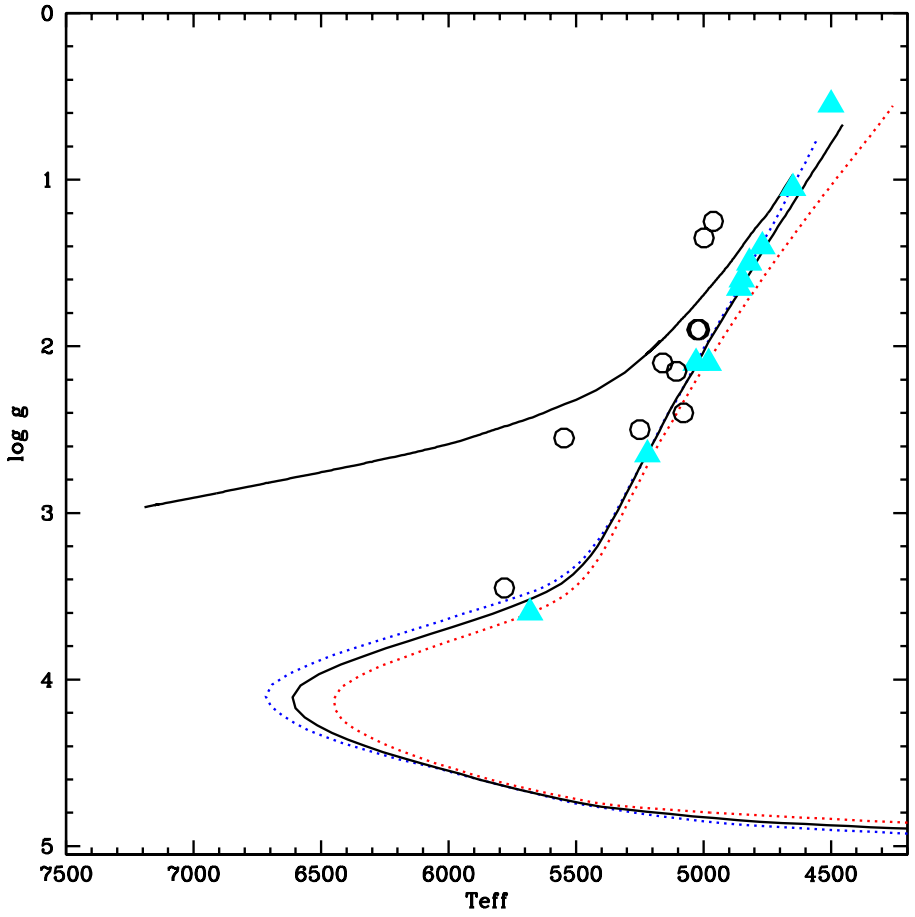

Figure 4.20 HR diagram of the 10 CASH sample stars (black open circles) in common with Roederer et al. (2014) (cyan filled triangles). Plotted are the Yale-Yonsei isochrones (Kim et al., 2002; Green et al., 1984) for 12 Gyr, at [Fe/H] = −2.0 (red line), −2.5 (black line), and −3.0 (blue line, as well as a horizontal-branch mass track from Cassisi et al. (2004).

presents higher metallicities as well. We also looked at the overall [X/Fe] ratios for each star. This quantity was calculated by averaging over Δ[X/Fe] for every element in a given star. We find mean Δ[X/Fe] = 0.12 for the 10 common stars over 11 elements. We then investigated each element individually. For elements with many lines covering the wavelength regime of the snapshot spectra, we find good agreement. The Mn abundances for the 10 common stars are significantly higher than those of Roederer et al.. We found this same trend over the whole sample, where the hyperfine structure needs to be better accounted for in the CASH analysis. Overall, we see that the CASH abundances are best interpretted as a whole, rather than individually. However, the agreement with Roederer et al. is encouraging, especially for Ba and Sr, which provide the best means for probing neutron-capture enhancement in the CASH sample.

4.8 Interesting Stars

4.8.1 Li Giant

We identified one previously undiscovered Li-enhanced giant in our sample. In this star, 53757−2316−395, A(Li) = 2.98, which is higher than the Spite plateau (Spite & Spite, 1982) value of 2.1. Even more notable, the stellar parameters indicate that the star is on the giant branch, thus it has undergone dredge up events and therefore its abundance is not reflective of the primordial Big Bang nucleosynthesis Li abundance. Hence, its Li must be produced during the lifetime of the star. One suggested Li production source

Table 4.10. Abundance Ratio Comparision with Roederer et al. (2014)

[X/Fe]	Δ[X/Fe][a] dex	$\sigma_{\Delta[X/Fe]}$ dex	MedianΔ[X/Fe] dex	N
[Mg/Fe]	−0.05	0.19	−0.02	10
[Ca/Fe]	−0.14	0.22	−0.08	10
[Sc/Fe]	−0.04	0.20	0.01	9
[Ti/Fe]	0.06	0.09	0.07	10
[Mn/Fe]	0.21	0.17	0.19	9
[Ni/Fe]	0.27	0.29	0.27	10
[Zn/Fe]	−0.02	0.22	−0.01	10
[Sr/Fe]	0.26	0.67	−0.05	10
[Y/Fe]	0.67	0.52	0.58	7
[Zr/Fe]	0.10	0.06	0.09	3
[Ba/Fe]	0.15	0.40	0.08	10

[a]Δ refers to CASH− Roederer et al. for all quantites.

is the Cameron-Fowler mechanism (Cameron & Fowler, 1971; Marigo et al., 2013). The [Ba/Fe] ratio is 0.80 in 53757−2316−395, while the [C/Fe]$\sim$ 0, thus it is not a CEMP star. One possibility is that it is an r-process enhanced giant.However, the S/N is too low in the blue to measure an [Eu/Fe] ratio. A similar star, HKII 17435−00532, was presented as part of Roederer et al. (2008), which has A(Li) = 2.1 and is also on the giant branch. However, HKII 17435−00532 is a CEMP-sA star, with [C/Fe] = 0.7. Follow up high-resolution observations of 53757−2316−395 would allow for a more precise determination of the stellar parameters. The C^{12}/C^{13} ratio could also be derived, which would better indicate the evolutionary status. It has been suggested (e.g., Kirby et al. 2012) that Li-enhancement is an extremely brief, though normal, stage of stellar evolution such that Li giants are exceedingly rare. A better understanding of the evolutionary stage of these stars would aid in testing this hypothesis.

4.8.2 CEMP Stars

CEMP stars are notoriously difficult to measure in an automated way because the C bandheads make continuum determination problematic and lines across the spectrum can be heavily blended with C features. For this reason Barklem et al. (2005) omitted CEMP stars from their initial analysis. Due to the way in which Robospect determines the continuum level, the equivalent widths of CEMP stars may be unreliable. HE 0414−0343 is a CEMP-sC star that was previously analyzed as a part of the CASH series. From a high-

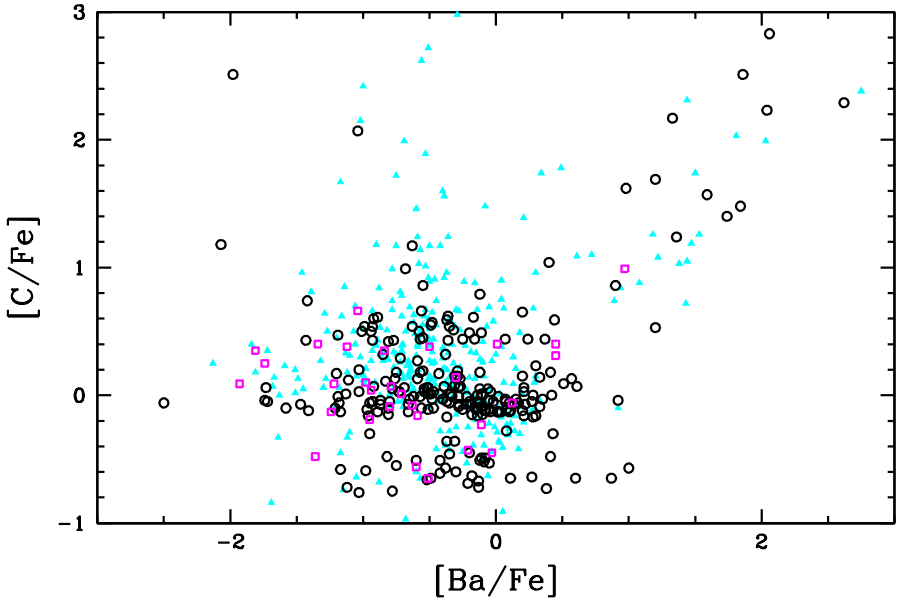

Figure 4.21 [Ba/Fe] plotted against [C/Fe] for the CASH sample (open black circles) plotted with the stars of Cayrel et al. (2004); François et al. (2007) (open magenta squares), and Roederer et al. (2014) (cyan filled triangles).

resolution spectrum and manual equivalent width measurements, its stellar parameters are derived as $T_{eff} = 4863$, $\log g = 1.25$, $v_{mic} = 2.2$ [Fe/H] $=-2.25$, determined from Fe I and Fe II lines and applying the temperature adjustment. In Figure 4.21, we show the [Ba/Fe] plotted against [C/Fe] for our sample and for those of Cayrel et al. (2004); François et al. (2007) and Roederer et al. (2014). Stars in the CASH sample (black circles) with [C/Fe] $= -1.05$ represent upper limits. The distribution of the CASH sample matches well with Roederer et al.. The spread in [C/Fe] ratios is much lower in Cayrel et al..

Table 4.11. Carbon-Enhanced Metal-Poor Stars

Star	[C/Fe]	Ba/Fe	[Fe/H]
HKII 16548−03778	2.23	2.04	−1.70
HKII 16942−01372	2.29	2.62	−1.90
HKII 17435−00532	1.04	0.4	−2.43
HKII 22183−00015	2.51	1.86	−2.20
HKII 22957−00027	2.51	−1.98	−2.57
HKII 29502−00092	1.18	−2.07	−2.92
HKII 30301−00015	2.17	1.33	−2.21
HKII 30312−02585	1.24	1.36	−2.37
51912−0468−209[a]	2.23	···	−2.64
52972−1213−507	1.69	1.2	−1.70
53090−1600−378[a]	1.91	···	−1.68
53384−2040−170	1.48	1.84	−2.31
54368−2803−459[a]	2.03	···	−2.34
54379−2308−227[a]	1.74	···	−1.66
54507−2941−222	2.07	−1.04	−2.14
54559−2950−466[a]	1.82	···	−1.77
54876−3005−348	0.99	−0.68	−2.24

However, despite the difficulty in measuring the stellar parameters and [C/Fe] ratio in these stars, it is quite easy to identify them, as the molecular C features can be spotted even in medium resolution spectra. The most C-rich stars also show strong C_2 features, notably at the λ5165 bandhead. We present the stars in Table 4.11 as CEMP stars, which merit follow up observations for a more precise and detailed analysis. Several of these stars do not have a well-determined set of stellar parameters and hence we did not calculate a Ba abundance. We have included preliminary C abundances for these stars.

Table 4.11 (cont'd)

Star	[C/Fe]	Ba/Fe	[Fe/H]
G108−033[a]	1.08	···	−2.55
HE 0414−0343	1.4	1.74	−2.16
S2_0592−207[a]	1.54	···	−1.45
S2_0742−484	1.62	0.98	−1.74
S3_1041−232	1.57	1.59	−1.93
S4_1571−617	1.17	−0.63	−1.70
S5_1659−091	0.86	−0.55	−1.96
SEG2183−549	2.83	2.06	−1.71

[a]Stellar parameters did not converge for these stars, hence they are not included in the full 262 star sample.

4.8.3 Double-Lined Spectroscopic Binary Stars

In early stages of data reduction, 7 stars were discovered to be double-lined spectroscopic binary (DLSB) stars. These stars are 52051−0623−261, 52995−1180−283, 53855−2491−389, S2_0592−207, HE 0434+0105, HE 1120−0153, and HE 1213+0247. Consequently, no stellar parameters nor abundances were determined for these stars. DLSB stars have two stellar spectra overlaid, thus special care must be taken to disentangle them in order to provide an accurate abundance analysis. Thompson et al. (2008) presents a careful decomposition and analysis of a C-enhanced DLSB pair. In order to analyze the pair, a MOOG module was created to calculate both spectra simultaneously. These DLSB stars, especially the HES stars, are good candi-

dates for high resolution observations to perform a similar analysis to better understand the mostly unexplored topic of metal-poor binary star abundances.

4.8.4 Extremely Metal-Poor Stars

Extremely metal-poor stars or those with [Fe/H]< -3 are of particular interest to those investigating the nucleosynthesis of the early universe. These stars formed in metal-poor gas that was previously enriched by, perhaps, only a single supernova outburst. Thus, EMP stars offer an opportunity to study individual nucleosynthetic events. Studies such as Hollek et al. (2011) and Yong et al. (2013) aim to discover these rare, old stars. In the CASH sample, we found 27 such stars. We additionally have 27 other stars with $-3.0 \leq$ [Fe/H]< -2.85. While not technically part of the EMP population, these stars fall within a standard deviation of the EMP metallicity criterion. Several of these stars were analyzed and presented as part of Hollek et al., but due to the effective temperature adjustment, the stellar parameters and thus [Fe/H] values for these stars have been re-calculated here. The new metallicities are higher by 0.12 dex, as a result of the higher effective temperature. However, alternate stellar parameter determinations may yield a cooler effective temperature and thus lower [Fe/H] values. Beyond their low metallicities, these stars are chemically diverse. As a few are CEMP, some have neutron-capture abundance enhancement, and some are both, that is CEMP stars with neutron-capture enhancement. In Table 4.12, we present [Fe/H] values and selected elemental abundances for all the EMP stars of the CASH sample.

Table 4.12. EMP Stars of the CASH Sample with [Fe/H] and Selected Abundance Ratios

Star	[Fe/H]	[C/Fe]	[α/Fe]	[Cr/Fe]	[Ba/Fe]
30325−00094	−3.30	−0.04	0.35	−0.30	−1.74
22183−00031	−3.29	0.06	0.38	−0.33	0.21
54095−2622−483	−3.27	−1.07	0.22	−0.20	−0.94
54441−2309−290	−3.25	0.17	0.37	0.02	−1.20
16084−00160	−3.24	−0.06	0.11	−0.29	−2.50
30312−03416	−3.21	−0.11	0.70	0.12	−0.97
16548−02637	−3.19	−0.13	0.21	−0.27	−1.17
16541−04917	−3.16	−0.05	0.46	−0.27	−0.93
22878−00101	−3.15	−0.10	0.39	−0.04	−0.56
HE 0013−0257	−3.14	0.03	0.46	−0.23	−0.73
53729−1914−357	−3.13	−1.07	0.15	−0.05	−1.51
HE 2138−0314	−3.13	0.54	0.26	−0.26	−0.93
16080−00093	−3.10	−0.57	0.41	0.11	−0.38
22957−00022	−3.09	0.03	0.35	−0.11	−0.73
HE 0324+0152	−3.09	0.01	0.48	−0.13	−1.13
16080−01635	−3.07	−0.76	0.27	−0.08	−1.03
HE 0311−1046	−3.06	−0.75	0.02	−0.48	−0.78

Table 4.12 (cont'd)

Star	[Fe/H]	[C/Fe]	[α/Fe]	[Cr/Fe]	[Ba/Fe]
HE 2123−0330	−3.06	0.50	0.39	−0.16	−1.01
16469−00075	−3.05	0.43	0.27	−0.08	−0.77
HE 2144−0829	−3.03	0.13	0.44	−0.23	−0.76
54368−2799−502	−3.02	−0.16	0.20	−0.14	−0.96
17586−03935	−3.01	−0.07	0.46	−0.11	−0.18
29516−00041	−3.01	−0.05	0.19	0.09	−1.72
HE 2123−0329	−3.01	0.32	0.42	−0.07	−0.85
HE 0420+0123	−3.00	0.14	0.41	−0.16	0.33
16542−00519	−2.99	−0.05	0.38	−0.12	−0.14
51820−0400−247	−2.99	0.11	0.19	−0.15	−0.83
16936−02204	−2.98	0.00	0.35	0.00	−0.14
HE 2324−0215	−2.96	−0.53	0.41	−0.15	−0.05
30325−00028	−2.95	0.62	0.44	−0.10	−0.36
53431−2054−033	−2.94	−0.58	0.23	−0.24	−1.17
54833−3183−489	−2.94	−0.11	0.33	−0.14	−0.08
29502−00042	−2.93	0.07	0.20	−0.18	−0.39
22952−00015	−2.92	−1.07	−0.15	−0.41	−0.73

Table 4.12 (cont'd)

Star	[Fe/H]	[C/Fe]	[α/Fe]	[Cr/Fe]	[Ba/Fe]
29502−00092	−2.92	1.33	0.37	−0.15	−1.33
HE 1311−0131	−2.92	−0.05	0.23	−0.24	−0.80
22175−00007	−2.91	0.29	0.40	−0.14	−0.72
53741−1502−261	−2.91	0.42	0.38	−0.05	−0.81
54802−3157−140	−2.91	0.47	0.25	−0.33	−1.19
HE 0013−0522	−2.90	0.60	0.36	−0.12	−0.92
16934−00002	−2.89	−0.10	0.68	−0.01	−1.58
17576−00074	−2.89	0.20	0.35	−0.18	−1.03
HE 0432−1005	−2.89	0.12	0.19	−0.20	−1.11
53299−1961−164	−2.88	0.18	0.44	0.22	−0.75
53401−2050−406	−2.88	0.43	0.44	−0.13	−1.43
g195−035	−2.88	0.07	0.33	−0.03	−0.92
16034−02049	−2.87	0.19	0.24	−0.05	−0.29
54860−3230−532	−2.87	0.54	0.19	−0.02	−0.99
SEG2183−228	−2.87	−0.30	0.52	0.19	0.43
54208−2714−429	−2.86	−0.07	0.27	−0.37	−1.47
HE 2304−0024	−2.86	0.79	0.38	−0.02	−0.12

Table 4.12 (cont'd)

Star	[Fe/H]	[C/Fe]	[α/Fe]	[Cr/Fe]	[Ba/Fe]
16548−00446	−2.85	0.03	0.38	−0.14	−0.47
16550−02649	−2.85	0.17	0.44	−0.05	−0.43
54524−2808−510	−2.85	0.61	0.30	0.23	−0.17
22886−00042	−2.83	−0.01	0.34	−0.11	−0.22
29516−00024	−2.83	0.05	0.42	−0.10	−0.78
52643−1078−265	−2.83	−0.07	0.28	−0.06	−0.87
HE 1523−0901	−2.83	−0.57	0.31	0.00	1.00
22965−00016	−2.82	−0.48	0.37	−0.18	−0.82
54515−2939−414	−2.82	0.65	0.40	−0.25	0.20
16934−00060	−2.81	0.50	0.29	−0.12	−0.94
g018−021	−2.81	−0.13	0.42	−0.01	0.01
53384−2040−407	−2.80	−1.07	0.10	−0.48	−1.47
54629−2178−485	−2.80	0.43	0.41	0.04	−0.36
bs17569−049	−2.80	−0.07	0.42	−0.20	0.14
16029−05926	−2.79	−0.12	0.15	−0.12	−1.41
HE 0117−0201	−2.79	−0.16	0.40	−0.11	0.21
SEG2380−094	−2.79	−0.05	0.23	−0.10	−0.02

Table 4.12 (cont'd)

Star	[Fe/H]	[C/Fe]	[α/Fe]	[Cr/Fe]	[Ba/Fe]
16078−00870	−2.78	−0.15	0.22	−0.22	−0.81
30306−00132	−2.78	0.15	0.47	−0.20	0.20
HE 1225+0155	−2.78	0.01	0.60	−0.17	−0.11
15623−01251	−2.77	0.05	0.31	−0.10	−0.54
31069−00064	−2.77	0.07	0.45	0.08	−0.27
54065−2441−309	−2.76	0.59	0.23	−0.35	0.44
HE 0015+0048	−2.76	0.61	0.30	−0.09	−0.89
17569−00049	−2.75	−0.13	0.44	−0.09	0.04
17440−01458	−2.74	−0.11	0.43	−0.11	−0.15
30329−00004	−2.74	−0.13	0.37	−0.25	−0.89
54368−2679−217	−2.74	0.32	0.28	0.05	−0.38
HE 0403−0954	−2.74	−0.65	0.37	0.03	0.87
17435−00024	−2.73	0.01	0.22	−0.18	... [a]
HE 2253−0849	−2.72	−1.07	0.31	−0.13	−0.05
53770−2387−530	−2.71	−0.59	0.24	−0.08	−0.98
30301−00094	−2.70	0.15	0.48	−0.08	−0.31
53740−2337−168	−2.70	0.06	0.34	−0.16	−0.52

Table 4.12 (cont'd)

Star	[Fe/H]	[C/Fe]	[α/Fe]	[Cr/Fe]	[Ba/Fe]
53759−2380−094	−2.70	−0.05	0.07	−0.15	−0.37
HE 2238−0131	−2.70	−0.65	0.27	−0.35	−0.49
G193−026	−2.69	−0.10	0.10	−0.01	−1.21
HE 2125−0417	−2.69	−0.46	0.24	−0.24	−0.35
22179−01563	−2.68	−0.51	0.30	−0.16	−0.12
16541−00909	−2.67	−1.07	0.40	0.11	−0.99
HE 2325−0233	−2.67	−0.06	0.30	−0.15	−1.18
SEG2387−530	−2.67	−0.72	0.24	−0.19	−1.12
53446−2053−188	−2.66	−0.10	0.22	−0.29	−0.47
HE 2319−0303	−2.65	0.03	0.42	−0.06	−0.04

[a]Ba abundance was unable to be measured in this star due to cosmic ray lines in the spectrum.

4.9 Conclusions

We present results for 262 stars as part of the Chemical Abundances of Stars in the Halo project. The stellar parameters and abundances for these stars were derived from snapshot spectra observed with the HRS on the Hobby-Eberly Telescope at McDonald Observatory. We measured equivalent widths for the stars using the automated equivalent width measurement software Robospect. We then used these equivalent widths in Cashcode, a stellar parameter and abundance pipeline. The equivalent widths of Ti I, Ti II, Fe I, and Fe II were used to derive stellar parameters. The effective temperatures were determined using the temperature calibration of Frebel et al. (2013) and the $\log g$ was determined from the ionization balance of Fe I/Fe II and Ti I/Ti

II, with the microturbulence value based on the derived $\log g$. These stellar parameters were then used to create Kurucz model atmospheres and which were then used to derive abundances.

We derived abundances via equivalent width measurements of O I, Mg I, Ca I, Sc II, Ti I, Ti II, Cr I, Mn I, Fe I, Fe II, and Ni I. We determined abundances for Li, C, Zn I, Sr II, Y II, Zr II, and Ba II via spectral synthesis. We find enhancements compared to the solar ratios for the $\alpha-$elements of O, Mg, Ca, and Ti. We find deficiencies for the Fe-peak elements of Sc, Cr, and Mn. We compared the [X/Fe] ratios of our sample against three different studies: Cayrel et al. (2004), Barklem et al. (2005), and Roederer et al. (2014). We find that our results are generally in agreement with these samples. Differences include Mg, Sc, and Ni. These differences are likely due to multiple reasons, most importantly the lower resolution of our spectra as compared with the other studies and the spectral lines available for measurement.

Within the sample, we identified several groups of chemically unique stars. These include a Li-enhanced giant star, with A(Li) = 2.98. This star is similar to another star that was earlier identified within the CASH data, HKII 17432-00035 (Roederer et al., 2008). We also identified several CEMP stars and present preliminary abundances. The CASH machinery is not well-suited to analyze these stars, but they are easy to spot from manually inspecting their spectra. We determine a carbon-enhancement frequency of $\sim 5\%$ over the full sample. We also find a group of stars with neutron-capture abundance enhancements and find that $\sim 10\%$ of our sample is chemically anomalous, ex-

hibiting abundance enhancements in Li, C, or the neutron-capture elements. We also present a list of stars with [Fe/H]< -3.00, as EMP candidates. We also present another list of stars with [Fe/H]< -2.65 as potential EMP stars, given that the uncertainty in our [Fe/H] values is 0.35. Finally, we present a list of double-lined spectroscopic binary stars, for which no further analysis has been performed, but they provide an interesting opportunity to understand metal-poor binary stars.

The Hobby-Eberly Telescope (HET) is a joint project of the University of Texas at Austin, the Pennsylvania State University, Stanford University, Ludwig-Maximilians-Universität München, and Georg-August-Universität Göttingen. We are grateful to the Hobby-Eberly staff for their assistance in obtaining the data collected for this paper. We appreciate useful conversations with Kyle Penner and Harriet Dinerstein.

Chapter 5

The Chemical Abundances of Stars in the Halo (CASH) Project. III. A New Classification Scheme for Carbon-Enhanced Metal-poor Stars with S-process Element Enhancement

We present a detailed abundance analysis of 23 elements for a newly discovered carbon-enhanced metal-poor (CEMP) star, HE 0414−0343, from the Chemical Abundances of Stars in the Halo (CASH) Project. Its spectroscopic stellar parameters are $T_{eff} = 4863\,\mathrm{K}$, $\log g = 1.25$, $\xi = 20\,\mathrm{km\,s^{-1}}$, and [Fe/H] = −2.24. Radial velocity measurements covering seven years indicate HE 0414−0343 to be a binary. HE 0414−0343 has [C/Fe] = 1.44 and is strongly enhanced in neutron-capture elements but its abundances cannot be reproduced by a solar-type s-process pattern alone. It could be classified as "CEMP-r/s" star but we find that no r-process component is required as explanation of this and other similar stars classified as "CEMP-s" and "CEMP-r/s" stars. Rather, based on comparisons with AGB star nucleosynthesis models, we suggest a new physically-motivated classification scheme, especially for the still poorly-understood "CEMP-r/s" stars. Importantly, it reflects the continuous transition between these so-far distinctly treated subgroups: CEMP-sA,

CEMP-sB, and CEMP-sC. The [Y/Ba] ratio parametrizes the classification and can thus be used to classify any future such stars. Possible causes for the transition include the number of thermal pulses the AGB companion underwent and the effect of different AGB star masses on their nucleosynthetic yields. We then speculate that higher AGB masses may explain "CEMP-r/s" or now CEMP-sB and CEMP-sC stars, whereas less massive AGB stars would account for "CEMP-s" or CEMP-sA stars. Based on a limited set of AGB models, we suggest the abundance signature of HE 0414−0343 to have come from a $> 1.3 M_{\odot}$ mass AGB star and a late-time mass transfer, thereby making it a CEMP-sC star.

5.1 Introduction

Metal-poor Population II (Pop II) stars were formed from gas that contained the nucleosynthetic signatures of the first chemical enrichment events and thus preserve this information in their atmospheres until today. By understanding the chemical abundance patterns of metal-poor stars, we can probe the formation, initial mass function, and fates of the first stars. Altogether, metal-poor stars allow for a detailed reconstruction of the chemical enrichment sources and processes operating in the early universe and leading to the chemical evolution of the Milky Way: from core collapse supernovae of the earliest, massive stars, to the later contributions from the nucleosynthesis of lower-mass, evolved asymptotic giant branch (AGB) stars, and even the type Ia supernovae.

Many metal-poor stars have prominent molecular carbon features in their spectra. The G-band feature near 4290 Å, the bandhead at 4313 Å, and the smaller band near 4323 Å are all CH molecular features. These all become strong to the point of saturation in the presence of large amounts of C. There are CN features across the spectrum, including a prominent feature near 8005 Å. The C_2 molecule is not often detected in metal-poor stars with [C/Fe][1] ratios near the solar ratio; however, in stars with large C abundances, the bandheads near λ4735, 5165, and 5635 often become strong enough from which to derive a [C/Fe] ratio.

Beers & Christlieb (2005) define a carbon-enhanced metal-poor (CEMP) star to be any metal-poor star with [C/Fe] ≥ 1. Aoki et al. (2007) presented a revised CEMP definition of [C/Fe] > 0.7 for stars with $\log(L/L_\odot) \leq 2.3$ and [C/Fe] $> 3 - \log(L/L_\odot)$ for stars with $\log(L/L_\odot) \geq 2.3$. The CN cycle greatly reduces the amount of C in the surface composition of a star over the course of the later stages of stellar evolution on the giant branch. Hence this definition allows for more evolved stars with lower C abundances to be considered in the study of C in the early universe.

CEMP stars can be subdivided into distinct chemical subgroups. The Masseron et al. (2010) study provides a comprehensive description and study of the different types of CEMP stars, which we will briefly outline here. CEMP-no stars are CEMP stars with normal neutron-capture abundances (indicated

[1] [A/B]= $\log(N_A/N_B) - \log(N_A/N_B)_\odot$ for N atoms of elements A, B, e.g., [Fe/H] = -2.0 is 1/100 of solar Fe abundance.

by [Ba/Fe] $\leq$ 0) and otherwise typical abundances for metal-poor stars. The three most iron-poor stars discovered are CEMP-no stars (Christlieb et al., 2002; Frebel et al., 2005; Keller et al., 2014). The majority of CEMP stars have neutron-capture abundance enhancements. Among these, CS 22892−052 is the only one discovered to date with a pure rapid neutron-capture (r-) process abundance pattern (Sneden et al., 2000). The largest subgroup of CEMP stars is the CEMP-s stars (Masseron et al., 2010), which contain enhancements in the slow neutron-capture (s-) process elements. Finally, so-called CEMP-r/s stars are another CEMP group with neutron-capture overabundances but their abundance distributions do not display either a pure r- or pure s-process pattern (Bisterzo et al., 2009); both processes have been suspected to have contributed.

The designation of the CEMP-"r/s" stars has undergone much evolution. The term was introduced in Beers & Christlieb (2005) as "CEMP-r/s". This term referred to stars with [C/Fe] >1.0 and 0< [Ba/Eu] < 0.5. Jonsell et al. (2006) used the term "r+s" to refer to stars with [Ba/Fe] >1.0 and [Ba/Eu] >0 or [Eu/Fe] >1 omitting the Ba criteria altogether, making no mention of the C abundance in the definition criteria, but noting that all of these r+s stars had significant C enhancement. Masseron et al. (2010) essentially combined the two previous definitions into the "CEMP-rs" designation for stars with [C/Fe] >0.9 and [Eu/Fe] >1 and [Ba/Eu] <0, or [C/Fe] >0.9 and [Ba/Fe] >2.1. The [Ba/Fe] criterion allowed for stars with no Eu abundance to also be classified. The Jonsell et al. (2006) designation was presented

along with abundances for HE 0338−3945, an r+s star near the main sequence turn-off with [Fe/H] = −2.42. They presented nine possible scenarios for its formation, including the suggestion that these stars themselves formed from an r-enhanced gas cloud, although this scenario would be difficult to confirm observationally. Masseron et al. (2010) aimed to disentangle the contributions of AGB nucleosynthesis to the abundance patterns in CEMP stars by investigating processes that occur during the mass transfer from an AGB binary companion onto the observed CEMP star. No satisfactory solution to explain the abundance patterns of CEMP-r/s stars has been presented thus far.

The s-process occurs in the outer fusion layers of evolved, low-mass AGB stars (e. g., Gallino et al. (1998)) and operates on timescales of tens of thousands of years. Seed nuclei acquire neutrons one at a time and then β-decay as they climb the valley of stability on the chart of the nuclides. Bismuth is the termination point of the s-process. There are three stable peaks in the s-process pattern. They are centered around Sr, Ba, and Pb and these elements are particularly enhanced in s-process enriched metal-poor stars. This enrichment occurs when a low-mass star receives s-process enhanced material from a binary companion that underwent its AGB phase; observed today is the low-mass recipient of the AGB material. Many of these stars, including CEMP-s and CEMP-r/s stars, have been monitored for radial velocity variations and been shown to be binary stars (Lucatello et al., 2005). This principally confirms the mass-transfer scenario for these stars.

The Chemical Abundances of Stars in the Halo (CASH) project is a

study that aims to understand the chemical abundance trends and frequencies of metal-poor halo stars as well as discover individual astrophysically interesting stars, based on the chemical abundances for $\sim$ 500 stars from "snapshot" spectra observed using the Hobby-Eberly Telescope (HET) at McDonald Observatory. The spectra have moderate signal-to-noise ratios ($\sim$65) and resolution (R$\sim$15,000). CEMP and s-process stars make up perhaps $\sim$ 20% of the population of metal-poor stars. The first result from this project, Roederer et al. (2008), was the discovery of a CEMP-r/s giant star, HK II 17435-00532, with an enhanced Li abundance. The second paper, Hollek et al. (2011), presented the calibration of the automated stellar parameter and abundance pipeline, Cashcode, using both the HET snapshot spectra and higher-resolution, higher-S/N Magellan/MIKE spectra of 16 new extremely metal-poor stars to test it, along with the resultant comprehensive abundance analysis of the sample.

In this paper, we discuss HE 0414$-$0343, a CEMP star initially identified in the Bright Metal-Poor Star (BMPS) sample of Frebel et al. (2006) and included in the CASH project for further follow-up observations. This star was initially slated to be part of the sample from Hollek et al. (2011), but was singled out for special attention in order to obtain an even higher-resolution spectrum to better study this unique star. We discuss the observations and binary status for HE 0414$-$0343 in Section 5.2. We present the analysis methods used to determine the stellar parameters and abundances in Section 5.3 and the chemical abundance results in Section 5.4. In Section 5.5 we analyze neutron-

capture abundance ratios. We compare the abundances of HE 0414−0343, as well as those of a literature sample to abundance yields of AGB star models in Section 5.6 and propose a new classification scheme based on our analysis of this star. In Section 5.7, we use the classification to present a comprehensive explanation of the origin of CEMP stars with neutron-capture element enhancement associated with the s-process. We discuss the limitations of our analysis in Section 5.8, and finally summarize our results in Section 5.9.

5.2 Observations

HE 0414−0343 has an R.A. of 04 h 17 m 16.4 s and declination of −03° 36′ 31.″0. Thus, it is accessible from both the northern and southern hemispheres. Four separate spectra were obtained for HE 0414−0343 between 2004 and 2011. A medium-resolution spectrum was observed in September 2004 as part of the the Hamburg/ESO Bright Metal-Poor Star Sample. See Frebel et al. (2006) for details of this observation. A high-resolution spectrum was obtained using the Magellan-Clay Telescope at Las Campanas Observatory using the MIKE instrument (Bernstein et al., 2003) in September 2006. The observation was taken using the 0.″7 slit with 2×2 on-chip binning, yielding a resolution of $R \sim 35,000$ in the blue and 28,000 in the red. MIKE spectra have nearly full optical wavelength coverage from ∼ 3500 - 9000 Å. In October 2008, HE 0414−0343 was observed as part of the CASH project using the fiber-fed High Resolution Spectrograph (Tull, 1998) on the HET at McDonald Observatory. All CASH spectra were obtained with a 2.″0 fiber yielding $R \sim 15,000$.

The 2×5 on-chip CCD binning leads to 3.2 pixels per resolution element. Two CCDs were used to record the red and blue portions of the spectrum, spanning a wavelength range from 4200 - 7800 Å.

The highest resolution spectrum, taken in March 2011, was used for the stellar parameter and chemical abundance determinations. This spectrum was also obtained using the MIKE instrument on the Magellan-Clay Telescope, but taken with a $0\farcs5$ slit. The spectral resolution is $R \sim 56,000$ at 4900 Å and $\sim 37,000$ at 5900 Å as measured from the ThAr frames. Table 5.1 lists the details of the observations for HE 0414−0343. The high resolution spectra for HE 0414−0343 were reduced using an echelle data reduction pipeline made for MIKE[2], initially described by Kelson (2003). We then utilized standard IRAF[3] routines to co-add and continuum normalize the individual orders into a one-dimensional spectrum.

[2]Available at http://obs.carnegiescience.edu/Code/python.

[3]IRAF is distributed by the National Optical Astronomy Observatories, which is operated by the Association of Universities for Research in Astronomy, Inc., under cooperative agreement with the National Science Foundation

Table 5.1. Observations

R	UT Date	UT Time	t_{exp} s	S/N at 5180 Å	Telescope	v_{rad} km s^{-1}
2000	2004 September 20	18:13	120	50	SSO2.3m/DBS	−36
35,000	2006 September 27	9:30	450	65	Magellan-Clay/MIKE	−83.8
15,000	2008 October 10	9:19	239	85	Hobby-Eberly/HRS	4.0
56,000	2011 March 11	00:12	3000	120	Magellan-Clay/MIKE	11.3

5.2.1 Binary Status

We measured the radial velocity of HE 0414−0343 using four independent observations taken over the course of seven years. All of the following radial velocities have the heliocentric correction applied. The radial velocity for the medium resolution spectrum taken in 2004 was determined in Frebel et al. (2006) as $v_{rad/medres} = -36\,\mathrm{km\,s^{-1}}$. We used Robospect (Waters & Hollek, 2013), an automated equivalent width measurement code that can calculate radial velocity shifts in spectra using a cross-correlation method, to determine the radial velocity for the $R \sim 35,000$ MIKE spectrum from 2006. We find $v_{rad/MIKE35} = -83.8\,\mathrm{km\,s^{-1}}$. The radial velocity from the HET snapshot observation taken in 2008 was determined via the Mg b triplet also through a cross-correlation technique. Details of the radial velocity determination can be found in Hollek et al. (2011). We find $v_{rad/CASH} = 4.0\,\mathrm{km\,s^{-1}}$. The radial velocity for the $R \sim 56,000$ MIKE spectrum was determined by measuring the average velocity offset for a set of 15 unblended lines in the red portion of the spectrum. We find $v_{rad/MIKE56} = 11.3\,\mathrm{km\,s^{-1}}$. Typical radial velocity uncertainties for medium resolution spectra are $\sim 10\,\mathrm{km\,s^{-1}}$, for snapshot spectra are $\sim 3\,\mathrm{km\,s^{-1}}$, and for high-resolution spectra are ∼1-2 $\mathrm{km\,s^{-1}}$. We find that the radial velocity does vary significantly over these seven years, indicating that the star has an unseen binary companion. Establishing the binary status of HE 0414−0343 aids in understanding the nature and mechanism of the star's carbon-enhancement and the overabundances in neutron-capture elements.

5.3 Spectral Analysis

5.3.1 Line Measurements

The equivalent widths were measured with a customized ESO/Midas program that automatically fits Gaussian profiles to each line. The user can adjust the fit to the continuum level by selecting line-free continuum regions, if necessary. This code takes into account any possible non-zero slope of the continuum, which becomes most important when a line is in the wing of another line. The linelist for these stars is the same that was used in Hollek et al. (2011) for the MIKE spectra; however, we rejected all Fe I and Fe II lines with wavelengths shorter than 4450 Å due to severe blending with molecular C features. We also omitted any strongly blended lines for the other elements whose abundances were determined via equivalent width measurements. Table 5.2 lists the equivalent widths and corresponding line abundances that are partially obtained through spectrum synthesis (see also Section 5.4).

Table 5.2. Equivalent Widths and Abundances

Species	λ [Å]	χ [eV]	log gf	W mÅ	logϵ(X)
C_2	5165	···	···	Synth	7.63
C^{12}/C^{13}	···	···	···	Synth	5[a]
Mg I	4571.09	0.00	−5.69	98.7	5.94
Mg I	4702.99	4.33	−0.38	111.1	5.81
Mg I	5172.68	2.71	−0.45	240.5	5.75
Mg I	5528.40	4.34	−0.50	107.2	5.84
Mg I	5711.09	4.34	−1.72	24.7	5.76
Ca I	4455.89	1.90	−0.53	88.6	4.76
Ca I	5581.97	2.52	−0.56	34.0	4.51
Ca I	5588.76	2.52	0.21	80.2	4.49
Ca I	5590.12	2.52	−0.57	25.5	4.35
Ca I	5594.46	2.52	0.10	85.8	4.70
Ca I	5598.48	2.52	−0.09	68.6	4.60
Ca I	5601.28	2.53	−0.52	40.4	4.60
Ca I	5857.45	2.93	0.23	55.7	4.54
Ca I	6102.72	1.88	−0.79	63.5	4.46

Table 5.2 (cont'd)

Species	λ [Å]	χ [eV]	log gf	W mÅ	logϵ(X)
Ca I	6122.22	1.89	−0.32	97.4	4.53
Ca I	6162.17	1.90	−0.09	102.1	4.39
Ca I	6439.07	2.52	0.47	102.0	4.55
Ca I	6449.81	2.52	−0.50	54.4	4.76
Ca I	6499.64	2.52	−0.82	35.2	4.76
Sc II	4415.54	0.59	−0.67	109.5	1.14
Sc II	5031.01	1.36	−0.40	71.9	1.02
Sc II	5031.01	1.36	−0.40	79.9	1.14
Sc II	5239.81	1.46	−0.77	68.0	1.43
Sc II	5526.78	1.77	0.02	70.0	1.01
Sc II	5641.00	1.50	−1.13	24.7	1.11
Sc II	5657.90	1.51	−0.60	51.2	1.04
Sc II	5658.36	1.50	−1.21	24.2	1.18
Sc II	5667.16	1.50	−1.31	28.5	1.37
Sc II	5684.21	1.51	−1.07	18.2	0.90
Ti I	3998.64	0.05	0.01	83.3	2.63

Table 5.2 (cont'd)

Species	λ [Å]	χ [eV]	log gf	W mÅ	logϵ(X)
Ti I	4518.02	0.83	−0.27	42.6	3.06
Ti I	4533.24	0.85	0.53	67.0	2.66
Ti I	4534.78	0.84	0.34	58.0	2.70
Ti I	4535.56	0.83	0.12	55.8	2.87
Ti I	4548.76	0.83	−0.30	35.1	2.95
Ti I	4555.49	0.85	−0.43	35.2	3.11
Ti I	4656.47	0.00	−1.29	31.9	2.91
Ti I	4681.91	0.05	−1.01	63.8	3.20
Ti I	4840.87	0.90	−0.45	22.5	2.91
Ti I	4840.87	0.90	−0.45	25.1	2.97
Ti I	4981.73	0.84	0.56	85.7	2.88
Ti I	4981.73	0.84	0.56	90.8	2.98
Ti I	4991.07	0.84	0.44	87.1	3.02
Ti I	4991.07	0.84	0.44	96.5	3.20
Ti I	5007.20	0.82	0.17	85.6	3.25
Ti I	5007.20	0.82	0.17	88.2	3.29

Table 5.2 (cont'd)

Species	λ [Å]	χ [eV]	log gf	W mÅ	logϵ(X)
Ti I	5016.16	0.85	−0.52	26.8	3.00
Ti I	5016.16	0.85	−0.52	28.5	3.04
Ti I	5020.02	0.84	−0.36	28.0	2.86
Ti I	5024.84	0.82	−0.55	26.8	3.00
Ti I	5024.84	0.82	−0.55	28.8	3.04
Ti I	5035.90	1.46	0.26	28.1	2.95
Ti I	5035.90	1.46	0.26	35.9	3.10
Ti I	5036.46	1.44	0.19	19.0	2.79
Ti I	5036.46	1.44	0.19	23.5	2.90
Ti I	5039.96	0.02	−1.13	55.6	3.12
Ti I	5039.96	0.02	−1.13	57.3	3.15
Ti I	5064.65	0.05	−0.94	71.1	3.20
Ti I	5210.39	0.05	−0.83	65.3	2.99
Ti II	4418.33	1.24	−1.97	84.1	3.12
Ti II	4441.73	1.18	−2.41	85.3	3.51
Ti II	4464.44	1.16	−1.81	97.1	3.10

Table 5.2 (cont'd)

Species	λ [Å]	χ [eV]	log gf	W mÅ	logϵ(X)
Ti II	4470.85	1.17	−2.02	105.6	3.49
Ti II	4488.34	3.12	−0.82	21.2	3.03
Ti II	4529.48	1.57	−2.03	77.7	3.43
Ti II	4563.77	1.22	−0.96	138.8	3.17
Ti II	4583.40	1.16	−2.92	27.2	3.01
Ti II	4589.91	1.24	−1.79	90.0	3.01
Ti II	4636.32	1.16	−3.02	29.5	3.16
Ti II	4657.20	1.24	−2.24	58.6	2.94
Ti II	4708.66	1.24	−2.34	67.8	3.17
Ti II	4779.97	2.05	−1.37	62.7	3.07
Ti II	4798.53	1.08	−2.68	61.0	3.21
Ti II	4805.08	2.06	−1.10	84.7	3.17
Ti II	4805.08	2.06	−1.10	89.8	3.25
Ti II	4865.61	1.12	−2.81	29.8	2.89
Ti II	4865.61	1.12	−2.81	45.7	3.15
Ti II	4911.17	3.12	−0.34	43.8	2.97

Table 5.2 (cont'd)

Species	λ [Å]	χ [eV]	log gf	W mÅ	logϵ(X)
Ti II	5185.90	1.89	−1.49	62.7	2.97
Ti II	5226.53	1.57	−1.26	124.2	3.41
Ti II	5336.78	1.58	−1.59	96.0	3.21
Ti II	5381.02	1.57	−1.92	64.3	3.03
Ti II	5418.76	1.58	−2.00	46.7	2.86
Cr I	4545.95	0.94	−1.37	31.4	3.27
Cr I	4600.75	1.00	−1.26	40.1	3.38
Cr I	4626.18	0.97	−1.32	32.6	3.27
Cr I	4646.15	1.03	−0.74	69.1	3.36
Cr I	4652.15	1.00	−1.03	48.3	3.28
Cr I	5206.04	0.94	0.02	113.1	3.24
Cr I	5247.56	0.96	−1.64	18.8	3.24
Cr I	5296.69	0.98	−1.36	27.5	3.18
Cr I	5348.31	1.00	−1.21	35.9	3.21
Cr I	5409.77	1.03	−0.67	68.9	3.22
Mn I	4754.04	2.28	−0.09	Synth	2.71

Table 5.2 (cont'd)

Species	λ [Å]	χ [eV]	log gf	W mÅ	logϵ(X)
Mn I	4783.52	2.32	0.14	Synth	2.79
Fe I	4443.19	2.86	−1.04	71.1	5.32
Fe I	4466.55	2.83	−0.60	99.2	5.40
Fe I	4476.01	2.85	−0.82	88.6	5.42
Fe I	4484.22	3.60	−0.86	36.1	5.40
Fe I	4592.65	1.56	−2.46	79.8	5.37
Fe I	4632.91	1.61	−2.91	51.8	5.41
Fe I	4643.46	3.64	−1.15	21.1	5.41
Fe I	4678.84	3.60	−0.83	39.3	5.41
Fe I	4859.74	2.88	−0.76	92.7	5.41
Fe I	4859.74	2.88	−0.76	92.7	5.41
Fe I	4903.31	2.88	−0.93	60.4	5.01
Fe I	4903.31	2.88	−0.93	67.9	5.13
Fe I	4918.99	2.85	−0.34	99.3	5.08
Fe I	4918.99	2.85	−0.34	99.3	5.08
Fe I	4924.77	2.28	−2.11	39.9	5.17

Table 5.2 (cont'd)

Species	λ [Å]	χ [eV]	log gf	W mÅ	logϵ(X)
Fe I	4924.77	2.28	−2.11	47.1	5.29
Fe I	4938.81	2.88	−1.08	58.5	5.13
Fe I	4938.81	2.88	−1.08	63.6	5.21
Fe I	4966.08	3.33	−0.87	41.0	5.15
Fe I	4966.08	3.33	−0.87	46.7	5.25
Fe I	4973.10	3.96	−0.95	17.6	5.45
Fe I	4994.13	0.92	−2.97	97.9	5.39
Fe I	4994.13	0.92	−2.97	98.8	5.42
Fe I	5006.11	2.83	−0.61	87.1	5.07
Fe I	5006.11	2.83	−0.61	88.7	5.11
Fe I	5014.94	3.94	−0.30	44.1	5.33
Fe I	5014.94	3.94	−0.30	44.9	5.34
Fe I	5041.07	0.96	−3.09	96.9	5.54
Fe I	5041.75	1.49	−2.20	98.4	5.30
Fe I	5049.82	2.28	−1.35	89.4	5.22
Fe I	5049.82	2.28	−1.35	93.6	5.30

Table 5.2 (cont'd)

Species	λ [Å]	χ [eV]	log gf	W mÅ	logϵ(X)
Fe I	5051.63	0.92	−2.76	99.8	5.21
Fe I	5051.63	0.92	−2.76	99.8	5.21
Fe I	5068.76	2.94	−1.04	77.0	5.45
Fe I	5074.74	4.22	−0.20	35.2	5.39
Fe I	5079.22	2.20	−2.10	52.2	5.25
Fe I	5127.36	0.92	−3.25	83.4	5.39
Fe I	5141.73	2.42	−2.24	30.2	5.27
Fe I	5142.92	0.96	−3.08	99.2	5.55
Fe I	5192.34	3.00	−0.42	95.5	5.22
Fe I	5198.71	2.22	−2.09	50.8	5.24
Fe I	5202.33	2.18	−1.87	72.5	5.31
Fe I	5216.27	1.61	−2.08	85.9	5.07
Fe I	5217.39	3.21	−1.16	37.0	5.22
Fe I	5242.49	3.63	−0.97	20.4	5.17
Fe I	5263.30	3.27	−0.88	49.4	5.21
Fe I	5266.55	3.00	−0.39	87.5	5.04

Table 5.2 (cont'd)

Species	λ [Å]	χ [eV]	log gf	W mÅ	logϵ(X)
Fe I	5281.79	3.04	−0.83	62.6	5.11
Fe I	5283.62	3.24	−0.52	77.3	5.27
Fe I	5302.30	3.28	−0.72	64.1	5.30
Fe I	5307.36	1.61	−2.91	46.1	5.26
Fe I	5324.17	3.21	−0.10	93.5	5.09
Fe I	5332.90	1.55	−2.78	56.4	5.22
Fe I	5339.93	3.27	−0.72	59.0	5.20
Fe I	5364.87	4.45	0.23	34.6	5.20
Fe I	5365.40	3.56	−1.02	19.7	5.11
Fe I	5367.46	4.42	0.44	39.2	5.04
Fe I	5369.96	4.37	0.54	53.0	5.11
Fe I	5389.47	4.42	−0.41	13.1	5.27
Fe I	5410.91	4.47	0.40	36.5	5.08
Fe I	5415.19	4.39	0.64	52.6	5.02
Fe I	5424.06	4.32	0.52	74.7	5.43
Fe I	5569.61	3.42	−0.54	66.3	5.29

Table 5.2 (cont'd)

Species	λ [Å]	χ [eV]	log gf	W mÅ	logϵ(X)
Fe I	5572.84	3.40	−0.28	71.7	5.10
Fe I	5576.08	3.43	−1.00	44.6	5.43
Fe I	5586.75	3.37	−0.14	78.4	5.03
Fe I	5615.64	3.33	0.05	98.5	5.15
Fe I	5624.54	3.42	−0.76	51.4	5.28
Fe I	5658.81	3.40	−0.79	46.7	5.21
Fe I	5662.51	4.18	−0.57	15.4	5.23
Fe I	5701.54	2.56	−2.14	26.1	5.22
Fe I	6065.48	2.61	−1.41	71.0	5.26
Fe I	6136.61	2.45	−1.41	82.8	5.26
Fe I	6137.69	2.59	−1.35	74.8	5.24
Fe I	6191.55	2.43	−1.42	84.4	5.27
Fe I	6200.31	2.61	−2.44	20.2	5.41
Fe I	6213.42	2.22	−2.48	44.6	5.46
Fe I	6230.72	2.56	−1.28	84.0	5.28
Fe I	6252.55	2.40	−1.69	68.5	5.25

Table 5.2 (cont'd)

Species	λ [Å]	χ [eV]	log gf	W mÅ	logϵ(X)
Fe I	6254.25	2.28	−2.44	47.3	5.53
Fe I	6322.68	2.59	−2.47	20.7	5.43
Fe I	6335.33	2.20	−2.18	48.1	5.19
Fe I	6393.60	2.43	−1.58	84.4	5.42
Fe I	6400.00	3.60	−0.29	65.5	5.20
Fe I	6411.64	3.65	−0.59	47.9	5.28
Fe I	6421.35	2.28	−2.01	64.1	5.35
Fe I	6430.84	2.18	−1.95	87.8	5.54
Fe I	6592.91	2.73	−1.47	52.2	5.15
Fe II	4489.18	2.83	−2.97	47.7	5.28
Fe II	4508.28	2.86	−2.58	68.5	5.26
Fe II	4515.34	2.84	−2.60	75.8	5.38
Fe II	4520.22	2.81	−2.60	64.1	5.15
Fe II	4583.84	2.81	−1.93	95.3	5.05
Fe II	4620.52	2.83	−3.21	36.3	5.32
Fe II	4731.43	2.89	−3.36	29.4	5.40

Table 5.2 (cont'd)

Species	λ [Å]	χ [eV]	log gf	W mÅ	logϵ(X)
Fe II	4993.35	2.81	−3.67	13.6	5.19
Fe II	4993.35	2.81	−3.67	17.9	5.33
Fe II	5197.58	3.23	−2.22	62.7	5.18
Fe II	5234.63	3.22	−2.18	61.9	5.11
Fe II	5276.00	3.20	−2.01	70.7	5.06
Fe II	5284.08	2.89	−3.19	30.2	5.21
Fe II	5325.55	3.22	−3.16	16.1	5.22
Fe II	5534.83	3.25	−2.93	27.1	5.29
Fe II	6247.54	3.89	−2.51	20.5	5.42
Fe II	6432.68	2.89	−3.71	22.2	5.51
Fe II	6456.38	3.90	−2.08	37.2	5.34
Ni I	4605.00	3.48	−0.29	22.5	4.10
Ni I	4648.65	3.42	−0.16	23.7	3.92
Ni I	4855.41	3.54	0.00	20.7	3.81
Ni I	4904.41	3.54	−0.17	12.2	3.71
Ni I	4904.41	3.54	−0.17	20.3	3.97

Table 5.2 (cont'd)

Species	λ [Å]	χ [eV]	log gf	W mÅ	logϵ(X)
Ni I	4980.16	3.61	−0.11	22.6	4.05
Ni I	4980.16	3.61	−0.11	25.0	4.10
Ni I	5035.37	3.63	0.29	22.7	3.67
Ni I	5035.37	3.63	0.29	34.7	3.92
Ni I	5080.52	3.65	0.13	34.2	4.09
Ni I	5081.11	3.85	0.30	15.6	3.71
Ni I	5084.08	3.68	0.03	16.1	3.80
Ni I	5754.67	1.94	−2.33	25.2	4.37
Ni I	6643.64	1.68	−2.30	33.4	4.14
Ni I	6767.77	1.83	−2.17	34.6	4.20
Zn I	4810.52	4.08	−0.13	Synth	2.38
Sr II	3464.45	3.04	0.49	Synth	1.11
Y II	4883.68	1.08	0.07	Synth	0.13
Y II	5087.42	1.08	−0.17	Synth	0.21
Zr II	4208.99	0.71	−0.46	Synth	0.71
Zr II	4613.95	0.97	−1.54	Synth	0.87

Table 5.2 (cont'd)

Species	λ [Å]	χ [eV]	log gf	W mÅ	logϵ(X)
Zr II	5112.28	1.66	−0.59	Synth	0.99
Ba II	5853.69	0.60	−0.91	Synth	1.80
Ba II	6141.73	0.70	−0.08	Synth	1.77
Ba II	6496.91	0.60	−0.38	Synth	1.87
La II	4740.28	0.13	−0.94	Synth	0.45
La II	4748.73	0.93	−0.54	Synth	0.42
La II	4824.05	0.65	−1.19	Synth	0.64
La II	6262.29	0.40	−1.24	Synth	0.40
La II	6390.48	0.32	−1.45	Synth	0.41
Ce II	4739.51	1.25	−0.53	Synth	0.67
Ce II	4739.52	0.53	−1.02	Synth	0.69
Ce II	4747.26	0.90	−1.79	Synth	0.89
Ce II	4882.46	1.53	0.19	Synth	0.70
Pr II	4744.91	0.20	−1.14	Synth	−0.17
Nd II	5310.04	1.14	−0.98	Synth	0.83
Nd II	5311.45	0.98	−0.42	Synth	0.87

Table 5.2 (cont'd)

Species	λ [Å]	χ [eV]	log gf	W mÅ	logϵ(X)
Nd II	5319.81	0.55	−0.14	Synth	0.73
Sm II	4318.93	0.28	−0.25	Synth	0.04
Sm II	4434.32	0.38	−0.07	Synth	0.17
Sm II	4519.63	0.54	−0.35	Synth	0.21
Eu II	6645.06	1.38	0.20	Synth	−0.49
Dy II	4449.70	0.00	−1.03	Synth	0.45
Er I	3682.70	0.89	−0.38	Synth	0.24
Yb II	3694.19	0.00	−0.82	Synth	0.03
Pb I	3683.46	0.97	−0.46	Synth	1.97
Pb I	4057.81	1.32	−0.22	Synth	2.11

[a]The C^{12}/C^{13} value is a ratio and not a log ϵ(X) value.

5.3.2 Stellar Parameters

Stellar parameters and elemental abundances derived from equivalent widths were determined using the spectroscopic stellar parameter and abundance analysis pipeline, Cashcode. Cashcode is written around the LTE line analysis and spectral synthesis code, MOOG (Sneden, 1973). It employs the latest version of MOOG (Sobeck et al., 2011), which properly treats Rayleigh scattering, an opacity source that is important in cool giants like HE 0414−0343. We used a Kurucz stellar atmosphere with α-enhancement (Castelli & Kurucz, 2004). Cashcode iterates to determine the set of stellar parameters which yield a flat relation between the line abundances and ex-

citation potential, a flat relation between the line abundances and reduced equivalent width values, and to ensure that the Fe I and Fe II abundance values are consistent with each other. See Hollek et al. (2011) for a detailed description of the stellar parameter determination technique.

We determined the spectroscopic stellar parameters using equivalent width measurements of 88 Fe I and 18 Fe II lines resulting in $T_{eff} = 4660\,K$, $\log g = 0.75$, $\xi = 2.05\,km\,s^{-1}$ and [Fe/H] $= -2.38$. The resonance lines of Fe I were excluded in this analysis, as they are strong enough that they are often are near the flat portion of the curve of growth. It should be noted that photometric temperatures are difficult to determine in CEMP stars because the molecular carbon bands interfere with the different photometric band passes in varying degree, thus making the photometric temperatures unreliable. Spectroscopic temperatures are often several hundred degrees cooler than photometrically-derived values. We thus adjusted the stellar parameters to make them more closely reflect photometric stellar parameters, following the procedure outlined in Frebel et al. (2013). These values are $T_{eff} = 4863\,K$, $\log g = 1.25$, $\xi = 2.20\,km\,s^{-1}$ and [Fe/H] $= -2.24$, which we adopt. In Figure 5.1, we show the derived effective temperature and surface gravity for HE 0414−0343 plotted together with 12 Gyr Yale-Yonsei isochrones (Kim et al., 2002; Green et al., 1984) for [Fe/H] $= -2.0$, -2.5, and -3.0 as well as a Cassisi et al. (2004) horizontal branch track.

We determined the random uncertainty in the surface gravity by allowing the Fe I and Fe II values to vary until they no longer agree within the

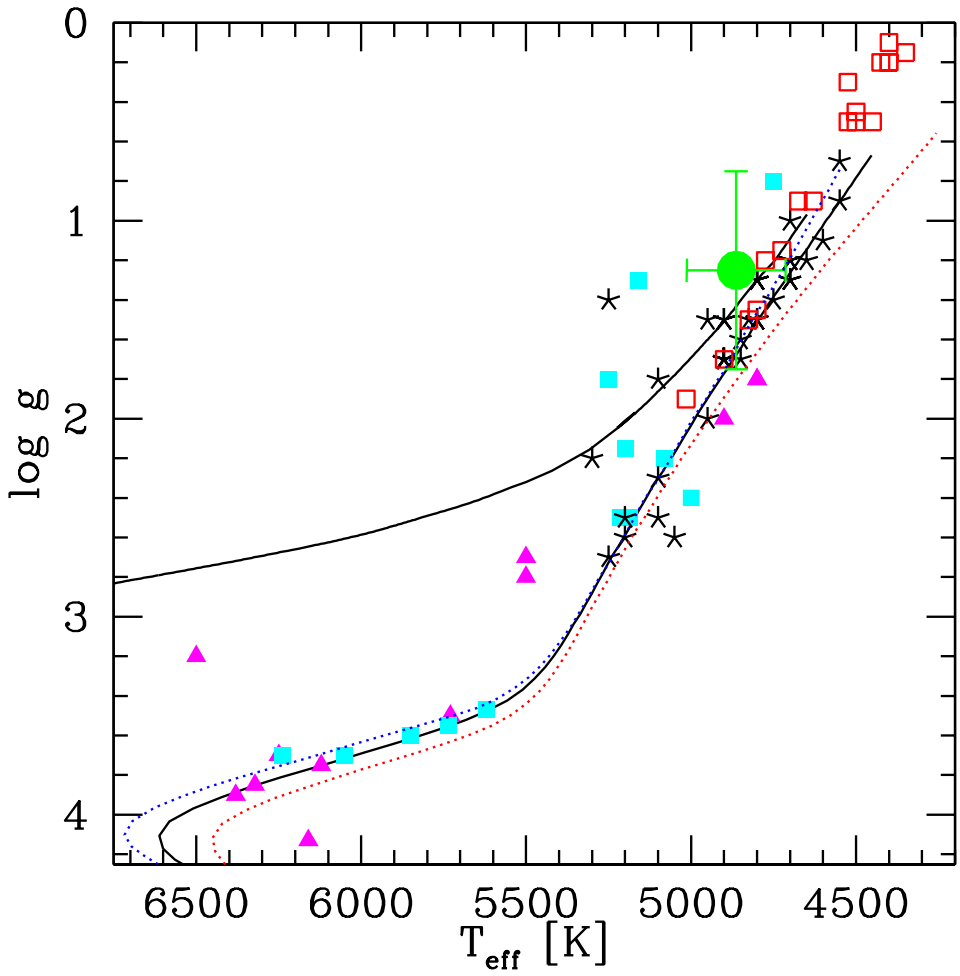

Figure 5.1 HR diagram with HE 0414−0343 (green filled circle) plotted against the Hollek et al. (2011) sample (red open squares), the Cayrel et al. (2004) sample (black stars), and selected s-process (cyan filled squares) and r/s-process (magenta filled triangles) enhanced stars as collated by Placco et al. (2013). Overplotted are the Yale-Yonsei isochrones (Kim et al., 2002; Green et al., 1984) for 12 Gyr, at [Fe/H] = −2.0 (red line), −2.5 (black line), and −3.0 (blue line, as well as a horizontal-branch mass track from Cassisi et al. (2004).

uncertainty of Fe I, which is 0.13 dex. Since HE 0414−0343 is on the giant branch, uncertainties in effective temperature at the $\sim$ 150 K level lead to changes in the surface gravity of $\sim$ 0.5 dex. We conservatively adopt this as our σ_{logg} uncertainty. We determined the standard error of the mean Fe I abundance to be $\sim$ 0.01 dex; however, we adopt the scatter of the individual Fe line abundances as our final [Fe/H] uncertainty ($\sim$ 0.13 dex) as the standard error is quite low and does not account for uncertainties in the continuum placement for each measured line, which is especially difficult in a CEMP star.

5.4 Chemical Abundance Analysis

The equivalent widths were used to determine abundances for seven different elements as well as the stellar parameters. Spectral syntheses of blended lines or lines with hyper-fine structure were performed manually, given the often severe blending due to the C-enhancement in the star. Table 5.3 lists the abundances. Solar abundances of Asplund et al. (2009) were used to calculate [X/H] and [X/Fe] values. Further details on the elemental abundances are given below.

Table 5.4 lists our abundance uncertainties. We determined the systematic uncertainties by varying the stellar parameters of effective temperature, log g, and microturbulence in the model atmosphere used in proportion to the uncertainty of each parameter. The abundances were then recalculated with the new model atmospheres either by averaging the individual line abundances determined from equivalent width or by re-fitting a synthetic spectrum. The

random uncertainty for each abundance determined via equivalent width was taken as the standard deviation of the individual line abundances. We use the standard deviation rather than the standard error because it better reflects that our abundances are hampered by the presence of molecular C. For the abundances derived via spectral synthesis, we used the original model atmosphere and varied the abundance of the synthetic spectrum until the fit no longer matched the input spectrum. In the cases where there were fewer than 5 measurements, we used a special treatment for low number statistics. We adopt a minimum standard deviation of 0.12 dex and use this for all measurements with formally calculated smaller values. The systematic uncertainties based on the stellar parameters and the random uncertainties were then added in quadrature to determine the total error value.

5.4.1 Carbon, Nitrogen, and Oxygen

There are several strong molecular C features in the spectrum of HE 0414 −0343, as seen in Figure 5.2. In fact, the CH features at 4313 Å (the G-band) and another smaller feature at 4323 Å are essentially saturated. The bandhead of the λ5165 C_2 feature is not saturated and thus was used to determine the C abundance via spectral synthesis. We find [C/Fe] = 1.44. However, attempting to measure the G-band and λ4323 features yield [C/Fe] = 1.39 and 1.44, respectively. These are consistent with the adopted abundance ratio. The CH and CN linelists (B. Plez 2006, private communication) are described in Frebel et al. (2007), with further description of the CN linelist available in Hill et al.

Table 5.3. Elemental Abundances of HE 0414−0343

Element	logϵ(X)	σ	[X/Fe]	n	logϵ(X)$_\odot$	Method
C (C_2)	7.63	0.30	1.44	1	8.43	Synth
Mg I	5.82	0.12	0.46	5	7.60	EW
Ca I	4.57	0.13	0.47	14	6.34	EW
Sc II	1.14	0.16	0.23	10	3.15	EW
Ti I	2.99	0.17	0.28	30	4.95	EW
Ti II	3.14	0.18	0.43	24	4.95	EW
Cr I	3.26	0.12	−0.14	10	5.64	EW
Mn I	2.75	0.12	−0.44	2	5.43	Synth
Fe I	5.26	0.12	···	88	7.50	EW
Fe II	5.26	0.13	···	18	7.50	EW
Ni I	3.97	0.20	−0.01	15	6.22	EW
Zn I	2.38	0.20	0.06	1	4.56	Synth
Sr II	1.11	0.30	0.48	1	2.87	Synth
Y II	0.17	0.20	0.20	2	2.21	Synth
Zr II	0.85	0.15	0.51	3	2.58	Synth
Ba II	1.81	0.15	1.87	3	2.18	Synth
La II	0.46	0.15	1.60	5	1.10	Synth
Ce II	0.74	0.15	1.40	3	1.58	Synth
Pr II	−0.17	0.30	1.35	1	0.72	Synth
Nd II	0.81	0.15	1.63	3	1.42	Synth
Sm II	0.14	0.15	1.42	3	0.96	Synth
Eu II	−0.49	0.30	1.23	1	0.52	Synth
Dy II	0.45	0.30	1.59	1	1.10	Synth
Er I	0.24	0.30	1.56	1	0.92	Synth
Yb II	0.03	0.30	1.43	1	0.84	Synth
Pb I	2.04	0.20	2.53	2	1.75	Synth

Table 5.4. Abundance Uncertainties

Element	Random Unc.	ΔT_{eff} +150 K	$\Delta \log g$ +0.5 dex	Δv_{micr} +0.3 km s^{-1}	Total[a] Unc.
C (C_2)	0.30	0.25	−0.10	0.00	0.40
Mg I	0.12	0.12	−0.12	−0.09	0.23
Ca I	0.13	0.12	−0.05	−0.07	0.19
Sc II	0.16	0.06	0.16	−0.05	0.23
Ti I	0.17	0.21	−0.07	−0.05	0.28
Ti II	0.18	0.05	0.15	−0.09	0.25
Cr I	0.12	0.19	−0.07	−0.05	0.24
Mn I	0.12	0.16	−0.06	−0.04	0.21
Fe I	0.12	0.17	−0.06	−0.08	0.23
Fe II	0.13	0.00	0.17	−0.04	0.21
Ni I	0.20	0.14	−0.04	−0.02	0.25
Ba II	0.12	0.10	0.10	−0.25	0.31

[a]Obtained by adding all uncertainties in quadrature.

(2002). The linelist used to determine the adopted C abundance from the C_2 feature is based on the Kurucz (1998) linelist. In Figure 5.2 we show the best fit abundances derived from the λ5165 C_2 feature, as well as those from the CH G-band and the 4323 Å features. The large [C/Fe] ratio of HE 0414−0343 categorizes it as a CEMP star using both the Beers & Christlieb (2005) and Aoki et al. (2007) definitions, as demonstrated in both panels of Figure 5.3.

In order to obtain an accurate C abundance, we also needed to determine the $^{12}C/^{13}C$ ratio. We derived the $^{12}C/^{13}C$ ratio from the ^{12}CN and ^{13}CN features near λ8005 seen in Figure 5.4. In order to determine the $^{12}C/^{13}C$ ratios from CN features, the N abundance was used as a free parameter. HE 0414−0343 has a low surface gravity and, therefore, high luminosity indicating that it is an evolved red giant star. Therefore, we expect the $^{12}C/^{13}C$ ratio to be low due to the mixing of CN-cycled material into its atmosphere

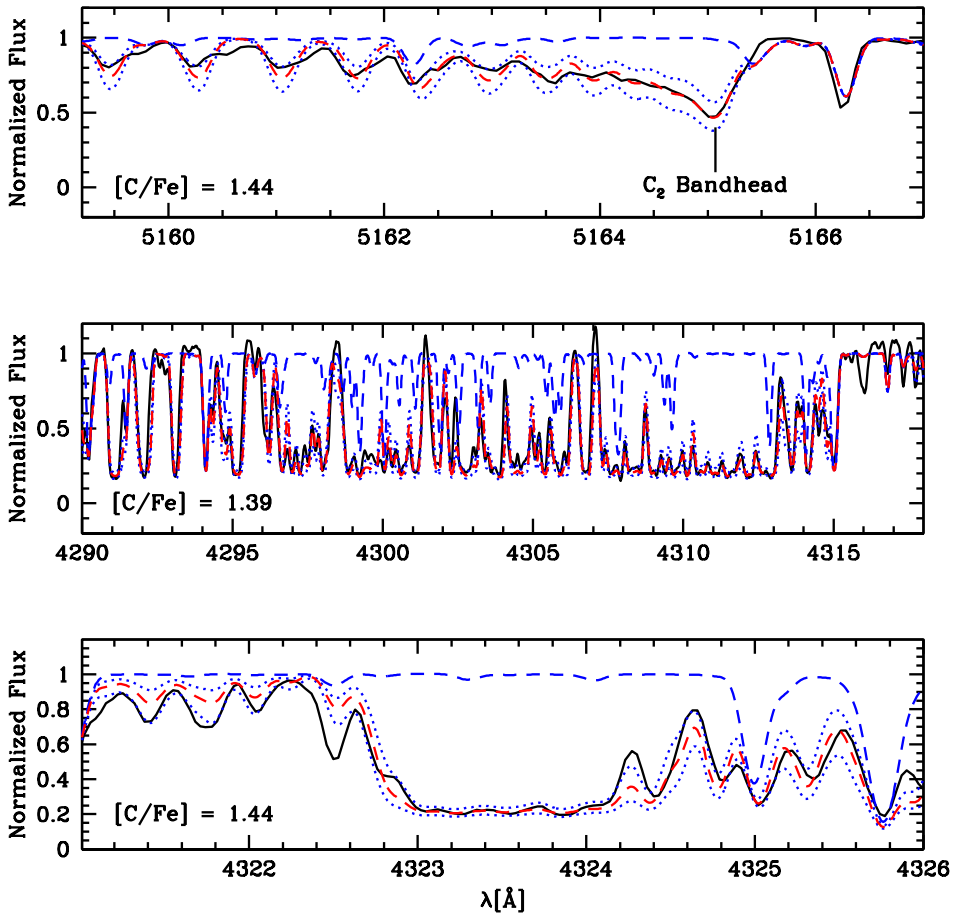

Figure 5.2 Top panel shows the λ5165 C_2 feature of the HE 0414−0343 spectrum (solid black line), along with the best fit synthetic abundance (red dashed line) with [C/Fe] = 1.44, C abundances changed a factor of two above and below the best fit abundance (blue dotted line), and a synthetic spectrum for which no C is present (blue dashed line). The bottom panels include the same for the CH G-band (middle) and the 4323 Å CH feature (bottom), yielding [C/Fe] = 1.39 and 1.44, respectively, confirming the [C/Fe] = 1.44 abundance ratio adopted from the λ5165 C_2 feature.

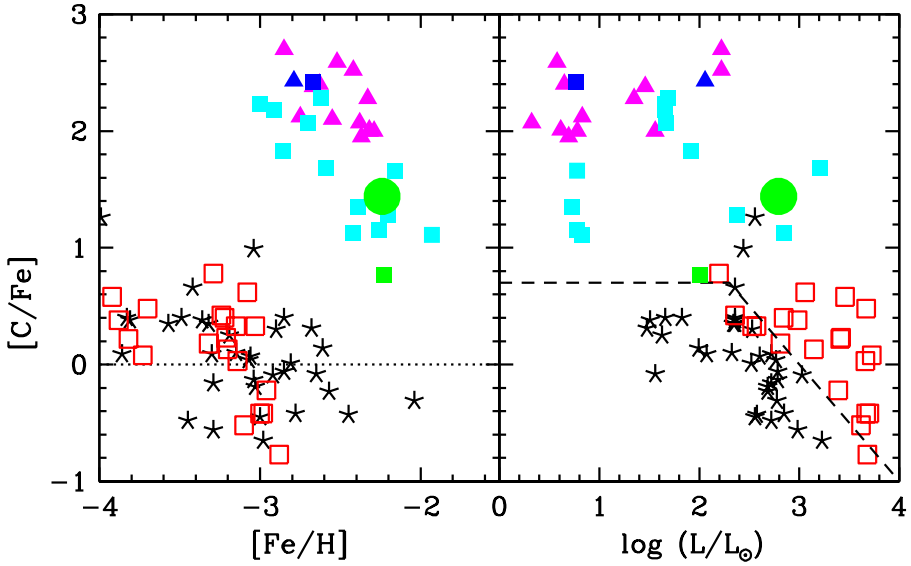

Figure 5.3 Left panel shows [C/Fe] plotted against [Fe/H], where the green filled circle represents HE 0414−0343, the red open squares are stars from Hollek et al. (2011), and the black stars represent Cayrel et al. (2004) data. The magenta triangles correspond to CEMP-r/s stars, the cyan squares represent CEMP-s stars, and the blue stars are those from Placco et al. (2013) with the triangle and the square representing the CEMP-r/s and CEMP-s stars respectively. The right panel plots the [C/Fe] abundance against luminosity, with the black dashed line representing the CEMP cut-off as prescribed by Aoki et al. (2007).

with much of the ^{12}C converted to ^{13}C. We confirm this behavior by finding $^{12}C/^{13}C = 5$, which was adopted uniformly throughout subsequent spectrum syntheses that required the C abundance.

We measured two other molecular C features, the CN bandhead near 4215 Å and the CH feature near 4237 Å, to confirm our $^{12}C/^{13}C$ result. From both features, we derive a ratio of ∼5-10. Using a new C_2 linelist from Brooke

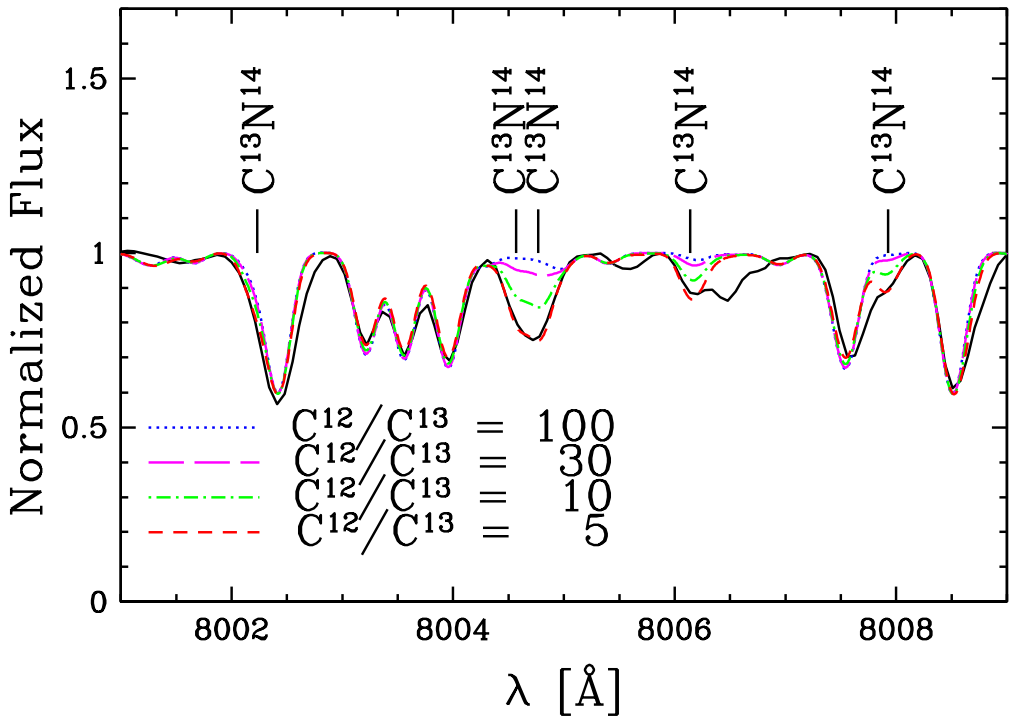

Figure 5.4 λ8005 CN feature in HE 0414−0343 (solid black line) from which the ^{12}C/^{13}C ratio was derived, along with synthetic spectra of varying ^{12}C/^{13}C ratios where ^{12}C/^{13}C= 5 (red dashed line), ^{12}C/^{13}C = 10 (green dotted-dashed line), ^{12}C/^{13}C = 30 (magenta long dashed line), and ^{12}C/^{13}C = 100 (blue dotted line).

et al. (2013) and Ram et al. (2013), we determined the [C/Fe] ratio $\sim$ 1.4 using several features across the spectrum, including one near the λ4736 C_2 bandhead, which confirms our C abundance. We also used this linelist to calculate a ^{12}C/^{13}C ratio and again confirmed our result.

The N abundance can be determined from diatomic CN and monatomic NH. While it is desirable to determine the N abundance independently, we were

unable to derive an abundance from the λ3360 NH molecular feature given its blue wavelength and the corresponding low S/N ratio. The N abundance in the CN molecule was treated as a free parameter and also yielded no useful N abundance given the overwhelming amount of carbon in these features.

The O abundance is difficult to measure in metal-poor stars due to the paucity of lines. The O features principally available in HE 0414−0343 are the [O I] forbidden line at 6300 Å and the O triplet. The forbidden line is weak and is difficult to discern from molecular C in our spectrum. We measured the equivalent widths of the three lines of the O triplet near 7772 Å in this star; however, no reliable abundance could be determined since these lines all give varying abundances.

5.4.2 Light elements: Z $\leq$ 30

Figure 5.5 shows the abundances of HE 0414−0343 together with those of the Cayrel et al. (2004) and Hollek et al. (2011) studies. We now discuss individual elements and abundance results.

We do not detect the λ6707 Li I doublet in our spectra. The Li abundance in evolved stars is expected to be low due to the low temperatures at which it can be destroyed. During the first and second dredge-ups, the Li surface abundance is greatly diluted, as Li-poor material is brought to the surface. Our non-detection of Li in HE 0414-0343 is consistent with this standard scenario. We derived a 3σ upper limit of A(Li) = 1.08. We also do not derive an abundance from the Na features near 5890 Å, as they are heavily

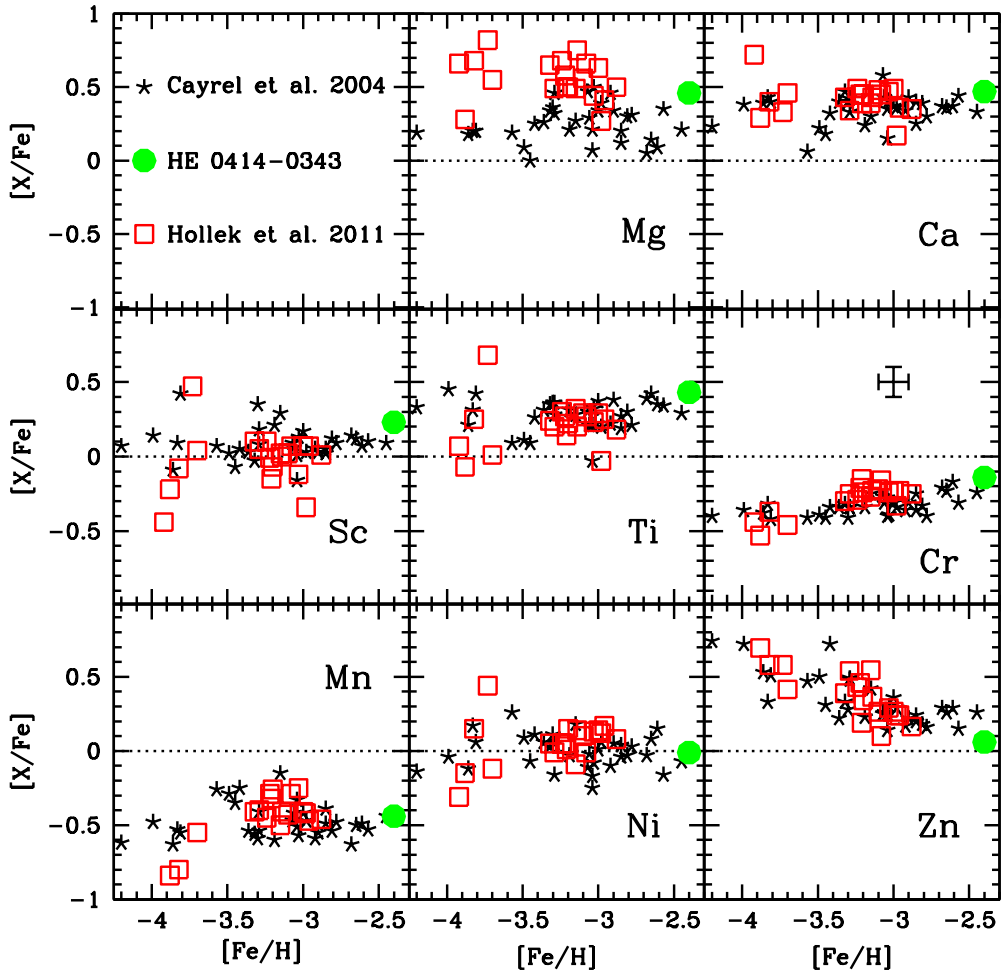

Figure 5.5 [X/Fe] abundance ratios vs. [Fe/H] for elements up to Zn measured in the spectrum of HE 0414−0343 (green filled circle) compared with the Cayrel et al. (2004) (black stars) and the Hollek et al. (2011) abundances (red open squares). The black dotted line represents the solar abundance ratio. The Zn and Mn abundances were determined via spectral synthesis while the rest were determined from equivalent width measurements. In the Cr panel, we include a typical error bar.

blended with interstellar Na. We did not calculate the Al or Si abundance because the corresponding lines are located exclusively in the blue portion of the spectrum between 3900 and 4105 Å and are heavily blended with CH lines. Additionally, the λ4102 Si line is located in the pseudocontinuum of the nearby Hδ line. The Co I lines available are λ3502, λ3995, and λ4020, all of which are well within a C-rich region and give spurious results. Thus, we do not present an abundance for Co.

With the exceptions of C, Mn, and Zn, all Z$\leq$30 elemental abundances were derived from equivalent width measurements. The abundances derived for the light elements are all consistent with what is expected from the typical metal-poor halo star. We find enhancement in the α-elements of Mg, Ca, and Ti, with [α/Fe] = 0.49. For the purposes of synthesis, plotting, and determining the [α/Fe] ratio, we adopt the Ti II abundance as the Ti abundance, as Ti I and Ti II differ by 0.16 dex. Using only those Ti I lines with newly-determined gf values from Lawler et al. (2013) and Ti II lines from Wood et al. (2013), the abundance discrepancy shrinks to 0.12 dex. This agreement supports our Fe-derived $\log g$ value. We find depletion in the Fe-peak elements of Cr, Mn, and Ni and enhancement of Sc and Zn, all of which is consistent with the Hollek et al. (2011) and Cayrel et al. (2004) studies.

For Mn and Zn, we derived abundances from synthetic spectrum computations. We obtain [Mn/Fe] = -0.48 from the λ4754 line and [Zn/Fe] = 0.06 from the λ4810 line.

5.4.3 Neutron-Capture Elements

All abundances for neutron-capture elements discussed in this section were determined with spectrum synthesis due to blending with other species or hyperfine structure. We discuss each element in detail below.

The Sr abundance was obtained from the λ3464 Sr II line, yielding [Sr/Fe] = 0.48, though it is in a region of low S/N, this line has the cleanest spectral region. The typical Sr lines used in abundance analyses of metal-poor stars, λ4215 and λ4077, both suffer from extensive blending with molecular C features. In fact, the λ4215 line is blended with so much CN that we were able to use that feature to measure the $^{12}C/^{13}C$ ratio, but could not determine a Sr abundance.

The Y abundance was determined from the λ4883 line, which is blended with CN accounted for in the linelist, and the unblended λ5087 line. We derived [Y/Fe] = 0.16 and 0.24 from these lines, respectively and adopted the average abundance, [Y/Fe] = 0.20.

The Zr abundance is based on the λ4208, λ4613, and λ5112 lines. Though the λ4208 feature resides within the same CN bandhead as the Sr II λ4215 line, it is strong and unblended enough to allow an abundance measurement. We adopt the mean value of these three lines, [Zr/Fe] = 0.52.

The Ba abundance was determined from the λ5854, λ6142, and λ6494 lines shown in Figure 5.6. Though available, the λ4554 line is on the damping portion of the curve of growth. The Ba lines in HE 0414−0343 are mostly

free of molecular C contamination. We adopted the mean abundance ratio, [Ba/Fe] = 1.87. For spectral synthesis of other elements in which Ba could possibly contribute, we used [Ba/Fe] = 1.80.

The La abundance was derived from five clean lines: λ4740, λ4748, λ4824, λ6262, and λ6390. We adopt the mean abundance, [La/Fe] = 1.48. The Ce abundance was derived from four lines: λ4739.51, λ4739.52, λ4747, and λ4882. The λ4739.51 and λ4739.52 lines are heavily blended; however, there is no other strong feature in the region of these lines, thus we derived their abundance simultaneously, as it is impossible to determine if either line yields a different abundance. We adopt [Ce/Fe] = 1.42 based on three lines, as we treat log ϵ(Ce λ4739.51) and logϵ(Ce λ4739.52) as a single abundance.

The Nd abundance was obtained from three clean lines in the red portion of the spectrum, shown in Figure 5.6: λ5310, λ5311, and λ5319. The mean abundance of these features, which are all in good agreement with each other, [Nd/Fe] = 1.63.

The Sm abundance was derived from λ4318, λ4434, and λ4519. The λ4318 line is in a C-rich region, while the λ4519 line is blended with C, thus the C abundance was treated as a free parameter to best fit the observed spectrum in these syntheses. Despite the blends, we are were still able to derive abundances that are in very good agreement with each other. We also evaluated λ4433 and λ4687, both of which are severely blended with C (and also Fe in the case of λ4687) and determined an upper limits for both features, that are very close to the final value. We obtain an average value of the

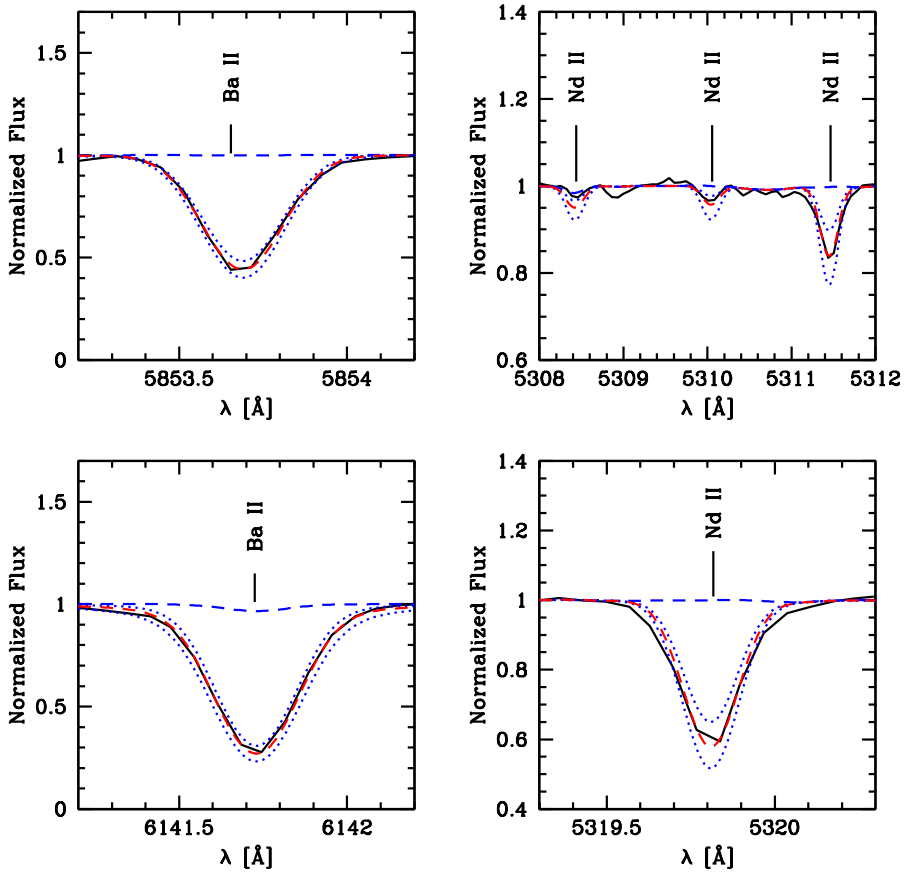

Figure 5.6 Ba features (left panels) in the HE 0414−0343 spectrum (solid black line), along with the best fit abundance (red dashed line), Ba abundances changed a factor of two above and below the best fit abundance (blue dotted line), and a synthetic spectrum for which no Ba is present (blue dashed line). The top left panel shows the λ4554 line, the middle left panel shows the λ5853 lines, and the bottom left panel shows the λ6141 line. The Nd features (right panels) are plotted in the same scheme as Ba. The top right panel shows the λ5310 and λ5311 lines, the middle right panel shows the λ5319 line, and the bottom right panel shows the λ5293 line.

abundance derived from the three measured lines: [Sm/Fe] = 1.42.

The Eu abundance was determined solely from the λ6645 line, yielding [Eu/Fe] = 1.23. As seen in the left panel of Figure 5.7, this line is blended with CN. Typically, the λ4129 line is used; however, the region surrounding that line is heavily blended with molecular CH features, as well as other neutron-capture elements, preventing any abundance measurements.

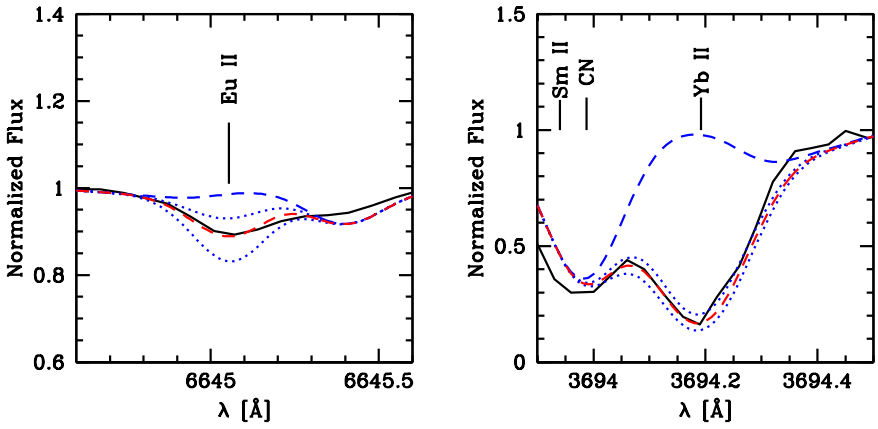

Figure 5.7 Eu feature at λ6645 Å (left panel) in the HE 0414−0343 spectrum (solid black line), along with the best-fit abundance (red dashed line), Eu abundances changed a factor of two above and below the best fit synthetic abundance (blue dotted line) of [Eu/Fe] = 1.23, and a synthetic spectrum for which no Eu is present (blue dashed line). The Yb feature located at 3694 Å (right panel) is plotted in the same way as Eu and yields a [Yb/Fe] ratio of 1.43.

The Dy abundance was determined from the λ4449 feature, which is heavily blended with molecular C. We had to increase the C abundance to match the features in this region. We therefore present the Dy abundance of

[Dy/Fe] = 1.59 with a larger uncertainty of 0.3 dex. However, we do include it in our analysis for diagnostic purposes with regard to the nature of the nucleosynthetic origins of HE 0414−0343. The magnitude of its abundance is similar to other abundances of neutron-capture elements that were easier to determine.

The Er abundance was derived from the λ3682 line yielding [Er/Fe] = 1.56. Given the low S/N and CH molecular features in the region, this abundance has a large uncertainty of 0.30 dex; however, similar to Dy, the magnitude of the derived abundance for Er is consistent with other neutron-capture elements in the star.

The Yb abundance was determined from the λ3694 line in the blue portion of the spectrum, as shown in the right panel of Figure 5.7. It resides on the red side of a blended feature which includes neutron-capture and Fe-peak elements, and has isotopic splitting. We derive [Yb/Fe] = 1.43.

Finally, we obtained the Pb abundance from the λ3683 and λ4057 features. We considered isotopic splitting by adopting the solar isotopic Pb ratios. We derived [Pb/Fe] = 2.45 from the λ3683 line. The λ4057 Pb feature is blended with CH. The linelist available for the CH features in that region is not complete, which leaves many lines unidentified. To reduce blending the effects, we adjusted the wavelengths of some of the features in the linelist to reflect those listed in Moore's Solar Atlas (Moore et al., 1966). We also adjusted the C abundance to match that of a nearby CH feature at 4058.2 Å and we modified the oscillator strengths of some nearby CH features to better reflect

the observed spectrum, with no impact on our Pb measurement. We derived a mean value [Pb/Fe] = 2.53. While each of the two lines individually has a large uncertainty due to many unknown (likely CH) blends and low S/N in the case of the λ3683 line, their agreement is encouraging. Given the strength of both lines, as seen in Figure 5.8, it is obvious that the Pb abundance is significant in this star. Since Pb is a neutral neutron-capture species, we use the NLTE-corrected value for our analysis and interpretation. We note here that non-LTE effects of neutral Pb in metal-poor stars are strong (Mashonkina et al., 2012) which become larger for cooler stars and lower metallicities. The Pb I correction for HE 0414−0343 is $\Delta_{\rm NLTE} = 0.56$ dex for the λ4057 line, which would increase our Pb abundance to [Pb/Fe]$\sim$ 3.09.

5.5 Classification of stars with overabundances in the neutron-capture elements associated with the s-process

In order to better understand the nature of CEMP-s stars and, more generally, metal-poor stars enriched in neutron-capture elements, one must first identify these stars as such. These classifications for s- and r-process stars reflect different nucleosynthetic processes that have either occurred before the star's formation (in the case of the r-process) or in a companion star during stellar evolution (in the case of the s-process). HE 0414−0343 shows the s-process, so we aimed to classify it based on its abundance pattern to better understand its origins.

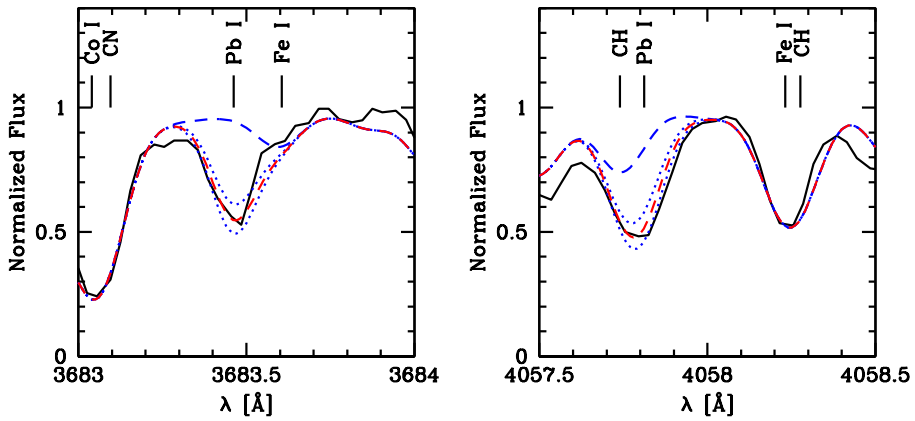

Figure 5.8 Pb features at 3683 Å (left panel) and 4057 Å (right panel) in the HE 0414−0343 spectrum (solid black line), along with the best fit abundance (red dashed line), Pb abundances changed a factor of two above and below the best fit synthetic abundance (blue dotted line), and a synthetic spectrum for which no Pb is present (blue dashed line). The λ3683 and λ4057 lines yield [Pb/Fe] abundance ratios of 2.53 and 2.60, respectively.

One classification method is to compare the stellar abundance patterns with the scaled Solar System s- and r-process patterns. While this has worked extremely well for strongly-enhanced r-process stars (owing to the universality of the r-process pattern, e.g., Sneden et al. (2000), Frebel et al. (2007)), in the case of the s-process, metallicity effects on the s-process pattern prevent a straightforward comparison between the Solar pattern and that of low-metallicity stars (e.g., Gallino et al. (1998)). Better suited for metal-poor stars, Ba and Eu abundances have been used as a proxy for distinguishing between s- and r-process element contributions, respectively. According to the Beers & Christlieb (2005) definitions, s-process enhanced stars are classified

by [Ba/Fe] > 1.0 and [Ba/Eu] > 0.5, while r/s-enhanced stars fall within the range of $0.0 <$ [Ba/Eu] < 0.5 and also having [Ba/Fe] > 1.0. Given the abundances of Ba and Eu and the overall pattern of HE 0414−0343, it would be classified as a CEMP-r/s star.

5.5.1 Assessing neutron-capture abundances ratios

In order to classify and better understand the origin of the abundance pattern of HE 0414−0343 in the context of other CEMP-s and CEMP-r/s stars, we used the stars from Table 6 of Placco et al. (2013), along with the two new stars presented in that paper as well as HE 1405−0822 (Cui et al., 2013). We inspected the overall abundance patterns of all these stars by plotting their logϵ(X) abundances of the (un-normalized) neutron-capture elements versus atomic number, Z. This is shown in the top panel of Figure 5.9. We included only stars with $-2.8 <$ [Fe/H] < -2.3 to attempt to remove gross metallicity effects expected to play a role in s-process nucleosynthesis. This reduced the sample to 11 CEMP-s and 14 CEMP-r/s stars. Again, we find the neutron-capture abundances to generally reflect the same trend: CEMP-r/s stars have higher $\log \epsilon$(heavy neutron-capture element) abundances than the CEMP-s stars. The overall ranges in the $\log \epsilon$(Ba) and $\log \epsilon$(Pb) abundances covered within this sample are very large at $\sim$ 2.0 dex, and the range in $\log \epsilon$(Y) and $\log \epsilon$(Eu) even larger at $\sim$ 2.5 dex. Interestingly, we find that the stars that make up our sample cover these large abundance ranges rather evenly, suggesting a continuum.

To better assess the origin and range of the observed neutron-capture patterns, we then normalized the abundances to $\log\epsilon(\mathrm{Ba}) = 1.0$. This can be seen in the middle panel of Figure 5.9. We use Ba for normalization because it is considered to be produced mainly in the s-process in the Solar System abundances (Arlandini et al., 1999). The CEMP-s stars have an average [Y/Ba]$\sim \log\epsilon(\mathrm{Y/Ba})$ ratio[4] of ~ -0.5 but with a spread of ~ 1 dex for Y abundances, when considering the Ba-normalized values. The CEMP-r/s stars have a lower average $\log\epsilon(\mathrm{Y/Ba})$ ratio of ~ -1, but a similar-sized spread of 1 dex for the Y abundances. By comparison, the Solar System ratio is ~ 0.0, which falls within the CEMP-s regime. For those stars with measured Pb abundances – a difficult task in CEMP stars – the $\log\epsilon(\mathrm{Pb/Ba})$ ratio varies greatly, > 2 dex, in the CEMP-s stars. This apparent spread in Pb is even larger in the Ba-normalized abundance patterns than in the absolute overall abundance patterns. Moreover, the $\log\epsilon(\mathrm{Pb/Ba})$ ratio is often negative then. In the CEMP-r/s stars, the $\log\epsilon(\mathrm{Pb/Ba})$ ratio is ~ 0 for most stars, while the Pb spread is only ~ 0.75 dex. Finally, we normalize the abundance patterns to $\log\epsilon(\mathrm{Eu}) = 0$, as shown in the bottom panel of Figure 5.9. We find that the $\log\epsilon(\mathrm{Pb/Eu})$ ratios for the CEMP-r/s stars are generally lower than those of CEMP-s stars. Also, there is a decreased spread among the $\log\epsilon(\mathrm{Pb})$ abundances. Overall, the behavior is similar to the Ba-normalized case.

We conclude from this exercise that when considering the $\log\epsilon(\mathrm{Y/Ba})$ ratio, there is a large spread but there is a fairly smooth transition between

[4]It should be noted that the [Y/Ba] ratio is 0.03 dex larger than the $\log\epsilon(\mathrm{Y/Ba})$ value.

CEMP-s and CEMP-r/s stars with no sharp dividing line. This transition can also be seen in Figure 1 of Masseron et al. (2010). Together with the $\log \epsilon$(Y/Ba) ratios, the $\log \epsilon$(Pb/Ba) and $\log \epsilon$(Pb/Eu)ratios also suggest that there is a transition and no clear, distinct separation into subgroups. Our star, HE 0414−0343, also demonstrates the continuum nature of the transition between CEMP-s and CEMP-r/s stars, as its abundance pattern is located between the more extreme CEMP-s and CEMP-r/s stars, as can be seen in Figure 5.9 (green line in all panels). Thus far, there is no known underlying physical mechanism that can explain the differences between CEMP-s and CEMP-r/s stars. We know that the s-process builds up in AGB stars over each thermal pulse after the third dredge up events begin. Mass transfer events of this enriched material onto the surfaces of the observed CEMP stars enrich the atmospheres and determine what the observed abundances will be. We thus hypothesize that the initial and ongoing conditions of this enrichment are what cause the continuum nature of the abundance patterns among all CEMP stars showing any s-process abundances. Modeling of AGB stars is then required to further investigate the details of the mass transfer and enrichment process(es) to confirm or refute this hypothesis.

Clearly, considering only observed [Ba/Eu] abundance ratios in CEMP-s and CEMP-r/s stars, as in the traditionally defined classification, is not sufficient to identify the origin of the neutron-capture element abundance patterns. This is especially true as evidenced by the smooth transition in the $\log \epsilon$(Y/Ba) ratio for our sample. Therefore, it appears limited to attempt to separate

this group of stars into two distinct subcategories of CEMP-s and CEMP-r/s. Moreover, the labeling of "CEMP-s" and "CEMP-r/s" may incorrectly suggest that there could be different underlying nucleosynthetic origins for these stars, and specifically an r-process component for r/s stars. A more comprehensive assessment and a physically-motivated explanation is needed to better understand metal-poor stars showing s-process element enhancement. Thus, to probe our above hypothesis, we compare the individual stellar abundance patterns in detail with yield predictions of models of s-process nucleosynthesis in AGB stars.

5.6 Comparison with model AGB s-process yields

To seek a physical motivation for the variety of s-process enriched stars, we investigated the physics of the s-process in AGB stars and how it relates to the derived abundances of HE 0414−0343 and the sample of literature stars. The s-process is thought to occur in thermally-pulsating AGB stars of $\simeq$0.8 to 8 $M_{\odot}$ (Busso et al., 1999) at low metallicities. The neutrons that fuel the s-process are primarily produced via the $^{13}C(\alpha,n)^{16}O$ reaction that occurs as a result of partial CN cycling (Abia et al., 2001; Smith & Lambert, 1990). The neutron-capture occurs in the He-shell and the newly created s-process elements are brought to the surface as a result of third dredge-up mixing episodes. Detailed calculations by Gallino et al. (1998), Bisterzo et al. (2009), and Lugaro et al. (2012), among others, have been performed to better understand the s-process. To reproduce observed s-process abundances in

metal-poor companion stars, models have been created that e.g., vary the mass and the metallicity of the AGB star, the size of the ^{13}C pocket, and take into account dilution effects.

Karakas et al. (2010) developed a new AGB nucleosynthesis model for a $1.3\,M_{\odot}$ star with [Fe/H] $= -2.5$. It was run with the the Mount Stromlo Stellar Evolutionary code (Karakas et al., 2010) and the model star was evolved from the zero age main sequence to the AGB. The model underwent 21 thermal pulses during the AGB phase, most of which included third dredge up events, resulting in a total dredge up of $0.049\,M_{\odot}$ from the core of the star to its surface. Using the Vassiliadis & Wood (1993) prescription for mass loss, they determined that $0.5\,M_{\odot}$ is lost during the AGB stage. The resultant abundances at each thermal pulse were calculated in the same manner as in Lugaro et al. (2012). The final abundance is reached at thermal pulse number 19, thereafter the surface abundances do not change.

Placco et al. (2013) found two new stars showing signs of s-process nucleosynthesis and compared their abundances to an earlier version of this model, along with the abundances of several stars classified as CEMP-s and CEMP-r/s stars in the literature. For comparison, they also used a range of other models spanning $0.9\ M_{\odot} \leq M \leq 6\,M_{\odot}$ at [Fe/H] $= -2.2$, some of which include pre-enrichment from the r-process. These models are presented in Karakas (2010) and Lugaro et al. (2012). Placco et al. (2013) considered the mass transfer event across a binary system, which necessarily results in dilution of the s-process material once it then is mixed onto the observed

star's outer atmosphere. Specifically, the AGB surface abundance yields after each thermal pulse were compared to the abundance patterns of the sample of CEMP-s and CEMP-r/s stars, and a best fit was determined based on a residual analysis. See Placco et al. (2013) for further details.

5.6.1 HE 0414−0343 Abundance Pattern Analysis

We first extended the Placco et al. analysis to HE 0414−0343 and then later also to their sample (see Section 5.6.2). To account for dilution of the s-process material in the receiver stars' outer atmosphere, we considered two different options: 5% and 50% cases, where the latter imitates a mass transfer event when the recipient star is a red giant having 50% of its mass in the convection zone and the 5% case represents a less-evolved star. Since we do not know how long ago the mass transfer event took place, we consider both options for HE 0414−0343 and each of the sample stars.

The analysis specific to HE 0414−0343 then consisted of two steps: a) comparison of its abundance pattern to the same set of models as in Placco et al. (2013) and in-depth analysis of the best fitting model and b) extraction of an r-process pattern from the overall abundance pattern model, and comparison of the "decontaminated" abundance patterns to all the models.

Regarding step a), the abundance pattern of HE 0414−0343 was input into fitting software first developed in Placco et al. (2013) that compares its abundance pattern to the abundance yields associated with each thermal pulse of the AGB model and selects the best fit based on the smallest residuals. We

furthermore determined at which thermal pulse the residuals were minimized for i) the full observed neutron-capture abundance pattern, ii) just abundances near the first peak of the s-process (Sr, Zr, Y), iii) just abundances near the second peak of the s-process (Ba, Sm), iv) just for abundances of the heaviest neutron-capture elements, e.g., Eu and above, and v) for only elements with Z$>$ 40, thus excluding the first peak abundances. The full residual can be misleading since an abundance pattern that is both under- and over-predicted for different elements by the model could have a very small full residual, despite its poor overall fit. Thus, breaking up the fitting procedure into these element groups helped to disentangle the build up of s-process elements at the surface of the AGB star. Over time, heavier and heavier s-process elements are created and dredged-up in the AGB star with each thermal pulse. The relative contributions to elements in groups ii) to iv) should thus be reflected in the residuals of the respective group. The results of this step are rather detailed and best understood in the context of the entire sample that we analyzed (which is described in Section 5.6.2). Hence, in Section 5.6.2 we discuss the results of the full sample analysis (including HE 0414−0343), together with our conclusion regarding the nature and origin of s-enriched CEMP stars.

Overall, and similar to what was found in Placco et al. (2013), the new updated low-metallicity model provided the best fit to the overall abundance pattern of HE 0414−0343. However, r-process elements such as Eu and Dy around the second peak were still overabundant compared to even the best fit model. This kind of discrepancy has also been found for the CEMP-r/s star

analyzed in Placco et al. (2013), suggesting HE 0414−343 to be in the same category. To first order this confirms why CEMP-r/s stars are not classified as CEMP-s – they have a curious relative overabundance of heavy neutron-capture elements compared to lighter ones. This could indicate a contribution of r-process elements.

Regarding step b), in order to investigate this heavy-element discrepancy as well as the nature of the CEMP-r/s abundance pattern and especially the "r" component of "CEMP-r/s", we "extracted" an arbitrary amount of r-process material (but following the r-process pattern) from the abundance pattern of HE 0414−0343. If the binary system formed in an r-process enriched gas cloud, extracting an r-process signature should leave a cleaner s-process signature since the s-process elements present were created during the AGB phase of the more massive star.

We decreased the logϵ(Eu) abundance in HE 0414−0343 by 0.5 and 1.0 dex. We used the abundance pattern of the r-process star CS 22892−052 (Sneden et al., 2003) to calculate the ratios of the neutron-capture elements to Eu in order to extract an r-process signature from these stars. These two "decontaminated" HE 0414−0343 abundance patterns were then compared with the models. Again, the best overall fit still did not reproduce the two decontaminated abundance patterns well. Although the heavy neutron-capture elements above Eu were better fit than before, the first and second peaks of the s-process were now poorly reproduced. Interestingly, using the [Fe/H] = −2.5 model and also a model with a pre-enrichment of 0.4 dex of r-process mate-

rial yielded nearly the same residuals for the two decontaminated abundance patterns (although both were not very good overall, with residuals ranging from 0.5−0.9 dex). According to the Beers & Christlieb (2005) criteria, the abundance pattern of HE 0414−0343 indicates that this star falls under the CEMP-r/s classification. However, our analysis indicates that there is no discernible r-process component, rendering the "-r/s" classification unsatisfactory in explaining the origins of this star.

5.6.2 Literature Sample Analysis

In the same way as HE 0414−0343, we then performed a detailed model comparison (step a) using just the updated low-metallicity AGB model yields at each thermal pulse and the abundances of the literature sample which included the new stars from Placco et al. (2013), the stars from their Table 6, and HE 1405−0822 (Cui et al., 2013). We then compared each of the five calculated residuals of the different atomic mass regions to the measured [Y/Ba] ratios for every star in the sample.

Despite the fact that the residuals have been minimized, there is still information in the amount and direction of any discrepancy between the model abundance and the abundance patterns. In Figure 5.10, we plot cases i)-iv) for the 5% and 50% dilution scenarios. In general, the CEMP-s stars seem to have larger [Y/Ba] ratios than the CEMP-r/s stars, though there is overlap from −1 to −1.25. For the CEMP-s stars, there is an anticorrelation between the full residual and the [Y/Ba] ratio in the 5% dilution case, and no correlation

in the 50% case. In the 5% case, strong anticorrelations are apparent between the second peak and Eu peak residuals to the [Y/Ba] ratio. In the 50% case, the first and second peak are relatively well fit, while there is a ~ 1 dex spread in the Eu residual. The CEMP-r/s stars show no correlation for the full residual across all peaks versus [Y/Ba] in the 5% case and a weak correlation in the 50% case. In the 5% case, there is a weak anticorrelation in the first peak residuals to the [Y/Ba] ratio whereas in the Eu peak residuals, there is perhaps a weaker correlation to [Y/Ba]. The 50% case essentially indicates no correlations between the residuals of any peak and the [Y/Ba] ratio. Additional results of this analysis will be given in Section 5.7.1

Given the complicated nature of the full abundance pattern residuals, we adopted the results of case v of the best-fit residual analysis presented in Figures 5.10 and 5.12. We made this choice because it is generally difficult to interpret the first-peak neutron-capture elements in the sample stars due to the many possible nucleosynthetic pathways (e.g., the poorly-understood light element primary process - Travaglio et al. (2004)) that led to their creation.

5.7 The classification and origin of CEMP-sA, -sB, -sC stars

Given the smooth transition between the CEMP-s and CEMP-r/s stars, we decided to explore a new classification scheme for our sample that would better account for this transition, by simply describing the magnitude of the s-process abundance. We designate these stars CEMP-sA, CEMP-sB, and

CEMP-sC, where the CEMP-sA stars have the "most traditional" s-process abundance pattern and the least negative [Y/Ba] ratios spanning the range $-0.9 <$[Y/Ba]< -0.3, CEMP-sC stars have an abundance pattern that deviates the most from the usual s-process abundance pattern, while still maintaining s-process enhancement and, correspondingly, have the largest negative [Y/Ba] ratios, with [Y/Ba]< -1.5. CEMP-sB stars fall in the middle, with $-1.5 <$ [Y/Ba]< -0.9. Table 5 lists our definitions and classifications for the literature sample we have employed in this study.

To facilitate future classifications of to be discovered s-process stars, we have provided a web-based program[5] that automatically classifies user-input stars based on their abundance patterns. It determines the best-fit thermal pulse number based on the low-metallicity model and provides plots of other stars that have been classified the same way such that a comparison of the entire neutron-capture element pattern is available.

Following the new classification it is important to investigate if there is an underlying physical mechanism that could explain the origin of the different s-process patterns and the continuum between them. Below we discuss three plausible evolutionary scenarios to explain the smooth transition from CEMP-sA to CEMP-sB to CEMP-sC.

[5]http://staff.gemini.edu/∼vplacco/sprocess_classes.html

Table 5.5. CEMP-sA,-sB,-sC classification scheme

Description	Definition	Abbreviation
low-mass AGB companion	[Ba/Fe] > 1.0 and $-0.9 <$ [Y/Ba] < -0.3	CEMP-sA
intermediate-mass AGB companion	[Ba/Fe] > 1.0 and $-1.5 <$ [Y/Ba] < -0.9	CEMP-sB
high-mass AGB companion.	[Ba/Fe] > 1.0 and [Y/Ba] < -1.5	CEMP-sC
carbon-enhanced stars with normal n-cap. abund.	[Ba/Fe] < 0.0	CEMP-no[a]
Star	**[Y/Ba]**	**Classification**
CS 22898−027	−1.52	CEMP-sC
CS 22942−019	−0.36	CEMP-sA
CS 22947−187	−0.99	CEMP-sB
CS 22948−027	−1.08	CEMP-sB
CS 22964−161	−0.89	CEMP-sA
CS 29497−030	−1.27	CEMP-sB
CS 29497−034	−0.75	CEMP-sA
CS 29526−110	−0.48	CEMP-sA
CS 31062−012	−1.41	CEMP-sB
CS 31062−050	−2.08	CEMP-sC
HD 196944	−0.56	CEMP-sA
HE 0024−2523	−0.47	CEMP-sA
HE 0058−0244	−1.44	CEMP-sB
HE 0202−2204	−0.91	CEMP-sB
HE 0338−3945	−1.50	CEMP-sB
HE 0414−0343	−1.70	CEMP-sC
HE 1031−0020	−0.88	CEMP-sA
HE 1105+0027	−1.62	CEMP-sC
HE 1135+0139	−0.69	CEMP-sA
HE 1405−0822	−1.66	CEMP-sC
HE 1509−0806	−0.90	CEMP-sA
HE 2138−3336	−1.43	CEMP-sB
HE 2148−1247	−1.45	CEMP-sB
HE 2258−6358	−1.53	CEMP-sC
LP 62−544	−1.84	CEMP-sC

Note. — All stars have [C/Fe] > 0.7.

[a]CEMP-no (Beers & Christlieb, 2005) stars are not part of the classification CEMP-sA-C scheme. We include it here for completeness.

5.7.1 Thermal Pulse Number Stratification

The thermal pulse number of the best-fit AGB model yield is a potential predictor of the CEMP classification. The abundance patterns of the CEMP-sA stars are best-fit by the corresponding nucleosynthesis to thermal pulse 5 in the 5% dilution case. When we examine the corresponding residuals we find that the abundances of the first s-process peak are consistently under-predicted in the AGB model by $\sim$ 0.2 dex. The second s-process peak is over-predicted in the model by $\sim$ 0.3 dex and the Eu region and third s-process peak are over-predicted by $\sim$ 0.2 dex, even when a +0.5 dex NLTE correction is applied to the Pb abundance. The CEMP-sC stars have the lowest residual value between the observed abundance pattern and the model. In this case, the first s-process peak is over-predicted by $\sim$ 0.5 dex, the second peak is under-predicted by $\sim$ 0.1 dex, and the third peak is even more under-predicted by $\sim$ 0.4 dex. The third peak is especially under-predicted when the NLTE correction is applied to Pb. Given the large abundance of second and third peak s-process elements, later thermal pulses, which have higher heavy neutron-capture element abundances, more closely match these stars. The CEMP-sB stars, predictably, fall in between the CEMP-sA and CEMP-sC stars.

The 50% dilution case is similar in that it reveals that the CEMP-sA stars and the CEMP-sC stars form distinct groups. This is especially apparent in the first s-process peak residuals where the first peak is under-predicted in the CEMP-sA stars by $\sim$ 0.2 dex and over-predicted in the CEMP-sC stars

by $\sim$ 0.3 dex. The second peak is somewhat well-fit in the CEMP-sA stars with an overprediction of only $\sim$ 0.1 dex, but under-predicted in the CEMP-sC stars by $\sim$ 0.4 dex. The third peak is underpredicted in all stars but one, with the average underprediction for the CEMP-sA stars being $\sim$ 0.3 dex and the average for the CEMP-sC stars at $\sim$ 0.8 dex. The best-fit thermal pulse numbers are larger in the CEMP-sA stars in this dilution case (7-19), which is expected since each thermal pulse represents less material. The CEMP-sC stars are all best fit at thermal pulse 19. As with the 5% dilution case, the CEMP-sB stars fall in the middle of these two extremes. While it is difficult to directly map the best-fit thermal pulse number to the classification, it does show some correlation.

Thus, we compared the best-fit thermal pulse number with the [Y/Ba] ratio and found that the CEMP-s and CEMP-r/s stars form distinct groups. We further investigated the best-fit thermal pulse number as a potential key to the physical origin of the [Y/Ba] continuum. We accomplished this in two stages. First, we attempted to identify the relationship between the CEMP s-process sub-classifications (both old and new) and the best-fit thermal pulse numbers. Second, we examined the nature of the corresponding residuals of the abundance patterns of the best-fit thermal pulse numbers to seek a physical explanation for the distribution of best-fit thermal pulse number and classification.

In the 5% dilution case, there is a large spread of $\sim$ 1 dex at in the [Y/Ba] ratio at 5 thermal pulses. A large number of stars are also best fit at

19 thermal pulses. All the CEMP-s stars are best fit at 5 thermal pulses, while the CEMP-r/s stars span a larger range of best-fit thermal pulse numbers from 5-19, with a majority of the stars being best fit at thermal pulse number 19. Before thermal pulse 5, the AGB star is not a suitable donor star. The first third dredge up event happens at that thermal pulse number in the model and then the increasing pulses allow for the AGB star to build up s-process material on its surface which later gets transferred onto the surface of the observed metal-poor star.

In the 50% dilution case, we see this same degeneracy of best-fit thermal pulse numbers again at 19 thermal pulses, but not at the low number end. The CEMP-r/s stars are the ones that are best fit over a tight range of thermal pulse numbers (18-19), while the CEMP-s stars span a range from 5-19 thermal pulses. The degeneracy at 19 thermal pulses is likely due to the fact that the model's surface abundances are stable once the star has undergone 19 thermal pulses, thus more thermal pulses may have occurred, but those post-19 thermal pulses do not alter the AGB star surface abundances any more.

Given the seemingly apparent connection between the old classifications and the best-fit thermal pulse number, we investigated how the new designations corresponded to the best-fit thermal pulse number to see if this might be the main driver in creating the different classes of CEMP s-process stars. The thermal pulse number and the classification of CEMP-sA, -sB, and -sC are correlated such that low numbers of thermal pulses (~ 5) tend to correspond with CEMP-sA stars and high numbers of thermal pulses (~ 19) correspond

with CEMP-sC stars, while the CEMP-sB stars have thermal pulse numbers between 5 and 19.

Given these results, we consider the thermal pulse number as a proxy for the physical nature of the mass transfer event. Specifically, it could represent the timing of the mass transfer. This would mean that a lower thermal pulse number might correspond to an earlier stage of the thermally pulsing AGB companion star soon after the onset of the s-process nucleosynthesis. Thus, the s-process pattern would not have built up heavier neutron-capture elements nearly as much as a later mass transfer. It could also represent the physical distance between the stars in the binary system, where two stars with close physical separation will undergo an earlier mass transfer, corresponding with a lower thermal pulse number. If the thermal pulse number alone is what causes the spread that we have seen in the [Y/Ba] ratios, then we would expect that there is only a small dispersion in the [Y/Ba] ratio for a given thermal pulse number. The degeneracy at both low and high thermal pulse numbers indicates that this can so far only partially explain the CEMP-sA to CEMP-sC transition.

5.7.2 Mass range in early AGB stars

While the thermal pulse number seemed to be a promising explanation for the old classification scheme, it falls short with the [Y/Ba] ratio diagnostic. That is not to say that the thermal pulse number holds no information. The best-fit model that we are using is based on a $1.3 M_{\odot}$ AGB star. We thus

compare more massive AGB star models (albeit at higher metallicity) from Karakas (2010) and Lugaro et al. (2012) against a given observed abundance pattern. The higher-mass model results in a different s-process pattern that has higher second and third peak s-process element abundances. The CEMP-sA stars were qualitatively well-fit with the low-metallicity, low-mass AGB model, especially with regard to the first peak elements, however there were systematic discrepancies between the abundance patterns of the CEMP-sC stars (and to a lesser degree, of the CEMP-sB stars) and the low-mass AGB model. Thus, an increase in the masses of the AGB companion stars, in addition to the timing of the mass transfer, may provide a plausible explanation for the transition from CEMP-sA to CEMP-sC.

This can also, qualitatively, be understood in a broader context. By definition, CEMP-sA stars have the [Y/Ba] values closest to 0, which means that their abundance ratios are closest to the Solar System ratio. According to our findings, lower-mass AGB stars would be responsible for this type of s-process pattern. Given that the Sun is a Population I star, it formed from many more successive generations of stellar birth and death from previous stars than the metal-poor stars of this study. Thus, due to the initial mass function of Pop I stars, the Solar System s-process can be thought to have been compiled predominantly from lower-mass AGB stars. With fewer generations of star formation occurring in the early universe, it is much easier to identify the relative effects of higher mass stars in localized star-forming gas clouds that are rarer than the near solar-mass stars that produce solar-type s-process

patterns. In addition, the initial mass function of the early universe may be different than that of Pop I stars, skewing towards higher mass stars. We thus speculate that these difficult-to-fit CEMP-sB and CEMP-sC stars are indeed a result of higher-mass AGB star nucleosynthesis local enrichment at work.

To further test this idea, we looked to the reflecting indicators of high-mass and low-mass AGB star nucleosynthesis. One of the most obvious differences is the source of neutrons that fuel the s-process. In the low-mass AGB stars, these neutrons come from ^{13}C(α,n)^{16}O reaction. At the lowest metallicities, the efficiency of the s-process is strongly dependent on the number of available Fe seed nuclei. One way to confirm this observationally is to examine the [Ba/C] ratio as a function of metallicity. The right panel of Figure 5 in Masseron et al. (2010) explores this and they find a tight correlation between [Ba/C] and [Fe/H] in their CEMP-s stars. In Figure 5.11, we plot the same axes, along with the empirical trend from Figure 5 of Masseron et al. (2010) in the black solid line, with the black dotted lines representing the area in which most of the CEMP-s stars are plotted. We find that our CEMP-sA stars mostly fall within this same region even over the narrow range of metallicity that was chosen.

High-mass AGB stars are hotter in their interior than their low-mass counterparts and thus the ^{22}Ne(α,n)^{25}Mg reaction becomes an important source of neutrons (Goriely & Siess, 2005). This allows for a convective s-process that occurs in the thermal pulses and depends upon the AGB mass rather than on [Fe/H]. In Figure 7 of Masseron et al. (2010), they find no correlation be-

tween [Ba/C] and [Fe/H] for their CEMP-rs stars. Similarly, the CEMP-sC stars in our Figure 5.11 do not show the same tight correlation between [Ba/C] and [Fe/H] that the CEMP-sA stars of our sample and the CEMP-s stars from Masseron et al. (2010) do. Interestingly, the convective s-process allows for the production of Eu nuclei (Goriely & Siess, 2005) whose abundance is underpredicted in the CEMP-sC stars by our low-mass AGB model. The CEMP-sB stars are split in terms of the correlation between [Ba/C] and [Fe/H]. Due to the narrow metallicity range, we are not able to draw conclusions from our sample alone. However, adding these stars to the Masseron et al. (2010) sample qualitatively supports the hypothesis of different neutron sources producing different metallicity relations and more specifically, our suggestion of different AGB stellar masses being responsible for the variety of s-process abundances in metal-poor stars.

5.7.3 Initial neutron-capture element abundances of the CEMP-sA, -sB, -sC stars

In neutron-capture-normal metal-poor stars, we observe large spreads in the [Sr/Fe] and [Ba/Fe] abundance ratios as a function of [Fe/H] (Frebel & Norris, 2013). It is possible that this spread in the general population of metal-poor stars is related to the variety of CEMP stars with s-process enrichment. It is interesting to determine if the observed s-process patterns are a composite of the stars' initial neutron-capture element pattern together with the s-process material received from the AGB star at later times. Could this scenario explain the variations in the patterns and the continuum between

the CEMP-sA, CEMP-sB, and CEMP-sC stars? In the 5% dilution case, we find a spread in [Y/Ba] > 1 at both the lowest and highest thermal pulse numbers; in the 50% dilution case, we find this spread at the highest thermal pulse number. Here we investigate the initial neutron-capture abundances as a possible cause for this signature.

In plots of [Ba/Fe] or [Sr/Fe] versus [Fe/H] of halo field stars (e.g., bottom panels of Figure 18 in Frebel & Norris (2013)), there is a huge spread of nearly 3 dex in regular halo stars with [Fe/H] < -2.0 (and no strong overabundance in carbon) that do not show any particular enhancement in neutron-capture elements, i.e., stars with [Ba/Fe] or [Sr/Fe] < 1. Similarly, in stars with enhanced s-process abundances, i.e., stars with [Ba/Fe] or [Sr/Fe] > 1, we also observe a > 2 dex spread (e.g., top panels of Figure 18 in Frebel & Norris (2013)).

Given that the spread in neutron-capture element abundances are roughly of the same magnitude in both regular metal-poor stars and s-process stars, one proposal is that the underlying mechanism that causes the spread among CEMP-sA, CEMP-sB, and CEMP-sC stars is the same, with CEMP-sA stars generally having lower initial neutron-capture abundances than CEMP-sC stars. The gas clouds from which any of these stars formed were pre-enriched with neutron-capture material at varying amounts due to the chemical evolution that occurred locally up to the time when the star formed and prior to any mass transfer events. S-process rich stars have only been found at metallicities of [Fe/H] > -3 (with one exception, i.e., Sivarani et al. (2006)) and the rise of

s-process enrichment through stellar winds from AGB stars has been placed at [Fe/H] ~ -2.6 (Simmerer et al., 2004), although with some scatter. This suggests that various chemical enrichment processes were already operating at [Fe/H] ~ -2.5, including different kinds of neutron-capture processes occurring in supernovae and the more massive AGB stars. Altogether, in a yet to be understood way, chemical evolution produced stars with huge spreads in neutron-capture abundances whereas their light element ($Z \leq 30$) abundance ratios (e.g., [Ca/Fe]) are nearly identical (e.g., Cayrel et al. (2004); Frebel & Norris (2013)).

We examined the [Sr/Fe] and [Ba/Fe] abundance ratios in our sample stars to test if the spreads of these abundance ratios could have been caused by large variations of the neutron-capture elemental abundances in their birth clouds. Specifically, we attempted to map them to the [Y/Ba] ratio used to classify the stars in order to determine if there is a clear connection between the initial abundances of the CEMP-sA, CEMP-sB, and CEMP-sC stars and the abundances that are now observed, due to mass transfer from their AGB binary companions. However, it is difficult to ascertain if these ratios can be used to match the [Y/Ba] ratio successfully. As described above, the spread in [Y/Ba] between the two extremes of CEMP-sA and CEMP-sC stars seems to cover the same range as seen in the neutron-capture and carbon-normal metal-poor stars. As in the case of our r-process pattern extraction, we now attempted the reverse. We adjusted the [Sr/Fe] and [Ba/Fe] abundance ratios by subtracting out an amount to represent the mass transfer s-process ma-

terial. Thus these adjusted abundances should reflect the initial amount of neutron-capture material in the receiver stars (i.e., prior to the mass transfer of neutron-capture and carbon-rich matter). However, the adjusted receiver stars do not map well from the CEMP-sA, -sB, and -sC stars to the neutron-capture/carbon-normal metal-poor stars. Given this mismatch between the CEMP-sA, CEMP-sB, and CEMP-sC stars and the neutron-capture and C-normal metal-poor stars, the idea that an initial spread in the abundances in the gas cloud caused the continuum is perhaps not as straightforward to investigate. More high resolution spectra of CEMP stars need to be taken and analyzed to better investigate this scenario.

5.8 Caveats and Considerations

In this work we have utilized, in the end, only one low-metallicity model to fit all stellar abundance patterns, given that currently few of these models exist and not all are applicable to this analysis. We have also made the assumption that the s-process pattern is built up in the same way for all stellar masses for a given metallicity although as a function of thermal pulses. Out of necessity, the biggest assumption is perhaps that the companion mass is the same for all our stars, but we discuss this further below. Despite this limitation, these assumptions are justified because we made a reasonable metallicity cut to select sample stars have similar metallicities from -2.7 to -2.3. This ensures that our stars span over the model metallicity of [Fe/H] $= -2.5$. This model does give the best fit to a CEMP-sA star compared to other models.

However, it is unlikely that the s-process is unique at a given metallicity. As discussed in Section 5.7, different masses of the companion AGB star can change the thermal pulse number, where more massive AGB star models typically correspond with a lower best-fit thermal pulse number in the CEMP-sB and CEMP-sC stars than in less massive AGB models. Thus, a continuum in the masses of the companion stars could create a spread seen between the CEMP-sA, CEMP-sB, and CEMP-sC stars. In fact, our analysis uses the thermal pulse number as a proxy in the argument in favor of a mass continuum of the AGB stars.

A more general issue that all AGB modelling faces is the formation and size of the ^{13}C pocket, from which the neutrons necessary for the s-process originate. The size of the pocket can be somewhat constrained by comparisons to observations of post-AGB stars. At the metal-poor end, spreads in the size of the pocket in the models of a factor of 3–6 are needed to account for the observation data (Bonačić Marinović et al., 2007; De Smedt et al., 2012). Furthermore, in CEMP stars, the spread needed to match the observational data can be upwards of a factor of 10 or higher (Bisterzo et al., 2011; Lugaro et al., 2012). Central to the issue as to the size of the ^{13}C pocket, is that it is not currently understand how it is formed in AGB stars. Of particular interest to this work, is that increasing the size of the ^{13}C pocket would likely decrease the [Y/Ba] ratio; however, this is still subject to metallicity effects. As more low-metallicity AGB models become available we will further analyze how different ^{13}C pocket assumptions would affect the [Y/Ba] ratio, which is

central to our diagnostic.

For future studies, it would be helpful to have a better understanding about the details of the mass transfer so that the dilution of the transferred s-process material can be more accurately be described. To summarize, in order to further investigate CEMP s-process star abundances, more AGB star models are needed that cover a range of masses and a larger low-metallicity range. More observations of newly discovered s-process stars are also needed in order to create a large statistical sample. These models and observed abundances can then be used to better probe AGB star mass and metallicity effects on the observed abundance patterns for a full physical explanation.

5.9 Summary and Conclusions

We have presented the red giant HE 0414−0343, a CEMP star with [Fe/H] = −2.24. Following a detailed abundance analysis, we find the star to possess a strong enhancement in the s-process elements. We also determined its radial velocity from four different spectra, taken between 2004 and 2011, and found it to vary significantly, indicating that it likely has an unseen binary companion. Based on its [Ba/Eu] and [Ba/Fe] ratios, this star falls under the older category of "CEMP-r/s" stars.

In order to better understand HE 0414−0343 and the nature of "CEMP-r/s" stars, we also analyzed the abundance patterns of a sample of literature "CEMP-s" and "CEMP-r/s" stars. The CEMP-s and CEMP-r/s categories as defined by Beers & Christlieb (2005) based on the [Ba/Eu] ratio have been

fundamental in recognizing the diverse nature of CEMP star abundances. By instead utilizing the [Y/Ba] ratio to characterize CEMP s-process stars with neutron-capture element enhancement, we aimed to gain a better understanding of the origin of the s-process pattern diversity. Investigation of the [Y/Ba] abundance ratio in our sample shows that there is a continuum between the "CEMP-s" and "CEMP-r/s" stars, rather than a distinct cut off separating the two groups of objects with different origins. We then suggested a new classification scheme for s-process stars, CEMP-sA, CEMP-sB, and CEMP-sC, following the different levels of [Y/Ba] ratio values. We assigned each sample star to one of the three new groups. "CEMP-s" would loosely correspond to CEMP-sA, "CEMP-r/s" to CEMP-sC, and those stars who fill in the continuum between are CEMP-sB. The advantage to using these two elements is that they are both easily measurable in CEMP stars. Moreoever, this provides an observable to test our hypothesis that there is a physical mechanism that causes the continuum of s-process abundance patterns in these stars.

We compared the abundance patterns to AGB nucleosynthesis models and found that the new low-metallicity 1.3 $M_{\odot}$ model from Placco et al. (2013) produced the best fits to all stellar abundance patterns in our sample. The CEMP-sA stars were best fit by the model. The CEMP-sB and CEMP-sC stars were increasingly problematic. Their abundance patterns have an excess in the heavy neutron-capture abundances around Eu and above compared to lighter element abundance, such as Sr, and the model yields. Upon investigation, we find that this excess cannot be explained by assuming these stars to have

formed from gas already enriched with r-process elements.

We further investigated two cases for diluting the material in the stellar atmosphere of observed stars after the mass transfer of s-enriched material from the AGB star. This takes into account the unknown timing of the mass transfer event during the receiver star's evolution. We also explored the build up of the s-process elements in the low-metallicity AGB star model as a function of its thermal pulses. We compared the model yields with the abundance patterns of the sample stars to find the best fit. We then examined the residuals between the best-fit abundance yields of the AGB model at a given thermal pulse and the abundance patterns of the sample stars. Considering elements Ba and heavier, the CEMP-sA stars' patterns can be reproduced by only few numbers of thermal pulses of their AGB star companion, whereas CEMP-sB and CEMP-sC stars require progressively more thermal pulses. This can be understood since the relative production of heavier to lighter neutron-capture elements takes longer, and CEMP-sC stars require larger amounts of the heaviest elements. This is consistent with the fact that lower thermal pulse numbers correspond to an earlier mass transfer event in the evolution of the AGB star compared to later ones.

In conclusion, the CEMP-sA stars are well-explained by the $1.3\,M_{\odot}$ model. In the absence of more low-metallicity models for different AGB star masses (but following some tests with higher metallicity, higher mass models), we speculate that the abundance patterns of CEMP-sB and CEMP-sC stars could better be reproduced by models with masses larger than $1.3\,M_{\odot}$ because

we suspect these models to produce larger amounts of the heaviest elements. This would imply that the three classes of CEMP-s stars are simply a reflection of their companion masses undergoing AGB s-process nucleosynthesis and potentially also the timing of the mass transfer as reflected by the number of thermal pulses.

The Hobby-Eberly Telescope (HET) is a joint project of the University of Texas at Austin, the Pennsylvania State University, Stanford University, Ludwig-Maximilians-Universität München, and Georg August Universität Göttingen. We are grateful to the Hobby-Eberly staff for their assistance in obtaining the data collected for this paper. We appreciate useful conversations with Christopher Waters and Harriet Dinerstein. J.K.H. acknowledges support for this work from NSF grants AST-0708245 and AST-0908978. A.F. acknowledges support from NSF grant AST-1255160. V.M.P. acknowledges support from the Gemini Observatory. This work was supported in part by NSF grant AST-1211585 to C.S.

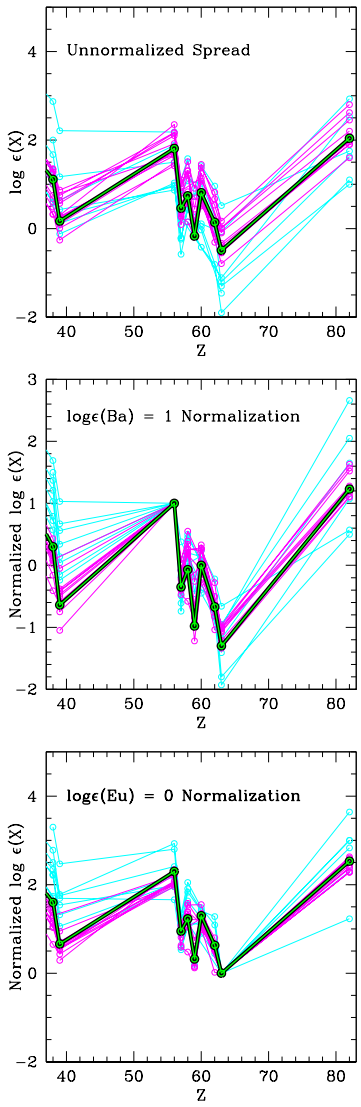

Figure 5.9 $\log \epsilon$(X) abundances plotted against atomic number, Z, (top), $\log \epsilon$(X) values that have been normalized to $\log \epsilon$(Ba) = 1.0 (middle), and a$\log \epsilon$(Eu) = 0.0 (bottom) of selected neutron-capture elements. These normalization values were chosen because a majority of the Ba and Eu abundances, respectively, were close to those values, however these values are arbitrary. The cyan lines correspond to the CEMP-s stars, the magenta lines correspond to the CEMP-r/s stars, and the green line corresponds to HE 0414−0343.

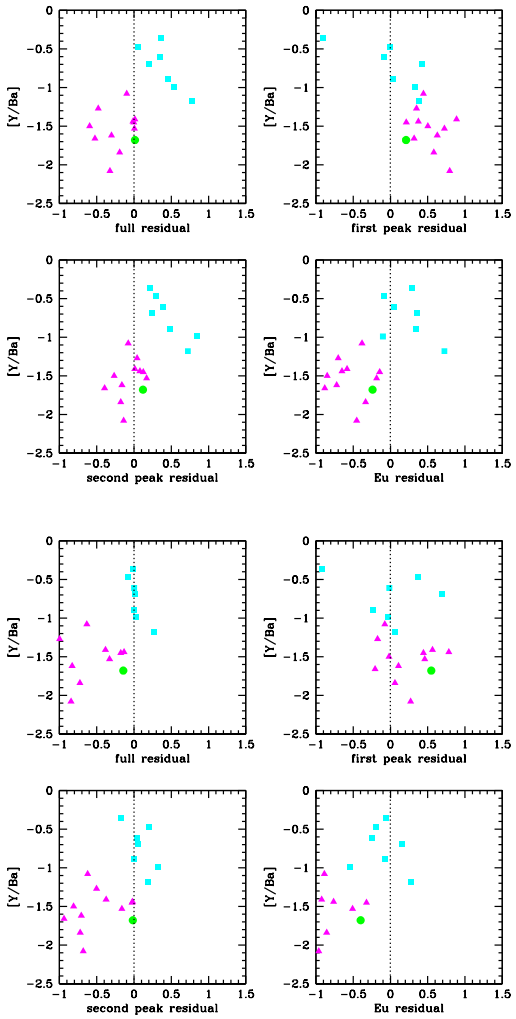

Figure 5.10 [Y/Ba] ratio plotted against the four cases of residuals obtained from comparing the s-process nucleosynthesis results of a [Fe/H] = −2.5 AGB star with the abundances of CEMP-s stars (cyan squares), CEMP-r/s stars (magenta triangles), and HE 0414−0343 (green circle). The top four panels depict the 5% dilution case, the bottom panels the 50% dilution case. See text for discussion.

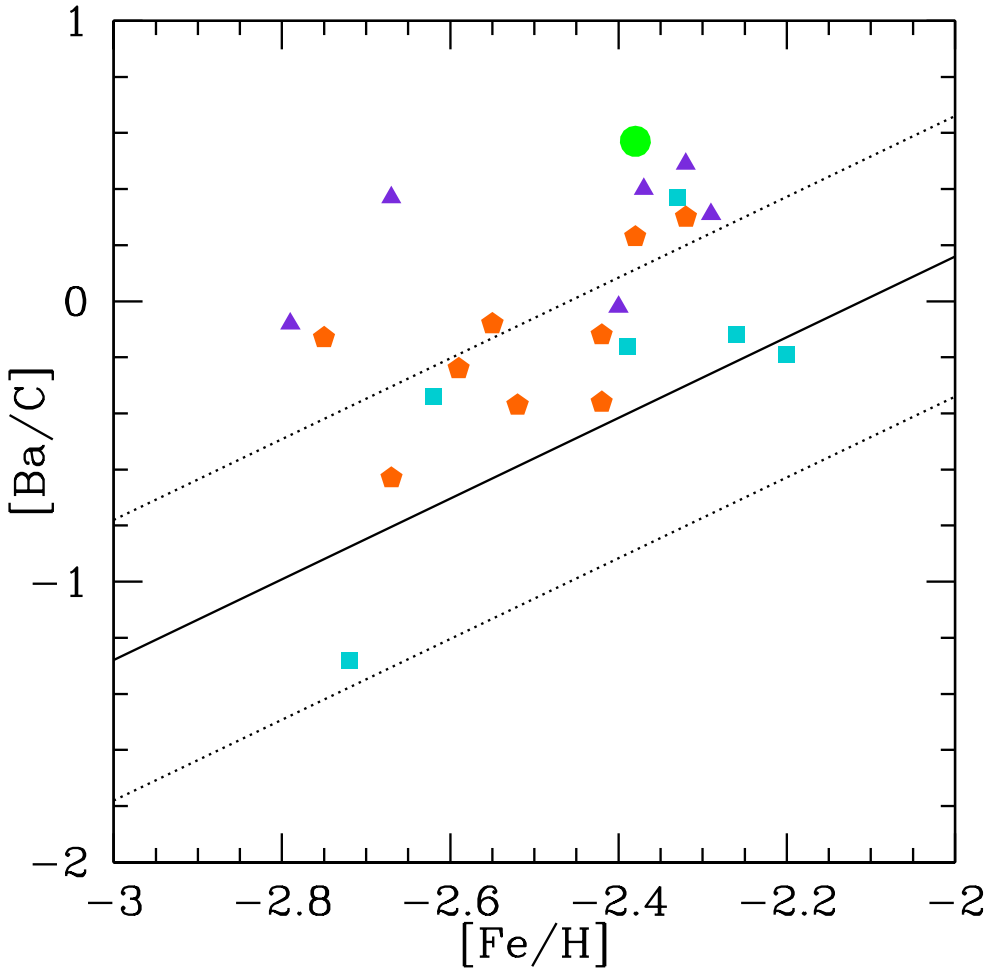

Figure 5.11 [Ba/C] abundance ratio plotted as a function of [Fe/H] of HE 0414 − 0343 and the entire literature sample. The green circle corresponds to HE 0414−0343, the turquoise squares represent the CEMP-sA stars, the orange pentagons correspond to the CEMP-sB stars, and the purple triangles correspond to the CEMP-sC stars. The solid black line corresponds to the relation that would be expected between [Ba/C] and [Fe/H] if the main neutron source for the s-process is C, empirically adopted from Figure 5 of Masseron et al. (2010). The black dotted lines represent the area on the plot where the majority of the CEMP-s stars resided in Figure 5 of Masseron et al. (2010) and correspond to the shaded region in the upper panel of their Figure 7.

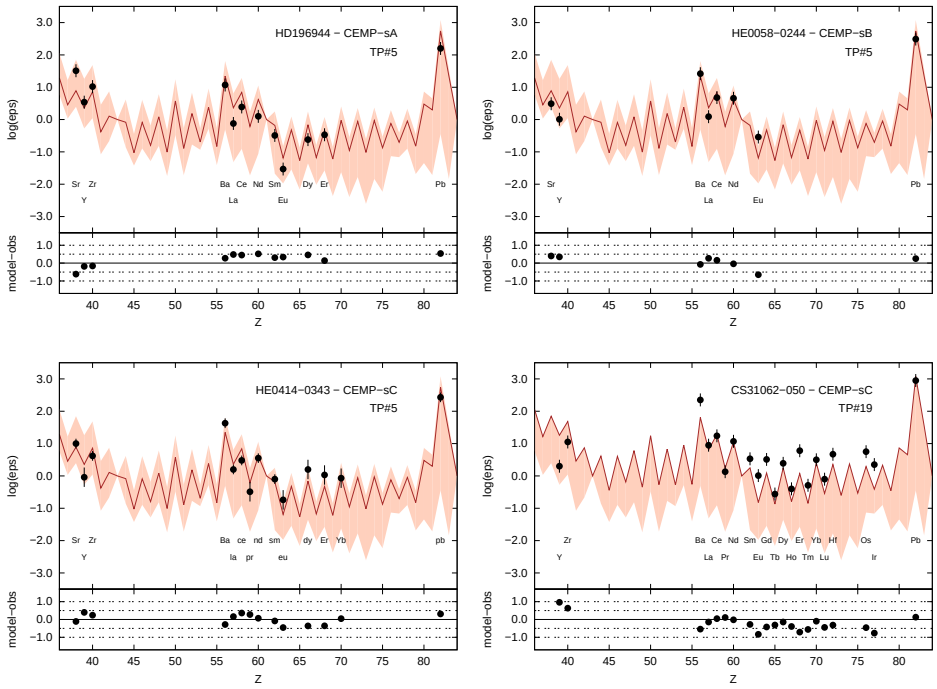

Figure 5.12 Logϵ(X) values plotted against atomic number for four stars, including our program star, HE 0414−0343. In the upper panel of each plot, the black dots represent the abundances, with bars to show the uncertainties. The red line is the best fit model and the peach shaded region corresponds to the range of abundance yields accumulating over each thermal pulse until thermal pulse 19. The bottom-most part of the peach section corresponds to the initial abundances at the start of the AGB phase in the model and the top-most part corresponds to the final abundance yields. In the bottom panel of each plot, the black dots represent the difference between the best fit model and the observed abundances. In the upper right corner of each plot, we show the star name, its classification, and which thermal pulse number corresponds to the best fit. We have included a star from each classification as well as HE 0414−0343.

Chapter 6

Summary of the Chemical Abundances of Stars in the Halo Project

In this thesis, we presented the Chemical Abundances of Stars in the Halo (CASH) Project. The goal of the CASH project was to study the chemistry of the stellar halo of the galaxy by identifying abundance patterns, trends, and frequencies. We also aimed to discover chemically interesting objects. Here we summarize the development of the CASH projet, its results, and the future outlook.

6.1 Observations and Analysis

The stars of the CASH project were observed using the High Resolution Spectrograph on the Hobby-Eberly Telescope at McDonald Observatory at R$\sim$ $15,000$ with median S/N$\sim$ 50 at 5200Å and moderate abundance uncertainties ($\sigma \sim 0.35$). These spectra are called "snapshot" spectra and are of high enough resolution to obtain individual line abundances, while being relatively quick to observe as compared to high-resolution spectra.

The analysis begins by determining the equivalent widths of the linelist specifically tailored to the resolution and quality of the CASH snapshot spec-

tra in the automated equivalent width determination software, Robospect. Robospect works iteratively to solve for a continuum, measure lines, and improve the line and continuum fits. For the CASH data, we determined that 5 iterations is the sweet spot between computational time and improvement to the continuum calculation and line fits. In order to test the accuracy of the Robospect measurements, we compared them with equivalent width measurements that were determined using manual methods for 5 CASH snapshot spectra. Each of these spectra represented a different S/N value, from 30-300. For S/N $\sim$ 65, the median S/N value for the HES data, we determined $\Delta_{ew} = 1 \pm 10$. This offset is of similar magnitude and uncertainty as that determined between our manual equivalent width measurements and those from Cayrel et al. (2004) and Hollek et al. (2011).

The equivalent width measurements are used in the stellar parameter and abundance pipeline, Cashcode. Cashcode is written around MOOG (Sneden, 1973; Sobeck et al., 2011) such that allows for an automatic iteration to determine a valid set of spectroscopic stellar parameters. It then creates a model atmosphere which is used to determine abundances from equivalent width measurements. Cashcode can also determine abundances based on spectral synthesis by using an equivalent width measurement of the line to create a set of 5 syntheses that vary in abundances, centered around the equivalent width-measured value. The code then interpolates between the syntheses to determine the best-fit abyundance. We tested Cashcode with a set of 15 stars for which we had snapshot spectra. We obtained high-resolution (R$\sim 35,000$)

spectra of these stars using the MIKE Spectrograph on the Magellan Clay Telescope to compare the results derived from each spectrum. For each high-resolution spectrum, we used a semi-automated equivalent width measurement program that fit gaussian profiles to each line profile. We used these equivalent widths to determine the stellar parameters and certain abundances in MOOG. We also derived abundances from synthesis for the high resolution spectra. When we compared these results to those of the Cashcode-derived results of the snapshot spectra, we find ΔT_{eff}=10 K, Δlog g = 0.0, $\Delta\xi = 0.05$, and Δ[Fe/H]= 0.02 dex. We find that the [X/Fe] values (where X is a given element) agree to within $\sim$ 0.05 dex.

Using the equivalent widths determined by Robospect, we used Cashcode to determine stellar parameters and abundances from equivalent width measurements and spectral synthesis for 262 stars using snapshot spectra as part of the CASH project. The stellar parameters were determined using the individual line abundances of Ti I, Ti II, Fe I and Fe II. The spectroscopic-based stellar parameters were then adjusted to better reflect those derived from photometry. A model atmosphere was then created using the derived stellar parameters and then used to determine the abundances of 10 species from equivalent width measurements (Mg I, Ca I, Sc II, Ti I, Ti II, Cr I, Mn I, Fe I, Fe II, and Ni I) and 8 species from syntheses (Li I, CH, O I, Zn I, Sr II, Y II, Zr II, and Ba II).

6.2 Results

6.2.1 Abundance Trends of the Full Sample

We reproduce the Spite plateau in the A(Li) values of our hottest sample stars. We find that for the majority of the evolved stars, there is a definite decrease in the A(Li) abundance, which reflects the depletion of Li over the course of stellar evolution due to convective mixing. The C abundances were difficult to accurately measure in our sample for the most C-rich stars. However, we generally reproduce the [C/Fe] distribution of Roederer et al. (2014).

Overall, we see no relation between metallicity, [Fe/H], and the [X/Fe] values of the $\alpha-$elements of Mg, Ca, and Ti. The exception to this is the O abundances, which have increasing [O/Fe] values with decreasing metallicity for both LTE and non-LTE corrected abundances. However, the non-LTE correction is likely insufficient when comparing the results of the CASH sample to those of Cayrel et al. (2004). We calculate [α/Fe] as [(Mg+Ca+TiII)/Fe] = 0.30 $\pm$0.01 over the full CASH sample, which agrees well with previous studies, including Roederer et al. (2014).

In general, the dispersions of the [X/Fe] ratios of other Fe-peak elements are larger than those of the $\alpha-$elements. This is likely due to the limited number of available lines and their locations, as Fe-peak elements tend to have fewer available features and most are in the blue portion of the spectrum, which is the lowest S/N region of the CASH snapshot spectra. The [X/Fe] ratios of Sc, Mn, and Ni show little relation to metallicity, while [Cr/Fe] decreases with decreasing metallicity and [Zn/Fe] increases with decreasing metallicity.

The neutron-capture elements available in the CASH spectra are primarily produced in the s-process. We find a similar spread in our abundances as Roederer et al. (2014) and Barklem et al. (2005). Ba is the most accessible neutron-capture element in our spectra and is measured in $> 99\%$ of the full sample. Sr is also measured in the vast majority of our stars, but it is in a much lower S/N region, thus has larger uncertainties than Ba. Y and Zr are less easily measured in the snapshot spectra than Ba and Sr; however, their abundances generally follow the overall trends of the other neutron-capture elements.

6.2.2 Extremely Metal-Poor Stars

In our calibration of Cashcode in Hollek et al. (2011), we selected the most metal-poor stars of the HES in the CASH sample. The overall trends of the CASH EMP stars match those of Cayrel et al. (2004) for the elements up to Zn and those of François et al. (2007) for the neutron-capture elements. Within this EMP sample, we identified four CEMP stars, four different neutron-capture element enhanced stars, and one binary candidate.

6.2.3 HE 0414−0343

As one of the goals of the CASH project is to discover unusual and interesting stars, we obtained a high-resolution follow-up spectrum of HE 0414−0343, identified from its snapshot spectrum to be CEMP, with an enhancement in the neutron-capture elements. We determined this star to be on the giant

branch, with [C/Fe] = 1.44. We also measured enhancement in the neutron-capture elements, such that the star could be further classified as "CEMP-r/s", following the prescription of Beers & Christlieb (2005). However, the origin of CEMP-r/s stars has still not been satisfactorily explained. Thus we investigated a sample of CEMP stars with neutron-capture element enhancements to explore the origins of these stars. These stars have traditionally been considered CEMP-r/s and CEMP-s stars.

6.3 Future Directions

The complete CASH sample is much larger than what is currently presented. Many of these stars were weeded out of the present study for various reasons. One of the largest groups of stars that are missing from the final sample are those that were contaminated by moonlight and therefore have the solar spectrum imprinted on their spectrum. Thus the measured continuum is incorrect. These stars could be added to the larger sample by processing out the Solar spectrum and then the previously described analysis could be performed. Preliminary results indicate that without processing these spectra, they give spuriously high microturbulence values and thus the stellar parameters are incorrect.

Another group of stars that were omitted were the CEMP stars. A somewhat accurate set of stellar parameters could be determined from these stars if lines blueward of 4500Å are excluded. Using photometry for these stars is undesirable because they often have bandheads that affect the magnitudes of

many wide-band photometric colors. Equivalent width measurements that are determined manually would likely yield the most accurate stellar parameters and then a C abundance could be easily determined. Adding these stars to the analysis would presumably increase the C frequency of the CASH sample.

We excluded stars that had spectra with S/N < 30. Some of these stars were considered low S/N because they have many cosmic ray hits interfering with their spectra. If these could be better cleaned, a reasonable stellar parameter and abundance determination might be possible. Many stars simply did not yield coherent stellar parameters. These stars could be further investigated to determine better stellar parameters and thus more accurate abundances. In fact, many of these are CEMP stars.

As noted previously, there were several interesting groups of stars discovered throughout the course of the CASH project. These stars merit follow up observations. These include the double-lined spectroscopic binary (DLSB) stars. Low-metallicity DLSB stars have not been well-studied. The work of Thompson et al. (2008) utilized a version of MOOG that enabled the study of DLSB spectra. This code, along with high-resolution observations of these stars would allow for an understanding of the abundance patterns of these stars.

Finally, we discovered two Li-enhanced giants in the sample. One of these is likely a CEMP star (Roederer et al., 2008) while the other shows no such C signature. High-resolution follow up of both of these stars would be beneficial to better determine their stellar parameters and abundances. This

would allow for a more exact determination of the evolutionary states, provide another radial velocity measurement to assess the possibility of binarity, and allow for further study of Li-enhanced giants.

Index

Bibliography

Abia, C., Busso, M., Gallino, R., et al. 2001, ApJ, 559, 1117

Alonso, A., Arribas, S., & Martínez-Roger, C. 1999, A&As, 140, 261

Andrievsky, S. M., Spite, M., Korotin, S. A., Spite, F., François, P., Bonifacio, P., Cayrel, R., & Hill, V. 2009, A&A, 494, 1083

Andrievsky, S. M., Spite, M., Korotin, S. A., Spite, F., Bonifacio, P., Cayrel, R., François, P., & Hill, V. 2010, A&A, 509, A88

Andrievsky, S. M., Spite, F., Korotin, S. A., François, P., Spite, M., Bonifacio, P., Cayrel, R., & Hill, V. 2011, A&A, 530, A105

Aoki, W., Beers, T. C., Christlieb, N., Norris, J. E., Ryan, S. G., & Tsangarides, S. 2007, ApJ, 655, 492

Aoki, W., Honda, S., Beers, T. C., Takada-Hidai, M., Iwamoto, N., Tominaga, N., Umeda, H., Nomoto, K., Norris, J. E., & Ryan, S. G. 2007b, ApJ, 660, 747

Arlandini, C., Käppeler, F., Wisshak, K., et al. 1999, ApJ, 525, 886

Asplund, M. 2005, ARA&A, 43, 481

Asplund, M., Lambert, D. L., Nissen, P. E., Primas, F., & Smith, V. V. 2006, ApJ, 644, 229

Asplund, M., Grevesse, N., Sauval, A. J., & Scott, P. 2009, ARA&A, 47, 481

Barklem, P. S., Christlieb, N., Beers, T. C., et al. 2005, A&A, 439, 129

Baumueller, D. & Gehren, T. 1997, A&A, 325, 1088

Beers, T. C. & Christlieb, N. 2005, ARA&A, 43, 531

Beers, T. C., Preston, G. W., & Shectman, S. A. 1985, AJ, 90, 2089

Beers, T. C., Preston, G. W., & Shectman, S. A. 1992, AJ, 103, 1987

Beers, T. C., Rossi, S., Norris, J. E., Ryan, S. G., & Shefler, T. 1999, AJ, 117, 981

Bergemann, M. & Gehren, T. 2008, A&A, 492, 823

Bernstein, R., Shectman, S. A., Gunnels, S. M., Mochnacki, S., & Athey, A. E. 2003, in Society of Photo-Optical Instrumentation Engineers (SPIE) Conference Series, ed. M. Iye & A. F. M. Moorwood, 1694

Bisterzo, S., Gallino, R., Straniero, O., & Aoki, W. 2009, Publications of the Astronomical Society of Australia, 26, 314

Bisterzo, S., Gallino, R., Straniero, O., Cristallo, S., Käppeler, F. 2011, MNRAS, 418, 284

Bohlin, R. C., Jenkins, E. B., Spitzer, L., York, D. G., Hill, J. K., Savage, B. D., & Snow, T. P. 1983, ApJS, 51, 277

Bonačić Marinović, A., Lugaro, M., Reyniers, M., & van Winckel, H. 2007, A&A, 472, L1

Bond, H. E. 1980, ApJS, 44, 517

Bonifacio, P., Molaro, P., Sivarani, T., Cayrel, R., Spite, M., Spite, F., Plez, B., Andersen, J., Barbuy, B., Beers, T. C., Depagne, E., Hill, V., François, P., Nordström, B., & Primas, F. 2007, A&A, 462, 851

Bromm, V. 2013, Reports on Progress in Physics, 76, 112901

Bromm, V., Coppi, P. S., & Larson, R. B. 1999, ApJ, 527, L5

Bromm, V., Coppi, P. S., & Larson, R. B. 2002, ApJ, 564, 23

Bromm, V. & Loeb, A. 2003, Nature, 425, 812

Brooke, J. S. A.,Bernath, P. F., Schmidt, T. W., & Backsay, G. B. 2013, J. Quant. Spec. Radiat. Transf., 124, 11

Busso, M., Gallino, R., & Wasserburg, G. J. 1999, ARA&A, 37, 239

Cameron, A. G. W., & Fowler, W. A. 1971, ApJ, 164, 111

Carney, B. W., Laird, J. B., Latham, D. W., & Aguilar, L. A. 1996, AJ, 112, 668

Carollo, D., Beers, T. C., Bovy, J., Sivarani, T., Norris, J. E., Freeman, K. C., Aoki, W., & Lee, Y. S. 2011, astro-ph/1103.3067

Cassisi, S., Castellani, M., Caputo, F., & Castellani, V. 2004, A&A, 426, 641

Castelli, F. & Kurucz, R. L. 2004, astro-ph/0405087

Cayrel, R. 1988, The Impact of Very High S/N Spectroscopy on Stellar Physics, 132, 345

Cayrel, R., Depagne, E., Spite, M., Hill, V., Spite, F., François, P., Plez, B., Beers, T., Primas, F., Andersen, J., Barbuy, B., Bonifacio, P., Molaro, P., & Nordström, B. 2004, A&A, 416, 1117

Christlieb, N. 2003, Reviews in Modern Astronomy, 16, 191

Christlieb, N., Wisotzki, L., Reimers, D., Homeier, D., Koester, D., & Heber, U. 2001, A&A, 366, 898

Christlieb, N., Bessell, M. S., Beers, T. C., Gustafsson, B., Korn, A., Barklem, P. S., Karlsson, T., Mizuno-Wiedner, M., & Rossi, S. 2002, Nature, 419, 904

Christlieb, N., Gustafsson, B., Korn, A. J., Barklem, P. S., Beers, T. C., Bessell, M. S., Karlsson, T., & Mizuno-Wiedner, M. 2004, ApJ, 603, 708

Christlieb, N., Beers, T. C., Barklem, P. S., Bessell, M.,Hill, V.,Holmberg, J., Korn, A. J., Marsteller,B.,Mashonkina, L.,Qian, Y.-Z.,Rossi, S.,Wasserburg, G. J.,Zickgraf, F.-J.,Kratz, K.-L., Nordström, B.,Pfeiffer, B.,Rhee, J.,Ryan, S. G. 2004, A&A, 428, 1027

Clark, P. C., Glover, S. C. O., Smith, R. J., et al. 2011, Science, 331, 1040

Cohen, J. G., McWilliam, A., Shectman, S., Thompson, I., Christlieb, N., Melendez, J., Ramirez, S., Swensson, A., & Zickgraf, F.-J. 2006, AJ, 132, 137

Cui, W. Y., Sivarani, T., & Christlieb, N. 2013, A&A, 558, A36

De Smedt, K., Van Winckel, H., Karakas, A. I., et al. 2012, A&A, 541, A67

Fabbian, D., Asplund, M., Barklem, P. S., Carlsson, M., & Kiselman, D. 2009, A&A, 500, 1221

François, P., Depagne, E., Hill, V., et al. 2003, A&A, 403, 1105

François, P., Depagne, E., Hill, V., et al. 2007, A&A, 476, 935

Frebel, A. 2010, Astronomische Nachrichten, 331, 474

Frebel, A., Aoki, W., Christlieb, N., Ando, H., Asplund, M., Barklem, P. S., Beers, T. C., Eriksson, K., Fechner, C., Fujimoto, M. Y., Honda, S., Kajino, T., Minezaki, T., Nomoto, K., Norris, J. E., Ryan, S. G., Takada-Hidai, M., Tsangarides, S., & Yoshii, Y. 2005, Nature, 434, 871

Frebel, A., Christlieb, N., Norris, J. E., Beers, T. C., Bessell, M. S., Rhee, J., Fechner, C., Marsteller, B., Rossi, S., Thom, C., Wisotzki, L., & Reimers, D. 2006, ApJ, 652, 1585

Frebel, A., Christlieb, N., Norris, J. E., Thom, C., Beers, T. C., & Rhee, J. 2007, ApJ, 660, L117

Frebel, A., Johnson, J. L., & Bromm, V. 2007a, MNRAS, 380, L40

Frebel, A., Norris, J. E., Aoki, W., Honda, S., Bessell, M. S., Takada-Hidai, M., Beers, T. C., & Christlieb, N. 2007b, ApJ, 658, 534

Frebel, A., Simon, J. D., Geha, M., & Willman, B. 2010, ApJ, 708, 560

Frebel, A., Casey, A. R., Jacobson, H. R., & Yu, Q. 2013, ApJ, 769, 57

Frebel, A. & Norris, J. E. 2013, Metal-Poor Stars and the Chemical Enrichment of the Universe, 55

Fryer, C. L., Woosley, S. E., & Heger, A. 2001, ApJ, 550, 372

Fulbright, J. P. 2000, AJ, 120, 1841

Fulbright, J. P. 2000, AJ, 120, 1841

Fulbright, J. P., & Johnson, J. A. 2003, ApJ, 595, 1154

Gallino, R., Arlandini, C., Busso, M., Lugaro, M., Travaglio, C., Straniero, O., Chieffi, A., & Limongi, M. 1998, ApJ, 497, 388

García Pérez, A. E. & Primas, F. 2006, A&A, 447, 299

Gehrz, R. 1989, Interstellar Dust, 135, 445

Goriely, S., & Siess, L. 2005, From Lithium to Uranium: Elemental Tracers of Early Cosmic Evolution, 228, 451

Gratton, R. G., Sneden, C., Carretta, E., & Bragaglia, A. 2000, A&A, 354, 169

Gratton, R., Sneden, C., & Carretta, E. 2004, ARA&A, 42, 385

Gratton, R. G. & Sneden, C. 1988, A&A, 204, 193

Green, E. M., Demarque, P., & King, C. R. 1984, BAAS, 16, 997

Hansen, C. J., Bergemann, M., Cescutti, G., et al. 2013, A&A, 551, A57

Harris, D. L., III 1948, ApJ, 108, 112

Heger, A. & Woosley, S. E. 2010, ApJ, 724, 341

Hill, V., Plez, B., Cayrel, R., Nordström, T. B. B., Andersen, J., Spite, M., Spite, F., Barbuy, B., Bonifacio, P., Depagne, E., François, P., & Primas, F. 2002, A&A, 387, 560

Hollek, J. K., Frebel, A., Roederer, I. U., et al. 2011, ApJ, 742, 54

Hollek, J. K., Frebel, A., Roederer, I. U., Sneden, C., Shetrone, M., Beers, T. C., Kang, S.-j., & Thom, C. 2011, ApJ, 742, 54

Hosokawa, T., Omukai, K., Yoshida, N., & Yorke, H. W. 2011, Science, 334, 1250

Jonsell, K., Barklem, P. S., Gustafsson, B., Christlieb, N., Hill, V., Beers, T. C., & Holmberg, J. 2006, A&A, 451, 651

Karakas, A. I. 2010, MNRAS, 403, 1413

Karakas, A. I., Campbell, S. W., & Stancliffe, R. J. 2010, ApJ, 713, 374

Keeping, E. S. 1962, Introduction to Statistical Inference (Princeton,N.J.: Van Nostrand)

Keller, S. C., Bessell, M. S., Frebel, A., et al. 2014, Nature, 506, 463

Kelson, D. D. 2003, PASP, 115, 688

Kim, Y.-C., Demarque, P., Yi, S. K., & Alexander, D. R. 2002, ApJS, 143, 499

Kirby, E. N., Fu, X., Guhathakurta, P., & Deng, L. 2012, ApJ, 752, L16

Kobayashi, C., Tominaga, N., & Nomoto, K. 2011, ApJ, 730, L14

Kurucz, R. L. 1993, Kurucz CD-ROM 13, ATLAS9 Stellar Atmosphere Programs and 2 km/s Grid, Cambridge: SAO

Kurucz, R. L. 1998, in IAU Symposium, Vol. 189, Fundamental Stellar Properties, ed. T. R. Bedding, A. J. Booth, & J. Davis, 217

Lai, D. K., Bolte, M., Johnson, J. A., et al. 2008, ApJ, 681, 1524

Lawler, J. E., Guzman, A., Wood, M. P., Sneden, C., & Cowan, J. J. 2013, ApJS, 205, 11

Lee, Y. S., Beers, T. C., Sivarani, T., et al. 2008, AJ, 136, 2022

Lemasle, B., François, P., Bono, G., et al. 2007, A&A, 467, 283

Li, H. N., Christlieb, N., Schörck, T., Norris, J. E., Bessell, M. S., Yong, D., Beers, T. C., Lee, Y. S., Frebel, A., & Zhao, G. 2010, A&A, 521, 10

Lucatello, S., Tsangarides, S., Beers, T. C., Carretta, E., Gratton, R. G., & Ryan, S. G. 2005, ApJ, 625, 825

Lucatello, S., Beers, T. C., Christlieb, N., Barklem, P. S., Rossi, S., Marsteller, B., Sivarani, T., & Lee, Y. S. 2006, ApJ, 652, L37

Ludwig, R. R., Greene, J. E., Barth, A. J., & Ho, L. C. 2012, ApJ, 756, 51

Lugaro, M., Karakas, A. I., Stancliffe, R. J., & Rijs, C. 2012, ApJ, 747, 2

Marigo, P., Bressan, A., Nanni, A., Girardi, L., & Pumo, M. L. 2013, MNRAS, 434, 488

Mashonkina, L., Ryabtsev, A., & Frebel, A. 2012, A&A, 540, A98

Masseron, T., Johnson, J. A., Plez, B., van Eck, S., Primas, F., Goriely, S., & Jorissen, A. 2010, A&A, 509, 93

Mathews, G. J., & Cowan, J. J. 1990, Nature, 345, 491

McWilliam, A. 1997, ARA&A, 35, 503

McWilliam, A., Preston, G. W., Sneden, C., & Searle, L. 1995, AJ, 109, 2757

Meléndez, J., Casagrande, L., Ramírez, I., Asplund, M., &Schuster, W. J. 2010, A&A, 515, 3

Meynet, G., Ekström, S., & Maeder, A. 2006, A&A, 447, 623

Moore, C. E., Minnaert, M. G. J., & Houtgast, J. 1966, The solar spectrum 2935 A to 8770 A

Nomoto, K., Tominaga, N., Umeda, H., Kobayashi, C., & Maeda, K. 2006, Nuclear Physics A, 777, 424

Norris, J. E., Christlieb, N., Korn, A. J., Eriksson, K., Bessell,M. S., Beers, T. C., Wisotzki, L., & Reimers, D. 2007, ApJ, 670, 774

Norris, J. E., Gilmore, G., Wyse, R. F. G., Yong, D., & Frebel, A. 2010a, ApJ, 722, L104

Norris, J. E., Wyse, R. F. G., Gilmore, G., Yong, D., Frebel, A.,Wilkinson, M. I., Belokurov, V., & Zucker, D. B. 2010b,ApJ, 723, 1632

Pellegrini, E. W., Baldwin, J. A., & Ferland, G. J. 2010, ApJS, 191, 160

Piskunov, N. E. & Valenti, J. A. 2002, A&A, 385, 1095

Placco, V. M., Frebel, A., Beers, T. C., Karakas, A. I., Kennedy, C. R., Rossi, S., Christlieb, N., & Stancliffe, R. J. 2013, ApJ, 770, 104

Placco, V. M., Beers, T. C., Roederer, I. U., et al. 2014, ApJ, 790, 34

Qian, Y.-Z., & Wasserburg, G. J. 2003, ApJ, 588, 1099

Ram, R. S., Brooke, J. S. A., Bernath, P. F., Sneden, C., & Lucatello, S. 2013, ApJS, Submitted

Ramírez, I. & Meléndez, J. 2004, ApJ, 609, 417

Roederer, I. U., Frebel, A., Shetrone, M. D., Allende Prieto, C.,Rhee, J., Gallino, R., Bisterzo, S., Sneden, C., Beers, T. C., &Cowan, J. J. 2008, ApJ, 679, 1549

Roederer, I. U., Sneden, C., Thompson, I. B., Preston, G. W., & Shectman, S. A. 2010, ApJ, 711, 573

Roederer, I. U., Preston, G. W., Thompson, I. B., et al. 2014, AJ, 147, 136

Roederer, I. U., & Lawler, J. E. 2012, ApJ, 750, 76

Rossi, S., Beers, T. C., Sneden, C., Sevastyanenko, T., Rhee, J., & Marsteller, B. 2005, AJ, 130, 2804

Ryan, S. G. & Deliyannis, C. P. 1998, ApJ, 500, 398

Ryan, S. G., Beers, T. C., Deliyannis, C. P., & Thorburn, J. A. 1996, ApJ, 458, 543

Ryan, S. G., Aoki, W., Norris, J. E., & Beers, T. C. 2005, ApJ, 635, 349

Ryan, S. G. & Norris, J. E. 1991, AJ, 101, 1835

Sbordone, L., Bonifacio, P., Caffau, E., et al. 2010, A&A, 522, A26

Schlegel, D. J., Finkbeiner, D. P., & Davis, M. 1998, ApJ, 500, 525

Schörck, T., Christlieb, N., Cohen, J. G., Beers, T. C.,Shectman, S., Thompson, I., McWilliam, A., Bessell, M. S., Norris,J. E., Meléndez, J., Ramírez, S., Haynes, D., Cass, P.,Hartley, M., Russell, K., Watson, F., Zickgraf, F., Behnke, B.,Fechner, C., Fuhrmeister, B., Barklem, P. S., Edvardsson, B.,Frebel, A., Wisotzki, L., & Reimers, D. 2009, A&A, 507, 817

Shetrone, M., Cornell, M. E., Fowler, J. R., et al. 2007, PASP, 119, 556

Sterling, N. C., Dinerstein, H. L., Bowers, C. W., & Redfield, S. 2005, ApJ, 625, 368

Simmerer, J., Sneden, C., Cowan, J. J., Collier, J., Woolf, V. M., & Lawler, J. E. 2004, ApJ, 617, 1091

Sivarani, T., Beers, T. C., Bonifacio, P., et al. 2006, A&A, 459, 125

Smith, V. V., & Lambert, D. L. 1990, ApJS, 72, 387

Sneden, C. A. 1973, PhD thesis, The University of Texas at Austin

Sneden, C., Cowan, J. J., Ivans, I. I., Fuller, G. M., Burles, S., Beers, T. C., & Lawler, J. E. 2000, ApJ, 533, L139

Sneden, C., Cowan, J. J., Lawler, J. E., Ivans, I. I., Burles, S., Beers, T. C., Primas, F., Hill, V., Truran, J. W., Fuller, G. M., Pfeiffer, B., & Kratz, K.-L. 2003, ApJ, 591, 936

Sneden, C., Cowan, J. J., & Gallino, R. 2008, ARA&A, 46, 241

Sobeck, J. S., Kraft, R. P., Sneden, C., Preston, G. W., Cowan, J. J., Smith, G. H., Thompson, I. B., Shectman, S. A., & Burley, G. S. 2011, AJ, 141, 175

Sobeck, J. S., Kraft, R. P., Sneden, C., Preston, G. W., Cowan, J. J., Smith, G. H., Thompson, I. B., Shectman, S. A., & Burley, G. S. 2011, AJ, 141, 175

Spite, F. & Spite, M. 1982, A&A, 115, 357

Stacy, A., Greif, T. H., & Bromm, V. 2010, MNRAS, 403, 45

Stacy, A., Greif, T. H., & Bromm, V. 2012, MNRAS, 422, 290

Starkenburg, E., Shetrone, M. D., McConnachie, A. W., & Venn, K. A. 2014, MNRAS, 441, 1217

Stetson, P. B., & Pancino, E. 2008, PASP, 120, 1332

Tegmark, M., Silk, J., Rees, M. J., et al. 1997, ApJ, 474, 1

Thompson, I. B., Ivans, I. I., Bisterzo, S., et al. 2008, ApJ, 677, 556

Travaglio, C., Gallino, R., Arnone, E., Cowan, J., Jordan, F., & Sneden, C. 2004, ApJ, 601, 864

Tull, R. G. 1998, in Society of Photo-Optical Instrumentation Engineers (SPIE) Conference, Vol. 3355, Optical Astronomical Instrumentation, ed. S. D'Odorico, 387

Turk, M. J., Abel, T., & O'Shea, B. 2009, Science, 325, 601

Vassiliadis, E. & Wood, P. R. 1993, ApJ, 413, 641

Wallace, L., Hinkle, K. H., Livingston, W. C., & Davis, S. P. 2011, ApJS, 195, 6

Waters, C. Z. & Hollek, J. K. 2013, PASP, 125, 1164

Wisotzki, L., Christlieb, N., Bade, N., et al. 2000, A&A, 358, 77

Wood, M. P., Lawler, J. E., Sneden, C., & Cowan, J. J. 2013, ApJS, 208, 27

Woosley, S. E. & Weaver, T. A. 1995, ApJS, 101, 181

Yanny, B., Rockosi, C., Newberg, H. J., et al. 2009, AJ, 137, 4377

Yong, D., Norris, J. E., Bessell, M. S., et al. 2013, ApJ, 762, 26

York, D. G., Adelman, J., Anderson, J. E., Jr., et al. 2000, AJ, 120, 1579